Fall 2011

Three dimensional sharp interface Eulerian computations of multi-material flows

Anil Kapahi
University of Iowa

Recommended Citation

Kapahi, Anil. "Three dimensional sharp interface Eulerian computations of multi-material flows." PhD (Doctor of Philosophy) thesis, University of Iowa, 2011.
https://doi.org/10.17077/etd.tlzxut6o

Follow this and additional works at: https://ir.uiowa.edu/etd
Part of the Mechanical Engineering Commons

THREE DIMENSIONAL SHARP INTERFACE EULERIAN COMPUTATIONS OF MULTI-MATERIAL FLOWS

by

Anil Kapahi

An Abstract

Of a thesis submitted in partial fulfillment
of the requirements for the Doctor of
Philosophy degree in Mechanical Engineering
in the Graduate College of
The University of Iowa

December 2011

Thesis Supervisor: Professor H.S. Udaykumar

ABSTRACT

This work presents a three-dimensional, Eulerian, sharp interface, Cartesian grid-technique for simulating the response of elasto-plastic solid materials to hypervelocity impact, shocks and detonations. The mass, momentum and energy equations are solved along with evolution equations of deviatoric stress and plastic strain using a higher order shock capturing Essentially Non-Oscillatory scheme (ENO). Material deformation occurs with accompanying nonlinear stress wave propagation; in the Eulerian framework the boundaries of the deforming material are tracked in a sharp fashion using level sets and the conditions on the boundaries are applied by suitable modifications of a ghost fluid approach. The dilatational response of material is modeled using the Mie-Gruneisen equation of state and the Johnson-Cook model is employed to characterize the material response due to rate-dependent plastic deformation. This work deals with modification of deviatoric stress ghost state so that physically correct boundary conditions can be applied at the material interfaces. An efficient parallel algorithm is used to handle computationally intensive three-dimensional problems. The computer code developed in this work is then used to solve several problems in high speed impact phenomena. Numerous examples pertaining to impact, penetration, void collapse and fragmentation phenomena are presented along with careful benchmarking to establish the validity, accuracy and versatility of the approach.

A detailed analysis of the response of a porous energetic material exposed to severe loadings (that are likely to trigger explosion) is studied using the established framework. Important insights into the effect of porosity on the material response to imposed shock loadings are obtained.

Abstract Approved: ______________________________

Thesis Supervisor

____

Title and Department

____

Date

THREE DIMENSIONAL SHARP INTERFACE EULERIAN COMPUTATIONS OF MULTI-MATERIAL FLOWS

by

Anil Kapahi

A thesis submitted in partial fulfillment
of the requirements for the Doctor of
Philosophy degree in Mechanical Engineering
in the Graduate College of
The University of Iowa

December 2011

Thesis Supervisor: Professor H.S.Udaykumar

Graduate College
The University of Iowa
Iowa City, Iowa

CERTIFICATE OF APPROVAL

PH.D. THESIS

This is to certify that the Ph.D. thesis of

Anil Kapahi

has been approved by the Examining Committee
for the thesis requirement for the Doctor of Philosophy
degree in Mechanical Engineering at the December 2011 graduation.

Thesis Committee: ______________________________
H.S.Udaykumar, Thesis Supervisor

____
Christoph Beckermann

____
Albert Ratner

____
Colby Swan

____
Olesya Zhupanska

ACKNOWLEDGMENTS

It is my pleasure to thank number of people who contributed to the completion of this thesis. First and foremost I offer my sincerest gratitude to my supervisor, Dr. H.S.Udaykumar, who has supported me throughout my thesis with his patience and knowledge. The best thing about Uday is the way he let you do things in your own way. Under his guidance, I learnt a lot and one could not wish for a better supervisor.

I would like to sincerely thank members of my committee. They have generously given their expertise and time to make this thesis better.

Sincere thanks to my family in India for their love and support throughout my life.

I would also like to thank all my past and present lab mates. Their friendship and knowledge have entertained and enlightened me for many years. I should also thank the staff members of Department of Mechanical Engineering for their help for last five years.

Very special thanks to my girlfriend Rohini for her patience and support when I was only thinking about Ghost Fluid Method.

This work was performed under grants from the AFOSR Computational Mathematics program (Program Manager: Dr. Fariba Fahroo) and from the AFRL-RWPC (Computational Mechanics Branch, Eglin AFB, Program Manager: Dr. Michael E. Nixon).

ABSTRACT

This work presents a three-dimensional, Eulerian, sharp interface, Cartesian grid-technique for simulating the response of elasto-plastic solid materials to hypervelocity impact, shocks and detonations. The mass, momentum and energy equations are solved along with evolution equations of deviatoric stress and plastic strain using a higher order shock capturing Essentially Non-Oscillatory scheme (ENO). Material deformation occurs with accompanying nonlinear stress wave propagation; in the Eulerian framework the boundaries of the deforming material are tracked in a sharp fashion using level sets and the conditions on the boundaries are applied by suitable modifications of a ghost fluid approach. The dilatational response of material is modeled using the Mie-Gruneisen equation of state and the Johnson-Cook model is employed to characterize the material response due to rate-dependent plastic deformation. This work deals with modification of deviatoric stress ghost state so that physically correct boundary conditions can be applied at the material interfaces. An efficient parallel algorithm is used to handle computationally intensive three-dimensional problems. The computer code developed in this work is then used to solve several problems in high speed impact phenomena. Numerous examples pertaining to impact, penetration, void collapse and fragmentation phenomena are presented along with careful benchmarking to establish the validity, accuracy and versatility of the approach.

A detailed analysis of the response of a porous energetic material exposed to severe loadings (that are likely to trigger explosion) is studied using the established framework. Important insights into the effect of porosity on the material response to imposed shock loadings are obtained.

TABLE OF CONTENTS

LIST OF TABLES

LIST OF FIGURES

CHAPTER 1

INTRODUCTION

The phenomena of high speed impact are of interest in many applications including munitions-target interactions [1], geological impact dynamics [2], shock processing of powders [3], outer space explosions [4], material coating [5], formation of shaped charges [6], etc. Some of these applications are shown in Figure 1-1 and Figure 1-2. The large kinetic energies imposed in impact and penetration problems or in shock loading of materials is dissipated by plastic deformation of the material. Under the high-strain rate deformation conditions, the stress and strain fields are related through non-linear rate-dependent elasto-plastic yield surfaces [7]. Wave propagation in the interacting media is highly nonlinear and may result in localized phenomena such as shear bands, crack propagation, fracture and/or complete failure of the material. The two main components for simulating high speed flows are efficient numerical schemes to: 1) handle embedded interfaces as sharp entities through events like total fragmentation and 2) large scale computational setup to handle large deformation in realistic three dimensional problems. These two key components are addressed and devised in this work.

1.1 Motivation

Traditionally, the tools that have been used to solve problems involving high speed material dynamics have been termed hydrocodes [8], with the view that even when the materials are solids the nature of the material response places it in the category of a ―flow problem”. The broad range of available hydrocodes has been reviewed by [9] and [8]. The literature for two-dimensional and axis-symmetric problems for high speed impact and penetration type problems is vast[7, 10-12] . However, there are very few methods which have been extended to three dimensions to solve meaningful physical problems. To date, the test cases for high-speed impact and penetration problems in three dimensions involving hundreds of processors have been reported by very few researchers[13-18]. For example, Belytschko et al. [17] used a meshless method, the element-free Galerkin (EFG) method to simulate inclined Taylor bar impact, the method was then modified to extended element-free Galerkin (XEFG) to study crack initiation and propagation[19] . A commonly used approach for high velocity impact and penetration is the ALE method[20], used to simulate Taylor bar impacts and fluid-structure interaction problems in underwater explosions. Zhou et al. [16] have used smooth particle hydrodynamics (SPH) method to solve high velocity impact and penetration problem. A class of FEM methods such as parallel point interpolation method (PIM) [15], PRONTO3D code [14] have been used to simulate Taylor bar impact and an oblique impact of metal sphere[21] respectively. Ma et al. [22] have used material point method (MPM) to simulate impact and explosion problems and have also done the comparison [22, 23] of MPM method to FEM and SPH methods. Apart from these researchers, scientific establishments such as the Los Alamos National Labs have rather large investments of personnel and efforts to develop multi-material three-dimensional computer codes, such as the PAGOSA[18] code. Despite these large investments, however, a reliable, efficient and accurate facility for high speed multimaterial flow computation remains a matter of research and the present work represents work at the leading edge of research in this area.

1.2 Lagrangian v/s Eulerian

In this work, a sharp interface Cartesian grid-based flow code is developed to solve high-speed impact, collision, penetration and fragmentation type problems in three dimensional Eulerian setting using hundreds of processors. To place the present approach in perspective, a brief review of alternatives is presented.

The methods of choice for solving high-speed flow problems can be broadly categorized into Eulerian and Lagrangian. Both Lagrangian and Eulerian frameworks have been identified with certain issues and take different paths in formulating large deformation problems in elasto-plastically deforming materials[24, 25]. The major points of discussion related to these frameworks can be summarized as:

- Flow solvers can be based on a Lagrangian formulation, such as in EPIC and DYNA, where a moving unstructured mesh is used to follow the deformation, or an Eulerian formulation, such as CTH [11], where a fixed mesh is used and the boundaries are tracked through the mesh [26]. An intermediate approach, ALE (Arbitrary Lagrangian Eulerian) [8], combines Eulerian and Lagrangian frame of reference, allows the mesh to move so as to conform to the contours of the deforming object, but the mesh is not necessarily attached to material points [7]. The Lagrangian and to a lesser extent ALE methods have to contend with mesh entanglement and the burden of mesh management encountered frequently in large deformation problems. Therefore, for very large deformations which may include fragmentation of the interacting materials, the use of immersed boundary Eulerian methods relying on a fixed global mesh has emerged as a promising alternative.
- The definition of stress measure is different in Lagrangian and Eulerian methods with Cauchy stress tensor being used in Eulerian description and Piola-Kirchhoff stress tensor for Lagrangian description. The same is true with strain measures. The reason for different stress and strain measures is due to different reference configurations, which is the current configuration in Eulerian description and the initial configuration in Lagrangian description. This discrepancy occurs only for large deformation problems as in small deformation problems the difference between these reference configurations is almost negligible.
- Lagrangian methods adopt a multiplicative decomposition of deformation gradients [27] and a hyperelastic model for the elastic deformation [25]. Due to the presumed existence of a mapping to the undeformed state through the flow

process, they operate on the Piola-Kirchhoff stress tensor. For the severe deformation cases of interest in this work Xiao et al. [25] point out that the multiplicative model assumes the presence of an ―intermediate" configuration which can be mapped on to the original undeformed state. However, such an intermediate configuration may not satisfy geometric uniqueness[25]. Furthermore, it is not clear how a mapping to the original geometry is relevant following complete fragmentation and ejection of debris. The Eulerian methodology is typically based on an additive decomposition of the strain rate tensor [28]. In terms of constitutive laws, the elastic part of the deformation is governed by hypoelasticity in the Eulerian framework. There is an issue of non-integrability in the hypoelastic model which results in elastic dissipation by not fully recovering the elastic part of strain[25]; however, in simulations involving high speed impact and penetration elastic strains are rather negligible and of little interest when compared to the plastic strain.

- Another concern with Eulerian formulations is with regard to oscillatory solutions for a simple shear problem[29]; this problem has been shown to be resolved by using the objective rates such as Jaumann rate [28] for stress update.
- Another important issue related to this work is the loss/gain of mass of small filaments of material comparable to grid size undergoing a very large deformation [30, 31]. The level set methods used in this work incorporates periodic reinitialization [32] and velocity extension procedure [33] which help in minimizing errors related to mass conservation. On the contrary, the Lagrangian methods incorporate erosion techniques[34] to remove highly distorted elements formed due to severe compression and distortion faced in high speed impact and penetration problems.

Considering these issues, Eulerian methods are attractive due to the simplicity accruing from use of a fixed global grid, use of true stress state represented by the Cauchy stress tensor, and the ease of handling of contact and penetration using embedded interfaces.

1.3 Eulerian Methodology

In a traditional Eulerian approach, coexisting phases are carried through computational cells as a –mixed” material and a suitable mixture formulation is adopted to account for the dynamics of this mixed material[35]. These methods have limitations in terms of the number of materials that can be defined in a single computational cell as algorithms can become very complicated in defining the mixture properties and associated constitutive laws[9]; these latter are ad hoc models that cannot be tested against physical reality and therefore rest on rather tenuous foundations. They also tend to create numerical difficulties in the presence of strong shocks, associated with non-physical wave speeds that can arise from the ad hoc equation of state for pressure.

In a sharp interface method, in contrast with mixed-material type Eulerian methods , the interacting materials are sharply delineated by a tracked boundary[36]. Boundary conditions for flowfield solutions in the two distinct media are applied at the interface location. The advantage of the sharp interface treatment is that issues associated with defining mixture properties and constitutive laws are circumvented; on the other hand, care must be exercised in imposing physically correct boundary conditions on the (possibly highly distorted) embedded boundary. This approach was developed in several previous papers for the two-dimensional case [7, 26] for arbitrary material pairs and shock strengths.

In contrast, the present work develops the idea of treating all interfaces as sharp entities[10, 21-23], with fields on either side treated as comprised of distinct materials. A modified Ghost Fluid Method (GFM) [37] is applied to treat the embedded interface. In contrast to [9, 10], where the discretization scheme was modified to incorporate the boundary conditions at the interface, the present method decouples the discretization scheme from interface capturing. The present work addresses this issue by evaluating techniques to infuse the boundary conditions into the ghost cells. The interaction of the embedded boundaries with each other and the evolution of free boundaries is treated by applying appropriate boundary conditions at the resulting material-material and material-void boundaries[38-40]. The extension to three dimensions is demonstrated and the issues that arise in specifying interface conditions and solving the system in a parallelized computational framework are addressed.

1.4 Accomplishments of the Present Work

Large-scale computations are required to simulate the physical phenomena involving detonation and shock waves in supernova formation, explosions, hypervelocity impact, penetration and fragmentation phenomena. The fundamental challenges involved in these problems are presence of the non- linear wave propagation and the large deformations suffered by the interacting media [26].The interaction of these waves with multi-materials can result in a complex wave structures in two and three dimensions. In addition, the embedded materials may experience large motions and deformation under the influence of the high-speed flows. The hydrodynamic pressures realized in such problems often overwhelm the strength of the material[9], leading to short transients of elastic deformation followed by drastic plastic flow of the material. The fundamental challenges to a simulation capability designed to solve problems involving the physical phenomena listed above arise from the large deformations, culminating in total fragmentation of materials, occurring under high strain-rate conditions [26].

Numerical simulations of high speed impact and penetration phenomenon require vast computing power due to large deformations, number of time steps and other complex issues related to handling of contact[34]. Due to these challenges, any realistic simulation of a three dimensional problem requires handling of enormous amount of data making parallelization of computer codes inevitable. In this work, the main focus is on parallel implementation of a fixed Cartesian grid flow solver with moving boundaries. A higher order conservation scheme such as ENO (Essentially Non-Oscillatory)[41] is used for calculating the numerical fluxes and level sets are used to define the objects immersed in the flow field. Collisions between embedded objects are resolved using an efficient collision detection algorithm[40] and appropriate interfacial conditions are supplied. Key issues of supplying interfacial conditions at the location of the interface and populating the ghost cells with physically consistent values during and beyond fragmentation events are addressed in three dimensional setting.

The issues involved in parallelization of the moving boundary solver are presented with emphasis on strong shocks interacting with embedded interfaces (solid-solid) in the three-dimensional compressible flow framework. The handling of moving boundaries, tracked using narrow-band level sets leads to issues peculiar to the multi-processor environment; the solution to object passage between subdomains and treatment of ghost regions for inter-processor communication are also addressed. Numerous examples pertaining to impact, penetration, void collapse and fragmentation phenomena are presented along with careful benchmarking to establish the validity, accuracy and versatility of the approach.

Finally, the computer code developed in this work is used to study the response of an energetic material exposed to severe loadings (that are likely to trigger explosion). Fresh insights into the response of the material to shock loading as a function of the porosity content are obtained from the calculations. These case studies show the power of the techniques developed in analyzing the mechanics of complex materials to high-speed impact and high-strain rate loading.

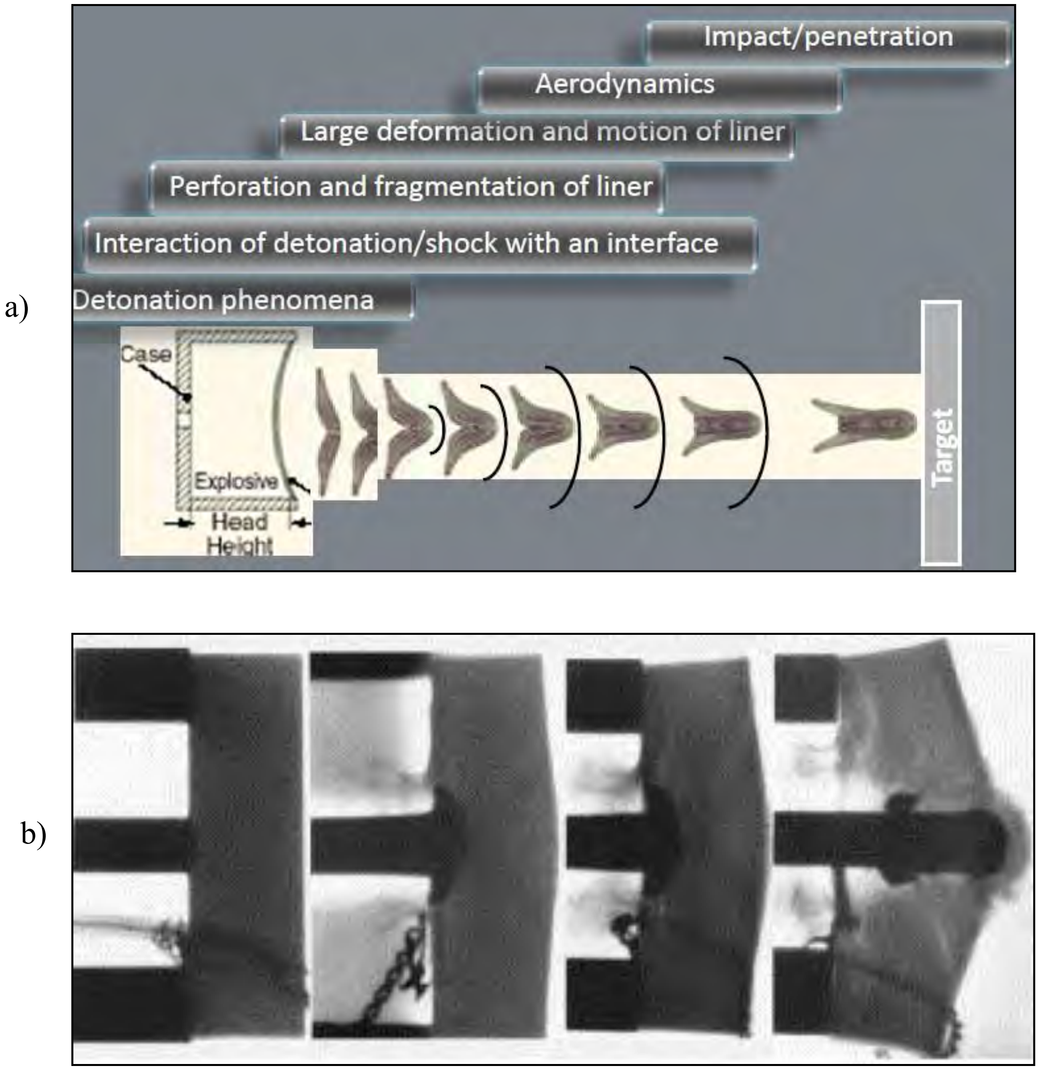

Figure 1-1.Applications: a) Formation of shape charges involving various physical phenomena ranging from detonation of an explosive to final penetration of the target. Picture courtesy: Wikipedia. b) Penetration of steel rod travelling at 540m/s into borosilicate glass. Picture courtesy: Bourne et al. J. Phys. IV France 7(C3) 157-162.

a)

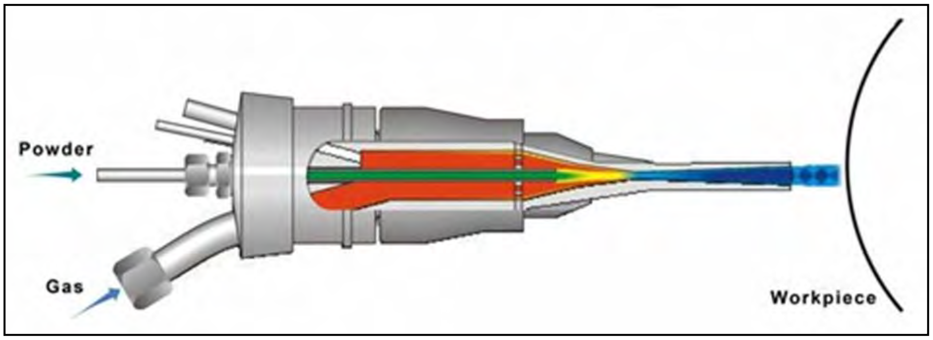

b)

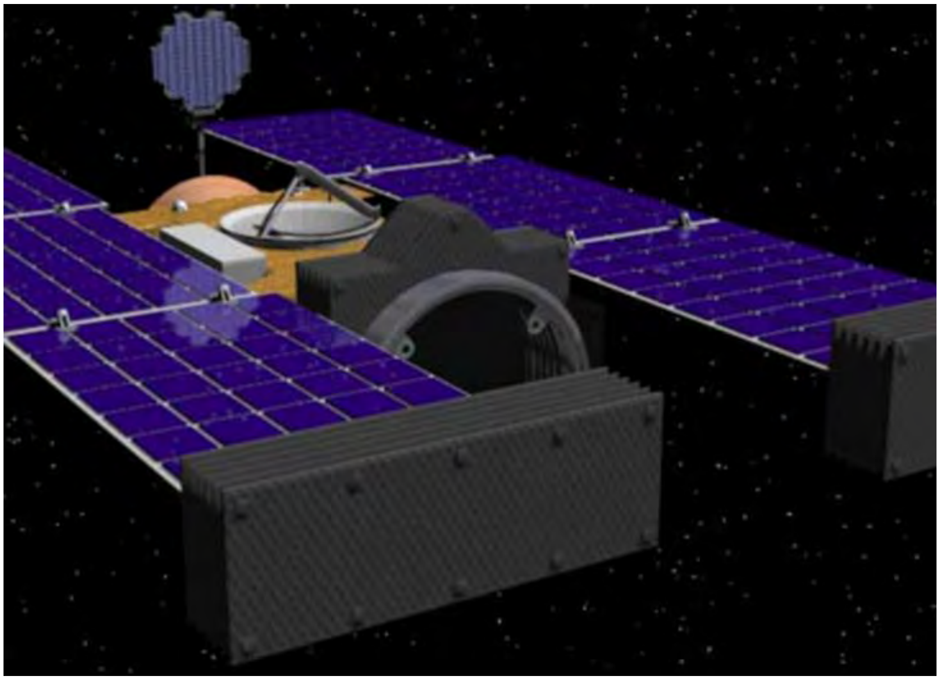

Figure 1-2. Applications a) Shock processing of material using cold gas dynamic spraying b) Whipple shield used on spacecraft to protect them from micrometeoroids and outer space debris.

CHAPTER 2

GOVERNING EQUATIONS

2.1 Governing Equations

Cast in Cartesian coordinates, the governing equations for the mechanics of materials experiencing compressible flow and deformation take the following form:

Mass balance:

$$\frac{\partial \rho}{\partial t} + div(\rho \vec{V}) = 0 \tag{2.1}$$

Momentum balance

$$\frac{\partial \rho \vec{V}}{\partial t} + div(\rho \vec{V} \otimes \vec{V} - \boldsymbol{\sigma}) = 0 \tag{2.2}$$

Energy balance:

$$\frac{\partial \rho E}{\partial t} + div(\rho E \vec{V} - \boldsymbol{\sigma} \cdot \vec{V}) = 0 \tag{2.3}$$

Evolution of deviatoric stresses in the case of a solid material:

$$\frac{\partial \rho \mathbf{S}}{\partial t} + div(\rho \vec{V} \mathbf{S}) + \frac{2}{3} \rho G tr(\mathbf{D}) \mathbf{I} - 2\rho G \mathbf{D} = 0 \tag{2.4}$$

In Eqs. 2.1-2.4, $\vec{V}$ is the velocity vector, ρ is the material density and E is the specific total energy of the material. The stress state of material is given by the Cauchy (true) stress tensor $\boldsymbol{\sigma}$ which consists of a deviatoric $\boldsymbol{S}$ and a dilatational part P. The strain rate tensor is denoted by $\boldsymbol{D}$ and G is the shear modulus of material. The integration of the mass, momentum and energy balance laws along with the evolution of the deviatoric stress components are performed assuming a pure elastic deformation (i.e. freezing the plastic flow) as an elastic predictor step, followed by a radial return mapping to bring the predicted stress back to the yield surface [42]. Eqs. 2.1-2.4 are cast in hyperbolic conservation law form in a conservative formulation with conserved variable, flux and source vectors are given in section 2.4. Other details pertaining to constitutive equations, radial return algorithm and the Mie-Gruneisen equation for determining dilatational response have been laid out in [26] and are reproduced in this chapter for completeness.

2.2 Material Models

The two main models used in this work for strain hardening materials are the rate independent Prandtl-Ruess material model [28] (Eq 2.5) and thermal softening based Johnson-Cook material model [43] (Eq 2.6), which are respectively:

$$\sigma_Y = A + B\left(\bar{\varepsilon}^P\right)^n \tag{2.5}$$

$$\sigma_Y = \left(A + B\left(\bar{\varepsilon}^P\right)^n\right)\left(1 + C\,ln\left(\frac{\dot{\bar{\varepsilon}}^P}{\dot{\bar{\varepsilon}}_0^P}\right)\right)\left(1-\theta^m\right) \tag{2.6}$$

Where the flow stress is σ_Y ; A, B, C, n, m, $\dot{\bar{\varepsilon}}_0^P$ are model constants and $\theta = \frac{T - T_0}{T_m - T_0}$.

T_m and T_0 are material melting and the reference room temperatures respectively. The specific values of the parameters used in the Johnson-Cook model [43] are given in Table 2-1, for materials used in the computations to follow.

2.3 Constitutive Relations

The response of materials (elasto-plastic) to high intensity (shock/impact) loading conditions are modeled by assuming the additive decomposition of strain rule,

$$D_{ij} = D_{ij}^E + D_{ij}^P \tag{2.7}$$

where D_{ij} is the total strain-rate tensor given as:

$$D_{ij} = \frac{1}{2}\left(\frac{\partial u_i}{\partial x_j} + \frac{\partial u_j}{\partial x_i}\right) \tag{2.8}$$

And D_{ij}^E , D_{ij}^P are the elastic and plastic strain-rate components respectively, and u_i, u_j are the velocity components. Assuming isochoric plastic flow (tr (D_{ij}^P) = 0), the volumetric or dilatational response is governed by an equation of state while the deviatoric response follows the conventional theory of plasticity[36]. Hence the total stress in material can be expressed as

$$\sigma_{ij} = S_{ij} - P\delta_{ij} \tag{2.9}$$

where σ_{ij} is the Cauchy stress tensor, S_{ij} is the deviatoric component and P is the hydrostatic pressure taken to be positive in compression. Using Eq 2.7, the rate of change of deviatoric stress component can be modeled using hypo-elastic stress strain relation (Hooke's law):

$$\hat{S}_{ij} = 2G(\bar{D}_{ij} - D_{ij}^{P}) \tag{2.10}$$

where G is the modulus of rigidity, $\hat{S}_{ij}$ is the Jaumann derivative [27].

$$\hat{S}_{ij} = \dot{S}_{ij} + S_{ik}\Omega_{kj} - \Omega_{ik}S_{kj} \tag{2.11}$$

and Ω_{ij} is the spin tensor[27]. The Jaumann derivative is used to ensure the objectivity of the stress tensor with respect to rotation. The spin tensor used in Eq 2.5 is given by:

$$\Omega_{ij} = \frac{1}{2}\left(\frac{\partial u_i}{\partial x_j} - \frac{\partial u_j}{\partial x_i}\right) \tag{2.12}$$

The deviatoric strain-rate component in Eq 2.10 is given by:

$$\bar{D}_{ij} = D_{ij} - \frac{1}{3}D_{kk}\delta_{ij} \tag{2.13}$$

The isochoric plastic strain-rate component ($D_{ij}^{P} = \bar{D}_{ij}^{P}$) in Eq 2.1 is modeled assuming a coaxial flow theory (Drucker's Postulate) for strain hardening material [28]:

$$D_{ij}^{p} = \Lambda N_{ij} \tag{2.14}$$

where $N_{ij} = S_{ij} \Big/ \sqrt{S_{kl}S_{kl}}$ is the outward normal to the yield surface and Λ is a proportional positive scalar factor called the consistency parameter[7].

2.4 Formulation

To solve high strain-rate deformation of materials, the traditional operator splitting algorithm is employed [26]. The integration of mass, momentum and energy balance laws are performed assuming pure elastic deformation to obtain elastic predictor step; this is followed by a radial return procedure [44] to project the predicted stress back to yield surface.

Because of high speeds involved in the interaction process, the governing equations comprise a set of hyperbolic conservation laws cast in Cartesian coordinates; the governing equations take the following form:

$$\frac{\partial \vec{U}}{\partial t}+\frac{\partial \vec{F}}{\partial x}+\frac{\partial \vec{G}}{\partial y}+\phi_{3D}\frac{\partial \vec{H}}{\partial z}=\vec{S} \qquad (2.15)$$

For the elastic predictor step, in addition to mass, momentum and energy equations, the constitutive models for deviatoric stress terms are evolved. Thus the conservative variable and the fluxes in Eq 2.15 take the form given below:

$$\vec{U}=\left(\rho,\rho u,\rho v,\rho w,\rho E,\rho S_{xx},\rho S_{xy},\rho S_{yy},\rho S_{xz},\rho S_{yz},\rho S_{zz}\right) \qquad (2.16)$$

$$\vec{F}=\left(\rho u,\rho u^{2}+p,\rho uv,\rho uw,u(\rho E+p),\rho uS_{xx},\rho uS_{xy},\rho uS_{yy},\rho uS_{xz},\rho uS_{yz},\rho uS_{zz}\right) \qquad (2.17)$$

$$\vec{G}=\left(\rho v,\rho uv,\rho v^{2}+p,\rho vw,v(\rho E+p),\rho vS_{xx},\rho vS_{xy},\rho vS_{yy},\rho vS_{xz},\rho vS_{yz},\rho vS_{zz}\right) \qquad (2.18)$$

$$\vec{H}=\begin{pmatrix}\rho w,\rho uw,\rho vw,\rho w^{2}+p,w(\rho E+p),\rho wS_{xx}, \\ \rho wS_{xy},\rho wS_{yy},\rho wS_{xz},\rho wS_{yz},\rho wS_{zz}\end{pmatrix} \qquad (2.19)$$

The Source term in Eq 2.15 can be written as:

$$\vec{S}=\begin{pmatrix}0,\frac{\partial S_{xx}}{\partial x}+\frac{\partial S_{xy}}{\partial y}+\Phi_{3D}\frac{\partial S_{xz}}{\partial z},\frac{\partial S_{xy}}{\partial x}+\frac{\partial S_{yy}}{\partial y}+\Phi_{3D}\frac{\partial S_{yz}}{\partial z}, \\ \Phi_{3D}\left(\frac{\partial S_{xz}}{\partial x}+\frac{\partial S_{yz}}{\partial y}+\frac{\partial S_{zz}}{\partial z}\right),S_{E},S_{S_{xx}},S_{S_{xy}},S_{S_{yy}},S_{S_{xz}},S_{S_{yz}},S_{S_{zz}}\end{pmatrix} \qquad (2.20)$$

where

$$S_E = \frac{\partial}{\partial x}\left(uS_{xx} + vS_{xy} + \Phi_{3D} wS_{xz}\right) + \frac{\partial}{\partial y}\left(uS_{xy} + vS_{yy} + \Phi_{3D} wS_{yz}\right) + \Phi_{3D} \frac{\partial}{\partial z}\left(uS_{xz} + vS_{yz} + wS_{zz}\right) \quad (2.21)$$

$$S_{S_{xx}} = 2\rho\Omega_{xy}S_{xy} + \Phi_{3D}2\rho\Omega_{xz}S_{xz} + 2\rho G\bar{D}_{xx} \quad (2.22)$$

$$S_{S_{xy}} = \rho\Omega_{xy}(S_{yy} - S_{xx}) + \Phi_{3D}\rho(\Omega_{xz}S_{zy} - \Omega_{zy}S_{xz}) + 2\rho G\bar{D}_{xy} \quad (2.23)$$

$$S_{S_{yy}} = 2\rho\Omega_{yx}S_{xy} + \Phi_{3D}2\rho\Omega_{yz}S_{yz} + 2\rho G\bar{D}_{yy} \quad (2.24)$$

$$S_{S_{xz}} = \Phi_{3D}\left\{\rho\Omega_{xz}(S_{zz} - S_{xx}) + \rho(\Omega_{xy}S_{yz} - \Omega_{yz}S_{xy}) + 2\rho G\bar{D}_{zz}\right\} \quad (2.25)$$

$$S_{S_{yz}} = \Phi_{3D}\left\{\rho\Omega_{yz}(S_{zz} - S_{yy}) + \rho(\Omega_{yx}S_{xz} - \Omega_{xz}S_{xy}) + 2\rho G\bar{D}_{yz}\right\} \quad (2.26)$$

$$S_{S_{zz}} = \Phi_{3D}\left\{2\rho\Omega_{yz}S_{yz} + 2\rho\Omega_{xz}S_{xz} + 2\rho G\bar{D}_{zz}\right\} \quad (2.27)$$

where Φ_{3D} takes the value 0 for two-dimensional problems.

The evolution of effective plastic strain ($\bar{\varepsilon}_p$) and temperature (T) included in governing equations are given by:

$$\frac{\partial\rho\bar{\varepsilon}_p}{\partial t} + \vec{\nabla}.(\rho\vec{u}\,\bar{\varepsilon}_p) = 0 \quad (2.28)$$

$$\frac{\partial\rho T}{\partial t} + \vec{\nabla}.(\rho\vec{u}T) = \frac{1}{c}(k\nabla^2 T - \frac{p}{3}\dot{\varepsilon}^e_{kk} + \beta\dot{W}_p) \quad (2.29)$$

where c is the specific heat, k is thermal conductivity, $\dot{W}_p$ is the stress power due to plastic work and β is the Taylor-Quinney parameter [11]. For the application considered in this work the conduction term ($\nabla^2 T$) is small compared to other two terms. Also the stress power due to plastic work is given by:

$$\dot{W}_P = \dot{\bar{\varepsilon}}_P S_e \quad (2.30)$$

The effective plastic stress (S_e) and the effective plastic strain-rate ($\dot{\bar{\varepsilon}}_P$) are given by:

$$S_e^{\,2} = \frac{3}{2}(S_{ij} : S_{ij}) \tag{2.31}$$

$$(\dot{\bar{\varepsilon}}_P)^2 = \frac{2}{3}(D_{ij}^P : D_{ij}^P) = \frac{2}{3}\Lambda^2 \tag{2.32}$$

2.5 Equation of State

In case of gases, the pressure is related to transfer of momentum by particles participating in thermal motion, and is proportional to temperature. However the behavior of solids is different as the atoms of solids are close to each other and interact strongly. In order to compress a solid it is necessary to overcome the repulsive forces, which increases rapidly as atoms are brought close together[45]. The contribution in increase of pressure due to above reason is known as cold pressure. Therefore the pressure can be represented as a sum of cold pressure and thermal pressure. A suitable equation of state is required for modeling pressure in case of shocked compression of solids. In this work the closure for the set of governing equations is obtained by modeling the dilatational (pressure) response of material using a Mie-Gruneisen equation of state[36, 45]. For this purpose, the pressure P, specific internal energy e and specific volume $(V = 1/\rho)$ are related through a relation of the form:

$$P(e,V) \approx \Gamma(V)\frac{(e - e_c(V))}{V} + P_c(V) = \Gamma\frac{e}{V} + f(V) \tag{2.33}$$

where e_c and P_c denote the reference specific internal energy and pressure at 0 K. $\Gamma(V)$ in Eq 2.33 is the Gruneisen parameter defined as

$$\Gamma(V) = V\left(\frac{\partial P}{\partial e}\right)\Big|_v = \frac{\Gamma_0\rho_0}{\rho} \tag{2.34}$$

where Γ_0 is a material parameter and ρ_0 is the density of unstressed material. The function $f(V)$ in above equation is given by

$$f(V)=\left\{\begin{array}{l}\dfrac{\rho_0 c_0^2\Phi}{(1-s\Phi^2)^2}\left[1-\dfrac{\Gamma}{2V}(V_0-V)\right]\forall V\le V_0\\ c_0^2\left(\dfrac{1}{V}-\dfrac{1}{V_0}\right)\forall V>V_0\end{array}\right\} \tag{2.35}$$

In the above expression, Φ is given by $1.0-\dfrac{\rho_0}{\rho}$, the constant c_0 is the bulk sound speed and s is related to the isentropic pressure derivative of the isentropic bulk modulus. The parameters for the Mie-Gruneisen E.O.S for some of the materials used in this work are given in Table 2-2.

2.6 Radial Return Algorithm

The plastic deformation of material is governed by the yield function that constrains the stress to remain on or within the elastic domain:

$f(S_{ij},\xi)\le 0$ => admissible stress state (2.36)

$f(S_{ij},\xi)>0$ => inadmissible stress state (2.37)

where f is a generic yield function and ξ is a scalar or tensor hardening parameter.

In an operator splitting algorithm for elasto-plastic material, if the predicted –trial” elastic state (determined by freezing the plastic flow) falls within the yield surface, i.e. $f<0$, then the deformation is purely elastic and the final stress state is indeed the predicted trial state. The yield and subsequent plastic flow is said to have occurred when $f=0$. The inadmissible trial state for $f>0$ is corrected by bringing the stress back to the yield surface by enforcing the consistency condition $\dot{f}=0$, along a direction normal to the yield surface ($\partial f/\partial\sigma_{ij}$, Figure 2-1). In this work , the algorithm[44] adopted is explained below.

The radial return algorithm due to Ponthot et al.[46] is based on J_2 Von-Mises flow theory which assumes the existence of yield function (for isotropic materials) of the form

$$f(S_{ij},\sigma_Y) = S_e - \sigma_Y = 0 \tag{2.38}$$

with hardening law given by

$$\dot{\sigma}_Y = \sqrt{\frac{2}{3}}h\Lambda \tag{2.39}$$

Where σ_Y is the current yield stress which can be determined using material models (Table 2-1) and h (also called plastic modulus) is the slope of effective stress versus effective plastic strain curve under uniaxial loading. Using Eq 2.32, the yield stress can be written as

$$\dot{\sigma}_Y = h\dot{\bar{\varepsilon}}_{ij}^P \tag{2.40}$$

When elastic deformation occurs, $f < 0$ and $\Lambda = 0$. Plastic deformation is said to occur when consistency condition holds true, $\dot{f}(S_{ij},\sigma_Y) = 0$. Thus, for elastic and plastic deformation, f and Λ can be obtained from the Kuhn-Tucker conditions of optimization theory [47]:

$$\Lambda f = 0, \Lambda \geq 0, f \leq 0 \tag{2.41}$$

In conjunction with operator splitting algorithm, deviatoric stress update

$$\dot{S}_{ij} + S_{ik}\Omega_{kj} - \Omega_{ik}S_{kj} = 2G(\bar{D}_{ij} - \bar{D}_{ij}^P) \tag{2.42}$$

is split into two parts- ―trial” and ―corrector” step. The ―trial” elastic state is obtained by freezing the plastic flow ($\bar{D}_{ij}^P = 0$),

$$\dot{S}_{ij,tr} + S_{ik,tr}\Omega_{kj} - \Omega_{ik}S_{kj,tr} = 2G\bar{D}_{ij} \tag{2.43}$$

where $S_{ij,tr}$ is the trial elastic stress tensor. The plastic corrector step is enforced to bring computed trial stress back to yield surface:

$$\dot{S}_{ij,cor} = -2GD_{ij}^P = -2G\Lambda N_{ij} \tag{2.44}$$

where $S_{ij,cor}$ is the corrected stress update and N_{ij} is the normal direction in which return mapping is effected:

$$N_{ij} = \frac{S_{ij,tr}}{\sqrt{S_{kl,tr}S_{kl,tr}}} \tag{2.45}$$

In discrete form, the plastic corrector step can be written as

$$S_{ij,cor} = S_{ij,tr} - 2GN_{ij,tr}\zeta \tag{2.46}$$

where $\zeta = \int_{t_0}^{t_1} \Lambda dt$, with t$_0$ and t$_1$ denoting the beginning and end of time interval of integration. The parameter ζ is determined by enforcing the generalized consistency condition, $\dot{f} = 0$, at time t=t$_1$.

$$f = \sqrt{\frac{3}{2}[(S_{ij,tr} - 2GN_{ij,tr}\zeta)(S_{ij,tr} - 2GN_{ij,tr}\zeta)]} - \sigma_Y^1 = 0 \tag{2.47}$$

Integrating Eqs 2.32 & 2.40 in time, we get

$$\bar{\varepsilon}_1^P = \bar{\varepsilon}_0^P + \sqrt{\frac{2}{3}}\zeta \tag{2.48}$$

$$\sigma_Y^1 = \sigma_Y^0 + \sqrt{\frac{2}{3}}h\zeta \tag{2.49}$$

where –0” and –1” denote the values at t$_0$ and t$_1$, respectively. Substituting for σ_Y^1, Eq 2.47 is simplified

$$(4G^2 - \frac{4}{9})\zeta^2 - (4G\sqrt{S_{ij,tr}S_{ij,tr}} + \frac{4}{3}\sqrt{\frac{2}{3}}h)\zeta + (S_{ij,tr}S_{ij,tr} - \frac{2}{3}(\sigma_Y^0)^2) = 0 \tag{2.50}$$

to obtain

$$\zeta = \frac{\sqrt{S_{ij,tr}S_{ij,tr}} - \sqrt{\frac{2}{3}}\sigma_Y^0}{2G(1 + \frac{h}{3G})} \tag{2.51}$$

Thus, once ζ is obtained, the correction of the predicted deviatoric stress is performed using Eq 2.46 and the consistency condition is enforced. Material models are required to determine the yield stress to enforce the consistency conditions in the return mapping algorithm. The material model used in this work is Johnson-Cook material model. The parameters corresponding to Johnson-Cook model is given in Table 2-1.

Table 2-1. Material model parameters with reference to Eq 2.6 where A = Y_0, T_0 = 298K and $\dot{\varepsilon}_0^P = 1.0 s^{-1}$

Material	Y_0 (GPa)	B (GPa)	N	C	m	G (GPa)	T_m (K)
Copper [26]	0.4	0.177	1.0	0.025	1.09	43.33	1358
Tungsten [26]	1.51	0.177	0.12	0.016	1.0	124.0	1777
High-hard steel[26]	1.50	0.569	0.22	0.003	1.17	77.3	1723
Aluminum[11]	0.324	0.114	0.42	0.002	1.34	26.0	925
Mild Steel	0.53	0.229	0.302	0.027	1.0	81.8	1836

Table 2-2 Parameters for Mie-Gruneisen Equation of State for different materials.

Material	$\rho_0 \frac{kg}{m^3}$	$c \frac{W}{m-K}$	$K \frac{J}{Kg-K}$	Γ_0	$c_0 \frac{m}{s}$	S
Copper	8930	383.5	401.0	2.0	3940.0	1.49
Tungsten	17600	477.0	38.0	1.43	4030.0	1.24
Steel	7850	134.0	75.0	1.16	4570.0	1.49
HMX	1900	1000.0	0.4	1.1	2058.0	2.38

.

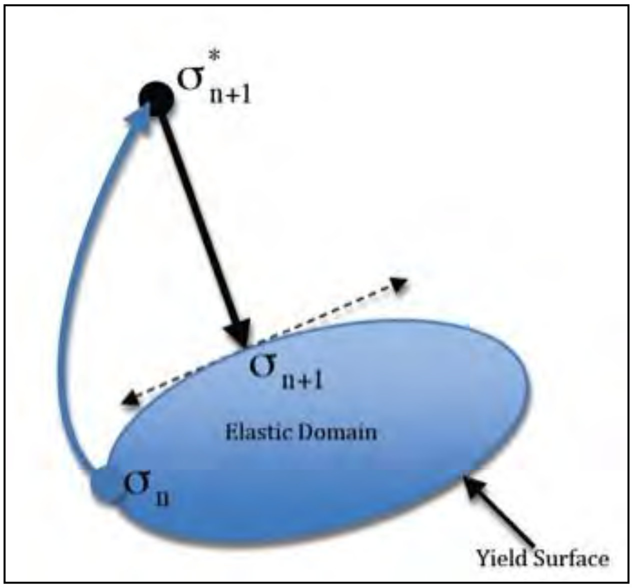

Figure 2-1. Radial return algorithm showing correction of trial stress by returning it back to the yield surface.

CHAPTER 3

NUMERICAL TECHNIQUES

In a sharp interface Eulerian setting; there are two key aspects of the numeric that must be addressed:

1. How to solve the governing equations accurately and stably in the presence of shocks and other steep gradients (shear layers, detonation fronts etc)?
2. How to evolve the embedded interfaces to represent the large deformation of materials including the challenging situations of interfaces that collide, collapse on themselves and fragment?

These two problems are not isolated from one another since the embedded interfaces in the problems of interest to this thesis interact with the flowfield in the bulk material. First, the interfaces are typically material boundaries and therefore the particle velocities computed by the bulk flow solver apply on the deforming interfaces as well. Second, as the interfaces evolve and interact with other interfaces, various type of interface conditions apply (as jump or compatibility conditions on the embedded material boundaries) on the bulk flow field. Thus, there is an intimate connection between flow solution and interface evolution as in other moving boundary problems.

The Ghost Fluid Method is a general framework for treating embedded interfaces that tackles the above two problems while maintaining sharp embedded interfaces. The Ghost Fluid Method was first proposed by Glimm [48], later adopted by Fedkiw [37], and is frequently employed to treat incompressible flow problems with embedded interfaces. The central idea is the definition of a band of ghost points corresponding to each phase of the interacting materials. In this work, the response of the material interface subject to high velocity impact and shock loading conditions is captured using a modified Ghost Fluid Method (GFM) [37]. In previous work[26, 36], boundary conditions were applied at the interface and the stencils used in the flux construction procedure were modified to accommodate the embedded interface. The novel aspect of the present work lies with the use of the GFM for the class of high speed elasto-plastic material interaction problems, particularly where the interactions can occur in the presence of nonlinear stress waves. The GFM relies on the definition of a band of ghost points corresponding to each phase of the interacting material[38, 40]. For instance, consider the case of two materials separated by an interface as shown in Figure 3-1. Once the ghost points are identified and populated with flow conditions, the two-material problem can be converted to two, single-material problems consisting of the real field and their corresponding ghost fields. With the GFM, the interface capturing scheme and the flux construction procedure are decoupled and the onus is shifted to populating the ghost nodes. Thus, since one deals with two separate single fluid problems following injection of the ghost field with appropriate values, the numerical scheme for integrating the system of hyperbolic conservation law can be drawn from the entire arsenal of standard single-fluid shock capturing schemes. In this work, a standard third-order convex ENO scheme [41] is employed to compute the fluxes at cell faces.Since the numerical schemes implemented in this work are well established and do not differ in any way from those that apply for single fluids[41], the implementation details are not presented here. Interested readers may refer to the original articles [41, 49] for details on the ENO and TVD Runge-Kutta schemes.

3.1 Tracking of Embedded Interfaces

3.1.1 Implicit Interface Representation Using Level Sets

Sharp interface treatment requires tracking and representation of material interfaces as the underlying global mesh does not conform to the shape of interface. In this work, level set methods[50, 51] are used to represent the embedded objects. The value of level set field, ϕ_l, at any point is signed normal distance from the l^{th} immersed object with $\phi_l < 0$ inside the immersed boundary and $\phi_l > 0$ outside (Figure 3-2). The interface is implicitly determined by the zero level set field i.e. $\phi_l = 0$ contour represents the l^{th} immersed boundary. The standard narrow band[50] level set algorithm is used to define the level set field. The embedded interfaces are propagated using level set advection equation.

$$\frac{\partial \phi_l}{\partial t} + \vec{V}_l . \vec{\nabla} \phi_l = 0 \tag{3.1}$$

where $\vec{V}_l$ denotes the level set velocity field for the l^{th} embedded interface. A fourth-order ENO scheme for spatial discretization and third-order Runge-Kutta time integration are used in solving the level set advection equation. The velocity of level set field $\vec{V}_l$, is defined only on the embedded interface (i.e. the zero level set contour). The value of velocity field at the grid points that lie in the narrow band around the zero level set is determined by solving the extension equation to steady state as given below:

$$\frac{\partial \psi}{\partial t} + \vec{V}_{ext} . \vec{\nabla} \psi = 0 \tag{3.2}$$

where ψ is any quantity such as interface velocity component $((\vec{V}_l)_x, (\vec{V}_l)_y$ or $(\vec{V}_l)_z)$ that needs to be extended away from the interface. The extension velocity $\vec{V}_{ext}$ is given by

$$\vec{V}_{ext} = sign(\phi_l) \vec{\nabla} \phi_l / \left| \vec{\nabla} \phi_l \right| \tag{3.3}$$

This populates any desired quantity across the narrow band region. A reinitialization procedure is carried out after level set advection to return ϕ_l field to a signed distance function such that $\left| \vec{\nabla} \phi_l \right| = 1$. The reinitialization procedure is done by solving the following equation to steady state

$$\frac{\partial \phi_l}{\partial t} + \vec{w} . \vec{\nabla} \phi_l = sign(\phi_l) \tag{3.4}$$

Where $\vec{w} = sign((\phi_l)_0) \dfrac{(\vec{\nabla} \phi_l)_0}{\left| (\vec{\nabla} \phi_l)_0 \right|}$ and $(\phi_l)_0$ is the level set field prior to reinitialization. The details of level set methods can be found in following reference [50].

The normal at a point is calculated using level set function

$$\hat{n} = \frac{\nabla\phi}{|\nabla\phi|} \tag{3.5}$$

3.1.2 Classification of Grid Points

In this work, the interfaces are moving entities on a fixed global mesh. The Ghost Fluid method requires interfaces to be defined using distinct set of points. Therefore the grid points on the Cartesian mesh can be classified as *bulk points* and *interfacial points*. The points which lie immediately adjacent to the interface are tagged as interfacial points as shown in

Figure 3-3. Identification of interfacial points is straightforward with the level set field (Figure 3-2). If $\O_{curr}.\O_{nbr} \leq 0.0$, where the subscript ―curr” denotes the current point and ―nbr” denotes the neighboring point, then the current and the neighboring point are tagged as interfacial points. All the other points are classified as bulk points. As shown in Figure 3-1, the Ghost fluid method can convert a two-material problem to two single material problems. This requires a band of ghost points to be defined for each phase of the interacting media as shown in Figure 3-3. The ghost point band typically extends up to 4 max (Δx, Δy, Δz) distance from the interface. Again, the level set field can be used to define the band of ghost points. The set of ghost points which are immediately adjacent to the interface are tagged as *interfacial ghost points* similar to the regular interfacial points.

3.1.3 Detecting and Resolving Collisions

In the present work, the material interfaces (represented by level sets) are expected to collide with other interfaces, collapse upon themselves or fragment. A typical example of the problems considered in this work is demonstrated in Figure 3-4. This is a snapshot during the initial stages of evolution of a high speed impact and penetration of a Steel target by a WHA long Tungsten rod [11]. A detailed analysis of this problem is presented in Chapter 5. At the instant shown in the figure, two objects have collided resulting in different portions of the surfaces of the objects interacting with different materials. Such events need to be tracked and appropriate interface conditions are to be applied. The procedure for accomplishing this is as follows.

At the beginning of the calculation, the materials enclosed inside and outside the interface defining an object are identified as *rigid solid*, *elasto-plastic solid* or *void*. Then a "base material" is identified, indicating that the embedded objects are immersed in this base material. For the example shown the base material is the void (i.e. vacuum) phase. No calculations are performed in the void phase. Unless a collision is detected, the embedded object is considered to interact with the surrounding base material and the corresponding interface conditions (i.e. free surface conditions) are enforced to populate the ghost nodes. The nodes straddling the material interface are maintained in a linked list called ―interfacial nodes”.

To detect collision, for each interfacial node corresponding to the levelset (object) indexed l, if a neighboring cell lies inside a different levelset (object) say, indexed(k), the distance between two objects is computed using the associated level set values from:

$$\delta_{lk} = \left|\phi_l + \phi_k\right| \forall l \neq k \qquad (3.6)$$

If this distance δ_{lk} computed between any two approaching level sets is less than a specified tolerance, then the node is marked as a ``colliding node" (Figure 3-4). The tolerance to flag collisions is set at $\kappa\Delta x$ where κ corresponds to the CFL number corresponding to interface advection. This preempts inter-penetration of level sets. Once a set of ―colliding nodes” are established the appropriate interface treatment at such nodes is adopted as described below.

3.2 Classification of the Interface and the Associated Boundary Conditions

Various situations may arise when two different objects move toward each other as shown in Figure 3-4. Thus it is necessary that the colliding objects are detected as described above and the interface conditions are applied; once a node is marked as a colliding node, the conditions corresponding to a material-material interface are enforced to populate the corresponding ghost node. Thus, for regions R1 in Figure 3-4, material-void/free surface conditions are enforced and for regions R2, material-material conditions are enforced. This process is repeated for each level set. At colliding interfaces continuity of normal velocities and normal stress are enforced. Slip is permitted so that frictionless contact is modeled. There are three key steps in populating the ghost field, viz.:

1. Obtain interpolated values at a reflected point IP1 (see Figure 3-5(a)) corresponding to a ghost point P.
2. Use extension, reflection or injection (depending on the type of interface condition to be applied) along axes oriented in the local interface normal and tangent coordinate to supply the values of all flowfield variables to the ghost point.
3. Transform/combine/correct the information at the ghost point into primitive variables to obtain the final ghost field that satisfies interface conditions.

These steps are explained below. Please note that the figures correspond to two dimensions in this section as it is difficult to draw three dimensional figures. However the procedure is explained for three dimensional frame work and a figure (Figure 3-6) depicting interface embedded in three dimensional cartesian grid is also shown.

3.2.1 Step 1: Obtaining the Value at the Reflected Node IP1:

The first step in supplying values to a point in the ghost field (point P in Figure 3-5(a)) is to obtain the interpolated value of field variables in the ―real” material at IP1. Point IP1 is obtained by reflecting the location of point P across the interface along the normal to the interface, i.e $\left|\vec{X}_{IP}-\vec{X}_{P}\right|=\left|\vec{X}_{IP}-\vec{X}_{IP1}\right|$. To define the ghost states at node P (Figure 3-5 (a)), a probe is inserted to identify the reflected node IP1 and the node IP on the interface. Points IP and IP1 can be identified by using the level set distance function ϕ:

$$\vec{X}_{IP} = \vec{X}_P + |\phi_P| \vec{N}_P \tag{3.7}$$

$$\vec{X}_{IP1} = \vec{X}_P + 2|\phi_P| \vec{N}_P \tag{3.8}$$

where $\vec{X}$ is the position vector, ϕ_P the level set value at node P and $\vec{N}_P$ is the normal vector at node P, which is obtained from the levelset field. Two schemes are investigated in the current work for obtaining the value of flow variables at IP1. The first is a straight-forward bilinear interpolation using surrounding data and the second is a least squares reconstruction which does not provide exact nodal interpolation. The techniques are evaluated by testing their ability to provide benchmark solutions, and also by addressing the main issues in handling fragmentation events. In problems of interest here, the materials can fragment; these fragments can consist of small structures, which may be resolved by very few grid points. In such cases, the robustness of the overall scheme for evolving interfaces depends on the ability to obtain sufficient interpolation points to populate the value at IP1 and thereby in the ghost nodes P. In the following two methods, the first offers a smaller stencil and strict interpolation, while the second uses a wider stencil and data-fitting. Bilinear interpolation is less computationally expensive than the least-squares estimation and therefore would be preferred in cases for which it is robust. Both methods work well prior to fragmentation, and the results obtained from both methods are shown (Chapter 5) to be comparable. However, it is demonstrated that the least-square fitting approach is robust and should be the method of choice for computing fragmentation events.

3.2.1.1 Bilinear Interpolation

To obtain the value at IP1, interpolation from surrounding nodes is performed using a bilinear interpolant:

$$\Psi = a_1 + a_2 x + a_3 y + a_4 z + a_5 xy + a_6 yz + a_7 zx + a_8 xyz \tag{3.9}$$

where (x,y,z) are the coordinates of the surrounding interpolation nodes.

To solve for the constants a_i values at the surrounding interpolating nodes and the interface condition at IP are used (Figure 3-5(a)). At the node IP on the interface, either the value of the flow variables (Dirichlet conditions) or the flow gradient (Neumann type conditions) is available. Thus it is necessary to embed the appropriate boundary conditions to complete the interpolation procedure.

For Dirichlet condition at IP, the Vandermonde matrix takes the following form:

$$\begin{pmatrix} 1 & x_1 & y_1 & z_1 & x_1y_1 & y_1z_1 & z_1x_1 & x_1y_1z_1 \\ 1 & x_2 & y_2 & z_2 & x_2y_2 & y_2z_2 & z_2x_2 & x_2y_2z_2 \\ 1 & x_3 & y_3 & z_3 & x_3y_3 & y_3z_3 & z_3x_3 & x_3y_3z_3 \\ 1 & x_4 & y_4 & z_4 & x_4y_4 & y_4z_4 & z_4x_4 & x_4y_4z_4 \\ 1 & x_5 & y_5 & z_5 & x_5y_5 & y_5z_5 & z_5x_5 & x_5y_5z_5 \\ 1 & x_6 & y_6 & z_6 & x_6y_6 & y_6z_6 & z_6x_6 & x_6y_6z_6 \\ 1 & x_7 & y_7 & z_7 & x_7y_7 & y_7z_7 & z_7x_7 & x_7y_7z_7 \\ 1 & x_{IP} & y_{IP} & z_{IP} & x_{IP}y_{IP} & y_{IP}z_{IP} & z_{IP}x_{IP} & x_{IP}y_{IP}z_{IP} \end{pmatrix} \begin{pmatrix} a_1 \\ a_2 \\ a_3 \\ a_4 \\ a_5 \\ a_6 \\ a_7 \\ a_{IP} \end{pmatrix} = \begin{pmatrix} \Psi_1 \\ \Psi_2 \\ \Psi_3 \\ \Psi_4 \\ \Psi_5 \\ \Psi_6 \\ \Psi_7 \\ \lambda_{IP} \end{pmatrix} \tag{3.10}$$

For Neumann condition at IP, the matrix is modified as follows

$$\begin{pmatrix} 1 & x_1 & y_1 & z_1 & x_1y_1 & y_1z_1 & z_1x_1 & x_1y_1z_1 \\ 1 & x_2 & y_2 & z_2 & x_2y_2 & y_2z_2 & z_2x_2 & x_2y_2z_2 \\ 1 & x_3 & y_3 & z_3 & x_3y_3 & y_3z_3 & z_3x_3 & x_3y_3z_3 \\ 1 & x_4 & y_4 & z_4 & x_4y_4 & y_4z_4 & z_4x_4 & x_4y_4z_4 \\ 1 & x_5 & y_5 & z_5 & x_5y_5 & y_5z_5 & z_5x_5 & x_5y_5z_5 \\ 1 & x_6 & y_6 & z_6 & x_6y_6 & y_6z_6 & z_6x_6 & x_6y_6z_6 \\ 1 & x_7 & y_7 & z_7 & x_7y_7 & y_7z_7 & z_7x_7 & x_7y_7z_7 \\ 0 & n_x & n_y & n_z & n_x y_{IP} + n_y x_{IP} & n_y z_{IP} + n_z y_{IP} & n_x z_{IP} + n_z x_{IP} & n_x y_{IP} z_{IP} + n_y x_{IP} z_{IP} + n_z x_{IP} y_{IP} \end{pmatrix}$$

$$\begin{pmatrix} a_1 \\ a_2 \\ a_3 \\ a_4 \\ a_5 \\ a_6 \\ a_7 \\ a_{IP} \end{pmatrix} = \begin{pmatrix} \Psi_1 \\ \Psi_2 \\ \Psi_3 \\ \Psi_4 \\ \Psi_5 \\ \Psi_6 \\ \Psi_7 \\ \nu_{IP} \end{pmatrix} \tag{3.11}$$

The last row of the coefficient matrix in Eq 3.11 is obtained by differentiating Eq 3.9, noting that

$$\frac{\partial \Psi}{\partial n} = \frac{\partial \psi}{\partial x} n_x + \frac{\partial \psi}{\partial y} n_y + \frac{\partial \psi}{\partial z} n_z \tag{3.12}$$

where n_x, n_y and n_z are the normal vector components and ν_{IP} corresponds to the value of the normal gradient at the point IP. The normal components can be determined using level set field such that

$$\hat{n} = \frac{\nabla \phi}{|\nabla \phi|} \tag{3.13}$$

Once the coefficients are determined, the flow properties at IP1 can be deduced using Eq 3.9.

3.2.1.2 Least-Squares Fitting

The least-squares method [52] is a standard method for approximating functions from an overdetermined set of data points. Though the bilinear interpolation method discussed above works very well with various impact and penetration problems, the interpolation procedure may fail when the real material consist of a few nodes as shown in Figure 3-5 (d). The least-squares approach adopted in this framework works adaptively and can handle tiny fragments encountered in severe deformation in case of very high speed impact and penetration. In addition, it is shown (CHAPTER 5) to produce results in close agreement with benchmarks and with the bilinear interpolation approach, for cases where the latter works.

To obtain a least-squares functional fit, the first step is to find the closest node (in the ―real” fluid) to the reflected point IP1. Once the closest node is found, all of the neighboring nodes to the closest node are selected. In 3D, there will be a total of twenty seven nodes including the closest node. This set of nodes which lie in the real material are used to construct a bilinear field based on least squares as show in Figure 3-5 (b). Again, similar to previous case, one can write generic bilinear fitting function as

$$\varphi = a_1 + a_2 x + a_3 y + a_4 z + a_5 xy + a_6 yz + a_7 zx + a_8 xyz \tag{3.14}$$

The error in the approximation can be written as

$$e = \sum_{i=1}^{n} (a_1 + a_2 x_i + a_3 y_i + a_4 z_i + a_5 x_i y_i + a_6 y_i z_i + a_7 z_i x_i + a_8 x_i y_i z_i - \varphi_i)^2 \tag{3.15}$$

Here n are the total number of nodes available for constructing the fitting function. It is required that the error should be minimum, differentiating Eq 3.15 w.r.t unknown coefficients results in

$$\frac{\partial e}{\partial a_i} = 0 \tag{3.16}$$

This will result in eight equations which can be written in a matrix form as shown below:

$$\begin{bmatrix}
\sum_{i=1}^{n} 1 & \sum_{i=1}^{n} x_i & \sum_{i=1}^{n} y_i & \sum_{i=1}^{n} z_i & \sum_{i=1}^{n} x_i y_i & \sum_{i=1}^{n} y_i z_i & \sum_{i=1}^{n} x_i z_i & \sum_{i=1}^{n} x_i y_i z_i \\
\sum_{i=1}^{n} x_i & \sum_{i=1}^{n} x_i^2 & \sum_{i=1}^{n} x_i y_i & \sum_{i=1}^{n} x_i z_i & \sum_{i=1}^{n} x_i^2 y_i & \sum_{i=1}^{n} x_i y_i z_i & \sum_{i=1}^{n} x_i^2 z_i & \sum_{i=1}^{n} x_i^2 y_i z_i \\
\sum_{i=1}^{n} y_i & \sum_{i=1}^{n} x_i y_i & \sum_{i=1}^{n} y_i^2 & \sum_{i=1}^{n} y_i z_i & \sum_{i=1}^{n} x_i y_i^2 & \sum_{i=1}^{n} y_i^2 z_i & \sum_{i=1}^{n} x_i y_i z_i & \sum_{i=1}^{n} x_i y_i^2 z_i \\
\sum_{i=1}^{n} z_i & \sum_{i=1}^{n} x_i z_i & \sum_{i=1}^{n} y_i z_i & \sum_{i=1}^{n} z_i^2 & \sum_{i=1}^{n} x_i y_i z_i & \sum_{i=1}^{n} y_i z_i^2 & \sum_{i=1}^{n} x_i z_i^2 & \sum_{i=1}^{n} x_i y_i z_i^2 \\
\sum_{i=1}^{n} x_i y_i & \sum_{i=1}^{n} x_i^2 y_i & \sum_{i=1}^{n} x_i y_i^2 & \sum_{i=1}^{n} x_i y_i z_i & \sum_{i=1}^{n} x_i^2 y_i^2 & \sum_{i=1}^{n} x_i y_i^2 z_i & \sum_{i=1}^{n} x_i^2 y_i z_i & \sum_{i=1}^{n} x_i^2 y_i^2 z_i \\
\sum_{i=1}^{n} y_i z_i & \sum_{i=1}^{n} x_i y_i z_i & \sum_{i=1}^{n} y_i^2 z_i & \sum_{i=1}^{n} y_i z_i^2 & \sum_{i=1}^{n} x_i y_i^2 z_i & \sum_{i=1}^{n} y_i^2 z_i^2 & \sum_{i=1}^{n} x_i y_i z_i^2 & \sum_{i=1}^{n} x_i y_i^2 z_i^2 \\
\sum_{i=1}^{n} x_i z_i & \sum_{i=1}^{n} x_i^2 z_i & \sum_{i=1}^{n} x_i y_i z_i & \sum_{i=1}^{n} x_i z_i^2 & \sum_{i=1}^{n} x_i^2 y_i z_i & \sum_{i=1}^{n} x_i y_i z_i^2 & \sum_{i=1}^{n} x_i^2 z_i^2 & \sum_{i=1}^{n} x_i^2 y_i z_i^2 \\
\sum_{i=1}^{n} x_i y_i z_i & \sum_{i=1}^{n} x_i^2 y_i z_i & \sum_{i=1}^{n} x_i y_i^2 z_i & \sum_{i=1}^{n} x_i y_i z_i^2 & \sum_{i=1}^{n} x_i^2 y_i^2 z_i & \sum_{i=1}^{n} x_i y_i^2 z_i^2 & \sum_{i=1}^{n} x_i^2 y_i z_i^2 & \sum_{i=1}^{n} x_i^2 y_i^2 z_i^2
\end{bmatrix}$$

$$\begin{bmatrix} a_1 \\ a_2 \\ a_3 \\ a_4 \\ a_5 \\ a_6 \\ a_7 \\ a_8 \end{bmatrix} = \begin{bmatrix} \sum_{i=1}^{n} \varphi_i \\ \sum_{i=1}^{n} \varphi_i x_i \\ \sum_{i=1}^{n} \varphi_i y_i \\ \sum_{i=1}^{n} \varphi_i z_i \\ \sum_{i=1}^{n} \varphi_i x_i y_i \\ \sum_{i=1}^{n} \varphi_i y_i z_i \\ \sum_{i=1}^{n} \varphi_i x_i z_i \\ \sum_{i=1}^{n} \varphi_i x_i y_i z_i \end{bmatrix} \tag{3.17}$$

The evaluated unknowns can be used to construct the ghost field at IP1using Eq 3.14. The least-squares method can be used for severe plastic deformation problems involving fragmentation and damage as will be shown in CHAPTER 5 and CHAPTER6.

3.2.2 Step 2: Dirichlet, Neumann and Continuity Conditions and Populating Values at the Ghost Node P:

In the impact and penetration problems studied here three types of interfaces can arise, viz. free surfaces or material-void interface (MVI) and impact surfaces or material-material interface (MMI) and material-rigid solid interface (MRI). The conditions that apply at these three types of interfaces reduce to Dirichlet, Neumann or continuity conditions. In general, the above set of conditions can be cast in a generic form as outlined below. Here Ψ_I corresponds to the flow variables for which boundary conditions are applied. The ghost points are supplied with flowfield variables such that the real field along with the corresponding ghost field satisfies the boundary conditions accurately at the interface.

Dirichlet condition: In this case, the ghost field is defined such that the linear interpolation between the ghost node P and the corresponding reflected node IP1 retains the exact value of flow variable, $\Psi_{IP} = \lambda_{IP}$ at the interface. The ghost value to satisfy the above condition can be obtained from:

$$\Psi_P^D = 2\lambda_{IP} - \Psi_{IP1}^{REAL} \tag{3.18}$$

where λ_{IP} is the value of Ψ^{REAL} at the interface.

Neumann Condition: This procedure is employed on those variables that are governed by Neumann conditions or variables that are discontinuous across the interface. Here, ghost values are found by extending values from the real field across the interface into the ghost region. For instance, when the extension procedure is employed for the ghost node at P, the flow values computed at IP1 are copied to the ghost node at P.

$$\Psi_P^N = \Psi_{IP1}^{REAL} \tag{3.19}$$

Since variables are extrapolated with constant value, the extension procedure ensures a zero gradient at point IP on the interface i.e. $\left(\frac{\partial \Psi}{\partial n}\right)_{IP} = 0$.

Continuity condition: In this procedure the value of continuous quantities are copied from real fluid to ghost fluid. The procedure itself is called injection as the ghost value is populated by directly injecting the real value.

$$\Psi_P^C = \Psi_P^{REAL} \tag{3.20}$$

where P is a point in ghost field as shown in Figure 3-6.

3.2.3 Step 3: Transforming and Combining the Information at P to Obtain Primitive Variables at the Ghost Node

The dependent variables at the selected interpolated nodes around IP1 (Figure 3-6) are transformed to local normal and tangential coordinates. The velocity components in transformed coordinates at the interpolation nodes are computed as follows:

$$u_n = |\vec{u}_n| = \vec{u}.\hat{n} \tag{3.21}$$

$$u_{t_1} = |\vec{u}_{t_1}| = \vec{u}.\hat{t}_1 \tag{3.22}$$

$$u_{t_2} = |\vec{u}_{t_2}| = \vec{u}.\hat{t}_2 \tag{3.23}$$

where $\vec{u}$ is the velocity vector in the Cartesian coordinates, $\vec{u}_n$, $\vec{u}_{t1}$ and $\vec{u}_{t2}$ are the normal and tangential velocity vectors.

The total stress tensor in the normal and tangential coordinates is given by

$$\tilde{\boldsymbol{\sigma}} = J\boldsymbol{\sigma}J^T \tag{3.24}$$

where

$$J = \begin{pmatrix} n_x & n_y & n_z \\ t_{1x} & t_{1y} & t_{1z} \\ t_{2x} & t_{2y} & t_{2z} \end{pmatrix} \tag{3.25}$$

is the Jacobian matrix and $\hat{n}, \hat{t}_1$ and $\hat{t}_2$ are local normal and tangential vectors defined at the interface. The normal vector in above matrix is computed as

$$\hat{n} = \frac{\nabla\phi}{|\nabla\phi|} \tag{3.26}$$

Where ϕ is the level set[51] function. The tangential vectors are computed using procedure given in Kang et al.[53].

Three types of interface conditions apply in the types of problems interest in this work. If the node P lies in the void region then the condition corresponding to material-void interface (MVI) are enforced at the interface point IP. If the ghost node P lies in the deformable material and if P is tagged as a colliding node, then conditions corresponding to Material-Material Interface (MMI) are enforced at IP. If the node P lies in the rigid material then the material-rigid interface (MRI) conditions are enforced at IP. Note then in the following, superscripts D, N and C refer to Eqs. 3.18, 3.19 and 3.20 respectively for determining the ghost values.

3.2.3.1 Material-Void Interface (MVI)

Conditions corresponding to the physical correct wave reflection phenomena[45] are enforced at the interface. For instance, a compressive wave incident on a free surface is reflected as tensile wave and vice-versa. The physical constraint to be satisfied at the MV interface is the traction free state, where the traction vectors at different planes with normals $\hat{n}$, $\hat{t}_1$ and $\hat{t}_2$ are given by

$$\vec{T}_n = \tilde{\sigma}_{nn}\hat{n}_x + \tilde{\sigma}_{nt_1}\hat{n}_y + \tilde{\sigma}_{nt_2}\hat{n}_z \tag{3.27}$$

$$\vec{T}_{t_1} = \tilde{\sigma}_{t_1n}\hat{t}_{1x} + \tilde{\sigma}_{t_1t_1}\hat{t}_{1y} + \tilde{\sigma}_{t_2t_2}\hat{t}_{1z} \tag{3.28}$$

$$\vec{T}_{t_2} = \tilde{\sigma}_{t_2n}\hat{t}_{2x} + \tilde{\sigma}_{t_2t_1}\hat{t}_{2y} + \tilde{\sigma}_{t_2t_2}\hat{t}_{2z} \tag{3.29}$$

As zero traction is required at the interface, $\vec{T}_n.\hat{n} = 0$.The above condition results in normal components of the stress vanishing at the interface such that:

$$\tilde{\sigma}_{nn} = 0 \tag{3.30}$$

$$\tilde{\sigma}_{nt_1} = 0 \tag{3.31}$$

$$\tilde{\sigma}_{nt_2} = 0 \tag{3.32}$$

As the material enclosed at node P corresponds to free surface then conditions corresponding to MVI are enforced as follows:

$$\rho_P^G = \rho_P^N \tag{3.33}$$

$$P_P^G = P_P^D \tag{3.34}$$

$$\vec{u}_P^G = |\vec{u}_{nP}^N|\,\hat{n} + |\vec{u}_{t_1P}^N|\,\hat{t}_1 + |\vec{u}_{t_2P}^N|\,\hat{t}_2 \tag{3.35}$$

$$u_P^G = u_{nP}^N n_x + u_{t_1P}^N t_{1x} + u_{t_2P}^N t_{2x} \tag{3.36}$$

$$v_P^G = u_{nP}^N n_y + u_{t_1P}^N t_{1y} + u_{t_2P}^N t_{2y} \tag{3.37}$$

$$w_P^G = u_{nP}^N n_z + u_{t_1P}^N t_{1z} + u_{t_2P}^N t_{2z} \tag{3.38}$$

The total stress tensor is given by

$$\boldsymbol{\sigma} = \boldsymbol{S} - P\boldsymbol{I} \tag{3.39}$$

where $\boldsymbol{\sigma}$ and $\boldsymbol{S}$ are total and deviatoric stress tensors in Cartesian coordinates respectively, P is the hydrostatic pressure and $\boldsymbol{I}$ is the second order identity tensor. As at the MVI type of interface the zero traction condition should be enforced, the stress tensor is reconstructed by enforcing slip condition (Neumann) for the tangential components and zero traction (reflective/Dirichlet) for the normal components. The reconstructed total stress tensor at point P in local normal and tangential coordinates will be:

$$\tilde{\boldsymbol{\sigma}}_P^G = \begin{pmatrix} \tilde{\sigma}_{nn}^D & \tilde{\sigma}_{nt_1}^D & \tilde{\sigma}_{nt_2}^D \\ \tilde{\sigma}_{t_1n}^D & \tilde{\sigma}_{t_1t_1}^N & \tilde{\sigma}_{t_1t_2}^N \\ \tilde{\sigma}_{t_2n}^D & \tilde{\sigma}_{t_2t_1}^N & \tilde{\sigma}_{t_2t_2}^N \end{pmatrix}_P \tag{3.40}$$

Here these stress components are reflected and extended as indicated using the values at node IP1. The stress state at point IP1 is:

$$\tilde{\sigma}_{IP1} = \begin{pmatrix} \tilde{\sigma}_{nn} & \tilde{\sigma}_{nt_1} & \tilde{\sigma}_{nt_2} \\ \tilde{\sigma}_{t_1n} & \tilde{\sigma}_{t_1t_1} & \tilde{\sigma}_{t_1t_2} \\ \tilde{\sigma}_{t_2n} & \tilde{\sigma}_{t_2t_1} & \tilde{\sigma}_{t_2t_2} \end{pmatrix}_{IP1} \tag{3.41}$$

The individual volumetric components at the ghost node P in terms of stress values at the node IP1 can be written as

$$(\tilde{\sigma}^{D}_{nn})_{P} = -(\tilde{\sigma}_{nn})_{IP1} \tag{3.42}$$

$$(\tilde{\sigma}^{N}_{t_1t_1})_{P} = (\tilde{\sigma}_{t_1t_1})_{IP1} \tag{3.43}$$

$$(\tilde{\sigma}^{N}_{t_2t_2})_{P} = (\tilde{\sigma}_{t_2t_2})_{IP1} \tag{3.44}$$

Using Eqs. 3.42-3.44 one can write J_1 (deviatoric stress invariant) at both P and IP1 as:

$$(J_1)_{IP1} = (\tilde{\sigma}_{nn} + \tilde{\sigma}_{t_1t_1} + \tilde{\sigma}_{t_2t_2} + 3P)_{IP1} = 0 \tag{3.45}$$

$$(J_1)_{P} = (\tilde{\sigma}^{D}_{nn} + \tilde{\sigma}^{N}_{t_1t_1} + \tilde{\sigma}^{N}_{t_2t_2} + 3P^{D})_{P} \tag{3.46}$$

The trace of deviatoric stress J_1, at the ghost node P can be written in terms of stress components at the real node IP1 such that

$$(J_1)_{P} = (-\tilde{\sigma}_{nn} + \tilde{\sigma}_{t_1t_1} + \tilde{\sigma}_{t_2t_2} - 3P\ )_{IP1} \neq 0 \tag{3.47}$$

It can be seen clearly that at the ghost node P the J_1=0 condition is not satisfied, violating the fundamental invariance properties of the stress tensor. Therefore we fix this by correcting the stress state at the ghost node P. The procedure for this is shown below. Let $\tilde{\sigma}^{G}_{nn}$, $\tilde{\sigma}^{G}_{t_1t_1}$ and $\tilde{\sigma}^{G}_{t_2t_2}$ are the corrected states at the ghost point P such that

$$\tilde{\sigma}^{G}_{nn} = (\tilde{\sigma}^{D}_{nn})_{P} \tag{3.48}$$

$$\tilde{\sigma}^{G}_{t_1t_1} = (\tilde{\sigma}^{N}_{t_1t_1})_{P} + \Delta\sigma \tag{3.49}$$

$$\tilde{\sigma}^{G}_{t_2t_2} = (\tilde{\sigma}^{N}_{t_2t_2})_{P} + \Delta\sigma \tag{3.50}$$

In the above, $\Delta\sigma$ is the correction added to existing extended stress states. Now we can find $\Delta\sigma$ by enforcing J_1=0 condition at the ghost node P as follows:

$$(J_1)_{P} = (\tilde{\sigma}^{G}_{nn} + \tilde{\sigma}^{G}_{t_1t_1} + \tilde{\sigma}^{G}_{t_2t_2} + 3P^{G})_{P} = 0 \tag{3.51}$$

$$\Rightarrow (\tilde{\sigma}^{D}_{nn} + \tilde{\sigma}^{N}_{t_1t_1} + \tilde{\sigma}^{N}_{t_2t_2} + 3P^{D})_{P} + 2\Delta\sigma = 0 \tag{3.52}$$

$$\Rightarrow \Delta\sigma = (\tilde{\sigma}^{D}_{nn} + \tilde{\sigma}^{N}_{t_1t_1} + \tilde{\sigma}^{N}_{t_2t_2} + 3P^{D})_P / 2 \tag{3.53}$$

Once the total stress tensor at the ghost node P is constructed, the stress components in Cartesian coordinates are recovered back using Eq 3.24. This correction procedure is depicted clearly in Figure 3-7, where the comparison of J_1 is shown for corrected and uncorrected ghost stress

Finally, the deviatoric stress components for the ghost field are obtained using ghost pressure field as

$$\boldsymbol{S}^{G}_{P} = \boldsymbol{\sigma}^{G}_{P} + P^{G}_{P}\boldsymbol{I} \tag{3.54}$$

3.2.3.2 Material-Material Interface

The continuity of stresses and normal velocities must hold at MMI such that:

$$[\tilde{\sigma}_{nn}] = 0 \tag{3.55}$$

$$[\tilde{\sigma}_{nt_1}] = 0 \tag{3.56}$$

$$[\tilde{\sigma}_{nt_2}] = 0 \tag{3.57}$$

Now if the material enclosed at node P corresponds to Elasto-Plastic then conditions corresponding to MM are enforced such that

$$\rho^{G}_{P} = \rho^{N}_{P} \tag{3.58}$$

$$P^{G}_{P} = P^{C}_{P} \tag{3.59}$$

$$\vec{u}^{G}_{P} = |\vec{u}^{C}_{nP}|\hat{n} + |\vec{u}^{N}_{t_1P}|\hat{t}_1 + |\vec{u}^{N}_{t_2P}|\hat{t}_2 \tag{3.60}$$

$$u^{G}_{P} = u^{C}_{nP}n_x + u^{N}_{t_1P}t_{1x} + u^{N}_{t_2P}t_{2x} \tag{3.61}$$

$$v^{G}_{P} = u^{C}_{nP}n_y + u^{N}_{t_1P}t_{1y} + u^{N}_{t_2P}t_{2y} \tag{3.62}$$

$$w^{G}_{P} = u^{C}_{nP}n_z + u^{N}_{t_1P}t_{1z} + u^{N}_{t_2P}t_{2z} \tag{3.63}$$

Now, for the total stress tensor which is given by

$$\boldsymbol{\sigma} = \boldsymbol{S} - P\boldsymbol{I} \tag{3.64}$$

where $\boldsymbol{\sigma}$ and $\boldsymbol{S}$ are total and deviatoric stress tensors in Cartesian coordinates respectively, P is the hydrostatic pressure and $\boldsymbol{I}$ is the second order identity tensor. As at the MMI type of interface, the stress tensor is reconstructed by enforcing slip condition (Neumann) for the tangential components and continuity for the normal components. The reconstructed total stress tensor at point P in local normal and tangential coordinates will be :

$$\tilde{\boldsymbol{\sigma}}_P^G = \begin{pmatrix} \tilde{\sigma}_{nn}^C & \tilde{\sigma}_{nt_1}^C & \tilde{\sigma}_{nt_2}^C \\ \tilde{\sigma}_{t_1n}^C & \tilde{\sigma}_{t_1t_1}^N & \tilde{\sigma}_{t_1t_2}^N \\ \tilde{\sigma}_{t_2n}^C & \tilde{\sigma}_{t_2t_1}^N & \tilde{\sigma}_{t_2t_2}^N \end{pmatrix}_P \tag{3.65}$$

Here these stress components are injected and extended accordingly using the values at node P and IP1. The stress state at node IP1 is:

$$\tilde{\boldsymbol{\sigma}}_{IP1} = \begin{pmatrix} \tilde{\sigma}_{nn} & \tilde{\sigma}_{nt_1} & \tilde{\sigma}_{nt_2} \\ \tilde{\sigma}_{t_1n} & \tilde{\sigma}_{t_1t_1} & \tilde{\sigma}_{t_1t_2} \\ \tilde{\sigma}_{t_2n} & \tilde{\sigma}_{t_2t_1} & \tilde{\sigma}_{t_2t_2} \end{pmatrix}_{IP1} \tag{3.66}$$

As shown in MVI case, we can apply the correction procedure such that J_1=0 is satisfied at the MMI interface as shown:

The volumetric components at the ghost node P can be written as

$$(\tilde{\sigma}_{nn}^C)_P = (\tilde{\sigma}_{nn})_P \tag{3.67}$$

$$(\tilde{\sigma}_{t_1t_1}^N)_P = (\tilde{\sigma}_{t_1t_1})_{IP1} \tag{3.68}$$

$$(\tilde{\sigma}_{t_2t_2}^N)_P = (\tilde{\sigma}_{t_2t_2})_{IP1} \tag{3.69}$$

Using Eqs. 3.67-3.69 we can write J_1 (deviatoric stress invariant) at both P and IP1 in terms of total stress σ and hydrostatic pressure P.

$$(J_1)_{IP1} = (\tilde{\sigma}_{nn} + \tilde{\sigma}_{t_1t_1} + \tilde{\sigma}_{t_2t_2} + 3P)_{IP1} = 0 \tag{3.70}$$

$$(J_1)_P = (\tilde{\sigma}_{nn}^C + \tilde{\sigma}_{t_1t_1}^N + \tilde{\sigma}_{t_2t_2}^N + 3P^C)_P \tag{3.71}$$

The trace of deviatoric stress tensor, J_1 at the ghost node P can be written in terms of extended components from the real node IP1 and injected components from the real node P such that

$$(J_1)_P = (\tilde{\sigma}_{nn})_P + (\tilde{\sigma}_{t_1t_1} + \tilde{\sigma}_{t_2t_2})_{IP1} + (3P)_P \neq 0 \tag{3.72}$$

It can be seen clearly that at the ghost node P the J_1=0 condition is not satisfied. Therefore we fix this by correcting stress state at the ghost node P. The procedure for this is shown below. Let $\tilde{\sigma}^G_{nn}$, $\tilde{\sigma}^G_{t_1t_1}$ and $\tilde{\sigma}^G_{t_2t_2}$ are the corrected states at the ghost point P such that

$$\tilde{\sigma}^G_{nn} = (\tilde{\sigma}^C_{nn})_P \tag{3.73}$$

$$\tilde{\sigma}^G_{t_1t_1} = (\tilde{\sigma}^N_{t_1t_1})_P + \Delta\sigma \tag{3.74}$$

$$\tilde{\sigma}^G_{t_2t_2} = (\tilde{\sigma}^N_{t_2t_2})_P + \Delta\sigma \tag{3.75}$$

where $\Delta\sigma$ is the correction added to existing extended stress states. Now we can find $\Delta\sigma$ by enforcing J_1=0 condition at the ghost node P as follows:

$$(J_1)_P = (\tilde{\sigma}^G_{nn} + \tilde{\sigma}^G_{t_1t_1} + \tilde{\sigma}^G_{t_2t_2} + 3P^G)_P = 0 \tag{3.76}$$

$$\Rightarrow (\tilde{\sigma}^C_{nn} + \tilde{\sigma}^N_{t_1t_1} + \tilde{\sigma}^N_{t_2t_2} + 3P^C)_P + 2\Delta\sigma = 0 \tag{3.77}$$

$$\Rightarrow \Delta\sigma = (\tilde{\sigma}^C_{nn} + \tilde{\sigma}^N_{t_1t_1} + \tilde{\sigma}^N_{t_2t_2} + 3P^C)_P / 2 \tag{3.78}$$

Once the total stress tensor at the ghost node P is constructed, the stress components in Cartesian coordinates are recovered back using Eq 3.24. This correction procedure makes sure the correct ghost state is populated.

3.2.3.3 Material- Rigid Solid Interface (MRI)

The normal velocity at MRI interface satisfies the Dirichlet condition:

$$\vec{u}.\hat{n} = U_n \tag{3.79}$$

Where U_n is the normal velocity of the rigid solid object. In addition, the continuity of normal stresses and Neumann conditions for tangent velocity components (free slip) and tangential stress components are applied at the interface.

3.3 Note on Szz Component

Since J1, the first invariant of stress tensor by definition should be equal to zero irrespective of the coordinate system the *Szz* component can be computed as follows.

$$J_1 = Sxx + Syy + Szz = 0 \tag{3.80}$$

$$=> Szz = -(Sxx + Syy) \tag{3.81}$$

Most of the computer codes extract *Szz* using the above equation obviating the solution of an additional evolution equation for for *Szz*. A problem very peculiar to the current method will occur for both MVI and MMI as the state of ghost tensor is such that $J_1 = 0$ is not satisfied (section 3.3). Therefore, the procedure for extracting the ghost value of *Szz* using ghost *Sxx* and ghost *Syy* components will result in an incorrect ghost state. This can be avoided by either storing the ghost *Szz* component or by evolving the *Szz* equation. Avoiding these will result in elliptical base of bar as shown in Figure 3-8 (a).Moreover, even after storing or evolving *Szz* component, the $J_1=0$ condition will still be violated and will corrupt the solution at interface as shown in Figure 3-7. The correction given in last section clearly satisfy the $J_1=0$ condition and the modified ghost stresses can be used to calculate *Szz* eliminating the need to either store *Szz* ghost component or evolve the *Szz* equation separately. This correction will also ensure the circular base of bar as shown in Figure 3-8 (b).

3.4 Summary

This chapter clearly depicted the need for the modification of Ghost Fluid Method to solve three dimensional problems. It was clearly shown that the straight forward extension of two dimensional methods as is often mentioned by various researchers will not give a physically correct solution in three dimensions. The correction procedure mentioned here automatically satisfies the physical constraint on deviatoric stress tensor. The results corresponding to impact, penetration and fragmentation using the boundary conditions shown in this section are given in CHAPTER 5 and CHAPTER 6.

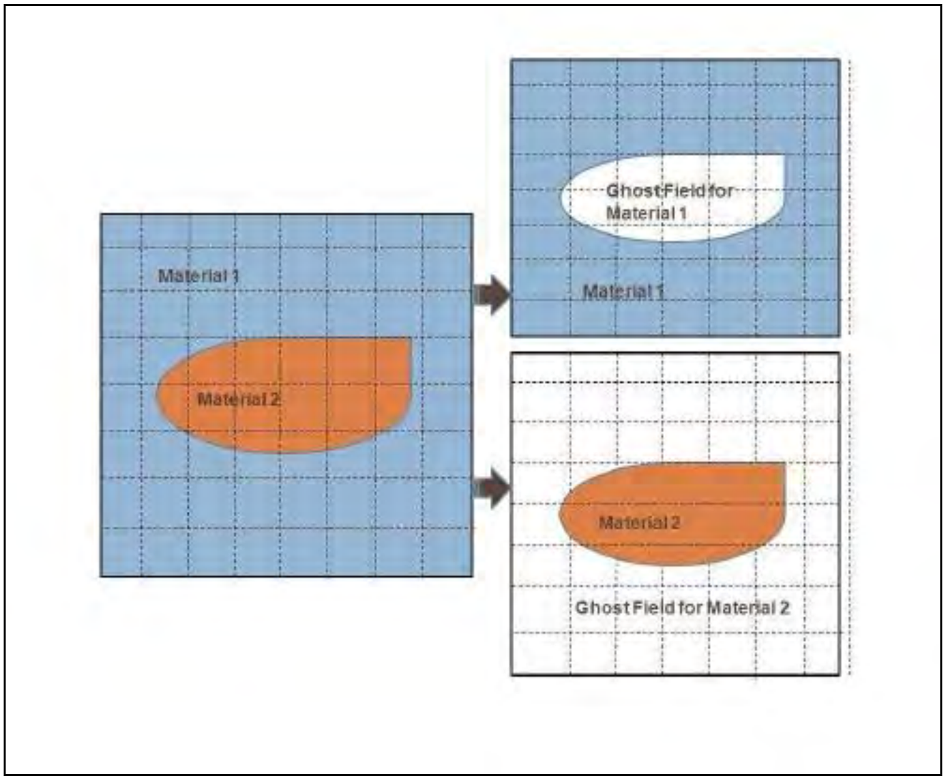

Figure 3-1.GFM approach converts a two-material problem to two single material problems.

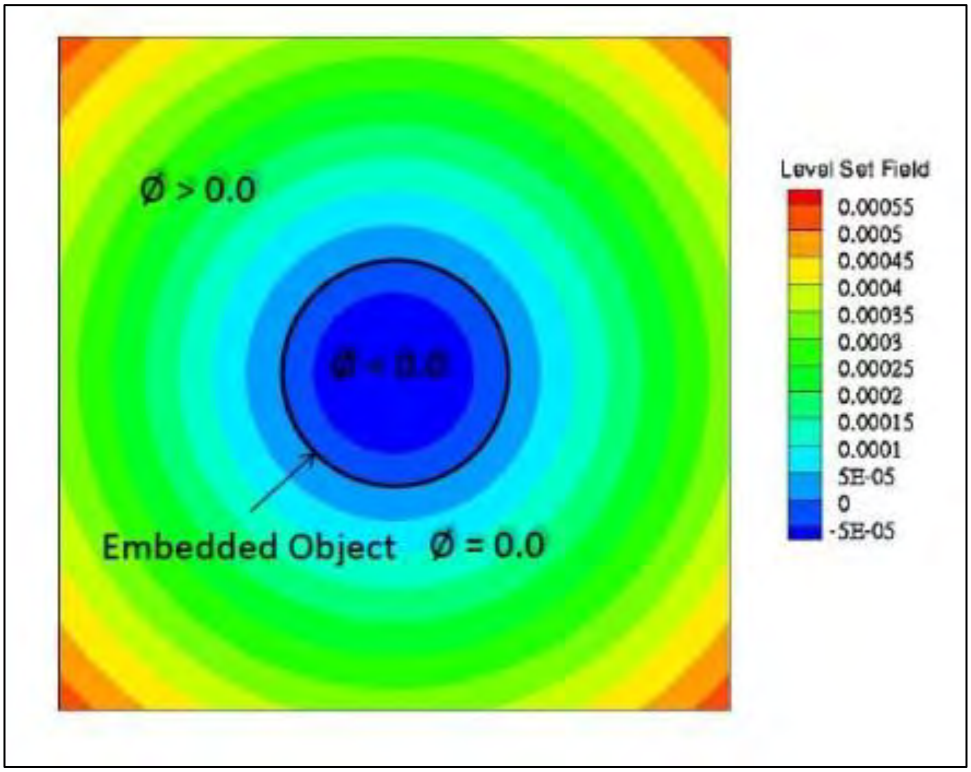

Figure 3-2. Level set field (Ø) for an embedded object (circle). The value of field inside the object is negative and outside the object is positive. The zero level set contour implicitly defines the location of the embedded object.

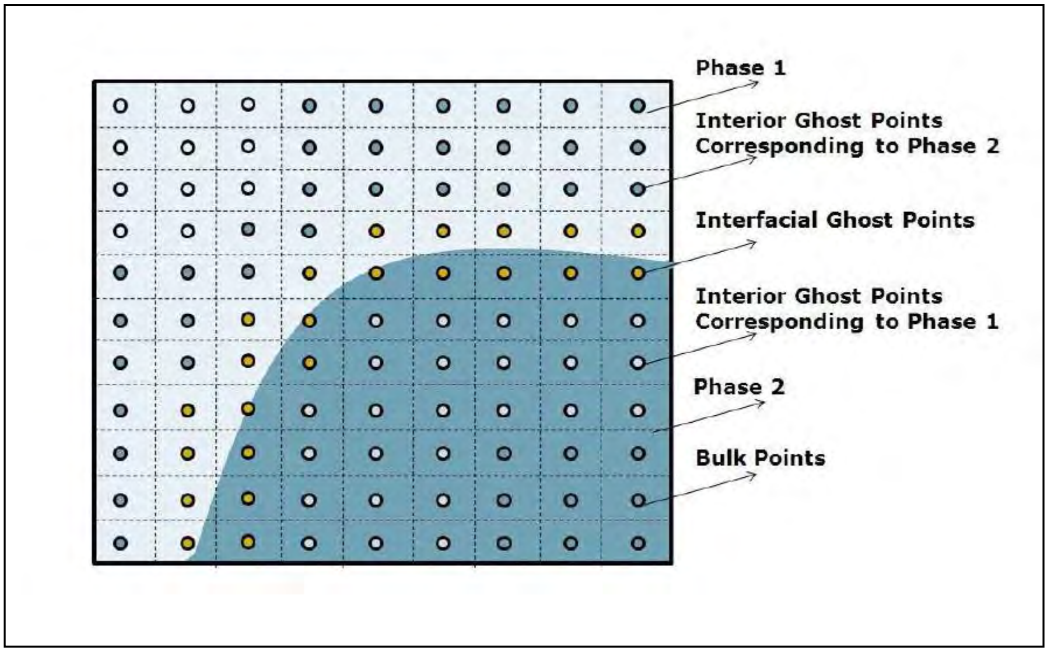

Figure 3-3. Classification of grid points in the computational domain using level set function.

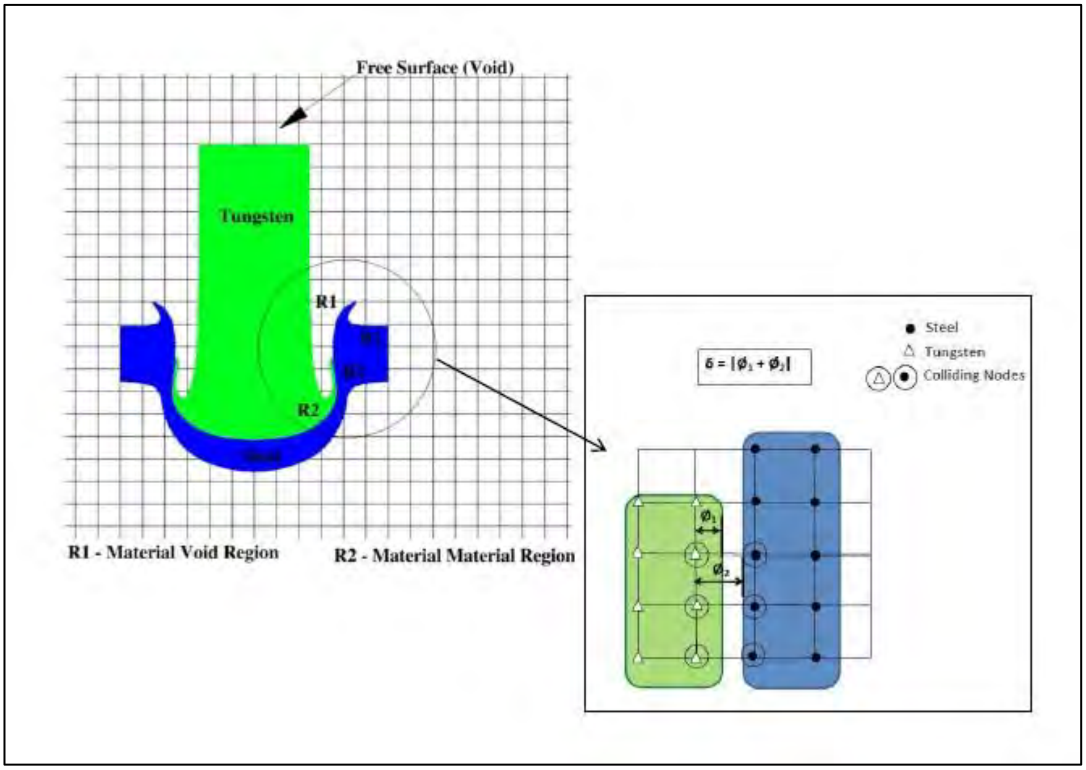

Figure 3-4. Procedure to detect collision between any two level sets; ϕ_l indicate the value of the level set function corresponding to the l^{th} material interface.

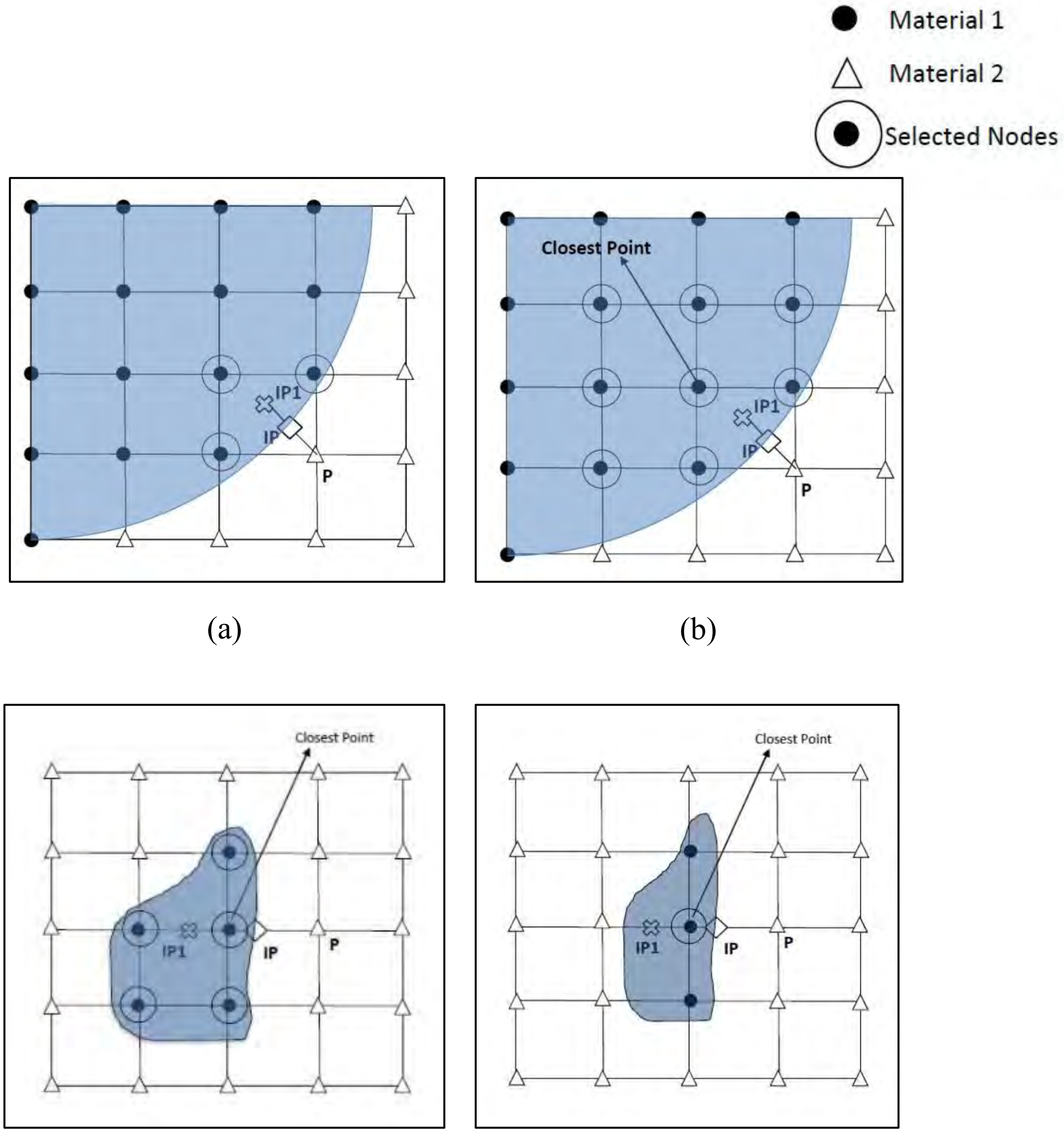

(a) (b) (c) (d)

Figure 3-5. Embedding the boundary conditions within the interpolation procedure (a) Bilinear Interpolation (b) Least Squares Procedure (c) Fragment involving sufficient number of nodes for bilinear interpolation (d) Fragment involving insufficient number of nodes for bilinear interpolation.

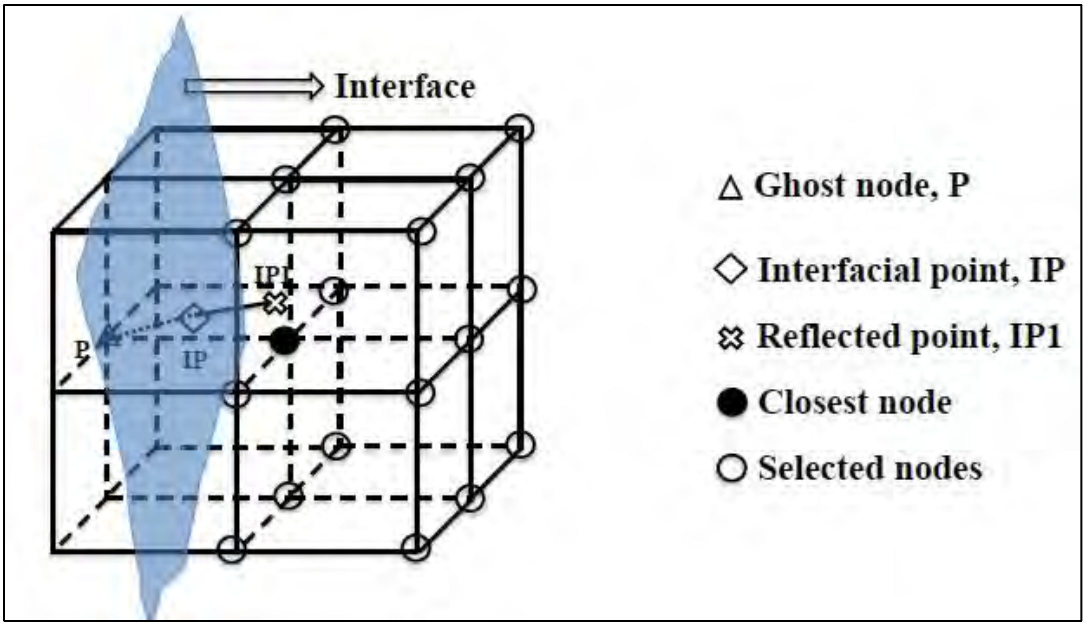

Figure 3-6. Three dimensional cartesian grid partially containing the interface showing the procedure of embedding the boundary conditions with the Least Square Method.

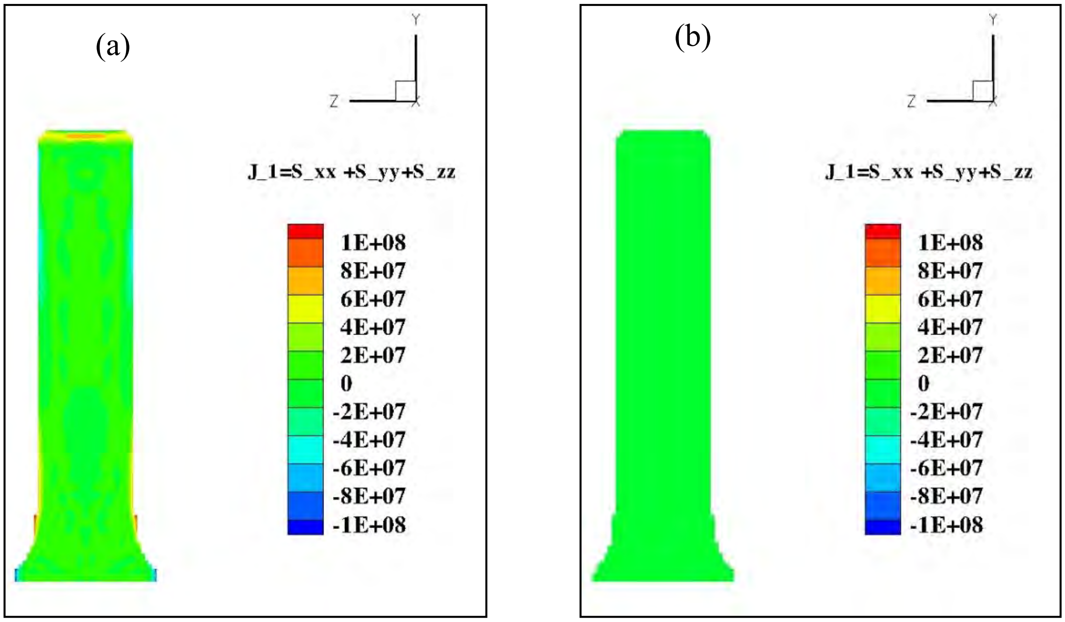

Figure 3-7. Taylor bar section showing the calculation for the first invariant of deviatoric stress at a section (a) uncorrected stress $(J_1 \neq 0)$. (b) corrected stress $(J_1 = 0)$.

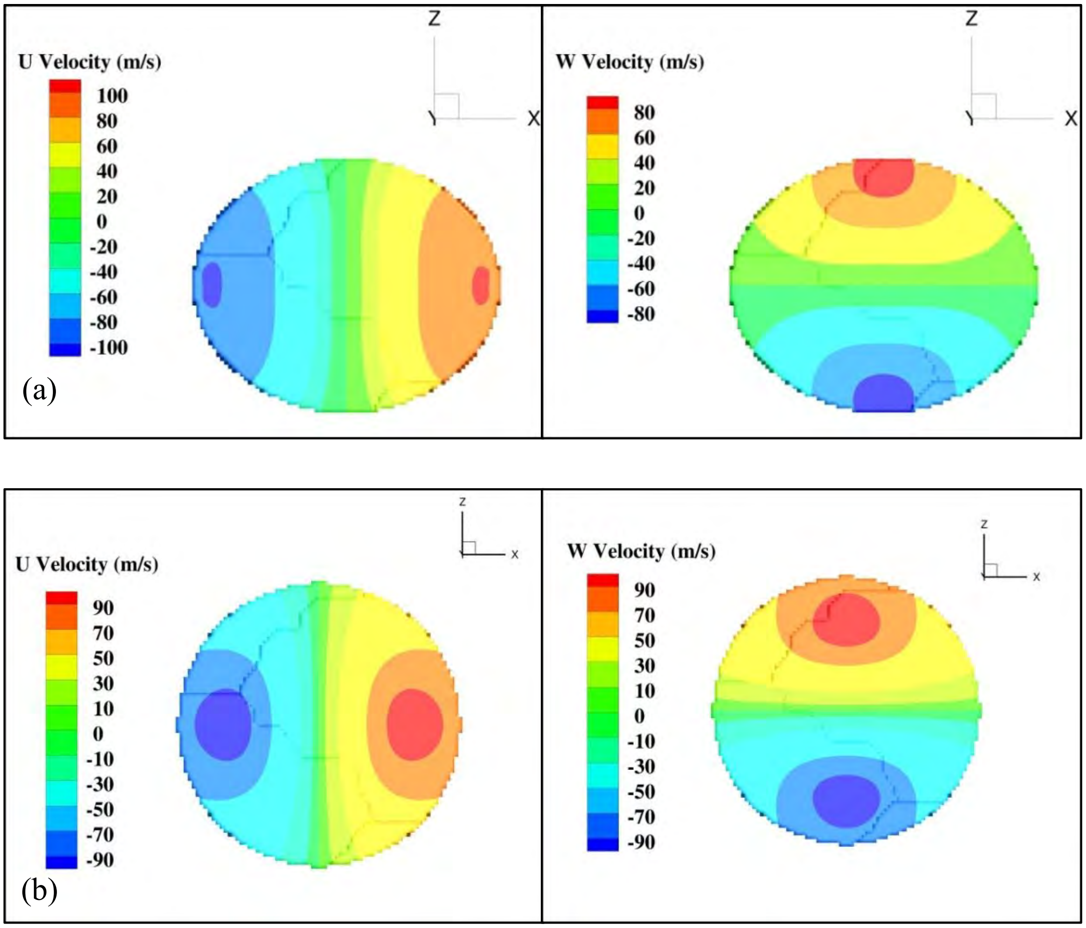

Figure 3-8. Contours of u-velocity and w-velocity for Taylor bar impact (Copper, 227 m/s): a) Elliptical shape of Taylor bar due to avoiding the storage of ghost Szz component b) Circular shape of the bar after correction.

CHAPTER 4

PARALLEL ALGORITHM

4.1 Introduction

The parallel implementation pursued herein seeks to avoid storage of global information proportional to the size of the overall problem on a single processor; this is in the interest of enabling solution of truly large scale problems where it is imperative to maintain data localization on processors and to exchange information between processors only as necessary. The algorithm is designed to execute on a distributed memory system such as PC clusters where each processor carries only a designated sub—domain of the overall domain and therefore executes only part of the overall computational task. The inter-processor communication is handled using MPI libraries [54]. A domain decomposition software that creates balanced partitions is highly desirable for parallel algorithms. In the following setup, METIS [55], a graph partitioning software, is used for load balancing so as to assign apportion uniform computational load to all processors. METIS uses the nodal connectivity as an input to generate partitions which are optimally load balanced. It also minimizes the communication time by minimizing the total number of edge cuts[55] . With the combination of MPI and METIS and local storage of data it is now possible to handle very large problems sizes.

The algorithm given here is for a two-dimensional problem but relevant examples and figures are provided in the results sections for three dimensions.

The step-by-step procedure for the parallel algorithm is as follows:

i. The initial flow domain shown in Figure 4-1 is divided into horizontal or vertical stripes and is distributed to different processors. The distribution is such that each processor gets allocated with one stripe and none of the processors stores the whole mesh right at the outset of the calculation. Once this subdivision of the domain is done the calculation never reverts back to a definition of the overall problem.

ii. The mesh is constructed individually on each processor with cell index running from 1- N_{max}. Here N_{max} corresponds to maximum number of cells on the individual processor.

iii. Two types of mappings are constructed for easy storage and retrieval of the information. These mappings relate the local index on a processor to the global index and vice versa. The details on these mappings will be explained later in this section.

iv. These blocks of mesh are fed to METIS to obtain a load-balanced domain. METIS only gives the information about cells that should be removed or added from a particular sub-domain. All cells are tagged with either –keep” or –send” status. This status also contains the information about the processor it has to go to. The required information is exchanged using MPI and the final load balanced domain is constructed as shown in Figure 4-2.

v. The –global to local” and –local to global” mappings are constructed again due to change in part of domain on individual processor.

vi. A collision detection algorithm is used to find the neighboring processors, which will be used to exchange data across the processor boundary.

vii. A single layer of ghost cells is constructed by tagging the cells on processor boundaries. These are the cells which are on the host processor and will be ghosts for neighboring processors. As the algorithm required for current work uses a third order ENO scheme[49], a ghost layer consisting of four cells is constructed. Multiple layers of ghost cells shown in Figure 4-3 are constructed using a Stencil algorithm explained in next section.

viii. The cell structure is constructed again with addition of ghost cells. The ―global to local” and ―local to global” mappings are augmented with addition of new ghost cells.

ix. The embedded objects using level set functions are defined at this point.

x. The initial conditions are prescribed on each processor individually according to the part of domain assigned to that processor.

xi. The boundary conditions are read on one processor and are broadcast to other processors.

xii. The primitive variables for ghost region are communicated across the processor boundaries for the construction of fluxes and source terms for host cells for all the processors.

xiii. The flux terms and source terms are used to compute primitive variables for host cells.

xiv. The process explained in step xii is repeated till the final time step.

4.2 Issues With Parallelizing the Sharp-Interface Level Set-Based Approach

In this section the critical problems while parallelizing the code in the present framework will be explained. These problems are related to handling (storage/retrieval) of global data, definition and construction of ghost layers, special treatment for moving boundaries and handling of GFM at processor boundaries.

4.2.1 Handling of Global Data

The efficient handling of global data is the most important aspect of parallelization. The idea is to strictly avoid having any arrays of the size of global flow domain, Ω_g. As the flow domain is divided at the outset there does not exist a so-called ―master processor”[56] to take care for any global operations. The ―global to local”,Ω_{gl}

and ―local to global”,Ω_{lg} mappings are used for storage and retrieval of data. The mapping Ω_{gl} will use g_i as the global index and will return l_i as the local index. Similarly, the mapping Ω_{lg} will use l_i as the local index and return g_i as the global index. These mappings, shown in Figure 4-4 are constructed using a hash table [57]. The hash table [58] is a data structure which maps certain keys (global indices) to related values (local indices). The hash function is used to convert a key to an index of an array where corresponding local index is stored. This arrangement results in quick retrieval of information.

The integer hash function is used in current implementation. As the ghost layer is being added to each processor, the number of cells on each processor is augmented with the added ghost cells. The Ω_{gl} and Ω_{lg} mappings are augmented after the inclusion of ghost layer as every processor gets a set of ghost cells with new local indices. This operation is illustrated in Figure 4-5.

4.2.2 Definition and Construction of the Ghost Layer

Since the domain is being partitioned amongst the *p* processors one needs to define a set of cells to store information from neighboring processors. This is necessitated by the solution process for partial differential equations of all types since nearest neighbors are involved in constructing flux information in finite difference and finite volume schemes. These cells, which are used at the edges of the subdomains to effect inter-processor communication, are called ghost cells. The definition of ghost region can be explained using two processors A and B shown in Figure 4-6. If a given domain is divided using two processors A and B, there will be a set of cells called ―host cells” where the primitive variables are computed on the processor itself and a set of cells called ―ghost cells” where the primitive variables will be communicated from neighboring processor. This section will explain the need for a layer of ghost cells for a discretization scheme such as the central difference method. Here the cells with uppercase A and B are called host cells; on these cells, for discretization using a central difference scheme, the neighbor information can be obtained on the respective host processor itself. But for the cells having lowercase a and b, one needs information across the processor boundary for accurate construction of fluxes. For this purpose the fluxes for these cells are communicated from the neighboring processor. Hence the information for ghost layer of Processor A comes from host cells of Processor B and vice versa. This ensures that the same solution as obtained from a serial single processor computation will be achieved in parallel multi-processor calculation as well. In the present study, a third-order ENO scheme is used which requires four layers of ghost cells due to the adaptive stencil selection procedure implicit in such high-order schemes. The same logic applies for the construction of ENO[49] in all the three dimensions.

Particular attention must be paid to the construction of the ghost layer. The first layer of ghost cells touches the processor boundary and can be tagged easily as shown in Figure 4-7 (a). In tagging the subsequent layers recursive [59] computation will need to be employed leading to a computationally inefficient procedure. Here, the recursive algorithm is avoided by using a stencil-based construction of ghost layer. In the stencil-based construction the first layer of cells is constructed by tagging the cells on the processor boundary; then for every cell on processor boundary a set of cells is picked to serve as ghost cells for neighboring processors. The stencil based algorithm maps a predefined stencil with symbols –X” on the tagged single layer ghost cell as shown in Figure 4-7(b). The cells which lie outside the processor can be easily omitted from the ghost layer structure using the Ω_{gl} mapping. The mapping stencil for a three-dimensional case for a single computational will assume the form of a pyramid as shown in Figure 4-8 (a) and Figure 4-8(b). The different views of the three dimensional stencil are also shown in Figure 4-9 (a) and Figure 4-9 (b) for a better view of the definition of these cells in 3D.

4.2.3 Moving Boundary Problems

In the case of moving boundary problems, an embedded (i.e. immersed) object is free to move across the flow domain. Issues arise when this object enters from one processor to other, as illustrated in Figure 4-10 (a). Here an embedded object is defined using a level set field and is given a unit velocity in the negative y-direction. The level set is completely defined in processor A and processor B does not have any information about it. This results in corruption of the level set field when it crosses the processor boundary as seen in Figure 4-10 (b).

This problem is resolved by initializing the ghost region of neighboring processor with level set value of 0.0 as shown in Figure 4-11. This is done by tagging all the processors having a particular level set with flag = 1. Now for computation on a particular processor with flag = 1, if the neighboring processor has a value of flag = 0, the initialization mechanism of ghost layer should be triggered on the neighboring processor. This ensures the allocation of memory for an incoming object in processor B. Initially the information will be communicated to the ghost region of processor B and once this is done level set update and generation algorithm on processor B will take over; this results in smooth entry of the object from processor A into processor B through the ghost layer. The Figure 4-12 shows the successful entering of level set from one processor to another.

The above exercise shows how one can handle moving boundaries in this algorithm. The idea is to have information about the embedded object on the local processor and only initialize (i.e. allocate memory in) the ghost region of neighboring processors so that the correct values of level set function can be communicated. It should be noted that this problem will occur only for algorithms where the level set function is defined in a narrow band[50]. In cases where level set function is defined throughout the domain, it can be just treated like any other flow variable. However, we expect that typical level set based methods will employ narrow-band level set definitions and therefore the procedure detailed above is required.

The same issue of corruption of the level set function can arise in other situations as well. First, if the approaching object is not convex as seen by the processor boundary the level set function can get corrupted as shown in Figure 4-13. Secondly even for a convex surface like a sphere, the mesh partition can be such that the level set function can become corrupted as shown in Figure 4-14. The corruption of level set function can be prevented if we always initialize the neighboring processor's ghost layer so that the incoming level set can be accommodated. This is shown in Figure 4-15. Once the ghost region is ready to accommodate incoming level set field, the problems described above will not occur and the level set field will move smoothly from one processor to another as shown in Figure 4-16 and Figure 4-17.

4.2.4 GFM at Processor Boundaries

In the context of sharp interface techniques for compressible flow the original ghost fluid method proposed by Fedkiw and coworkers needs to be modified to handle strong shocks. The development of the GFM with a Riemann solver at embedded interfaces in a serial algorithm was developed in the PhD thesis work of S.Sambasivan [60]. In this section the parallel algorithm for implementing the ghost fluid method will be discussed. In the parallel framework there are two types of ghost cells, processor ghost cells and GFM ghost cells. Figure 4-18(a) shows a processor boundary with parallel ghost cells and GFM ghost cells corresponding to interface. The entire GFM region with parallel ghost cells is shown in Figure 4-18(b). Figure 4-19 clearly shows that some of the interface cells required for GFM operation lie in the parallel ghost region. The steps required to populate ghost field in parallel framework are:

1. Populate the ghost field (GFM) for interfacial cells on real domain of every processor. This is done in the same fashion as in a serial algorithm[40].

2. Communicate the constructed ghost field across the processor boundary.
3. Extend the ghost field to GFM ghost region on both real and ghost domain.
4. Communicate the extended ghost field across the processor boundaries.

Note that the extension process is done on all the cells of a particular processor. After the extension, the parallel communication is done to ensure correct values in whole GFM region (especially the region $\sum$) as the region $\sum$ (Figure 4-19) doesn't have any interface cells for populating correct ghost field.

The interface cells corresponding to the region $\sum$ are in the neighboring processor as shown in Figure 4-20. For clarity, only GFM cells corresponding to the interface are shown in Figure 4-20. The communication of extended ghost field ensures that the region $\sum$ gets populated with correct values.

4.2.5 Communication Using MPI

The inter-processor communication is the most important part of a parallel code. As mentioned above, Message Passing Interface (MPI) is used for data communication across processor boundaries. MPI specification is widely used for solving significant scientific and engineering problems on parallel architectures. MPI adds portability to computation code as it is hardware independent. The major MPI features used in this code are

i. MPI_ISEND, MPI_IRECV for non-blocking point-point communications during initial domain decomposition and for inter processor communication during ghost region exchange.
ii. MPI_BCAST for collective communication for broadcasting the inputs to all the processors.
iii. MPI_ALLGATHER and MPI_ALLREDUCE for collective communication such as providing correct CFL number to all processors.

iv. MPI_BARRIER for synchronization of code.

There are other data types like MPI_WTIME, MPI_ WAITALL which are used to handle data communication.

The exchange of ghost region information is the most important part of communications associated with a parallel computer code. This operation can be done in either a synchronous way using MPI_SEND / MPI_RECV or in an asynchronous way using MPI_ISEND / MPI_IRECV. The synchronous way of communication halts the computational operations till the communications operations are not complete. This can take a lot of time if two threads which want to communicate are on different computers and are connected through a network. This network can be 10 Mbps, 100 Mbps or an infiniband, there will be a substantial cost of sending the data. This type of communication ensures safe handling of data as data is not used till the communication is complete but leads to underutilization of computer resources.

The asynchronous communication is the key to get high performance as the threads can continue to do computing while communication with another thread is still pending. Unlike synchronous version these calls are non-blocking as if a thread uses a function to send data, the function will return immediately much before the data is finished being sent. Care must be taken as not to manipulate the data being sent in the buffer. MPI library provides a function call MPI_WAIT which can be used to ensure that the data being communicated has been received by the desired thread and it is safe to modify the buffer.

4.3 Results

In this section, validation of the parallel solution of moving boundary problems will be presented. First canonical 2-d gas dynamics test problem will be presented and then standard solid impact test case are solved to demonstrate the successful treatment of the GFM approach with an embedded boundary defined by a level set . The handling of multitude of objects in a shocked flow will also be shown at the end.

4.3.1 Emery Wind Tunnel Case

This is a standard case for testing the compressible fluid code introduced by Emery[61]. Here, the solution is carried out on a Cartesian grid with a level set defining the step and the GFM approach being used at the solid-fluid interface. The initial conditions corresponding to shock wave of strength Mach 3 was imposed on the west boundary. The north and south boundaries were prescribed with reflective boundary condition and the east boundary is prescribed with Neumann boundary conditions. The initial and boundary conditions are the same as used by previous authors[62, 63]. A uniform grid of 0.0025 on 3.0 X 1.0 domain is used with six processors. The results are in excellent agreement with existing literature[60, 62, 63].

The density contours plot shown in Figure 4-21 clearly captures the lambda pattern seen in this case. It also shows the contact discontinuity captured in the top part of domain.

4.3.2 Taylor Bar Impact at 227m/s and 400 m/s

The Taylor test [64] is used as a canonical test problem to verify and validate numerical and experimental observations. This is a two dimensional case in which a cylindrical rod made of copper impacts a rigid flat substrate at 227m/s. A computation domain of radius 15.0 mm and length of 34.0 mm is chosen for this simulation. The top and right ends of domain are prescribed with Neumann boundary conditions. The presence of rigid wall at the bottom end of domain is modeled by enforcing a reflective boundary condition. The left end of domain is prescribed with symmetry condition. The simulation used 4 processors with a mesh size of 0.075 mm. The rod has an initial density of 8930 kg/m^3, Young's Modulus of 117GPa, Poisson's ratio of 0.35, and yield stress of 400MPa. The calculations are carried up to 80μs at which point nearly all the initial kinetic energy has been dissipated as plastic work. Figure 4-22 shows the contours of pressure and effective plastic strain at the final time of 80μs. Table 4-1 shows the comparison of present results on the Taylor bar impact case with other computer codes. The same test was done for impact at 400m/s as the bar was expected to deform more severely. As can be seen from Figure 5-4, the impact at 400 m/s reduces the bar to almost one third of its initial length with effective plastic strain having the value 5.0 at 80μs.

4.3.3 Shock Diffraction Patterns in a Dusty Cloud

In this simulation, the DNS of a planar shock wave traversing through a dusty gas layer is performed. The problem was investigated by Fedorov et.al.[65] using a mixture model with Euler equations. The same problem is solved using the current parallel framework for shock strength of Mach 3. The computational domain of the problem is shown in

Figure 4-23. The domain size is 60 mm X 30 mm with uniform grid size of 0.02 mm. The shock wave in this problem interacts with randomly seeded 100 particles to generate complex shock diffraction and vortex shedding pattern as shown in Figure 4-24. This effort is a step towards the DNS of such large scale simulation. The different parts of Figure 4-24 clearly show that very minute details of interaction of shock wave with these particles are captured successfully.

4.4 Summary

The parallelization procedure for flow solver was presented in this chapter. The method has involved challenging tasks such as implementation of Ghost Fluid method in three dimensions, handling of level sets in parallel setting, localization of data with efficient storage and retrieval and efficient construction of ghost layer for inter processor communication.

Table 4-1.Comparison of axisymmetric Taylor impact results with other computational codes.

Case 227 m/s	Final length (mm)	Final Base Radius (mm)	Maximum EPSBAR
Current setting	21.45	6.8	3.0
Camacho et al[11]	21.42-21.44	7.21-7.24	2.97-3.25
Tran et al[26]	21.15	7.1	2.86

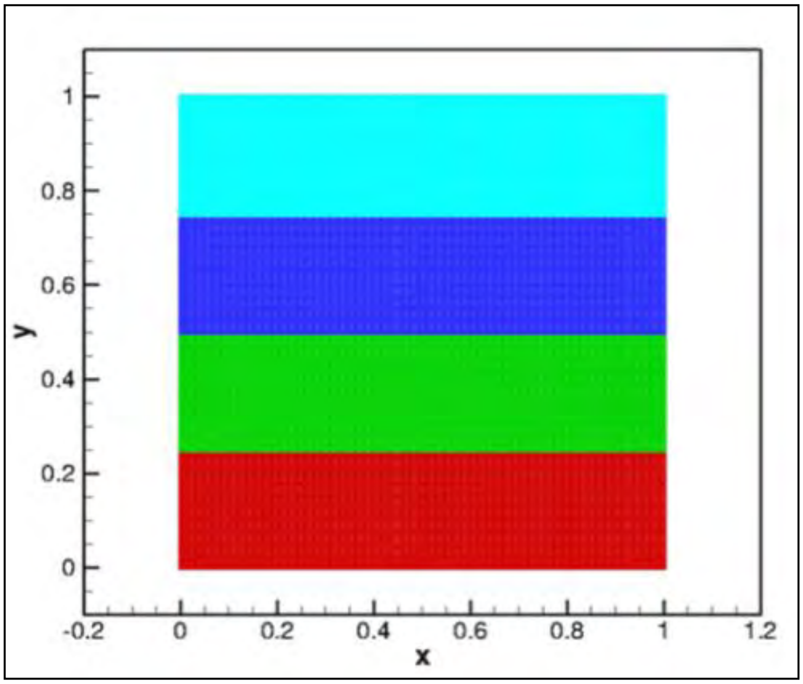

Figure 4-1 Initial computational domain assigned equally to different processors. Each color here denotes a different processor.

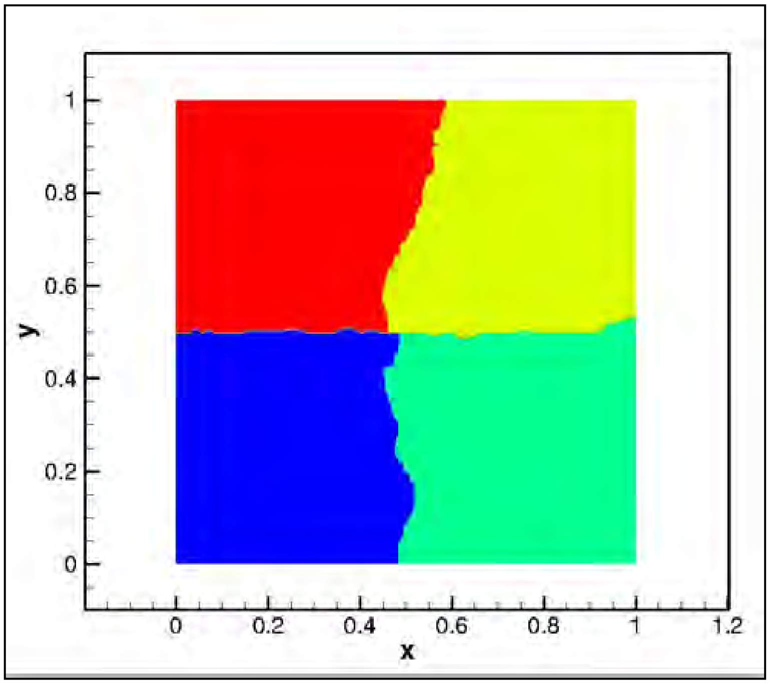

Figure 4-2. Load balanced domain obtained from domain decomposition software METIS. Each color here denotes a different processor.

a)

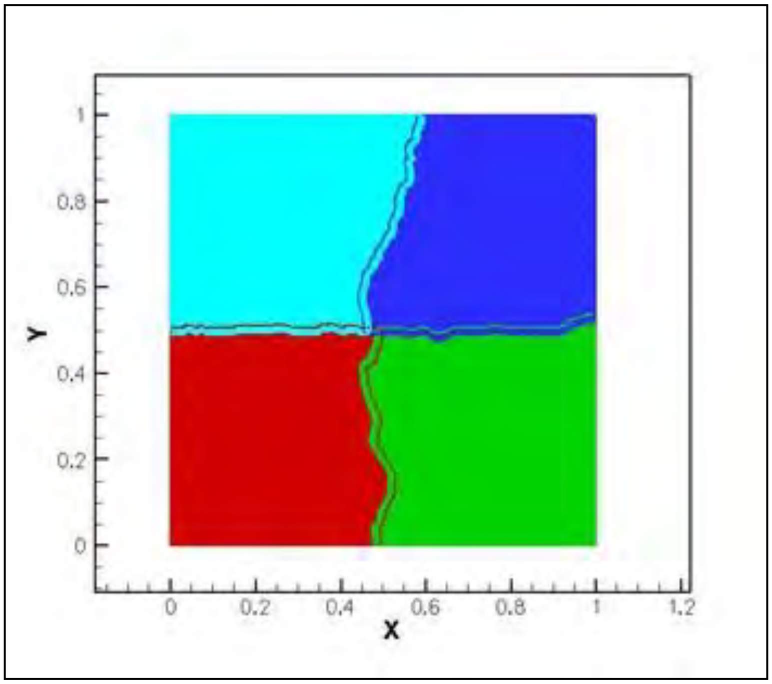

b)

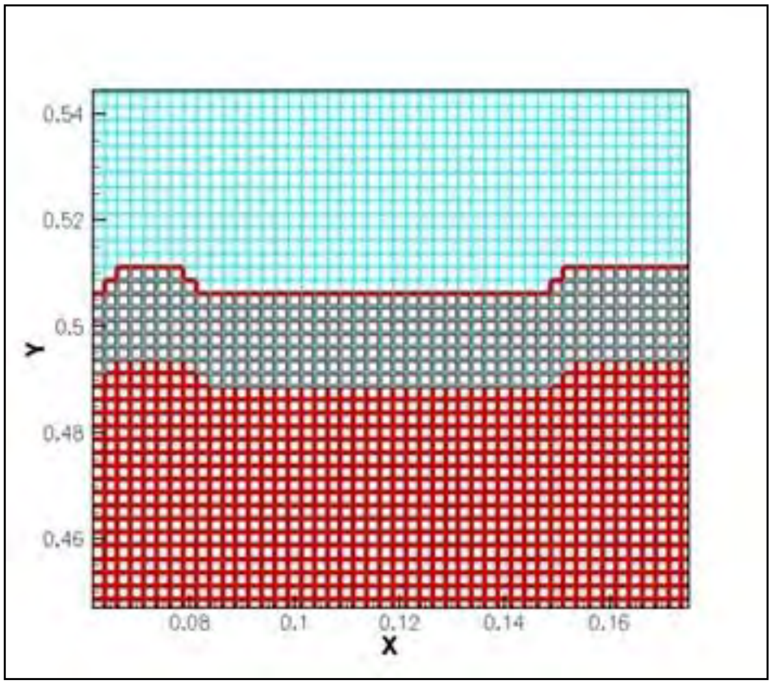

Figure 4-3. Computational domain with ghost layer: a) Augmentation of initial domain with ghost layer b) A 4 cells thick ghost layer for two processors.

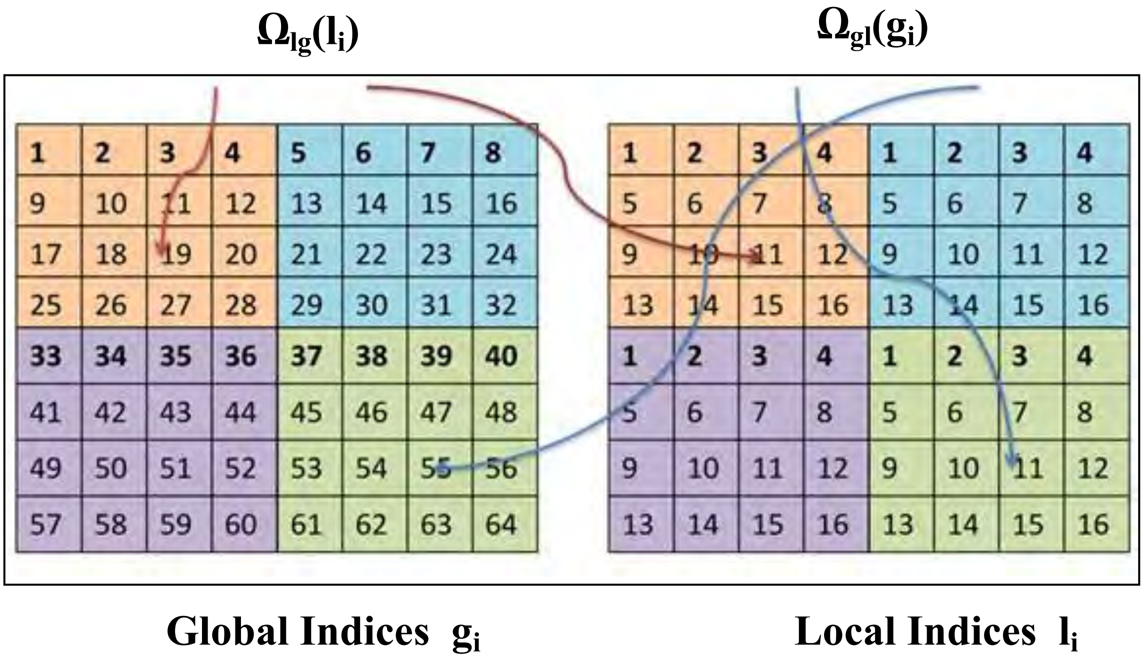

1	**2**	**3**	**4**	**5**	**6**	**7**	**8**
9	10	11	12	13	14	15	16
17	18	19	20	21	22	23	24
25	26	27	28	29	30	31	32
33	**34**	**35**	**36**	**37**	**38**	**39**	**40**
41	42	43	44	45	46	47	48
49	50	51	52	53	54	55	56
57	58	59	60	61	62	63	64

1	**2**	**3**	**4**	**1**	**2**	**3**	**4**
5	6	7	8	5	6	7	8
9	10	11	12	9	10	11	12
13	14	15	16	13	14	15	16
1	**2**	**3**	**4**	**1**	**2**	**3**	**4**
5	6	7	8	5	6	7	8
9	10	11	12	9	10	11	12
13	14	15	16	13	14	15	16

Figure 4-4.Illustration of initial ―local to global” and ―global to local” mappings before addition of ghost layer.

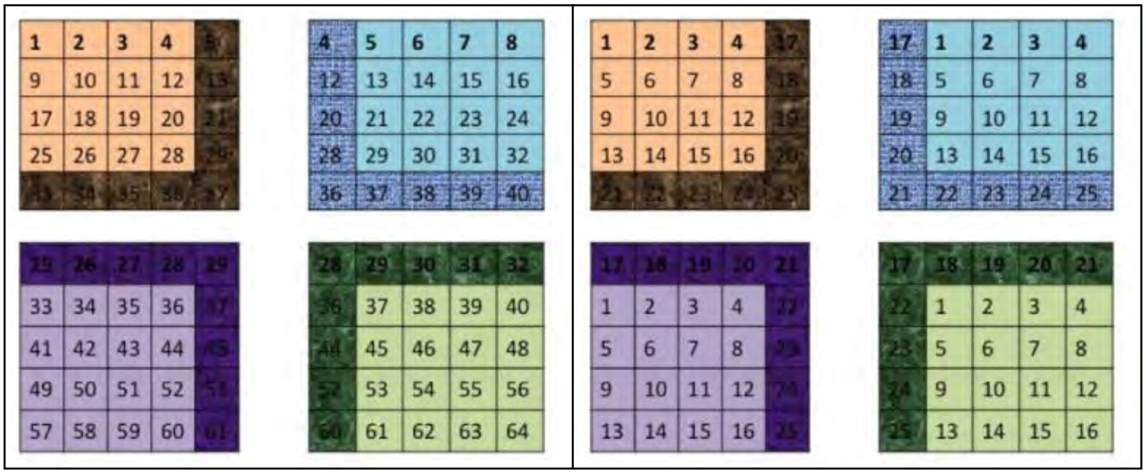

1	2	3	4	5
9	10	11	12	13
17	18	19	20	21
25	26	27	28	29
33	34	35	36	37

4	5	6	7	8
12	13	14	15	16
20	21	22	23	24
28	29	30	31	32
36	37	38	39	40

25	26	27	28	29
33	34	35	36	37
41	42	43	44	45
49	50	51	52	53
57	58	59	60	61

28	29	30	31	32
36	37	38	39	40
44	45	46	47	48
52	53	54	55	56
60	61	62	63	64

1	2	3	4	17
5	6	7	8	18
9	10	11	12	19
13	14	15	16	20
21	22	23	24	25

17	1	2	3	4
18	5	6	7	8
19	9	10	11	12
20	13	14	15	16
21	22	23	24	25

17	18	19	20	21
1	2	3	4	22
5	6	7	8	23
9	10	11	12	24
13	14	15	16	25

17	18	19	20	21
22	1	2	3	4
23	5	6	7	8
24	9	10	11	12
25	13	14	15	16

Figure 4-5. Mappings augmented with ghost layer as seen in shaded part. The ―local to global" and ―global to local" mappings are augmented due to addition of new cells during ghost layer construction procedure.

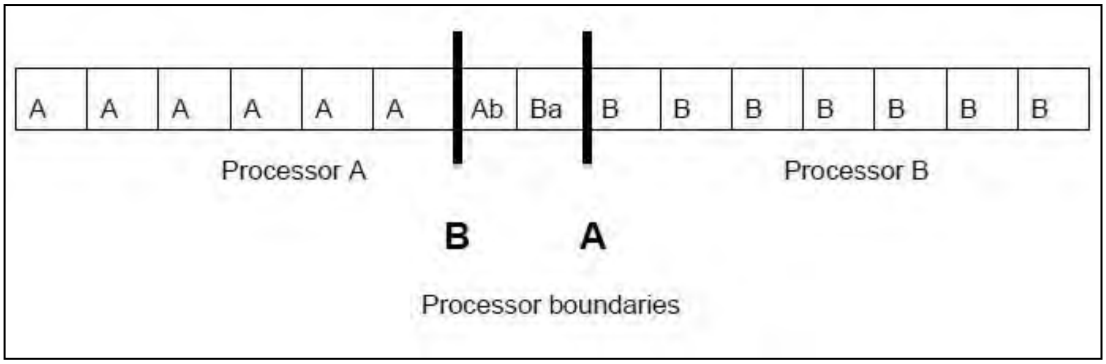

Figure 4-6. One-dimensional layer of host and ghost cells with processor boundaries. The cells with only uppercase characters are host cells and the cells with both uppercase and lowercase characters are ghost cells.

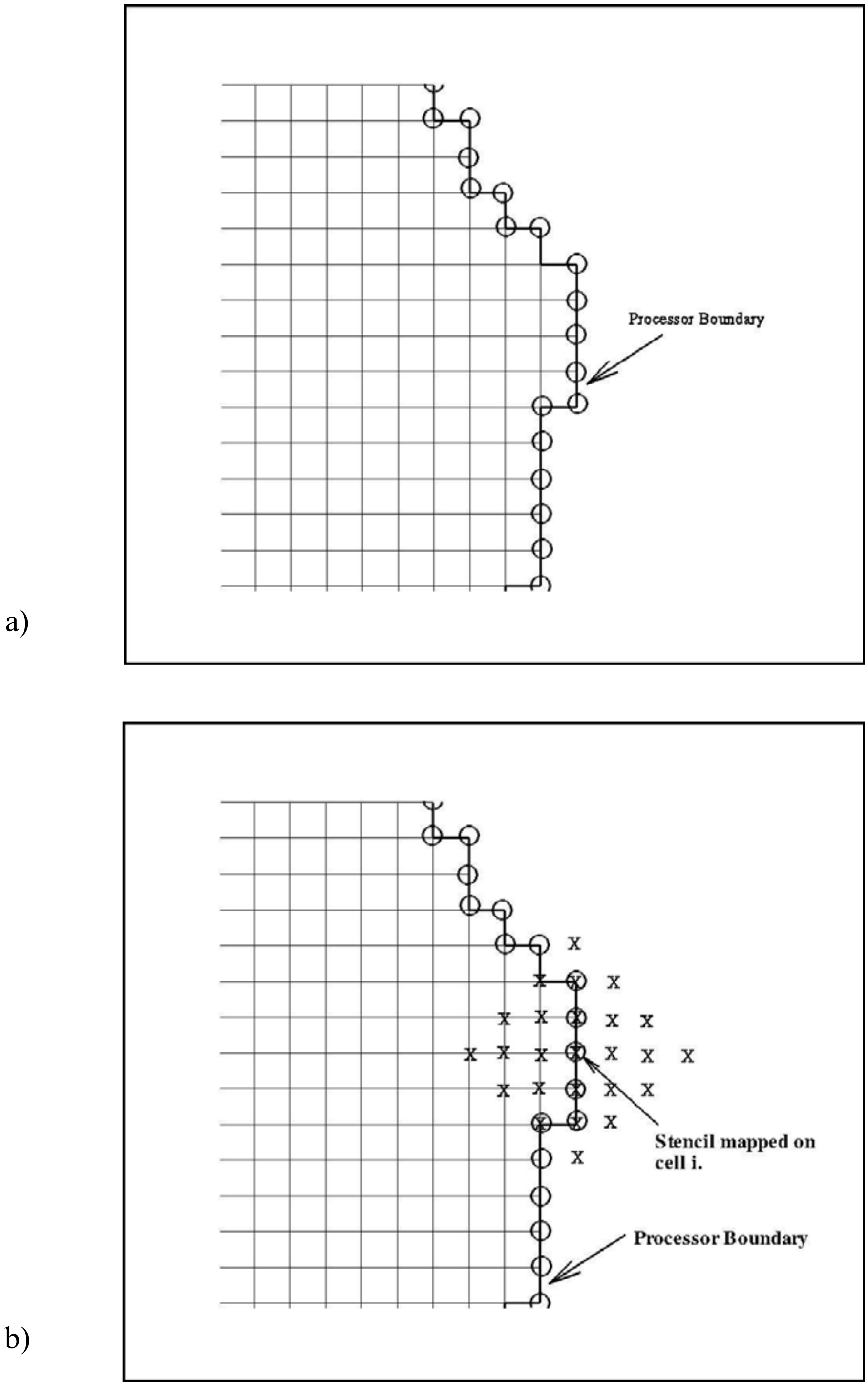

Figure 4-7. Stencil arrangement of two-dimensional setting: a) processor boundary with a single layer of ghost cells b) stencil mapped on a cell i to select neighboring cells for ghost layer construction.

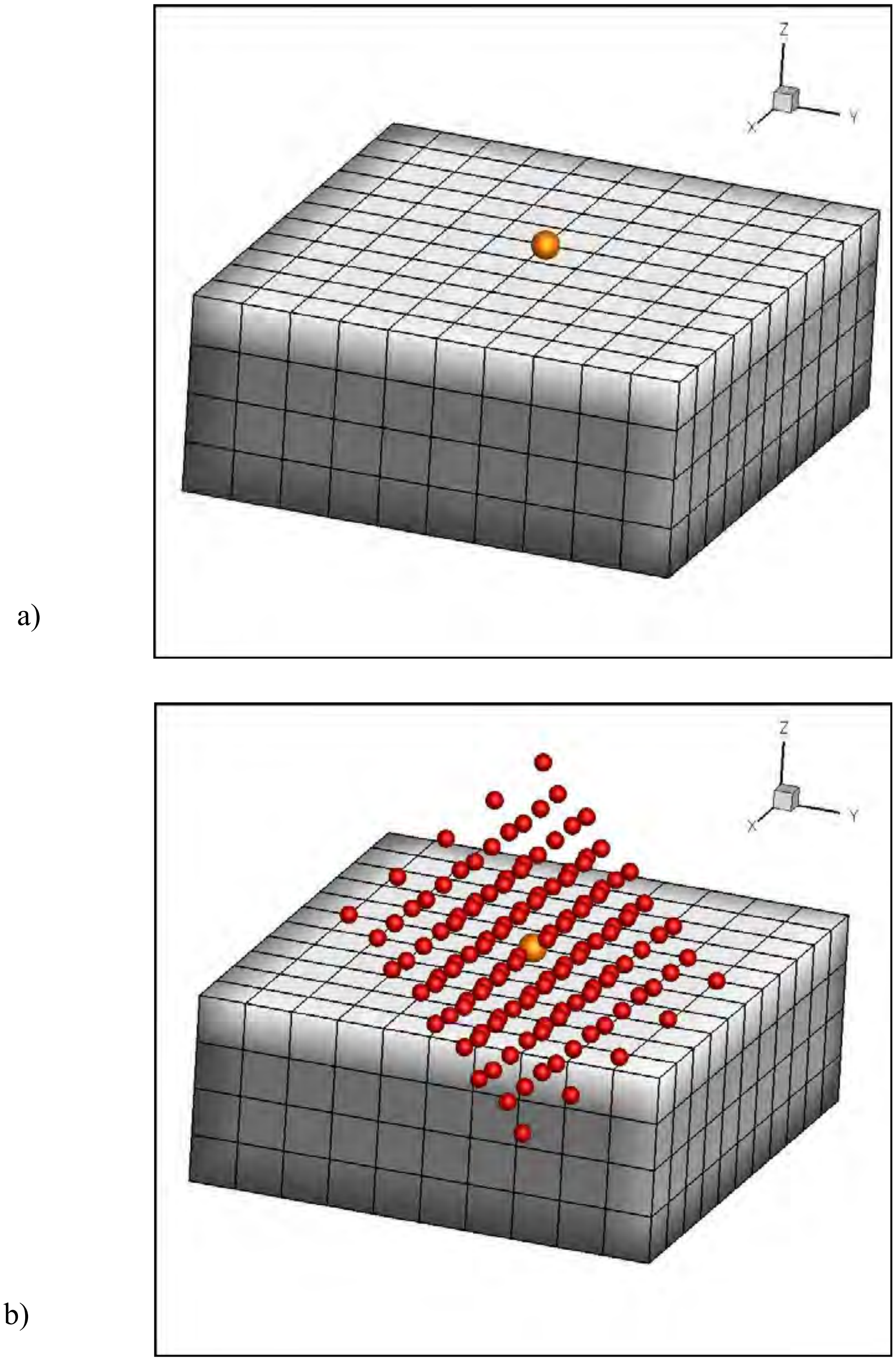

Figure 4-8. Stencil arrangement for the three-dimensional setting. a) Single cell tagged on the processor boundary b) Three dimensional stencil mapped on single cell to select neighboring cells for ghost layer construction.

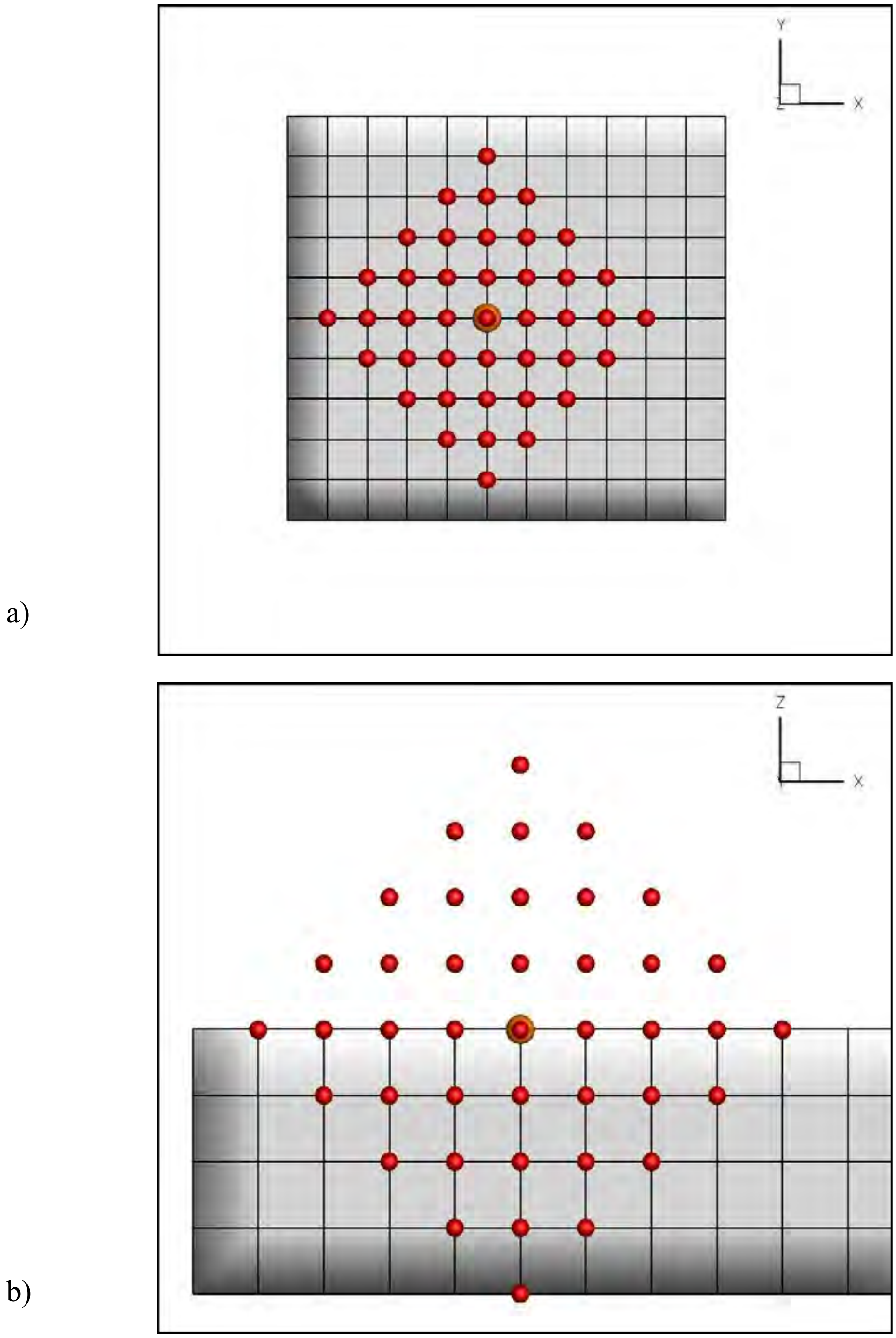

Figure 4-9. Stencil arrangement for three-dimensional setting. a) stencil as viewed from xy plane b) stencil as viewed from xz plane. The three-dimensional stencil is used to select cells for ghost layer construction.

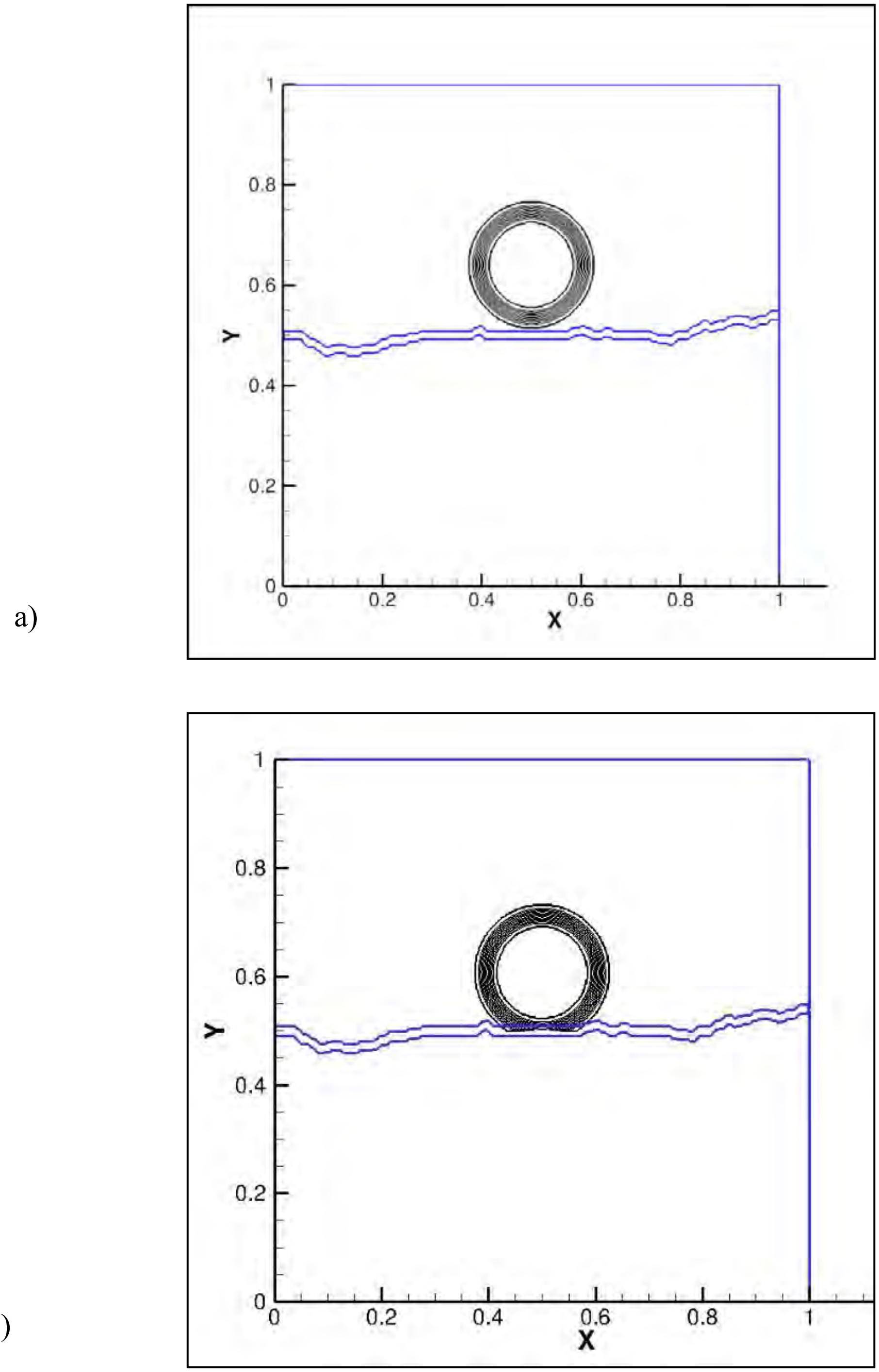

Figure 4-10. Corruption of level set field while going from one processor to another. The situation is peculiar to narrow band level set algorithms as the level set field is defined only in the shaded region.

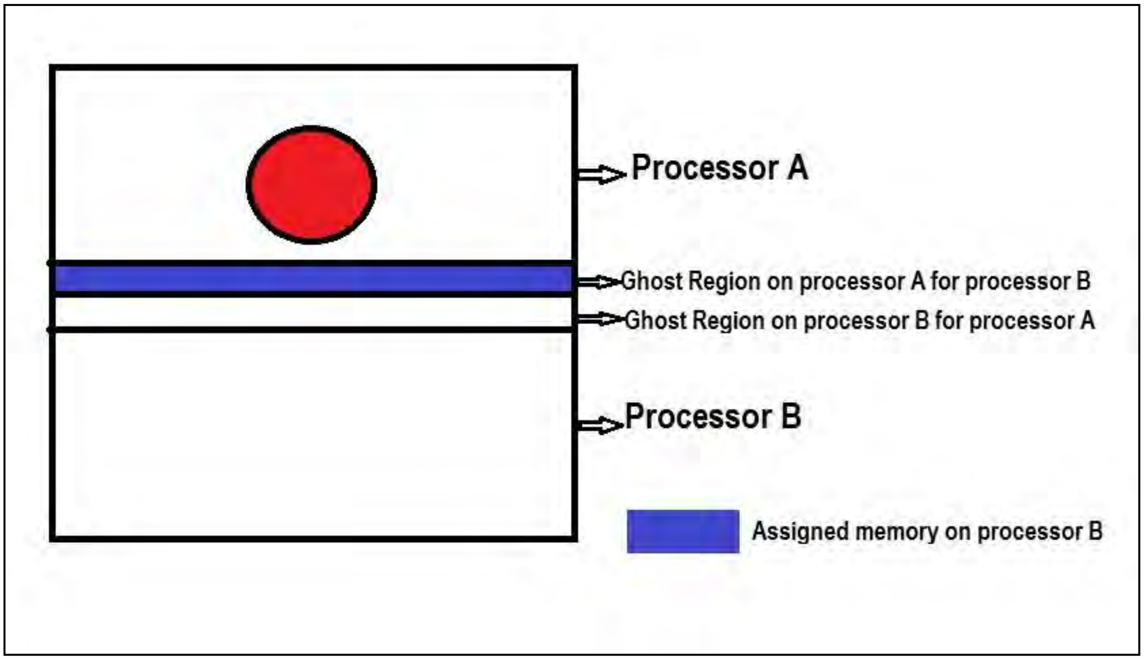

Figure 4-11. Allocation of memory for the level set field in ghost region of processor B to accommodate incoming moving object (shown in red color) from processor A.

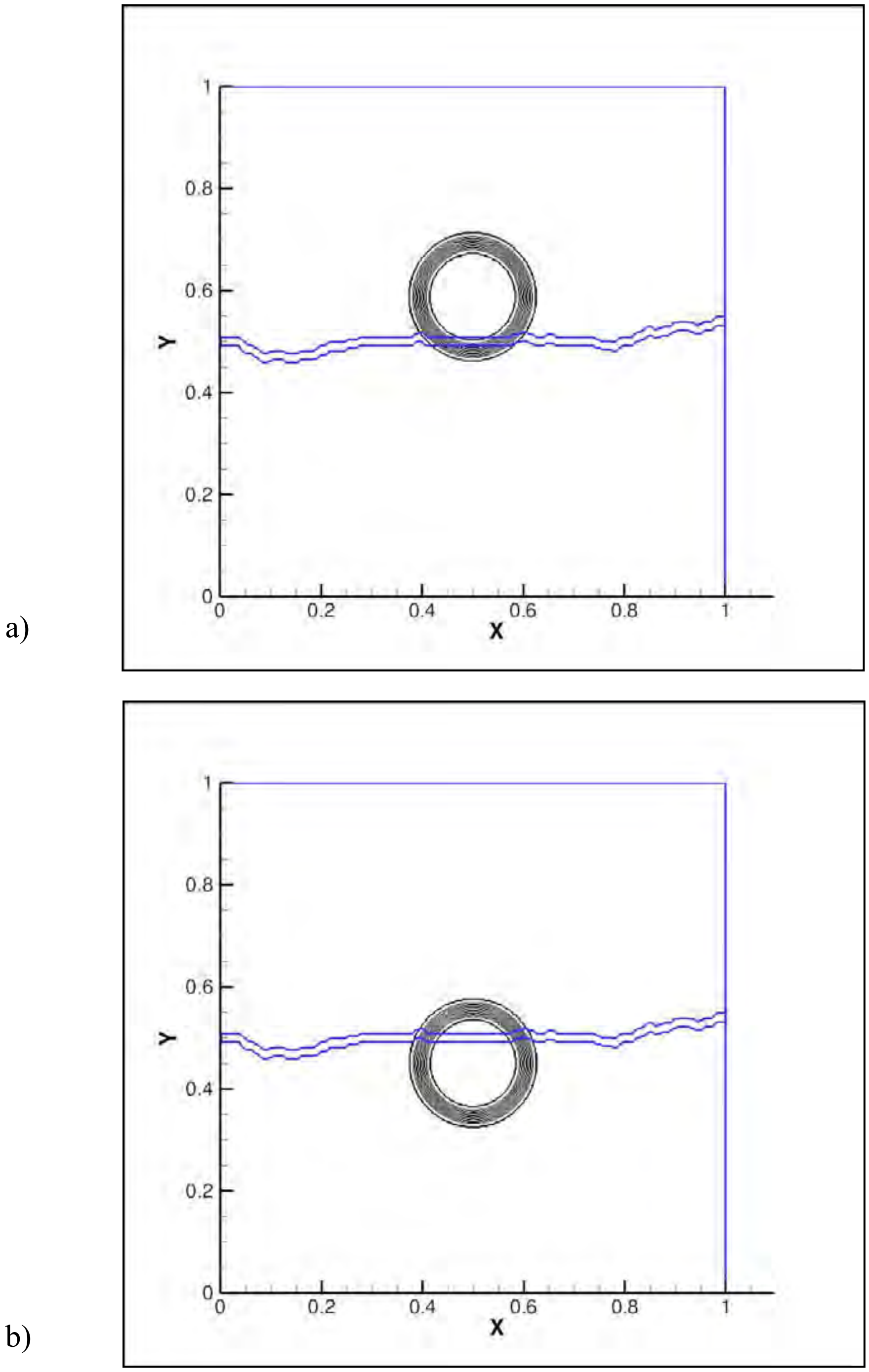

Figure 4-12. Smooth entry of the embedded object from one processor to another with the correct level set field.

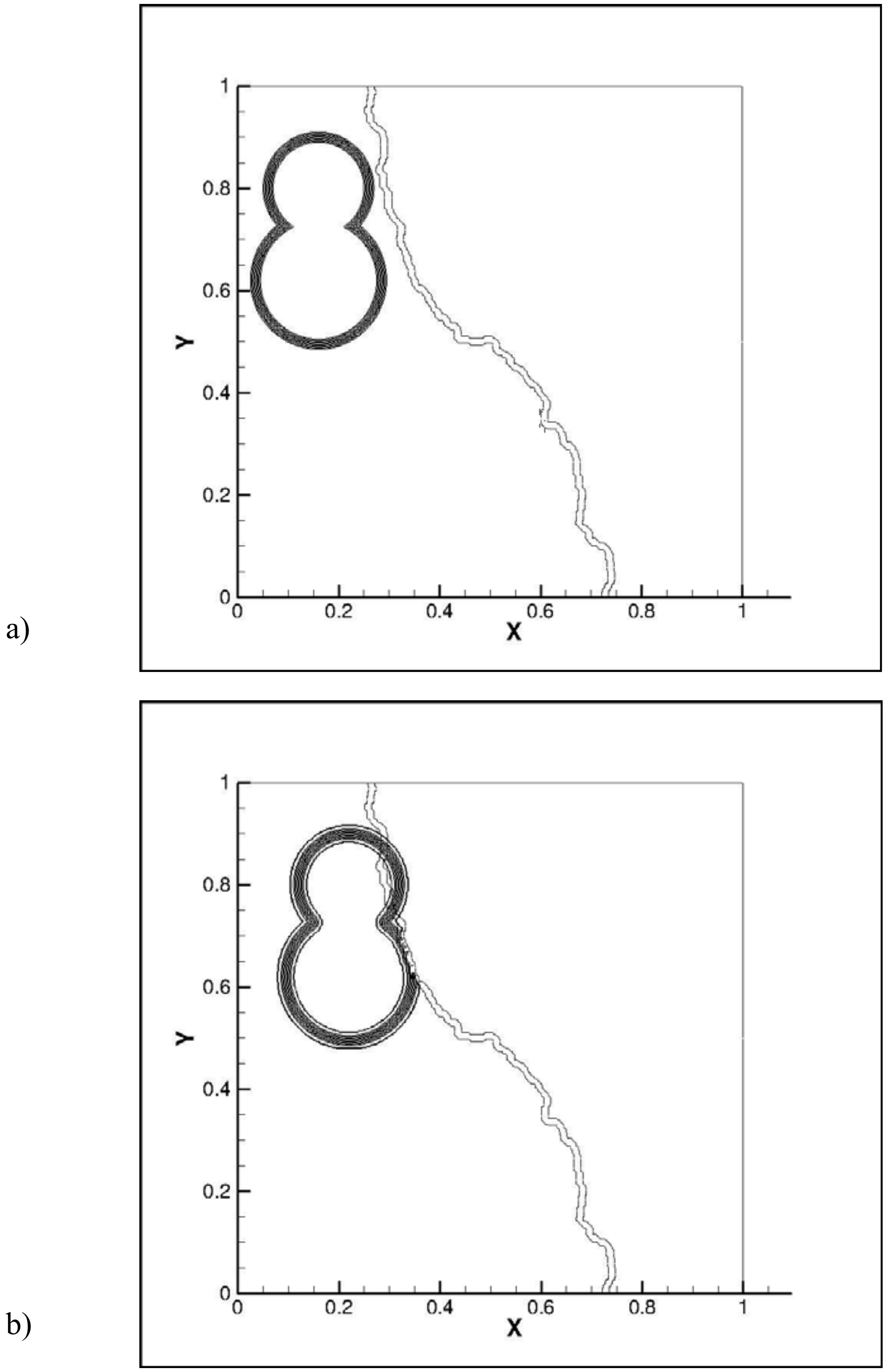

Figure 4-13. Corruption of level set field in case of non-convex embedded object. The situation is peculiar to narrow band level set algorithms as the level set field is defined only in the shaded region.

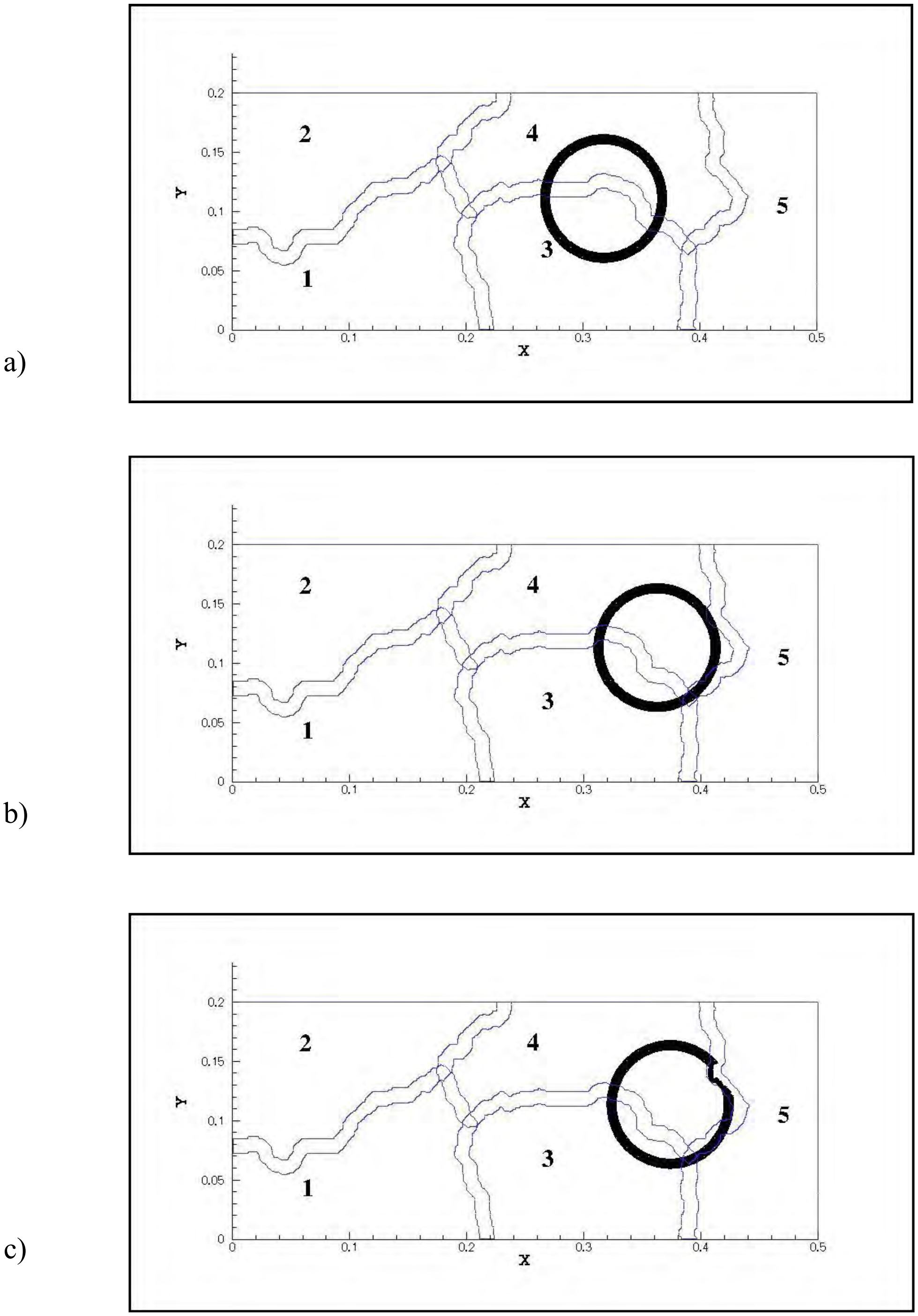

Figure 4-14. Corruption of level set field of a circular embedded object in a multi-processor setting. The situation is peculiar to narrow band level set algorithms as the level set field is defined only in the shaded region.

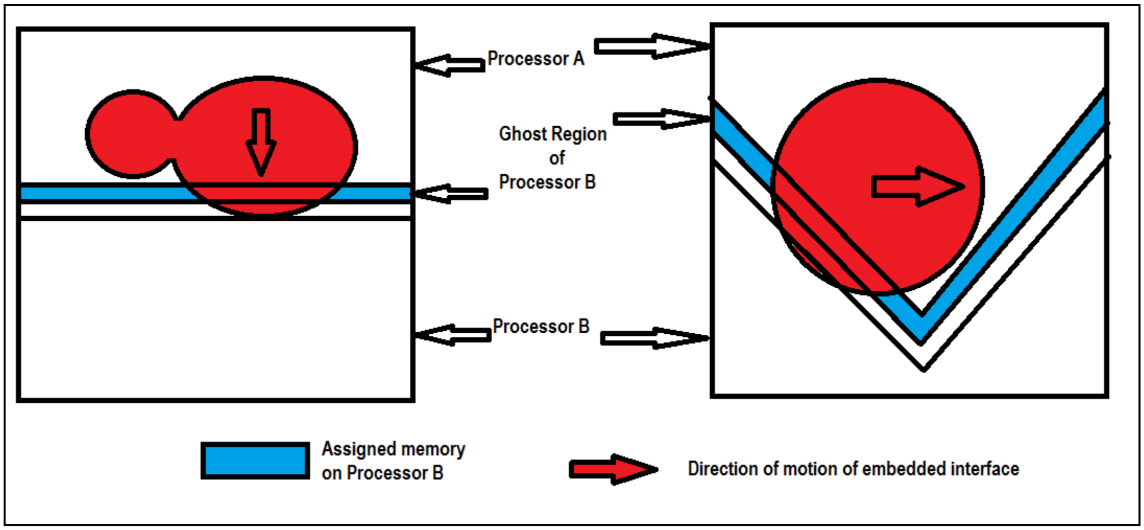

Figure 4-15. Allocation of memory for the level set field in the ghost region of processor B in two different scenarios. The incoming level set field can have entry from one processor to another at multiple points depending upon the shape of the embedded object (left) and intricate processor boundaries (right). The above procedure assures the allocation of memory to handle both the scenarios.

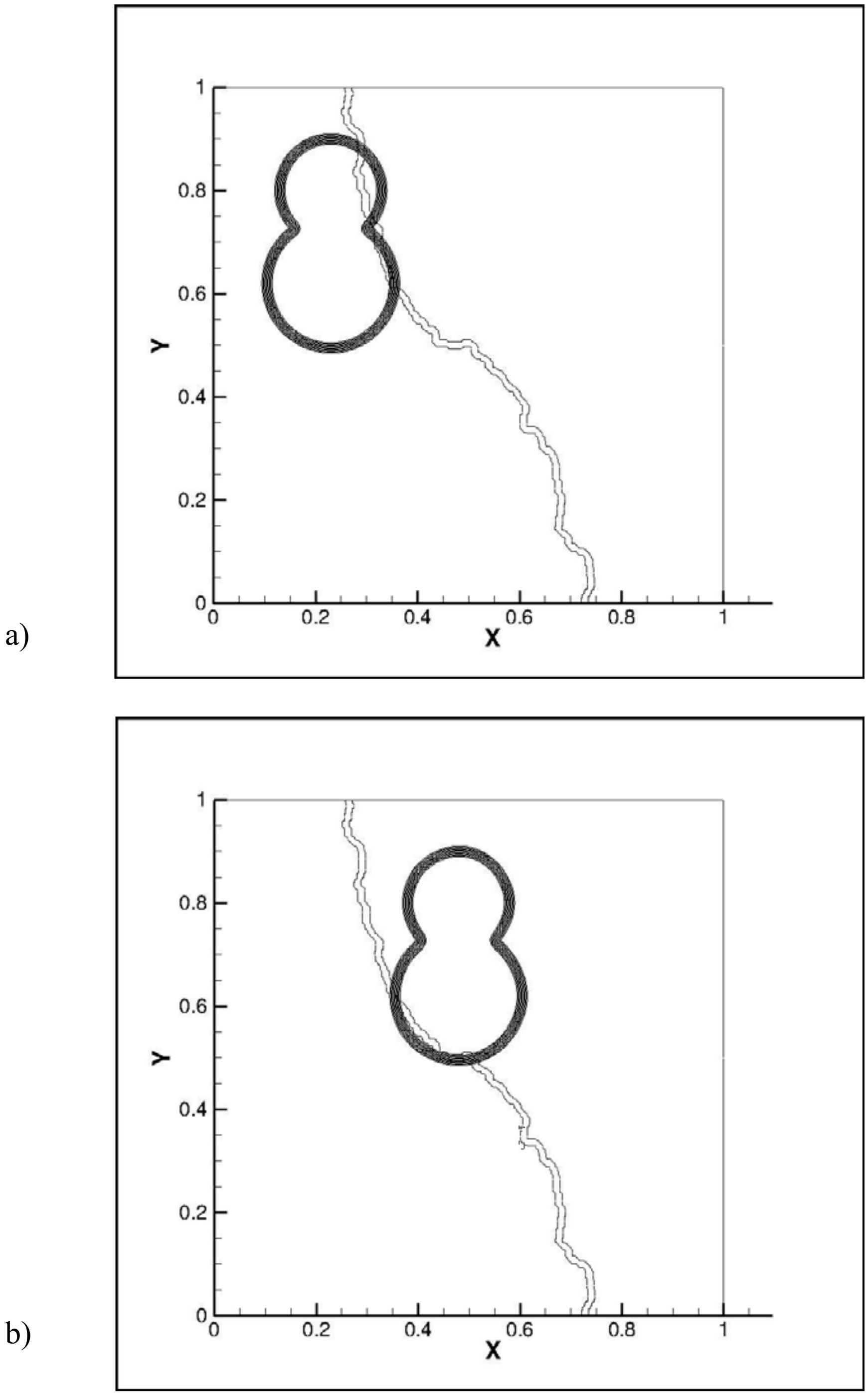

Figure 4-16. Embedded non-convex object moving with the correct level set field from one processor to another.

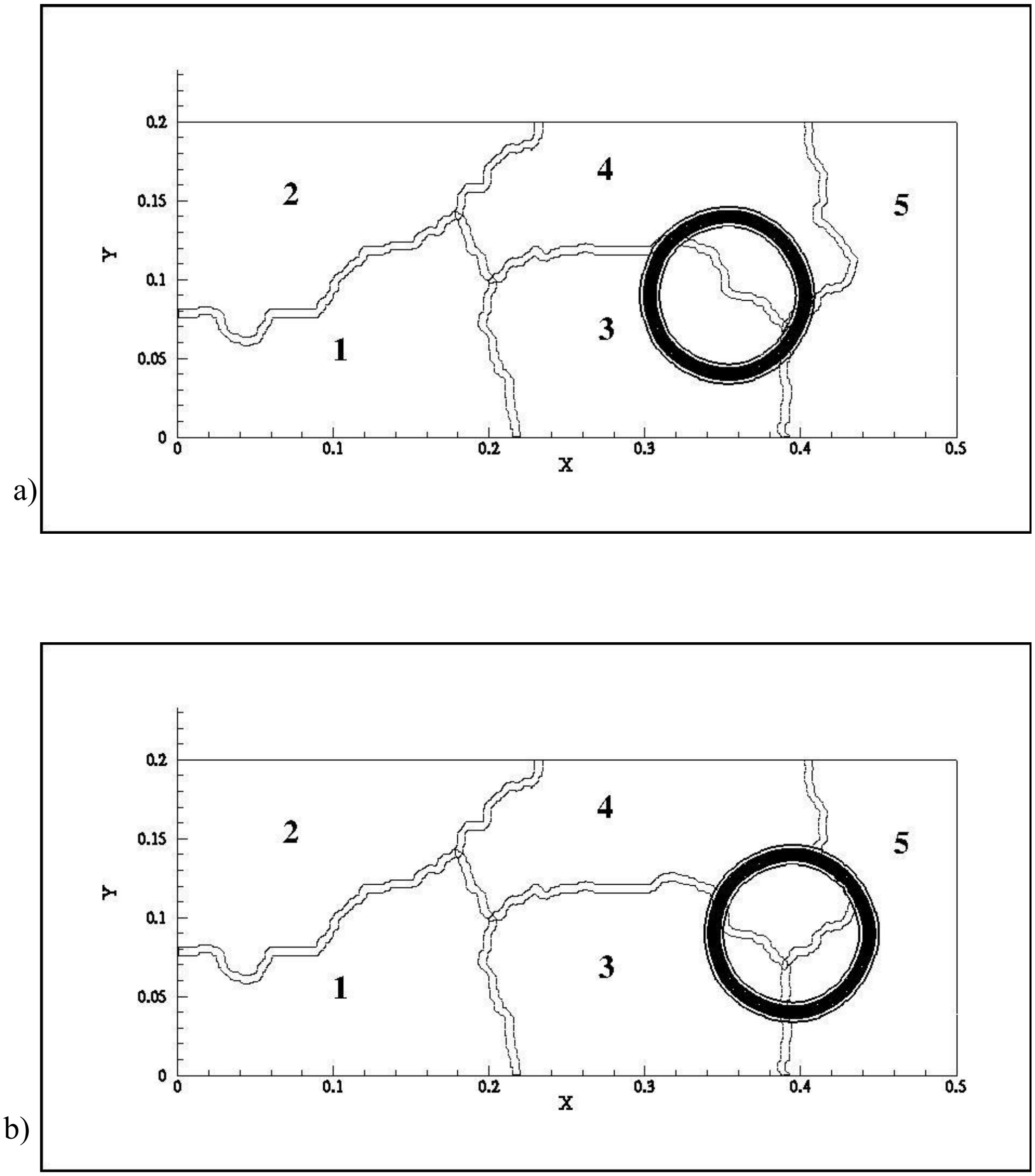

Figure 4-17. Embedded object moving with correct the level set field in a multi-processor setting.

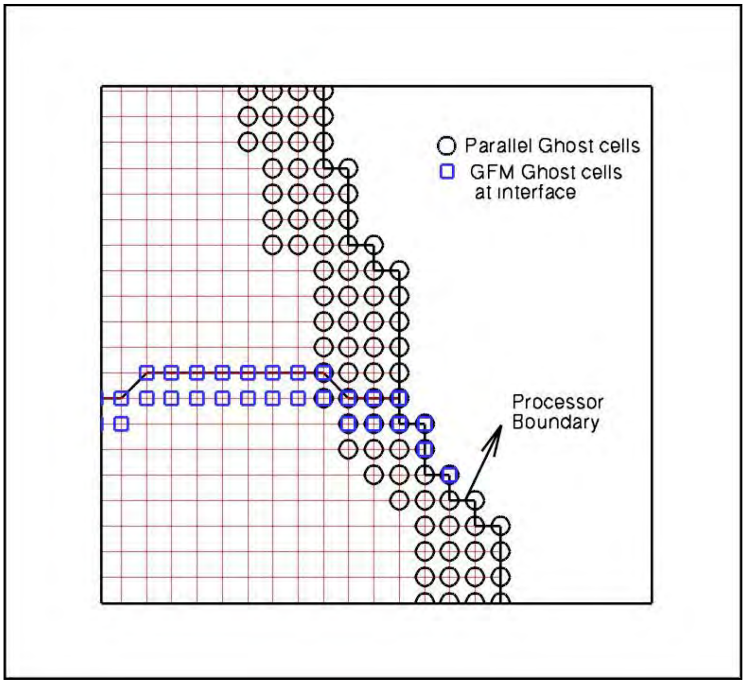

a)

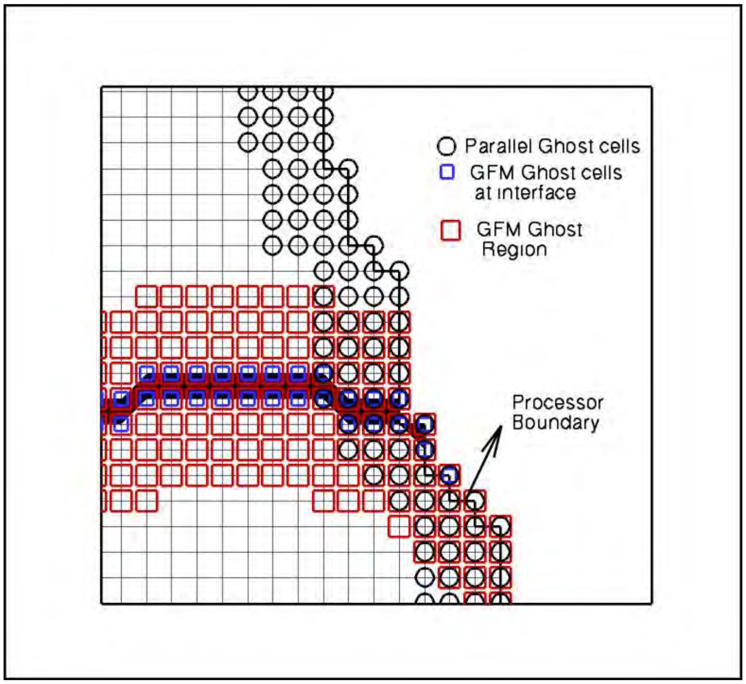

b)

Figure 4-18. Processor ghost region with interface a) processor ghost cells with a layer of cells (interface cells) defining GFM ghost cells b) Processor ghost cells with whole GFM ghost region.

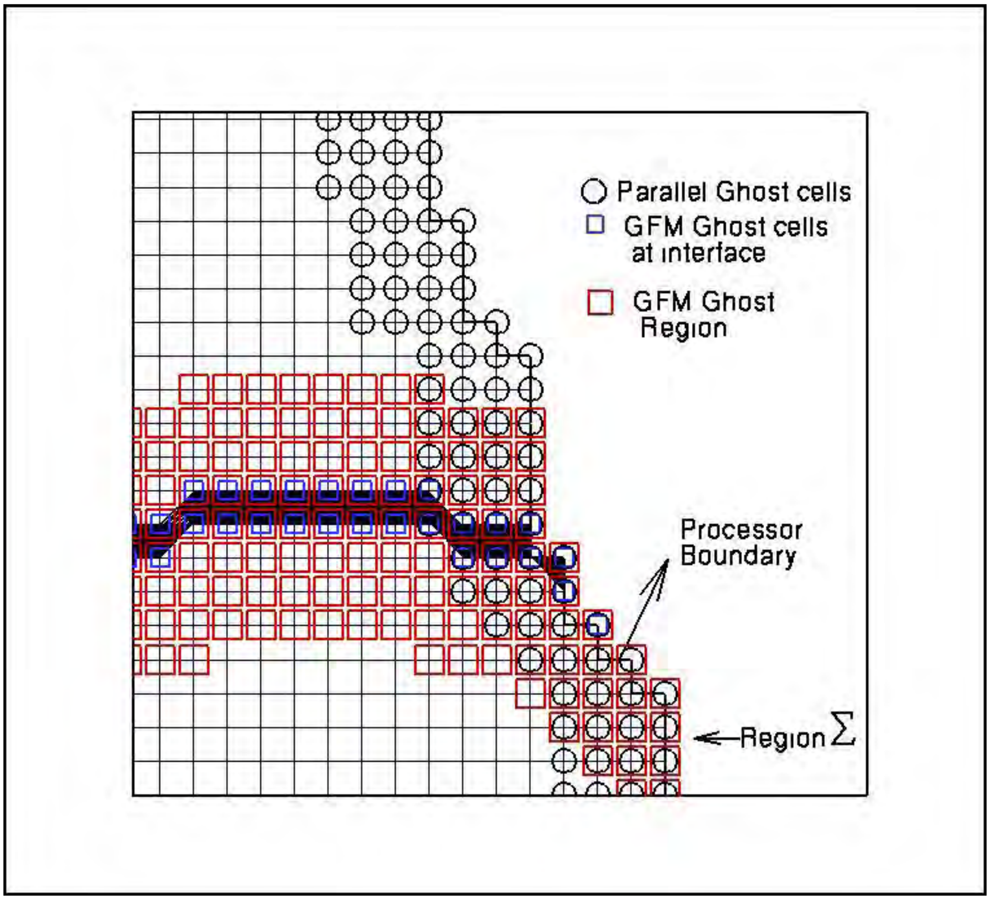

Figure 4-19.Parallel GFM cells with region ∑. The region ∑ does not have any interfacial cells required for extension procedure. The interfacial cells corresponding to region ∑ lie in neighboring processor.

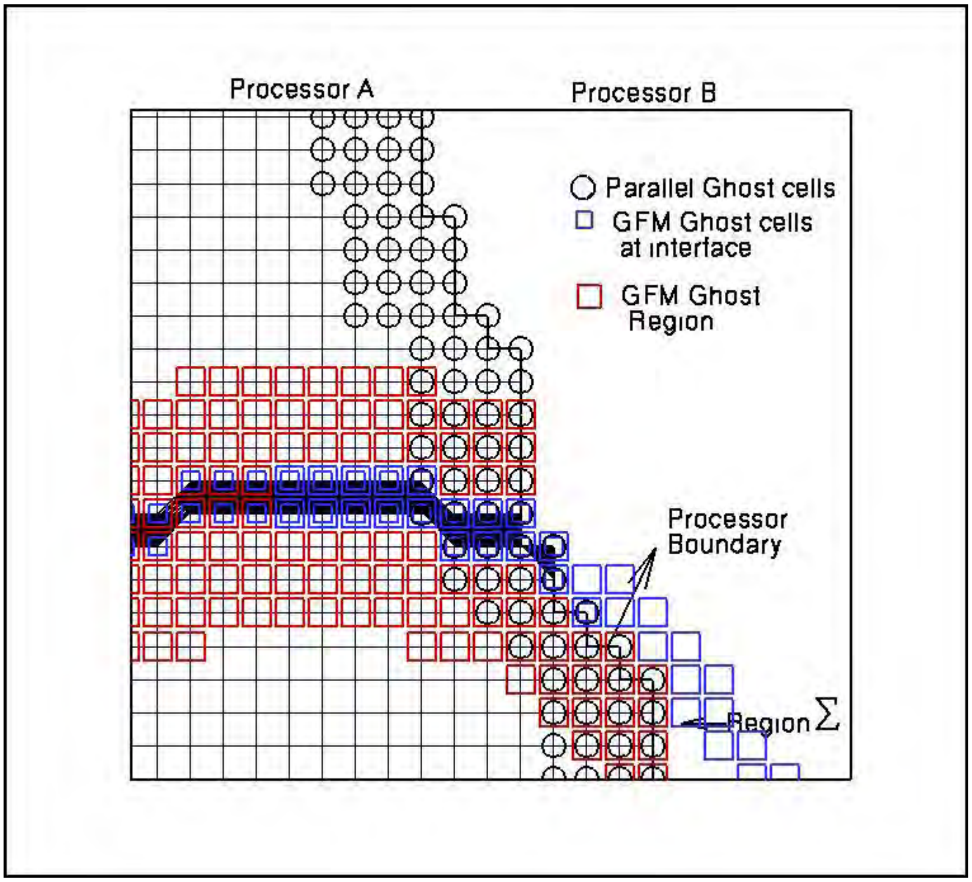

Figure 4-20. Parallel GFM with Region ∑ and its corresponding interface cells in the neighboring processor.

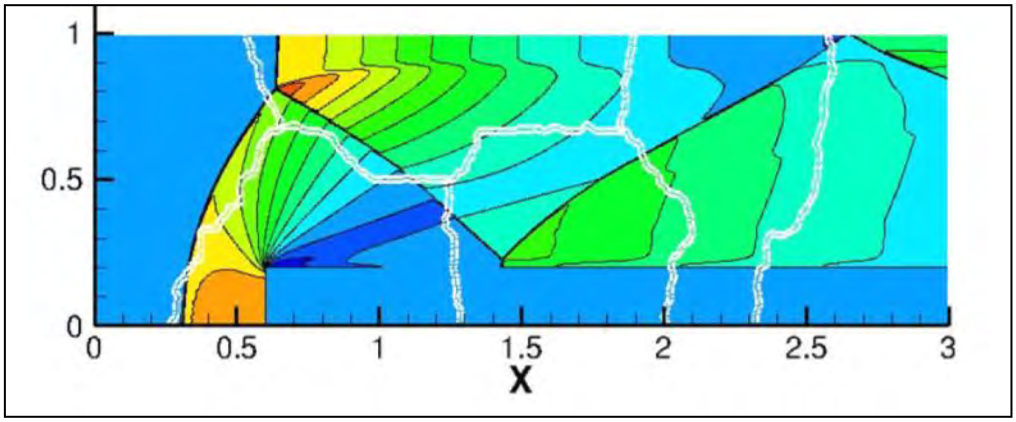

Figure 4-21. Density contours for Emery wind tunnel case. Emery wind tunnel case corresponds to interaction of a shock wave of strength Mach 3 with a rigid solid step.

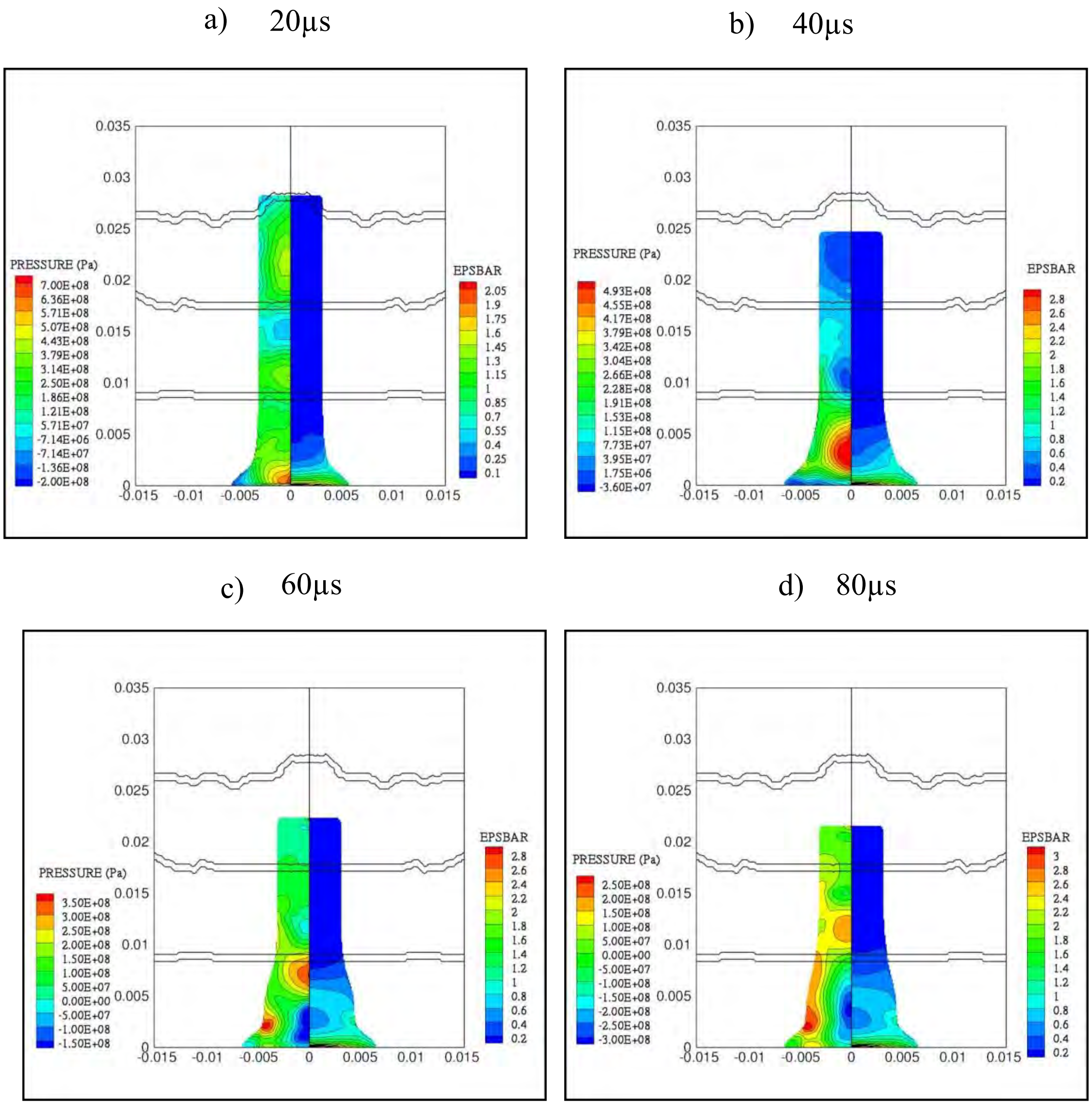
a) 20μs

b) 40μs

c) 60μs

d) 80μs

Figure 4-22. Illustration of the deformation of an axisymmetric Taylor bar (Copper, impact velocity = 227 m/s) in a multiprocessor calculation. The smooth passage of the bar through several processor boundaries is shown. Contours of pressure (left half of each bar) and effective plastic strain (ε_p) (right half of each bar) are shown in four different time instants in the deformation process: (a) t=20μs (b) t=40μs (c) t=60μs (d) t=80μs

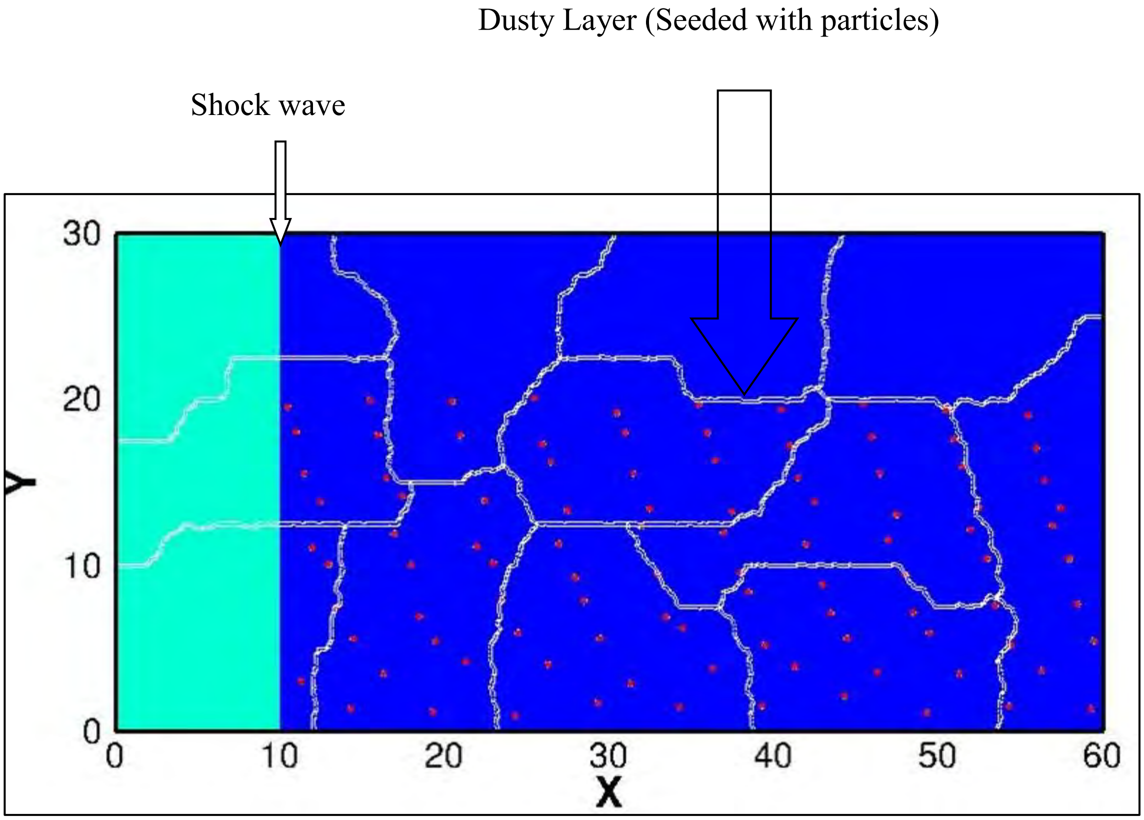

Figure 4-23. Initial Configuration of the domain for DNS of shock wave traversing through a dusty layer of gas. A shock wave of strength Mach 3 interacts with 100 stationary rigid solid particles.

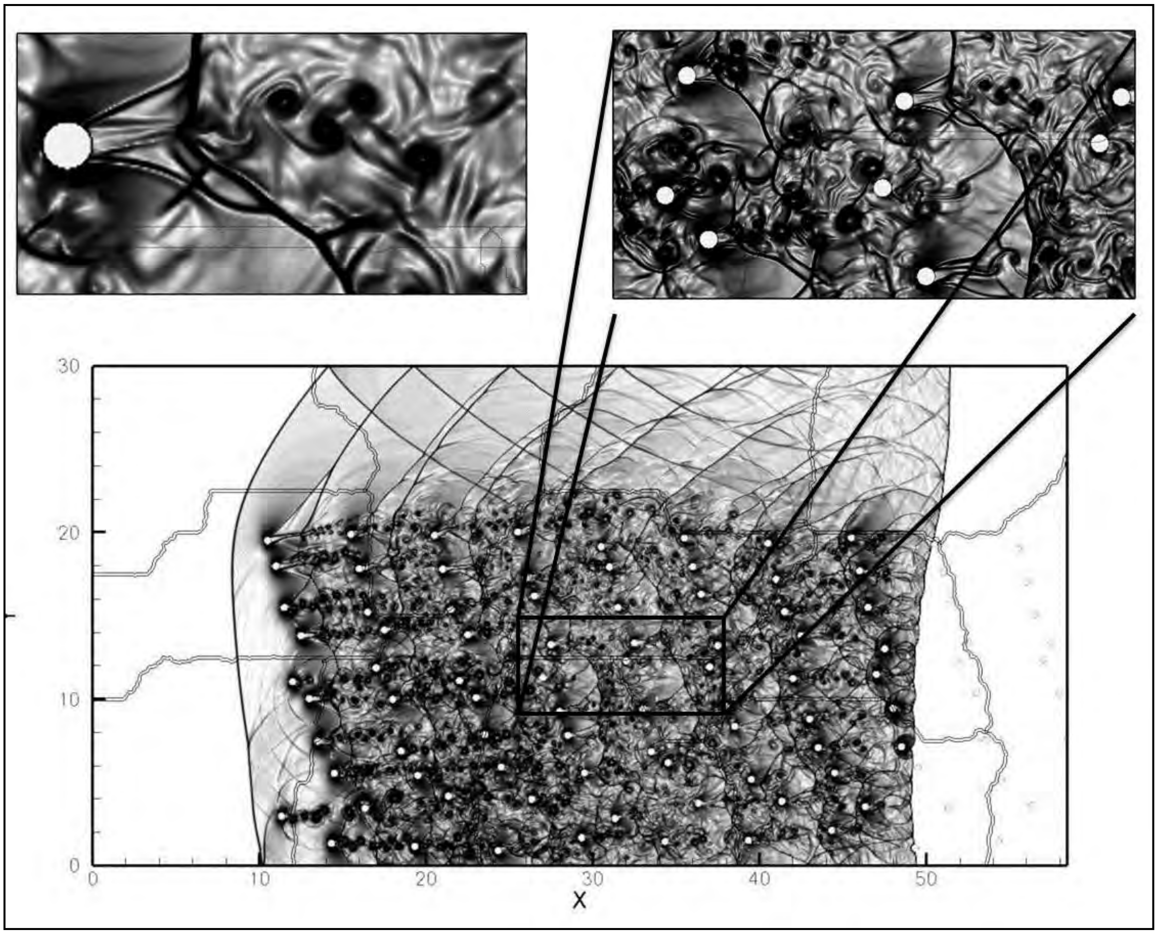

Figure 4-24. Numerical Schlieren Image for a Mach 3 shock wave traversing through dusty layer of gas. The shock wave interacts with 100 rigid solid particles in a multiprocessor environment.

CHAPTER 5

COMPUTATIONS OF TWO-DIMENSIONAL MULTIMATERIAL FLOWS

An array of 2-dimensional computations of multimaterial dynamics spanning phenomena of impact, penetration, collapse, ejection, extrusion and fragmentation are presented in this chapter using the parallelized algorithm described in the previous chapters. The cases are all benchmarked against computations of other researchers who have used various techniques for their calculations; in some cases experimental data are available and have been employed for validation of the present calculations as well.

The numerical results presented in this work are obtained by solving the hyperbolic system of equations (Eqs. 2.1 -2.4) using a third-order TVD-based Runge-Kutta scheme for time integration [49] and a third-order convex ENO scheme [41] for spatial discretization [26]. Since the numerical schemes implemented in this work are well established and do not differ in any way from those that apply for single fluids[41], the implementation details are not presented here. Interested readers may refer to the original articles [41, 49] for details on the ENO and TVD Runge-Kutta schemes. The parameters corresponding to Johnson-Cook material model and Mie-Grüneisen E.O.S. are listed in Table 2-1 & Table 2-2 respectively.

5.1 Impact of a Copper Rod over a Rigid Substrate - Axisymmetric Taylor Bar Experiment

The Taylor bar impact test is a standard test problem to verify and validate numerical simulations of elasto-plastic material dynamics. In the two-dimensional axisymmetric setting, a cylindrical rod made of copper with an initial radius of 3.2 mm and a length of 32.4 mm impacts a rigid flat substrate at 227 m/s (Figure 5-1).

A computational domain of radius 15 mm and length 34.0 mm is employed for this simulation. A uniform mesh size of 0.075 mm is used. The simulation is done using 4 processors. The top and right end of the computational domain are prescribed with Neumann conditions. The bottom end of the domain is modeled as target by imposing rigid surface boundary conditions. The left of the domain is prescribed with symmetry conditions, so that using axisymmetry one half of the cylinder is simulated. The rod has an initial density of 8930 Kg/m^3, Young's modulus $E = 117\ GPa$ and yield stress $\sigma_Y = 400MPa$. The material is assumed to harden linearly with a plastic modulus of *100 MPa*. The calculations are performed up to a time of $80\mu s$ (at which point nearly all the initial kinetic energy has been dissipated as plastic work). The CFL number is set to 0.4 for this computation.

The impact of the rod with the bottom rigid surface results in a precursor compressive elastic wave traveling in the bar followed by a slower nonlinear plastic wave front. The elastic wave travels the entire length and the width of the rod, and is reflected off the free surface as a relief wave. The deformation of the rod terminates with the reflected elastic wave interacting with the plastic wave, and the stress is reduced to zero [66]. The jetting of the rod continues along the line of contact up to $40\ \mu s$ at which point the material begins to harden (Figure 5-2). With the hardening of the material near the foot of the rod, the plastic wave moves up the rod resulting in the bulging of the base as shown in Figure 4. At around $80\ \mu s$, the rod comes to rest (Figure 5-2).

To validate the present approach, the results obtained from the current calculations are compared with previous numerical simulations[11, 26, 36, 67]. The parameters, such as the final radius of the mushroom foot, the final length and the maximum effective plastic strain, characterizing the impact of the rod computed in the present study agree well with the previously reported values (Table 5-1). The comparison of Taylor bar impact using the two different approaches (Biliear interpolation and Least-squares estimation, see Chapter 3) to obtain values at the point IP1 (Figure 3-5) is also shown in Figure 6. As can be seen from the figure, for this case both approaches provide nearly identical solutions. The added expense of the least-squares approach is not justified in this case. Not however that the interpolation to points IP1 along the interface occur in a lower dimensional set of points (i.e. only in a one-mesh-point thick set of points adjoining the interface). As will be demonstrated below the least-squares approach is robust through the fragmentation of interfaces while the bilinear interpolation fails for small fragments and sharp corners due to unavailability of interpolation points. The same test was done for impact at 400m/s as the bar was expected to deform more severely. As can be seen from Figure 5-4, the impact at 400 m/s reduces the bar to almost one third of its initial length with effective plastic strain having the value 5.0 at 80μs.

5.2 Axisymmetric Dynamic-Tensile Large-Strain Impact-Extrusion of Copper

An experimental study on the influence of grain size on the response of Copper was conducted in [68]. In this section, the numerical computations of the dynamic extrusion of a Copper sphere are presented. The example problem considered here consists of a Copper sphere of 7.6 mm in diameter undergoing a tensile extrusion process. The extrusion process is carried out by propeling the Copper sphere at 400 m/s towards the extrusion die. The extrusion die made of hardened Steel is designed with an entrance diameter of 7.62 mm and an exit diameter of 2.28 mm, a reduction of 70 % in cross sectional area as shown in the Figure 5-5.A uniform mesh of size $\Delta x_g = 0.075mm$ is chosen. The domain is decomposed using 24 processors. The Johnson-Cook material model is employed to capture the response of the sphere and the extrusion die. The interface topology during the course of simulation is shown in Figure 5-6 and Figure 5-7. The evolution of level set field with smooth passage from one processor to another is shown in Figure 5-8 and Figure 5-9.

Despite the lack of a damage model[43], the present calculations are able to predict the overall behavior of the extrusion process that matches well with the experimental predictions reported in [68]. The maximum equivalent plastic strain (ε_P)

was observed during the jetting phase and corresponds to a value of 7.8 (Figure 5-10). This value is in good agreement with effective plastic strain of 6-9 observed during stretching of shaped charged jets[68].

5.3 Handling of Fragments in Case of Severe Plastic Deformation

The cases shown in the previous examples deal with plastic deformation of material in the event of high speed impact or penetration. Generally in the event of a high speed impact or penetration of a hard impactor on a soft target, the target undergoes rapid elastic deformation followed by severe plastic flow. Finally if the speed of impactor is very high and the target is not thick enough to completely absorb the energy of incoming impactor, the resultant dynamics can lead to total fragmentation of the target material. The example consider here consists of a slender tungsten target penetrating a thin aluminium plate at 1250 m/s. The dimensions of impactor and target are shown in Figure 5-11. A computational domain of radius 15 mm and length 32.0 mm is chosen for this simulation. The top and right end of the computational domain are prescribed with Neumann conditions. The presence of a rigid wall on the bottom end of the domain is modeled by enforcing a free-slip, no-penetration condition. The left end of the domain is prescribed with symmetry conditions (with $S_{xy} = 0$).

The simulation was performed using three different mesh sizes of 0.0001 m, 0.00005m and 0.000025m respectively to test for grid dependence of the solution past fragmentation, as shown in Figure5-12. In these computations the least-squares approach was employed to obtain information at the IP1 points (Figure 3-5), as described in Chapter 3. The straightforward bilinear interpolation approach failed in the presence of the small fragments, which contain sharp corners with marginal resolution of such features. The Figure5-12 shows a snapshot of target and impactor at 12 microseconds for the different mesh sizes. It is observed that while the large scale features of the impactor and targer are independent of the mesh size, the small scale features are dependent on the mesh size, as would be expected for the numerical fracture that occurs in the present case. Physically correct fragments will only be produced by including physical damage models [43]. The results for total framentation, following the evolution of the interface up to 30 microseconds is shown in Figure 5-13. The tungsten rod completely penetrators the steel target resulting in small fragments. The projectile and the fragments of the target then interacts with the rigid surface resulting in the flattening of the impactor against the rigid surface, ejection of material through the left and right ends of the domain and a remnant of both the impactor and target that are seen in the final frame in Figure 5-13 (h) at time= 40 microseconds. At that final instant the fragments separate from the steel target interact and settle on what remains of the deformed tungsten projectile. The present techniques and computer program were able to compute the phenomena of fragmentation in a robust fashion.

Table 5-1. Comparison of axisymmetric Taylor impact results with other computational codes.

Case 227 m/s	Final length (mm)	Final Base Radius (mm)	Maximum EPSBAR
Current setting	21.45	6.8	3.0
Camacho et al[11]	21.42-21.44	7.21-7.24	2.97-3.25
Tran et al[26]	21.15	7.1	2.86

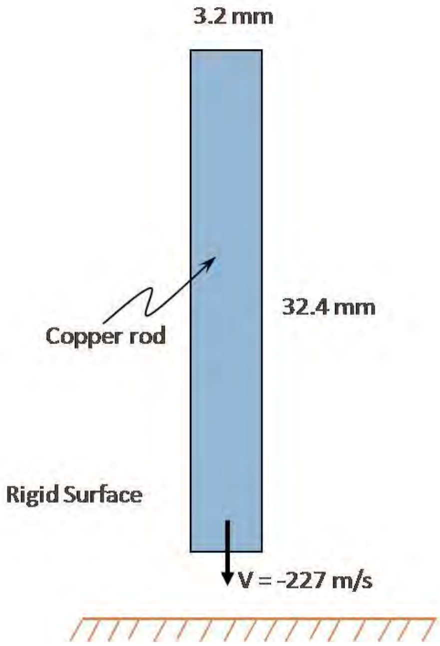

Figure 5-1. Initial configuration for two-dimensional axisymmetric Taylor test on a Copper rod at 227m/s.

a) T=20μs b) T=40μs

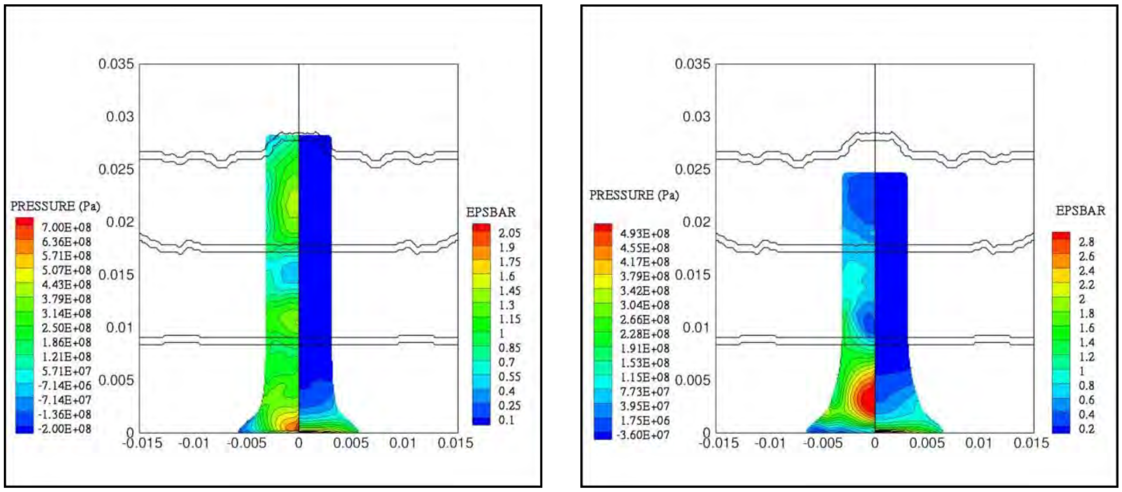

c) T=60μs d) T=80μs

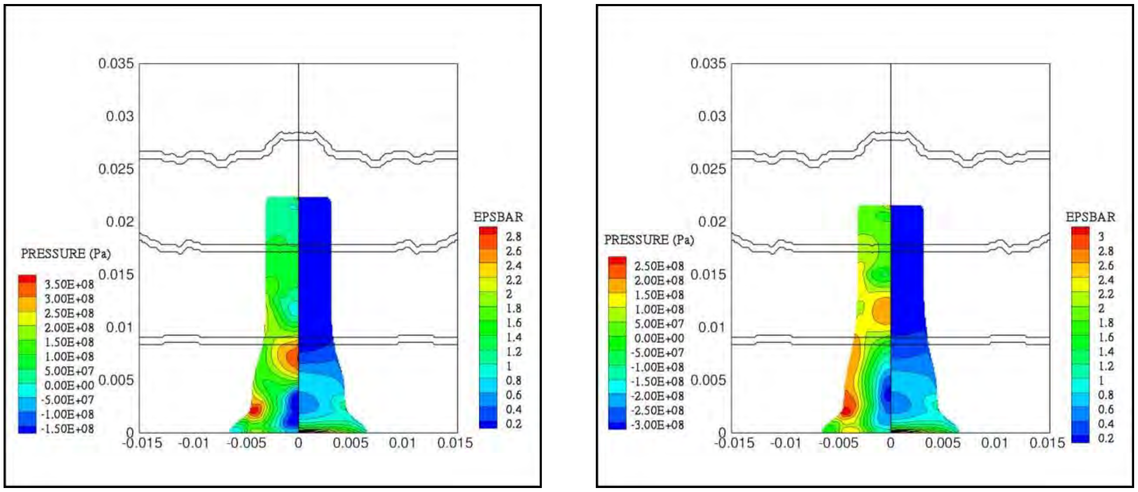

Figure 5-2. Illustration of the deformation of an axisymmetric Taylor bar (Copper, impact velocity = 227 m/s) in a multiprocessor calculation. The smooth passage of the bar through several processor boundaries is shown. Contours of pressure (left half of each bar) and effective plastic strain (ε_p) (right half of each bar) are shown in four different time instants in the deformation process: (a) t=20μs (b) t=40μs (c) t=60μs (d) t=80μs

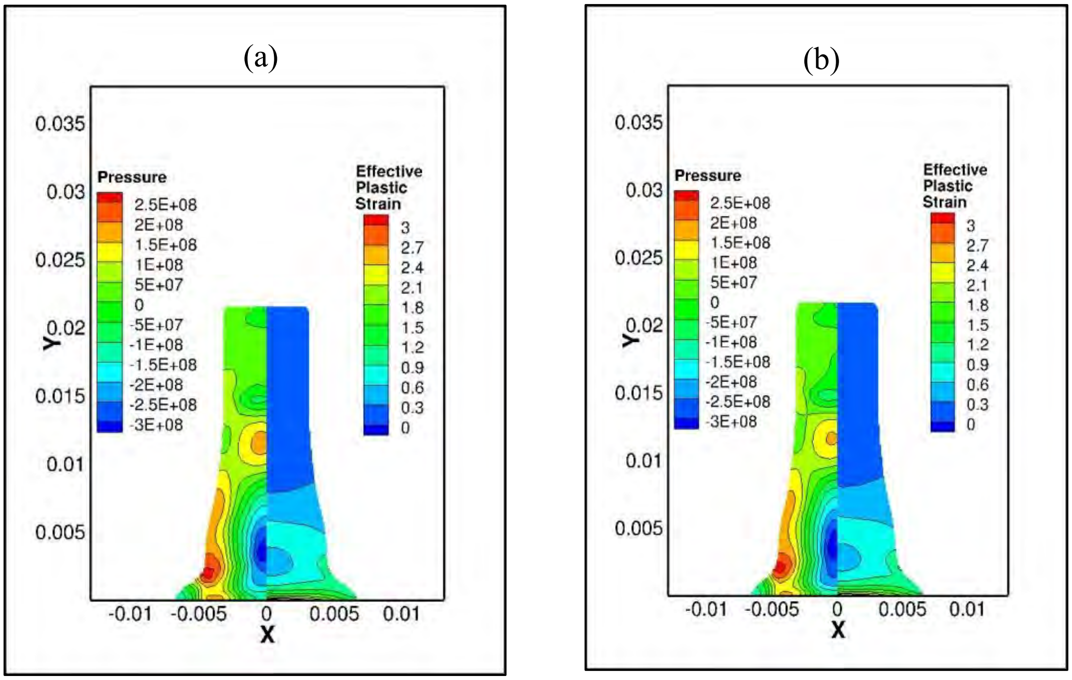

Figure 5-3. Taylor bar impact (Copper, 227 m/s) results at 80μs (a) Bilinear Interpolation (b) Least squares interpolation

a) T=20µs b) T=40

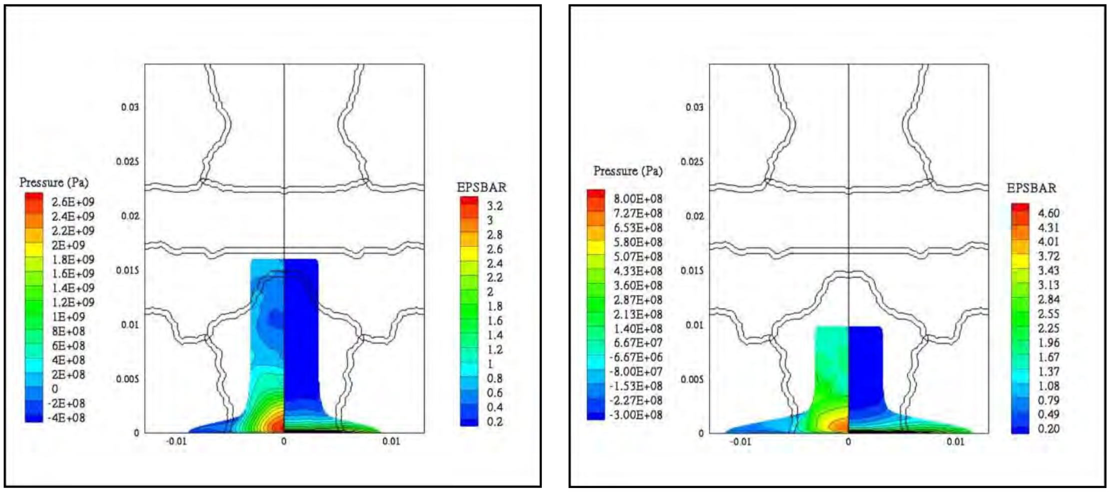

c) T=60µs d) T=80µs

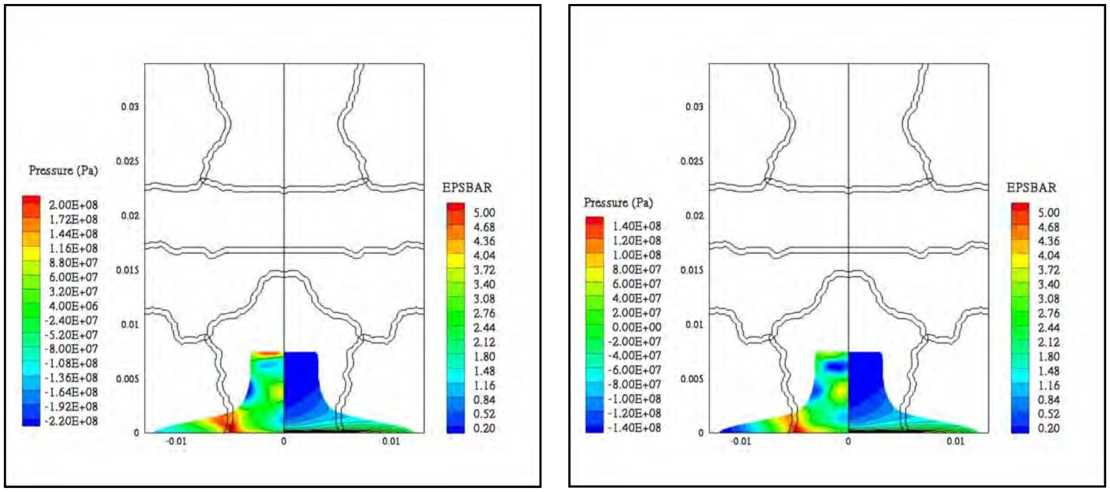

Figure 5-4. Illustration of the deformation of an axisymmetric Taylor bar (Copper, impact velocity = 400 m/s) in a multiprocessor calculation. The smooth passage of the bar through several processor boundaries is shown. Contours of pressure (left half of each bar) and effective plastic strain (ε_p) (right half of each bar) are shown in four different time instants in the deformation process: (a) t=20µs (b) t=40µs (c) t=60µs (d) t=80µs

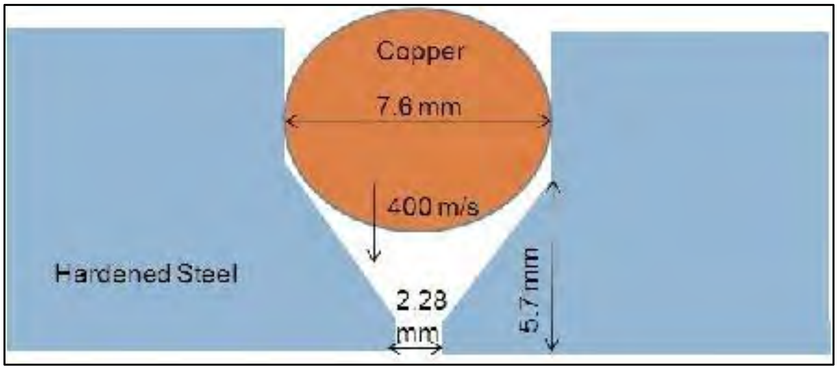

Figure 5-5. : Initial configuration for the axisymmetric extrusion of a copper sphere through a hardened steel die. The copper sphere propels towards the hardened steel die at 400 m/s.

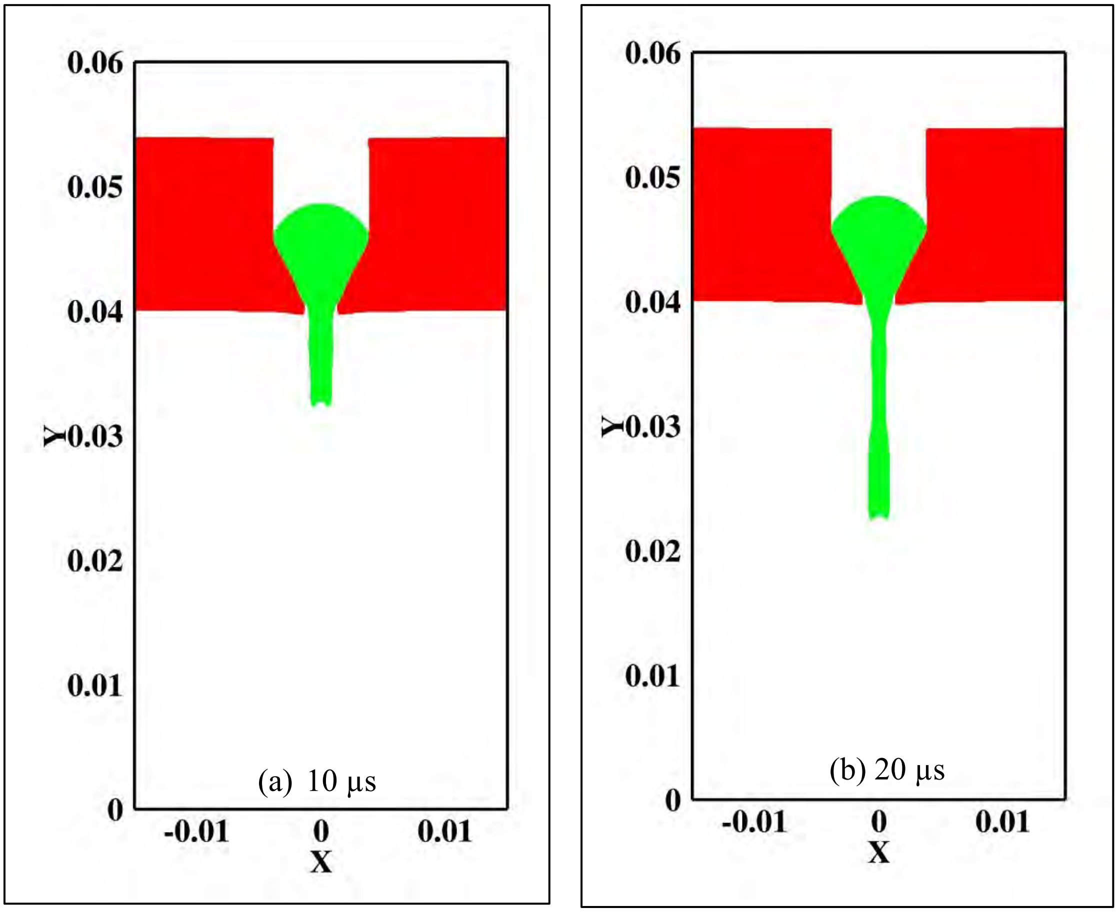

Figure 5-6. Evolution of the copper sphere interface extruded through hardened steel die at 400 m/s. The levelsets corresponding to the sphere (green) and die (red) are shown at two different times: a) 10µs b) 20µs

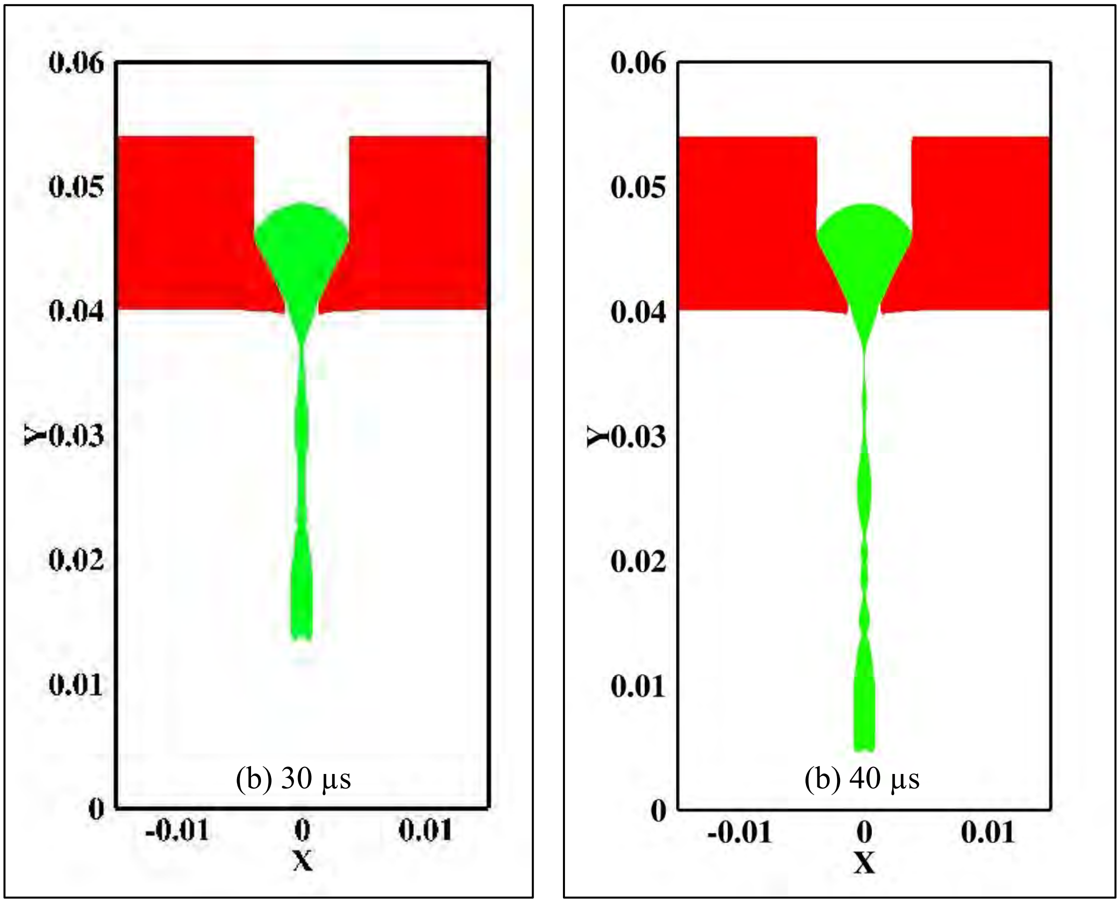

Figure 5-7. Evolution of the copper sphere interface extruded through hardened steel die at 400 m/s. The levelsets corresponding to the sphere (green) and die (red) are shown at two different times: a) 30µs b) 40µs

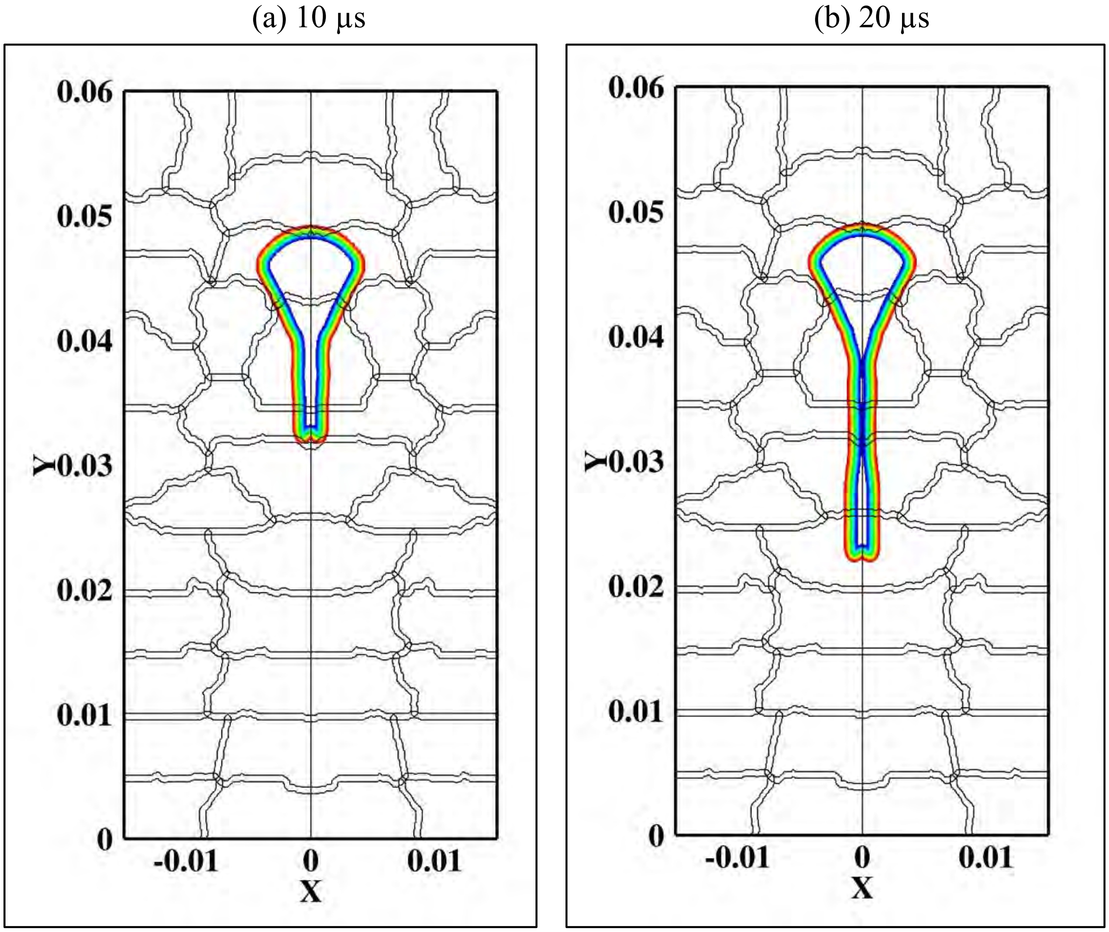
(a) 10 μs

(b) 20 μs

Figure 5-8. Level set field showing the evolution of copper sphere extruded through hardened steel die at 400 m/s: a) 10μs b) 20μs. Smooth evolutions of level set field across the processor boundaries depict the successful implementation of method.

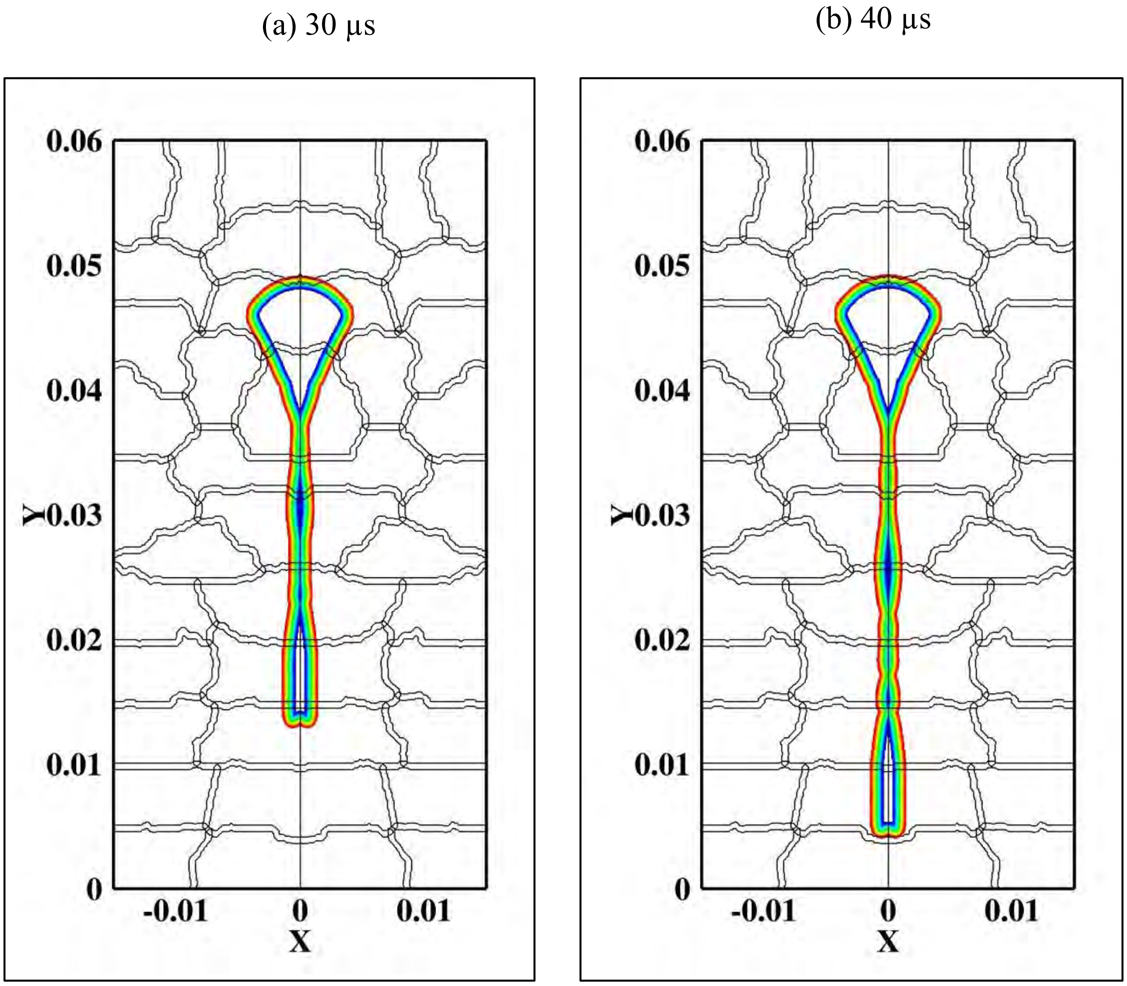

Figure 5-9. Level set field showing the evolution of copper sphere extruded through hardened steel die at 400 m/s: a) 30μs b) 40μs. Smooth evolutions of level set field across the processor boundaries depict the successful implementation of method.

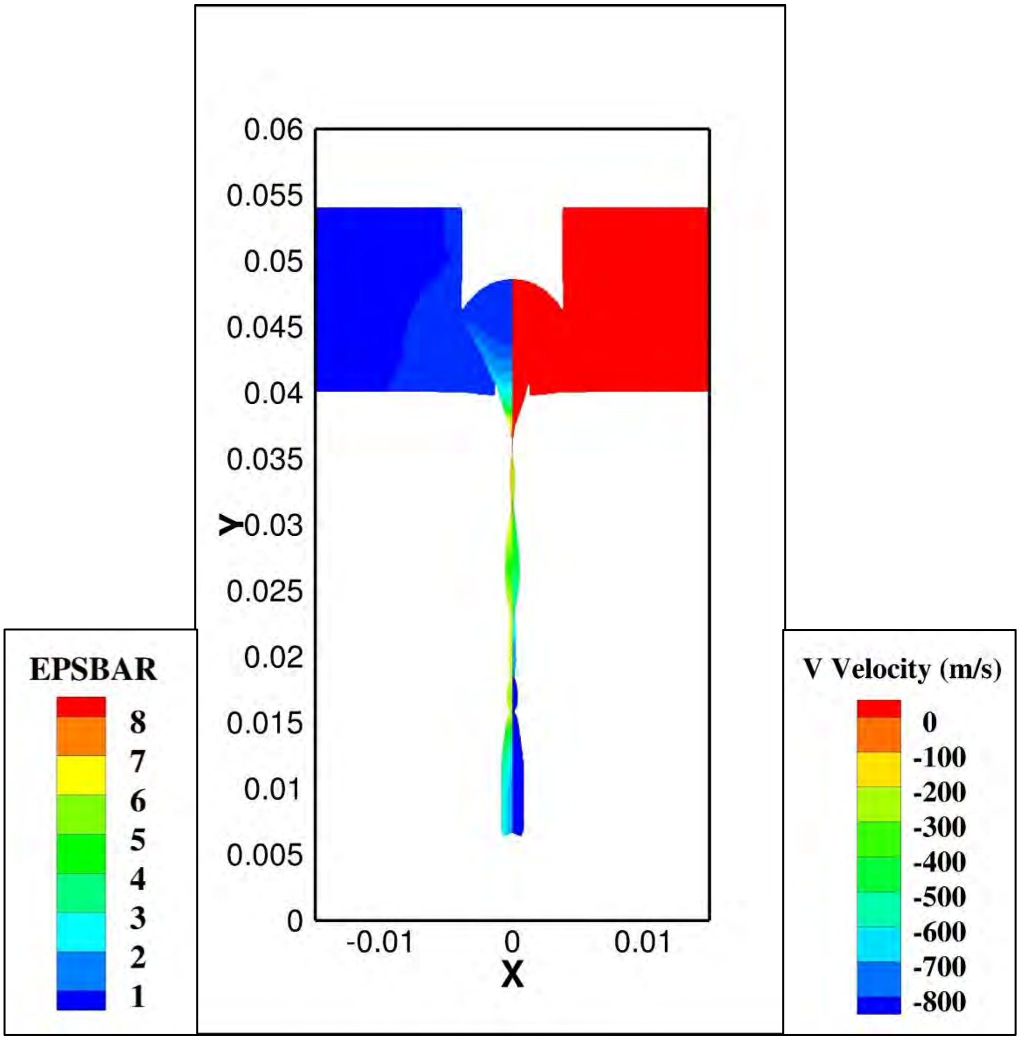

Figure 5-10. Evolution of copper sphere extruded through hardened steel die at 400 m/s. Contours of effective plastic strain (ε_p) (on the left half of bar) and velocity (on the right half of bar) are shown at an instant of 40μs.

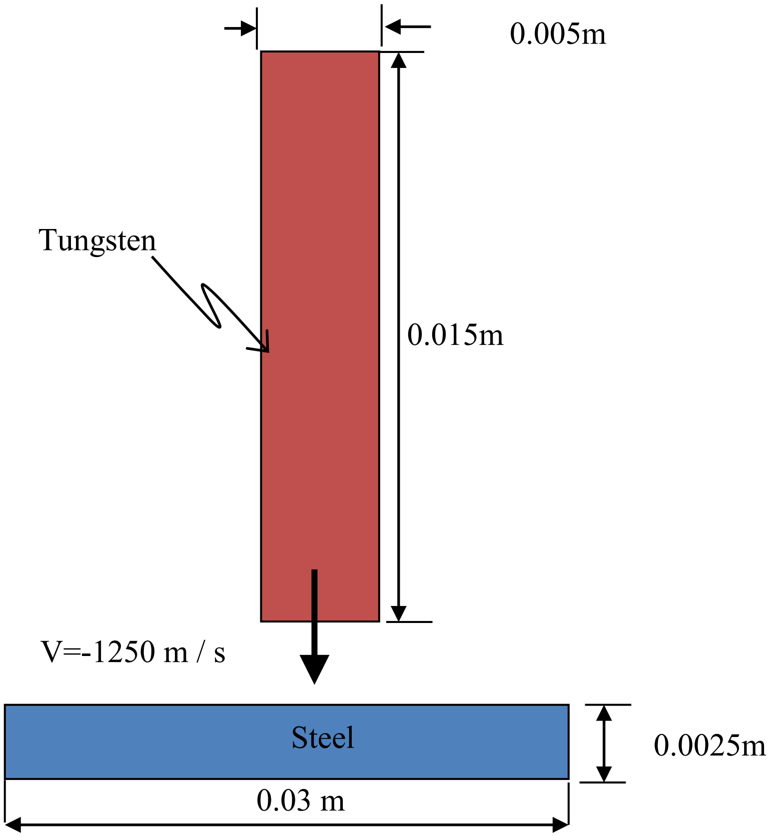

Figure 5-11. Initial configuration for the penetration and fragmentation of a steel plate by a tungsten rod moving at 1250m/s.

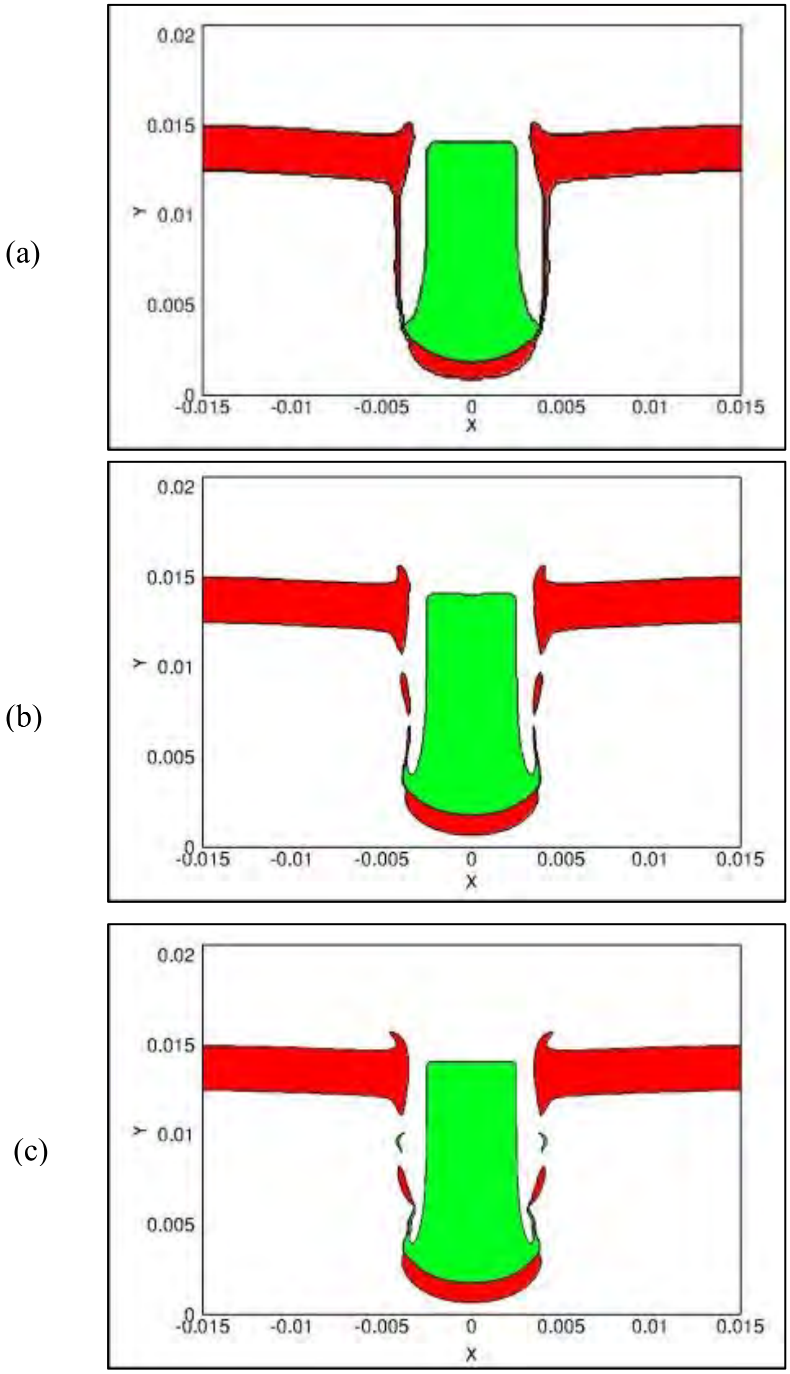

Figure5-12. Snapshot of tungsten rod penetrating into a steel target at 12μs for different mesh sizes (a) 0.0001 (b) 0.00005 (c) 0.000025

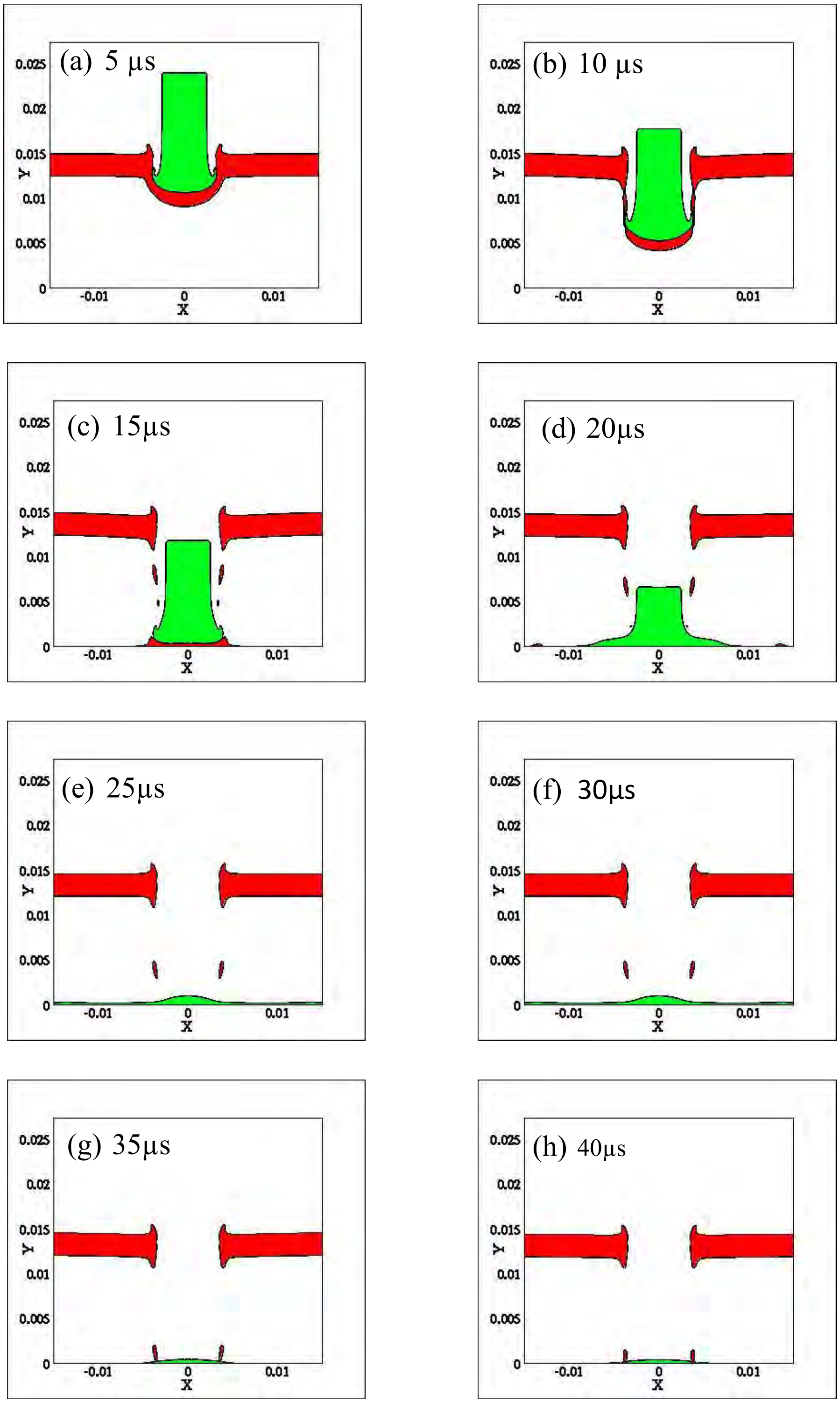

Figure 5-13: Total fragmentation of steel target at different times,(a)-(h),5µs - 40µs

CHAPTER 6

THREE –DIMENSIONAL COMPUTATIONS OF HIGH-SPEED MULTIMATERIAL FLOWS

This chapter presents the 3-dimensional computations for multimaterial flows showing impact, penetration and fragmentation phenomena. These simulations are done using GFM method devised in Chapter 3 and are first of a kind in eulerian framework. There are very few codes [15, 34]which are capable of performing these simulations due to a lot of intricacies involved. These intricacies are related to implementation of Ghost Fluid Method in three dimensions, handling of an enormous amount of data, parallelization of flow solver with moving interfaces and finally post processing of results. The cases are all benchmarked against computations of other researchers who have used various techniques for their calculations; in some cases experimental data are available and have been employed for validation of the present calculations as well.

6.1 Taylor Bar Impact

During World War II, Taylor conducted an analysis on specimens deformed at very high rates of strain [66]. These experiments [64] involved impact of a cylindrical specimen over a rigid flat substrate, depicted the deformation process as a sequence of elastic and plastic wave propagation into the cylinder. The Taylor bar impact test is a standard test problem to verify and validate numerical and experimental observations. First, to benchmark the three-dimensional computations by comparing with other computations and experiments, three-dimensional impact of a Taylor bar [64] is computed using the parallelized code. These results are obtained by solving the hyperbolic system of equations, Eqs. (2.1-2.4) using a third-order TVD-based Runge-Kutta scheme [49] for temporal discretization and a third-order convex scheme [41] for spatial discretization. These numerical schemes are well established and details for these can be obtained from the above-mentioned references. The parameters corresponding to

Mie-Gruneisen are provided in Table 2-2. In this section we show two cases of impact of a copper rod on a rigid surface. The first case is a benchmark problem, impact at 227 m/s and the second case is impact at 400m/s to show the handling of high deformation and strain rates.

6.1.1 Impact at 227m/s

A copper bar of length 32.4 mm and 3.2 mm radius impacts on a rigid flat surface at 227 m/s. The computational domain consists of cuboid of dimensions 16 mm X 16 mm X 34 mm. The domain decomposition and initial Taylor bar are shown in Figure 6-1. The problem is simulated using 8 processors. The ghost layer required for inter-processor communication is shown in Figure 6-2. The bottom surface of domain is given reflective boundary condition and all other surfaces are prescribed with Neumann boundary condition. The standard material properties for copper are used which can be found in high speed impact literature [11, 26] and are also provided in Table. The mesh chosen is uniform with mesh size of 0.15 mm. The numerical simulation is performed for 80 μs which marks the end of deformation process with material being deformed plastically. The results for Y-direction velocity during the course of simulation are shown in Three dimensional ghost layer required for inter-processor communication for eight processors. Each color denotes a different processor here.

. These results give good agreement with experimental analysis. The two key things found in experimental analysis was that the deformed part presents a ―mushroom" at the end that accentuates itself as the velocity of impact increases and the boundary between the plastically deformed and the undeformed regions cannot be seen easily. The ―mushroom" part is observed in following simulations with the radius of mushroom increasing with increase in impact velocity. Even the boundaries of deformed and undeformed regions in these simulations are not distinct.

As observed by Taylor[64], the process of deformation is a sequence of elastic and plastic wave propagating to cylindrical bar. Initially the elastic wave is faster than the plastic wave and travels until it reaches the back surface of Taylor bar. It then reflects towards the plastic wave as a relief wave marking the end of deformation process. We also noticed that the jetting phenomenon continued till 40 μs at which point material begins to harden resulting in bulging at the base of material. The other observable quantities such as pressure and effective plastic strain at the cross section of bar is shown in Figure 6-4 and Figure 6-5. We also observed that the effective plastic strain which is concentrated mostly at the base of bar, Figure 6-5. It is a scalar parameter which grows whenever a material is actively yielding i.e. whenever the state of stress is on the yield surface. We would also like to show the readers the advantage of using level set method which accurately defines the interface and can handle large deformation problems as shown in Figure 6-6 by mesh containing Taylor bar at the beginning and at the end of simulation. This also depicts the advantage of localization of information on each processor as explained in chapter 3.

Finally we compared the impact time history of the variation of the dimensions of the bar with LSDYNA 3D code [14], IPSAP method [14] and parallel 3D PIM code [15] as shown in Table 6-1. It was observed that the results are in good agreement with available literature.

6.1.2 Impact at 400 m/s

The behavior of the bar in the above low velocity impact situation is now compared to that at a higher velocity to highlight the effect of impact velocity on the deformation of the bar. The simulation shows that the present method can handle large deformations and strain rates. The results from this simulation are shown in Figure 6-7. It can be seen that the deformation is very severe in this case with the bar reducing to one third of its initial height. The shapes of the bars in the two cases are in excellent agreement with experimental views of the effects of impact velocity on Taylor bars and on the physical arguments of Taylor and others on the shapes assumed by bars impacting at different velocities[64, 66].

6.2 Perforation and Ricochet Phenomenon in Thin Plates

Although numerous studies have analyzed impact and penetration phenomena, most of these studies are limited to two-dimensional or axisymmetric inline impacts[10, 11, 26, 36]. However, the vast majority of impacts are oblique to the targets and are intrinsically three-dimensional. The real test of a three dimensional multi-material code is to simulate impact/penetration phenomena at an angle. In this section, three-dimensional high speed impact dynamics of two bodies is shown. A mild steel sphere with velocity of 610 m/s is impacted on a mild steel plate at an angle of 60 degrees. The diameter of mild steel is 6.35 mm and the dimensions of plate are 40 mm X 25 mm X 1.5 mm as show in Figure 6-8. A domain of size 40 mm X 25 mm X 20 mm is chosen for this computation. A uniform mesh size of 0.1 mm is used with total number of grid points close to 16 million. The simulation is done using 196 processors. The material properties and E.o.S. parameters are given in Table 2-1 and Table 2-2 respectively. The initial mesh topology of sphere and plate is shown in

Figure 6-9. The high speed sphere undergoes a severe deformation and ricochets from plate as shown by section view in Figure 6-10. The velocity vectors shown in Figure 6-10 illustrate the ricochet phenomena observed during impact at high angles. The section views of final deformation shown in Figure 6-11(a) and Figure 6-11(b) are in excellent agreement with experimental results[21] and Lagrangian numerical computations[13, 34]. The interface topology at different instants of time is shown in Figure 6-12. The velocity contours of inclined impact are shown in Figure 6-13 and Figure 6-14. The sphere at high speed comes to rest at 80μs. Figure 6-15 shows the initial and final location of deformed sphere for a section. It also shows the processor boundaries depicting the successful implementation of method.

6.3 Fragmentation of a Thin Plate

Generally in the case of high speed impact or penetration of a hard impactor on a soft target, the target undergoes negligible elastic deformation and then severe plastic deformation. Finally if the speed of impactor is very high and the target is not thick enough to completely absorb the energy of incoming impactor, the resultant scenario can lead to total fragmentation of target material. The example consider here consist of a slender tungsten target penetrating a thin aluminum plate at 2000 m/s. The material properties and E.o.S. parameters are given in Table 2-1 and Table 2-2 respectively. The diameter of impactor is 1.5mm and its length is 3.5mm. The thickness of target is 1 mm. A computational domain of 10mm X 10mm X 10mm is chosen for this simulation. All the faces except the bottom face of domain are prescribed with Neumann boundary conditions. The bottom face acts as a rigid wall resulting in enforcement of reflective boundary condition. The results for total fragmentation are shown in Figure 6-16. The individual impactor and target topology is also shown in Figure 6-17.The results shown here are totally based on resolution and not on a damage model[43]. The idea here is to extend the methodology by using a damage model where the parts of material will be physically separated due to the state of stress. The present techniques and computer program implemented in three dimensions were able to handle small fragments generated during high speed imapct and penetration phenomena in a robust fashion.

Table 6-1. Comparison of three-dimensional Taylor Bar Impact with other computer codes.

Code	Final length (mm)	Final Radius (mm)
Parallel 3D PIM [15]	21.6	7.1
IPSAP [14]	21.52	7.0
LS-DYNA [14]	21.23	6.18
Current work	21.80	6.36

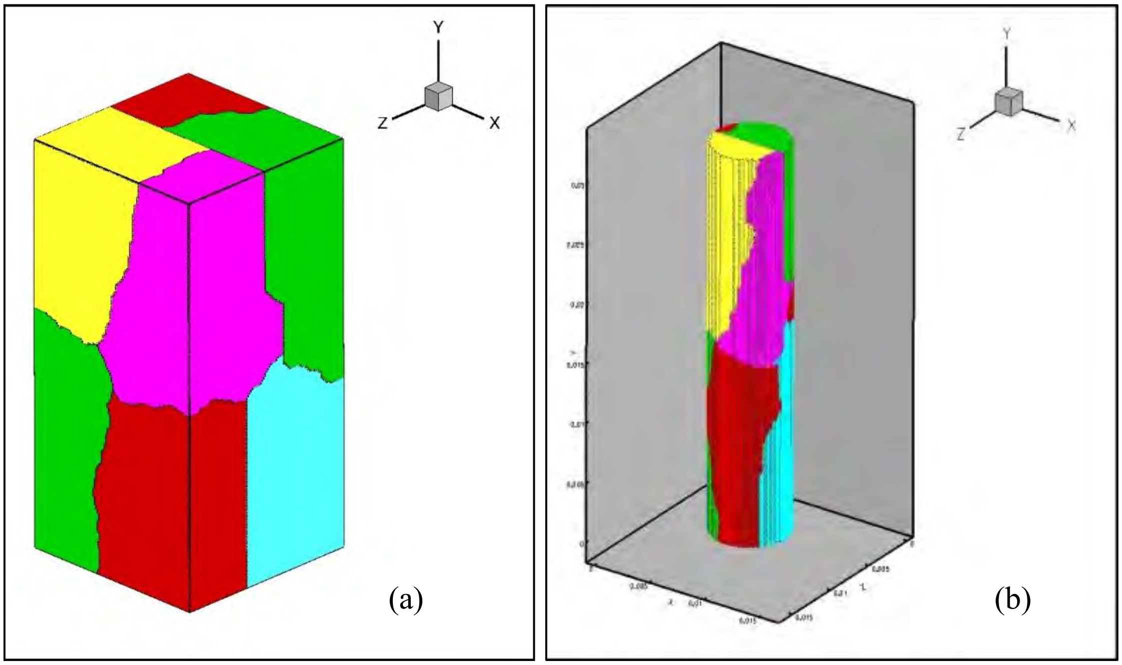

(a)

(b)

Figure 6-1. Load balanced domain decomposition created using partitioning software METIS where each color denotes a different processor: a) Decomposed domain b) Taylor bar.

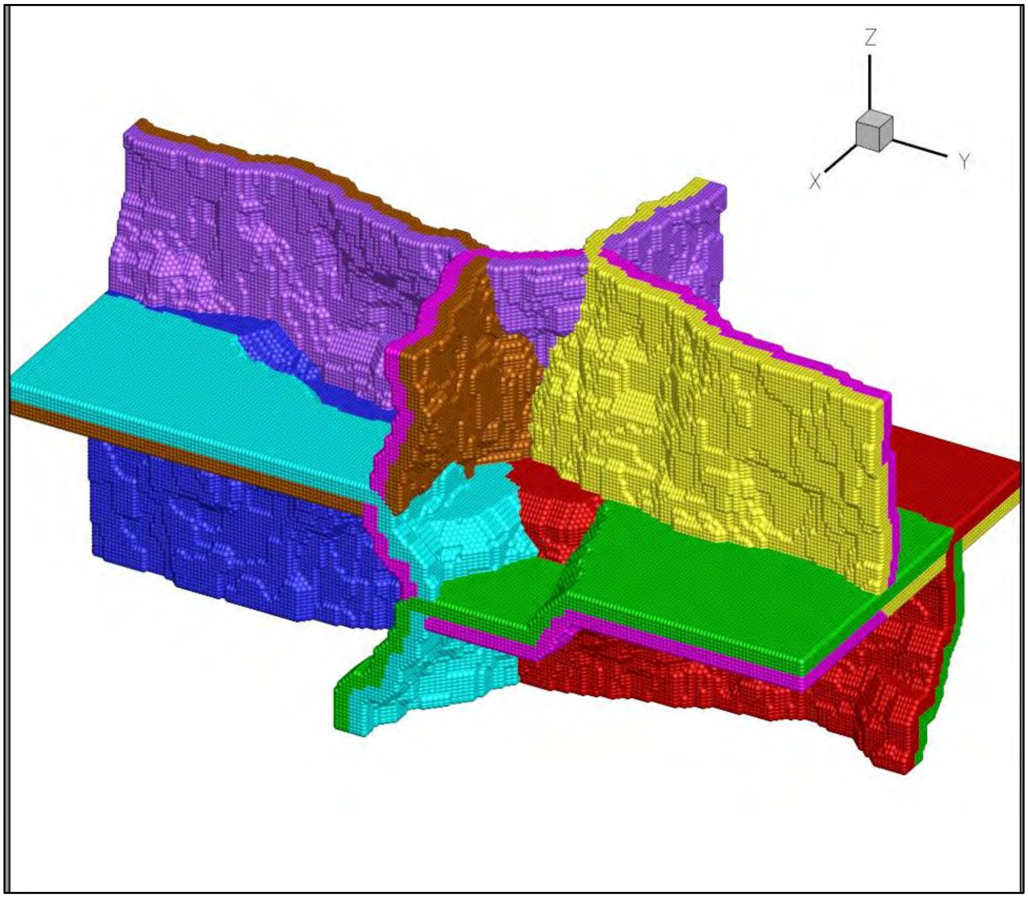

Figure 6-2. Three dimensional ghost layer required for inter-processor communication for eight processors. Each color denotes a different processor here.

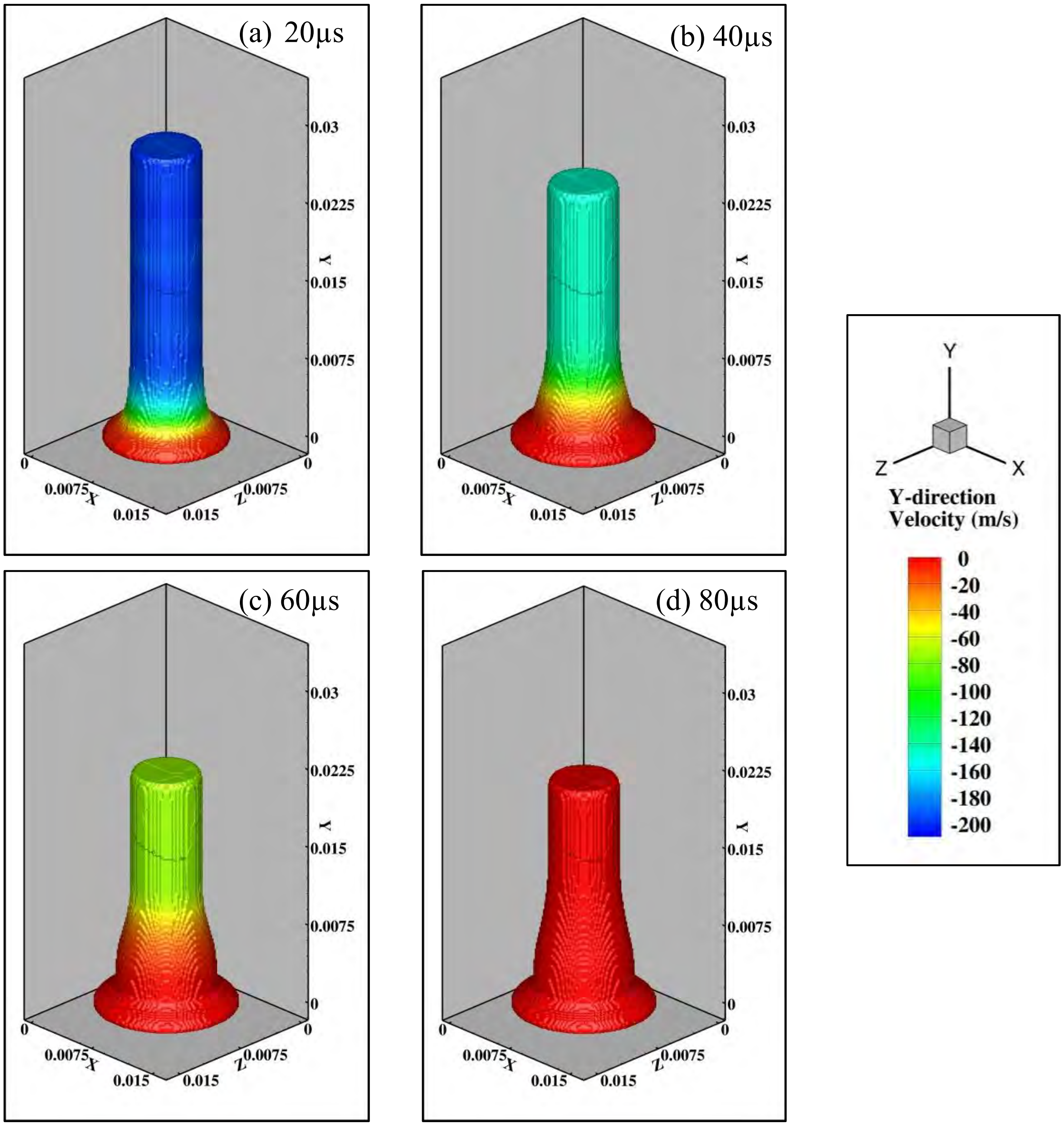

Figure 6-3. Y-direction velocity contours of Taylor bar impact at 227 m/s. The snapshots for a time interval of 20μs are shown depicting the phenomenon of jetting of bar till 40μs and finally hardening till 80μs.

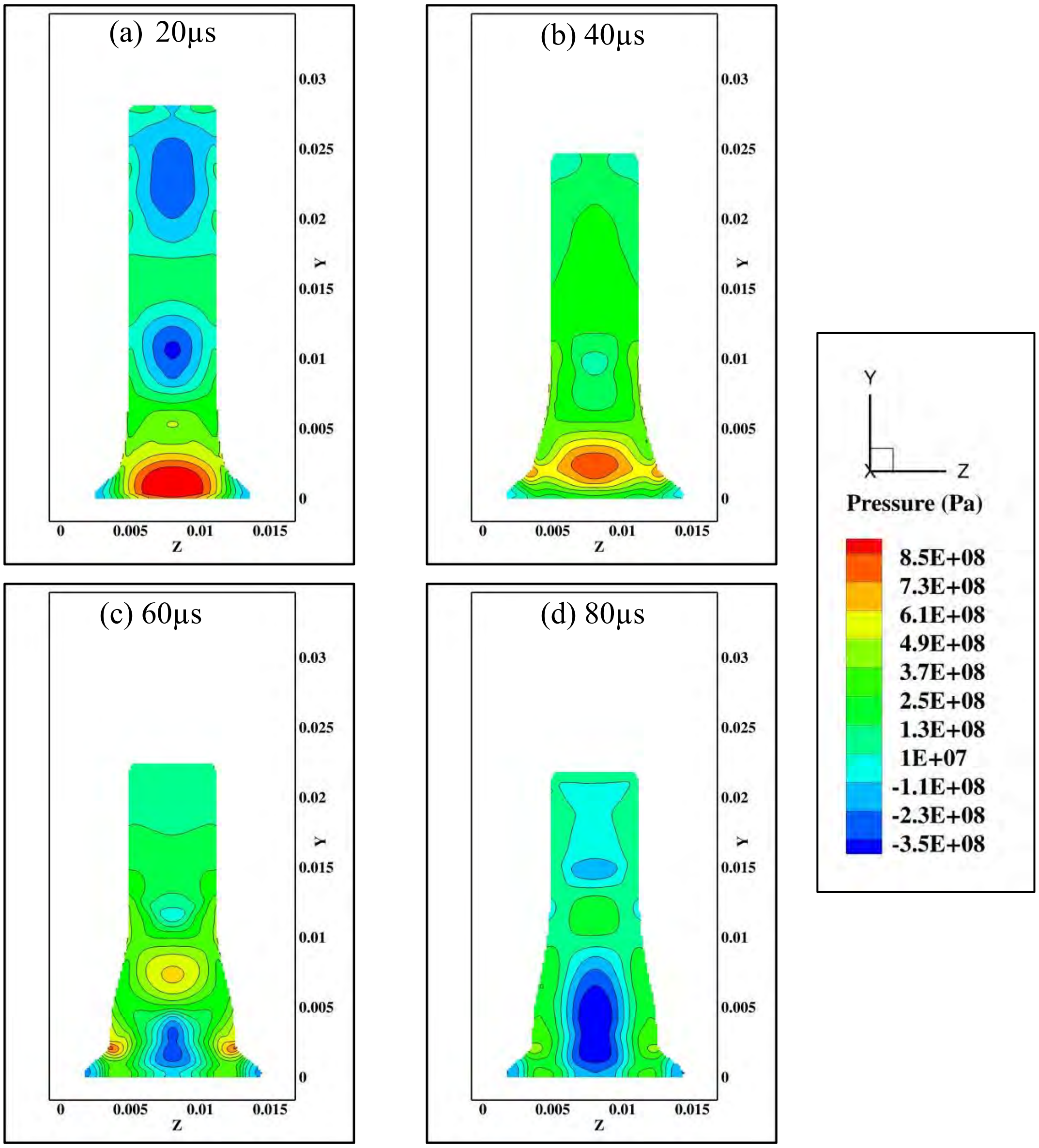

Figure 6-4. Pressure contours at a cross-section of Taylor bar at 20µs, 40µs, 60 µs and 80µs for an impact speed of 227 m/s.

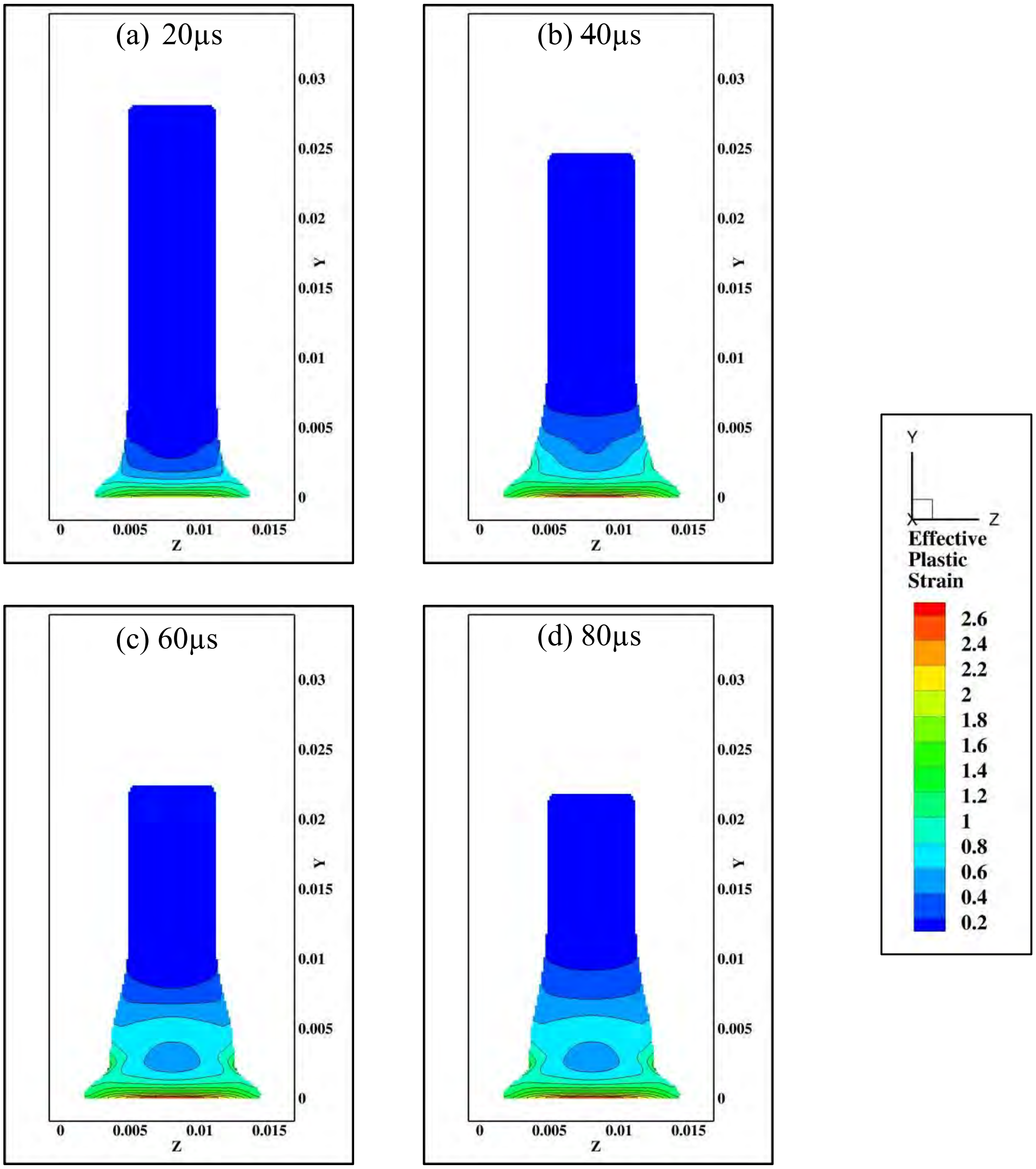

Figure 6-5. Effective Plastic Strain(ε_p) contours at a cross-section of Taylor bar at 20µs, 40µs, 60 µs and 80µs for an impact speed of 227 m/s. It can be seen clearly that plastic strain is mostly concentrated at the base of the bar.

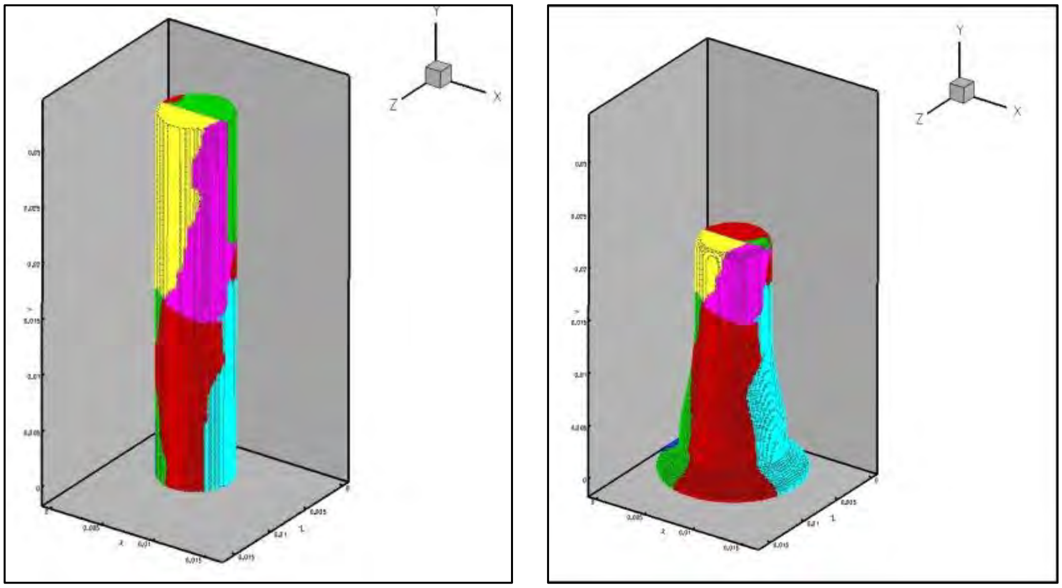

Figure 6-6. Mesh defining the topology of Taylor bar at the beginning (left) and at the end (right) of simulation.

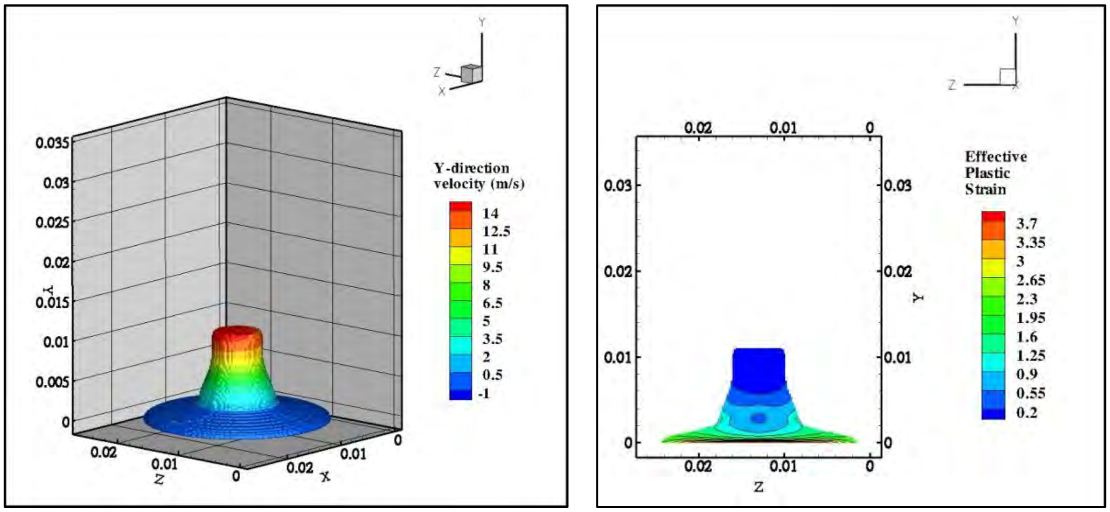

Figure 6-7. Y-direction velocity contours (left) and Effective plastic strain (ε_p) (right) for Impact at 400m/s at 80μs. The severe deformation of bar at high impact speed of 400m/s results in increased plastic strain accumulation.

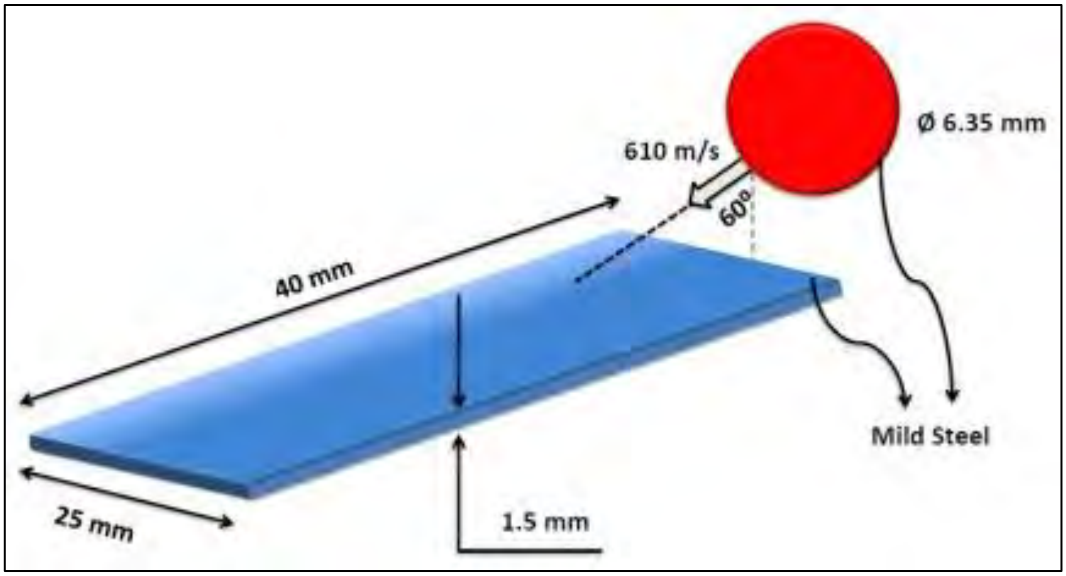

Figure 6-8. Initial setup of mild sphere impact on a thin mild steel plate. The mild steel sphere of 6.35 mm diameter is impacted at an angle of 60 degree on a flat mild steel plate of 1.5 mm thickness.

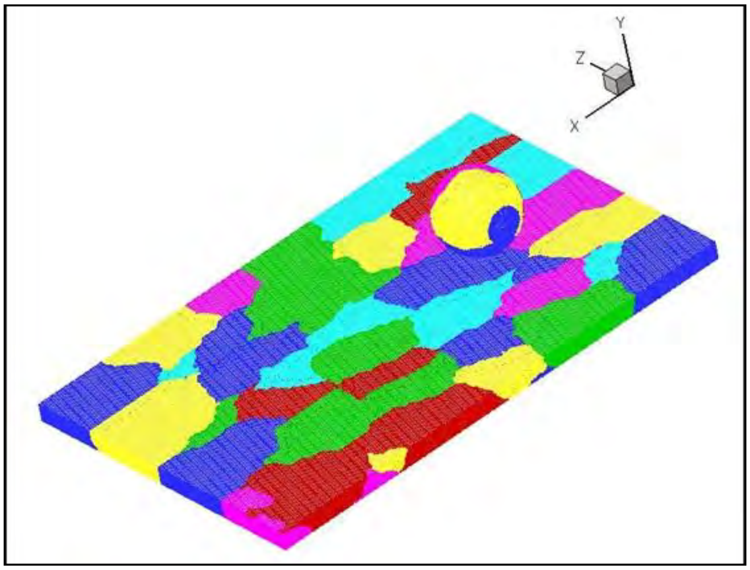

Figure 6-9. Initial mesh topology of mild steel sphere and mild steel plate. Each color denotes a different processor here with 196 processors being used for this computation.

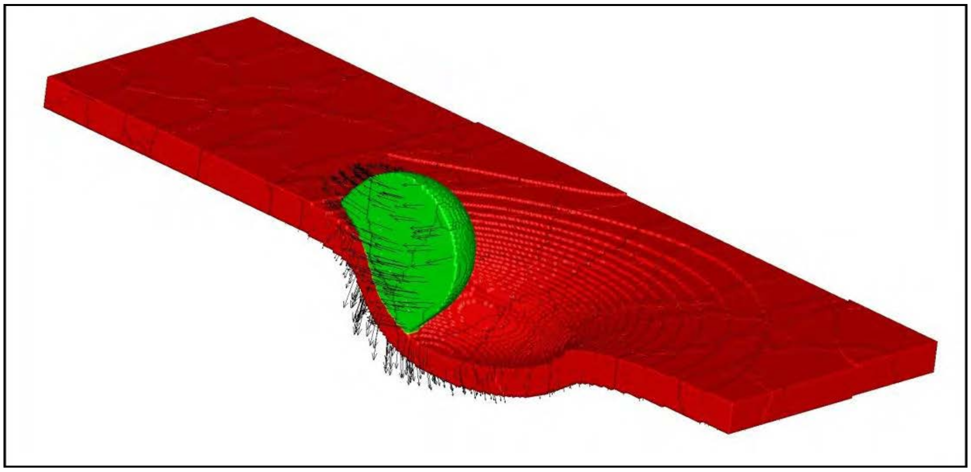

Figure 6-10. Section view of impacted sphere and plate with velocity vectors showing ricochet phenomenon. The mild steel sphere deforms and finally settles at the top of plate.

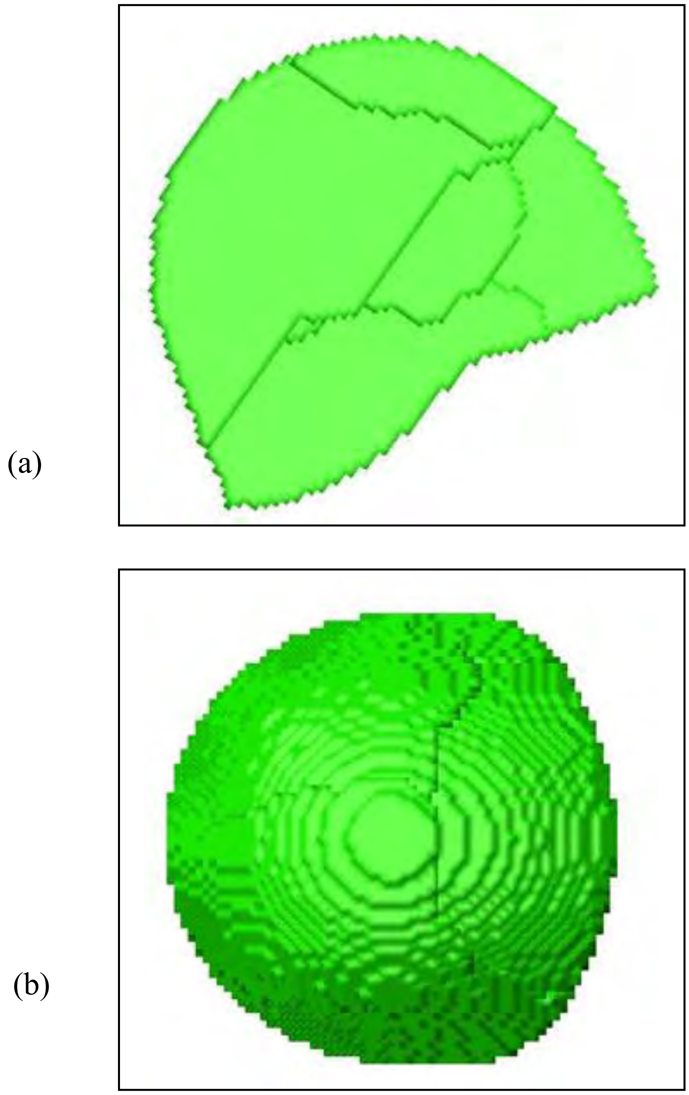

Figure 6-11. Mild steel impact at 610m/s (a) Side view of deformed sphere (b) Top view of deformed sphere. The figure also depicts the boundaries of processors containing the sphere.

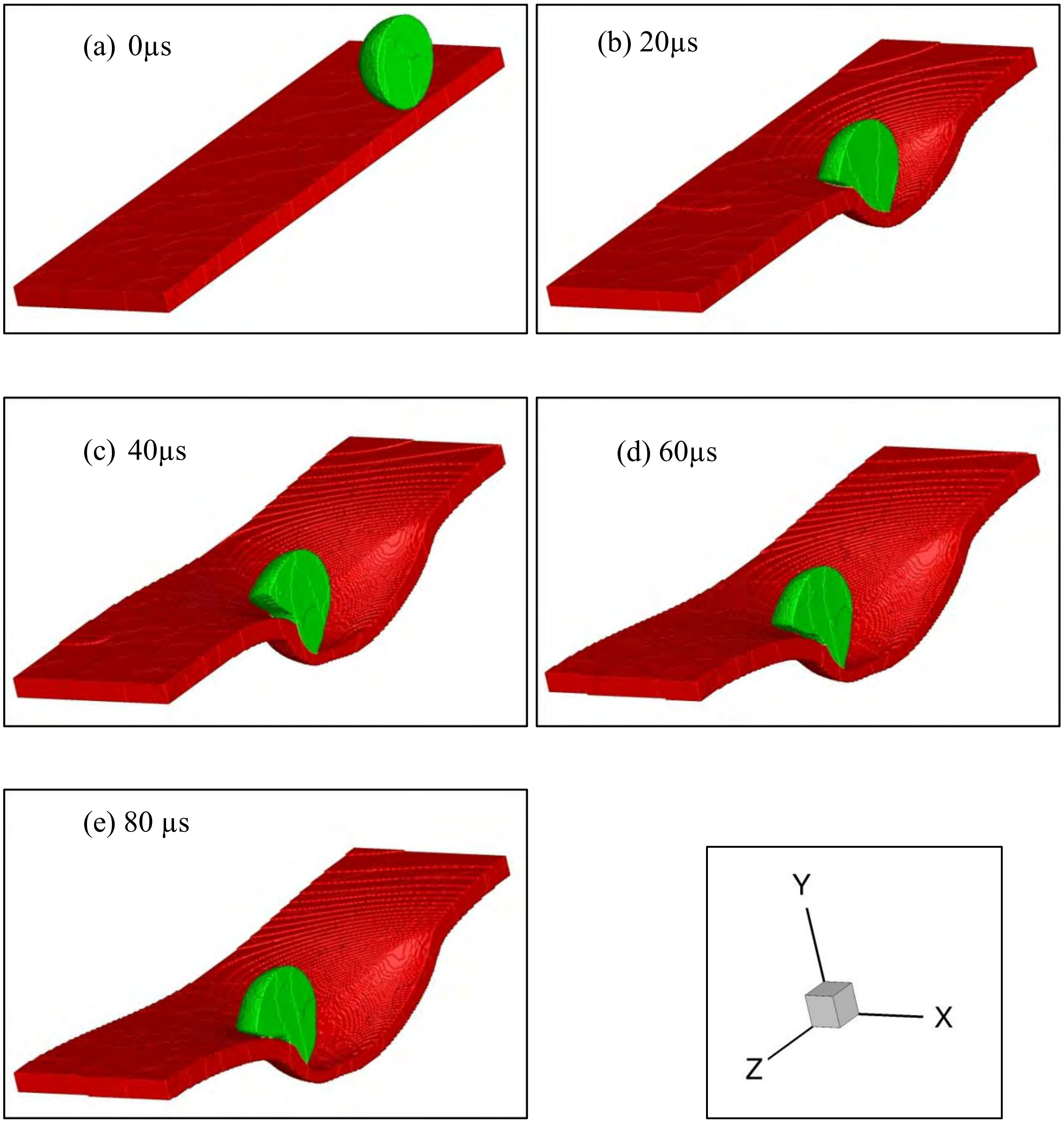

Figure 6-12. Interface topology for inclined impact of sphere (mild steel) on a plate (mild steel) at 610m/s at 0μs, 20μs, 40μs, 60 μs and 80μs.

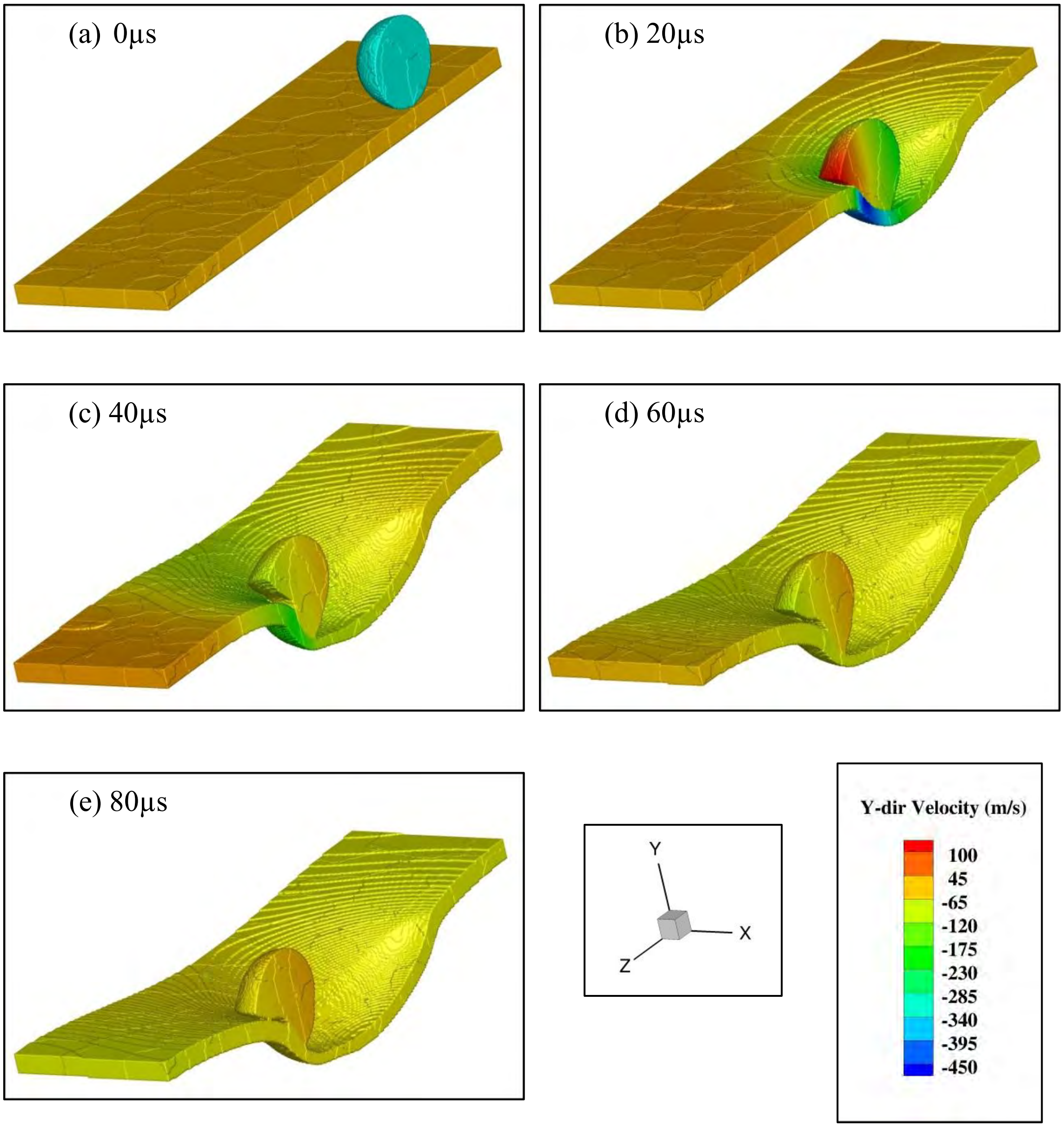

Figure 6-13. Y-direction velocity contours of mild steel sphere impact at 610m/s from 0μs to 80μs. The contours clearly depict the final settlement of sphere with Y-direction velocity going to zero.

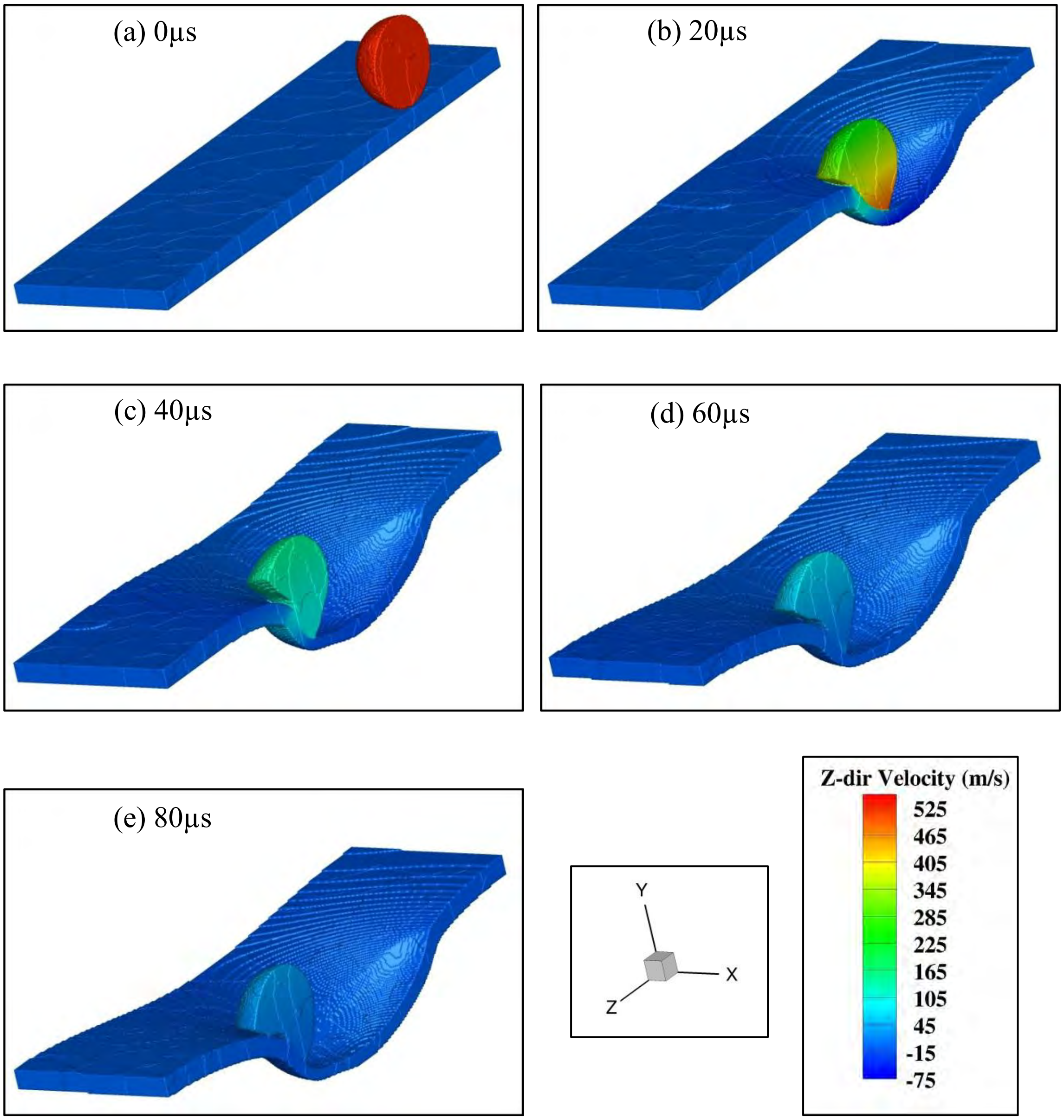

Figure 6-14. Z-direction velocity contours of mild steel impact at 610 m/s from 0μs to 80μs. The contours clearly depict the final settlement of sphere with Z-direction velocity going to zero.

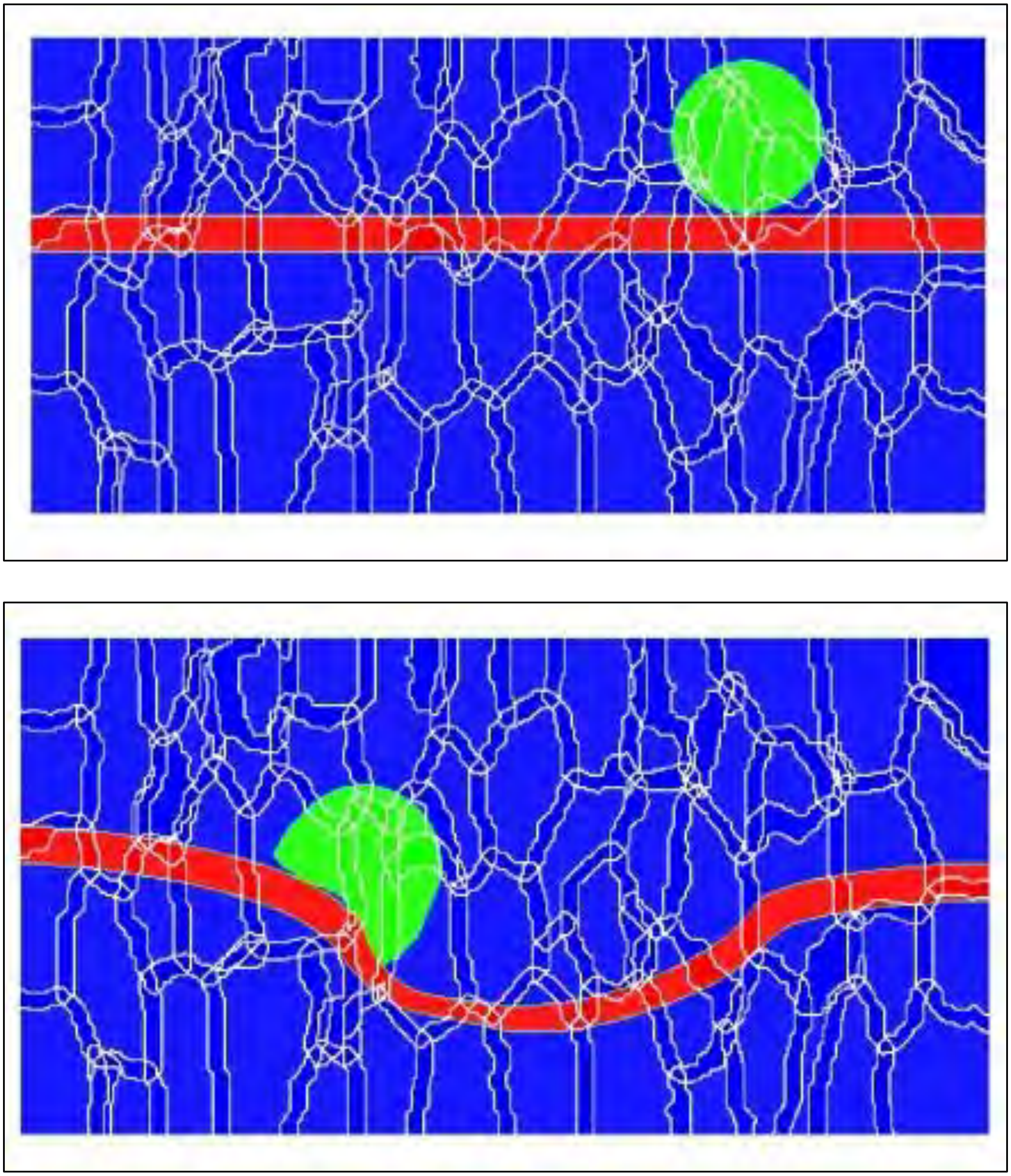

Figure 6-15. A snapshot of domain cross-section showing finally settled sphere at 80μs. The initial and final contours of both sphere and plate with processor boundaries clearly depict the ricochet phenomenon.

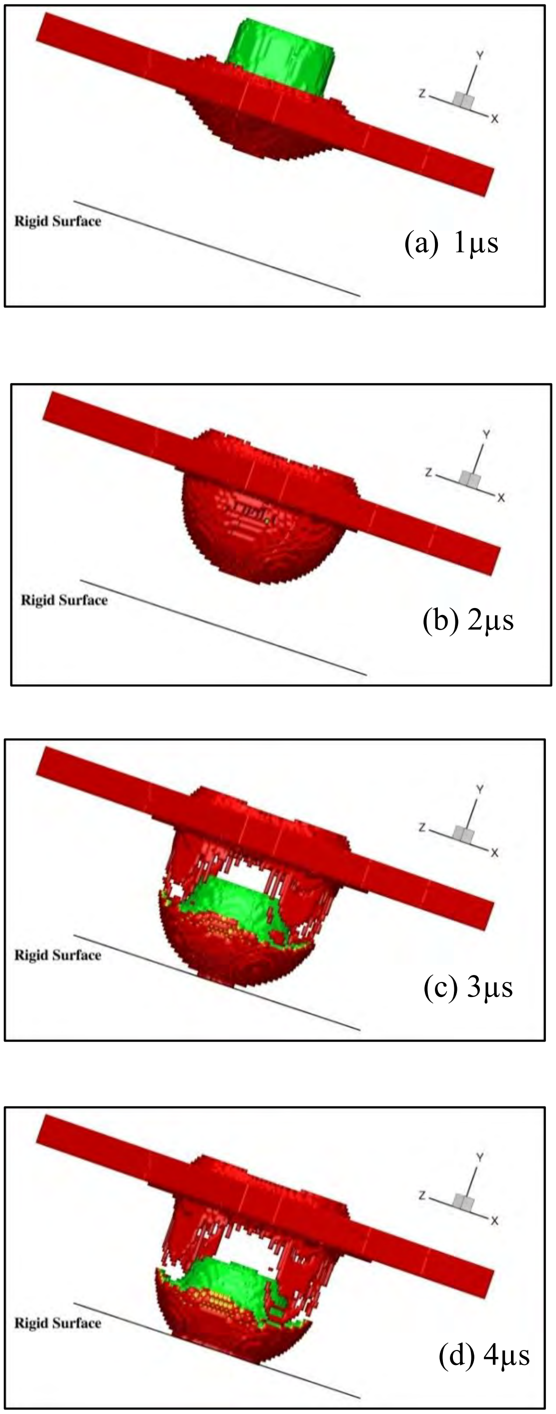

Figure 6-16. Interface topology of impactor and target showing total fragmentation from 1-4μs. The target and impactor also interact with rigid surface as shown above.

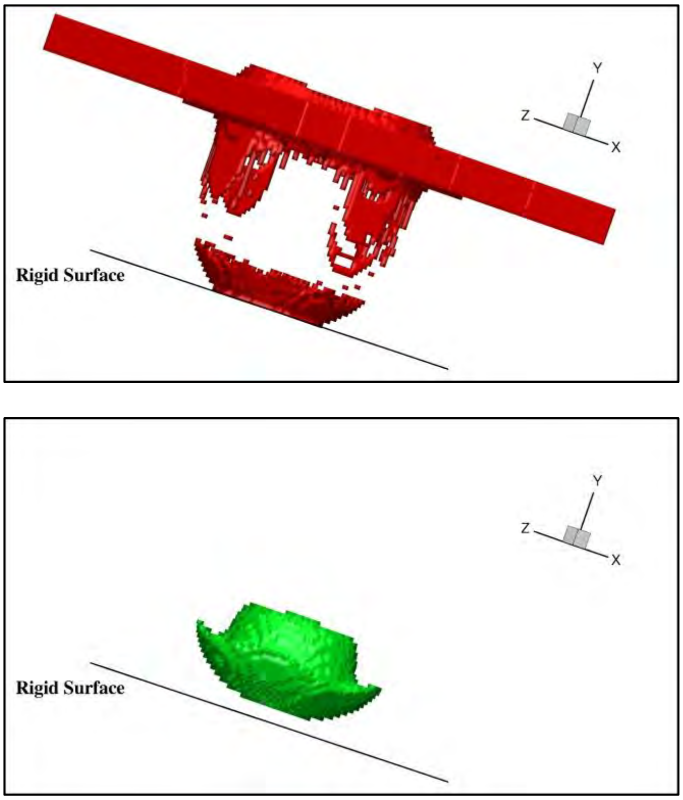

Figure 6-17. Interface topology of individual target (top) and impactor (bottom) showing total fragmentation.

CHAPTER 7

VOID COLLAPSE IN ENERGETIC MATERIALS

7.1 Introduction

Shock waves interacting with heterogeneous materials are important in studies related to impact, penetration and detonation in condensed media, with applications in propulsive devices, munitions and explosive-target interactions. The study of release of energy is a crucial requirement in these systems. Traditional models for these applications are based on continuum theories where the microstructural heterogeneities of the material is ignored or homogenized. These simulations, based on a continuum mechanics approach[35, 69] at the macro scale miss the key aspect of modeling energy release at a scale corresponding to particle size. Designing propulsion devices and munitions for precise operational performances demands comprehensive understanding and manipulation of the spatial and temporal distribution of energy release in activated energetic materials.

7.2 Mechanisms of Void Collapse

In the present work, the modeling of void collapse in a high explosive is chosen as the focus. Examples of such materials include the popular HMX [70]. Initiation of a heterogeneous explosive can occur when an impulse given to the material evolves into a detonation wave. This phenomenon of evolution of a shock wave into a detonation wave (which is a shock wave followed by a reaction front, where the shock is driven by energy supplied by chemical reaction) depends on the local heating of material, where temperature can be much higher compared to the bulk temperature. These localized regions of high temperature are known as hot spots and can result in initiation of detonation under certain conditions. Bowden and Yoffe[71] proposed the mechanism of detonation initiation due to collapse of voids in the material; purposeful introduction or incidental occurrence of voids in cast explosives introduces a potential site for hot spot formation under shocked loading of an energetic material. There are number of mechanisms which can contribute in formation of hot spots. These mechanisms can operate collectively depending on size of voids, material properties, strength of shock wave and regime of operation. The various mechanisms proposed over the years are as follows:

1. Compression of gas in the void: This mechanism can occur when a shock wave passes over the void, compressing the gas inside it. As the void is collapsed, the entrapped gas inside the void is compressed to high temperature and pressure. The temperature can reach a value high enough to initiate ignition. Chaudhri and Field[72] have showed in their work that this phenomenon is important only for the size ranging from 50-μm to 1-mm collapsed by a low strength shock ~ 0.1 GPa. Therefore the gas compression is a dominant mechanism when large pores are collapsed slowly.

2. Hydrodynamic Impact: This mechanism occurs when a heterogeneous explosive is loaded at high shock strengths. At high speeds, the wave amplitude far exceeds the plastic yield strength of material deforming the lower surface of void. The deformed downstream surface thus form a high-speed jet of material which impacts against the upper surface of void resulting in increase of temperature. In this phenomenon the high kinetic energy of downstream surface is converted into internal energy during impact resulting in very high temperature favorable for detonation initiation. This mechanism [73] therefore corresponds to the inertia-dominated regime.

3. Plastic work: When a solid material undergoes plastic deformation, the temperature rises due to conversion of plastic work into heat. Khasainov et al.[74] have pointed that significant heating can occur due to plastic work for smaller

void sizes, i.e. for void diameters less than micrometers and in short times of less than a microsecond.

Other mechanisms that may be important for formation of hot spots are shear heating[75], kinetic energy release due to inter-particle impact [76], melting at inter-particle boundaries[77], friction due to relative motion of particles and interfacial defects caused by shock passage [78]. All of these are local phenomena and occur at the scale of individual particles and are not reflected in a continuum model that operates on volume-average[35] or mixture formulation[69].

7.2.1 Importance of Modeling the Meso-Scale Dynamics of Heterogeneous Explosives

Typical analyses of the response of an energetic material exposed to severe loadings (that are likely to trigger explosion) have treated the energetic material as a macroscopically homogeneous material, which for heterogeneous explosives implies some form of homogenization or mixture theory[35, 69]. In such treatments the response of the material to a passing shock which initiates self-sustaining chemical reactions must somehow incorporate the microscopic, localized events such as hot-spots. In most hydrocodes [9] that compute such response the Lee-Tarver ―Ignition and Growth model” [69] is used to initiate reaction. This model provides a heat release rate at any point in a heterogeneous explosive as a function of the local shock pressures and the void fraction and can be used as a heat deposition source term in a homogenized multiphase model (such as the Baer-Nunziato model[35]). In the ignition and growth model a small fraction of the explosive is assumed to be ignited by the passage of the shock front; the reaction rate is controlled by pressure and surface area of the unreacted material, by adopting ideas from treatment of deflagration processes. The Lee-Tarver model[69] is a phenomenological model that provides the heat released behind the leading shock wave by modeling the energy release rate in the form:

$$\frac{\partial F}{\partial t} = I(1-F)^x \eta^r + G(1-F)^x F^y p^z \tag{7.1}$$

Here F is the fraction of unreacted explosive, I, G, x, y, r, and z are constants that are empirically established and,

$$\eta = \frac{V_0}{V_1} - 1 \tag{7.2}$$

Where V_0 is the initial specific volume of the explosive and V_1 is the specific volume of the shocked, unreacted explosive.

Note that in Eq 7.1 the first term accounts for ignition and the second for growth of the reaction front. The argument posed by Lee and Tarver is that ignition is supposed to depend on the compressive strength of the incident shock wave and also on the surface area corresponding to the fraction of unreacted explosive while growth of the reaction front depends on the pressure. This latter dependency is again an extension of the idea of burning fronts in deflagrating propellants. Note that in a heterogeneous medium ignition occurs at hot spots and buildup to detonation occurs as the reaction grows outward from these hot spots[69]. Thus the number and intensity of energy localizations at hot spots play a role in determining whether ignition and growth can lead to run-off to detonation. As shown by Khasainov and others[74, 75, 79] and demonstrated in results to be presented the formation of the hot-spots can lead to localized temperature and pressure excursions that are quite different than the imposed temperature and pressure fields in a shocked homogeneous material. Thus, the physics behind void collapse is not captured by arguments that are extended from deflagration phenomena in propellant stick burning.

The way in which hot spot phenomena are argued[74, 80] to be reflected in the Lee-Tarver model depends on the mechanism of hot spot formation that is considered to operate. For example, if the hydrodynamic void collapse leads to hot spots, the exponent r is assigned the value 3. This is due to an assumed relationship between the particle velocity u_p and void fraction η, viz. $u_p^2 \propto \eta^3$. Since the hydrodynamic void collapse is an inertial mechanism that converts the local kinetic energy of the jet formed in the underside of the void into thermal energy the ignition process is assumed to depend on the kinetic energy. If the hot spot is formed due to plastic work done in deforming the void as it collapses, then this work is assumed to be proportional to $\int p^2 dt$[80], where p is the pressure and the integral is over the time of collapse of the void. Since $p^2 \propto \eta^4$ the exponent is given the value 4[80]. Whether *r* should be 3 or 4 is determined by recourse to experiments and the other constants in the equation above are fit to experiments as well. This procedure of determining the value of *r* depends on the type of explosive in an ad hoc way and is non-generalizable. The rational for fitting the constants in the Lee-Tarver model appear to be based on semi-empirical and physical notions, but there is no specific understanding of how void collapse deposits energy and how this locally deposited energy leads to thermal runoff and detonation.

While the Lee-Tarver model is quite popular in making predictions of the overall response of energetic materials using hydrocodes, it is difficult to see clearly how the void collapse mechanism, in particular void-void interactions can be adequately reflected in such a phenomenological model. In more recent work Tarver[81] and others[70] have taken a more micro-scopic view by asking the question ―what is a shock wave to an explosive molecule"?[81] In this view, by assuming that reactions in the condensed phase explosive material follow conventional Arrhenius rate laws[82], a material comprised of molecules of energetic material will be ignited if the local temperatures exceed certain critical values and the local thermal energy deposition is high enough that the activation energy barrier can be overcome. Thus, there are two key elements that reflect whether a hot spot will lead to successful ignition: local temperature (connecting hot spot intensity to reaction rate kinetics through the activation energy required to trigger reactions) and the ―strength" of the hot spot. The latter measure depends on the size of the hot spot, the time scale over which local ignition conditions can be maintained etc. before dissipative mechanisms such as rarefaction waves, plastic work, thermal conduction, viscosity, and phase changes can draw energy away from the hot spot. Thus, Tarver et al.[81] have obtained values of critical temperatures for HMX and TATB explosives that are functions of the sizes of the voids; the smaller the voids the larges the ~~c~~ritical temperatures”. This implies that shocking a heterogeneous explosive with very small voids may not lead to ignition.

The viewpoint in the current work is that, along the lines of the more recent work of Tarver et al.[81] and others [75, 77, 78] , a truly micro-scopic viewpoint is required to understand and quantify the effect of a shock on voids in the heterogeneous material. The issue of whether there will be ignition is taken to hinge on the following factors:

1. When a void collapses what is the local temperature experienced by reactive molecules in the vicinity of the void? What is the time scale of relaxation of this local temperature?
2. How does this localization depend of the shock strength and void size?
3. When a piece of heterogeneous explosive containing a void (or a collection of voids) is exposed to shock loading what is its response? How does the input shock energy distribute itself into thermal and inertial modes in the material?
4. What effects do void-void interactions have in a heterogeneous explosive and how do these effects depend on the loading parameters and void characteristics (e.g. shock strength, void size and shape)?

7.3 Modeling of Shock-Induced Meso-Scale Dynamics

Simulations of energy deposition and transport in the presence of grain scale features have been pursued in a variety of contexts. Zhang et al.[83] have examined the effects of metallic particles (and small arrays of particles) of initially circular shape in an RDX explosive (modeled as a homogeneous substrate). Udaykumar et al. [79, 84] have examined the evolution and collapse of a void in an inert matrix and a reactive HMX matrix, demonstrating the different ways in energy localization can occur ranging from plastic work to hydrodynamic collapse. Cooper et al.[12] also studied void collapse in a metallic system using an Eulerian approach. Frost et al. [85] have used the detonation-shock-dynamics model for detonation propagation where the detonation front is tracked by means of a level set function. They examined the passage of a detonation wave through an array of inert particles. In all of these simulations the attempt was to examine the detailed micromechanics and energy localization phenomena pertaining to a single feature or small array of features embedded in an otherwise homogeneous substrate with properties pertaining to HEs. Reaugh[86] examined features of void collapse, inter-particle contact and deformation in a representative disordered mixture with realistic particle shapes simulating HMX crystals. Benson and coworkers[87] developed an Eulerian approach where the deformation field is mapped back to a fixed Eulerian mesh following a preliminary Lagrangian update step. Within each grid cell in the Eulerian mesh several particles can coexist, with a volume fraction based approach to keep track of each particle. Shock compaction of powders has been studied using this approach. Since particle surfaces are not explicitly tracked some of the mechanisms of energy deposition listed above (e.g. frictional, melting, and void collapse) cannot be included in the model. Menikoff[77] has used this framework to examine the compaction of a granular bed of HMX. The propagation of stress waves in the inhomogeneous medium and the energy localization in a mesoscale sample containing a collection of (regularly shaped) crystals was studied. Using the Eulerian computer code CTH, Baer[78] and coworkers have studied the mesoscale dynamics of HEs under the effect of imposed shocks. Detailed 3D simulations of compaction (i.e. inert cases) and detonation (i.e. reactive cases) have been simulated. The HMX crystals are loaded in the computational domain using algorithms for particle size distribution and shapes that yield desired packing fractions. The simulations were conducted with elastic-perfectly plastic models for the crystals. In these works details of void dynamics, particularly the interactions between several voids subject to shock loading have not been elucidated. This work, using sharp interface treatment of the voids through the collapse stage, investigates and reveals several key aspects of the physics of void collapse and void-void interactions in an otherwise homogeneous matrix.

7.4 Methodology

The main objective of this work is to characterize and analyze the mechanisms which are important at relatively high speeds (particle velocities at or above 500 m/s), i.e. strong shocks interacting with typical void sizes in HMX (void diameters of the order of 10μm) material without chemical reactions. In this setting the convective time scales are dominant, as these are very short (O~10^{-7}s) compared to diffusive and viscous time scales (O~10^{-5}s). This dominance allows us to exclude viscosity and thermal diffusion by treating HMX as an elastic – perfectly plastic material[70]. Therefore the physical mechanisms important in given regime will be plastic work and hydrodynamic impact. The response of a material (elastic- perfectly plastic) to high intensity (shock/impact) loading conditions is modeled. Details pertaining to material properties are listed in Table 2-1. The computation of void collapse is performed by integration of the mass, momentum and energy balance laws along with the evolution of the deviatoric stress components, assuming a pure elastic deformation (i.e. freezing the plastic flow) as an elastic predictor step, followed by a radial return mapping to bring the predicted stress back to the yield surface [42]. The details pretaining to governing equations, constitutive equations, radial return algorithm and the Mie-Gruneisen equation for determining dilatational response have been laid out in CHAPTER 2. A third-order TVD-based Runge-Kutta scheme [49] for temporal discretization and a third-order convex scheme [41] for spatial discretization is used. The void is defined as an embedded object using the level set [50] function, which is then tracked during the course of the simulation. The interface treatment is handled using a modified GFM (Ghost Fluid Method) approach. These numerical schemes are well established and significant details are provided in CHAPTER 3. The computational code has been validated by simulating a plethora of physical problems for high speed impact and penetration in both two and three dimensions (CHAPTER 5 and CHAPTER 6). A validation for a physical situation similar to the void collapse process, i.e. demonstrating the interaction of shock wave with a hemispherical groove is shown in the next section. Further validation of the calculations for void collapse with limit cases of theory on hydrodynamic collapse (Rayleigh) is also performed. Following the validation exercises the physics of void interactions in a porous material is carefully examined. The insights obtained from the present work are significant and novel and advance the understanding of the mechanics of void collapse when there are multiple voids interacting with shock loadings.

7.5 Validation of the Computational Technique

A phenomenon like void collapse, which occurs at very small temporal and spatial scales, is difficult to investigate experimentally due to large deformation and very high gradients in physical parameters. Therefore one takes recourse to computer simulations to investigate these physical phenomena. Therefore, it is important to validate the computer simulation for a problem which is similar to collapse of a void but does not present challenges to experimental visualization. In this regard, the interaction of a shock wave with a hemi-spherical groove can be considered as a physical problem that is similar to the computations performed by Cooper et al.[12]. A planar shock wave interacts with a copper plate with a hemispherical groove of radius 15 mm. The generated shock wave corresponds to particle velocity of 540 m/s and a pressure ratio of 230 Kbar. The interaction of the shock wave with the hemispherical groove results in a reflected expansion wave and the formation of a jet. The formation of a jet is confirmed in experimental work[88] and in the numerical calculations done by Cooper et al.[12]. The simulation was performed in an axisymmetric setting on computational domain of 150 mm X 300 mm with uniform mesh size of 0.5 mm. Figure 7-1 shows the formation of the jet in the copper material. The evolution of the shape of the jet along with velocity of the jet at one instant is also shown in Figure 7-1(b). The results were compared with the computed profiles of the jet at each instant of time shown in Figure 7-1(a) with the computations of Cooper et al. and the x-ray image of the jet and jet velocity obtained in the experiments of Mali et al[88]. Excellent quantitative agreement was obtained as listed in Table 7-1.

7.6 Analysis of Single Void

This section focuses on collapse of a cylindrical void in a HMX matrix material that is considered to be homogeneous. The computational setup is shown in Figure 7-2. A cylindrical void with a radius of 5µm, within a HMX material, undergoes deformation as a result of shocked loading by imposing a particle velocity of 500m/s at the bottom boundary as shown in Figure 7-2. The imposed shock is given a rise time equivalent to a fraction (10%) of the total time required by the shock to reach the lower surface of void.

7.6.1 Grid Independence Study

A grid independence study for a single void is performed to establish the framework for further analysis. A void size of 10µm in the HMX matrix is studied for different grid resolutions. A particle velocity of 500m/s is prescribed on the south boundary. For a fixed domain of size 30µm X 30µm, mesh sizes of 150 X 150, 200 X 200, 300 X 300 and 400 X 400 were used. Apart from the coarse case of 150 X 150, the other mesh sizes were observed to have the same maximum temperature rise as shown in Figure 7-3. The time at which the significant rise in temperature occurred is the same for all mesh sizes. The energy distribution in the material by evaluating the ratio of total internal energy to total kinetic energy was also observed for the whole simulation. All the cases showed similar results for change in slope of curve as seen in Figure 7-4. As all the fine mesh resolution cases showed the same rise in temperature at the same time and same contours for energy distribution, a mesh size of 300 X 300 is selected for further computations. This mesh size corresponds to 100 grid points across the void diameter. Thus, as the void collapses the number of grid points in the void diminishes but the adopted grid was found to be adequate to capture the dynamics of the collapse throughout the collapse process. It is noted that the present work carries the computations through and beyond complete disappearance of the void, which is quite infrequently the case in the literature. In Lagrangian methods for solving void collapse phenomena, it is rather challenging to follow the void shape close to or beyond total collapse. The present technique, with the least-squares treatment described in Chapter 3, succeeds in maintaining robustness through the collapse process.

7.6.2 Temperature Rise and Energy Distribution

When a homogeneous material is shock loaded, the rise in temperature is due to the bulk heating of material. However, in a heterogeneous material, the contribution to the rise in temperature comes from different mechanisms (Eq 2.29). It can be seen from Figure 7-5 heterogeneities like voids introduce enhanced sensitivity in the material and its response to an incoming shock changes entirely. The main contributions in the rise of temperature in the case of a heterogeneous material for the given regime are plastic work and hydrodynamic impact. The process of void collapse beginning from impact at the bottom surface to total hydrodynamic collapse of void and finally disappearance of void can be explained in five stages shown in Figure 7-6.

The stage 1 is the time before the shock reaches at the bottom surface of void. The energy of the shock wave itself causes ~60 K rise in temperature in the bulk solid material during stage 1. This stage is the same as impacting or shock loading a homogeneous material. In the second stage, the acceleration of material at the lower surface of the void occurs.

However this stage does not contribute much to temperature rise as shown in the Figure 7-5. As the material starts accelerating, plastic deformation (Stage 3) begins and the material begins to resist the deformation. The plastic work required to deform the material heats the material, resulting in a modest rise of temperature. Stage 4 comprises of total deformation of lower surface of void, jetting of the lower surface and impingement of the lower surface on the top surface resulting in hydrodynamic impact and a sharp rise in temperature to its peak (~1100 K) value. The impact phenomenon results in a secondary shock wave, which interacts with the initial shock wave resulting in complex wave patterns. Finally during stage 5, the hydrodynamic jet completely collapses the void and the void disappears. The interface evolution of the void collapse stages explained above is shown in Figure 7-9.

An alternate way of looking at the above stages is in terms of the distribution of kinetic energy and internal energy. This can be investigated by taking the ratio of the total internal energy to the total kinetic energy over the whole domain as shown in Figure 7-7. This measure is significant as it reveals the way in which energy becomes partitioned in the material due to the combined effects of shock loading and shock focusing at the void. It also leads to an understanding of the apportioning of energy in the material between the kinetic energy (inertia) and internal energy (thermal) modes. Figure 7-8 shows the velocity field at the five stages explained above depicting the role of kinetic energy in the material. The initial part, i.e. Stage 1, of the curve with zero slope represents the small rise in internal energy during the time taken by the shock to reach lower surface of void. At stage 2, the material at the bottom surface of void starts accelerating resulting in increase in the kinetic energy as seen from the negative slope shown in Figure 7-7. As explained earlier, the material resists this plastic deformation resulting in a modest increase in temperature and hence a rise in the internal energy. This can be seen in stage 3 where the slope of the curve decreases in magnitude (Figure 7-7). The stage 4 is seen where there is a sharp rise of slope due to conversion of the kinetic energy to the internal energy causing abrupt rise in temperature and pressure. This happens when the lower void surface impinges on the upper surface. Finally at stage 5, the void collapses fully resulting in the culmination of the energy redistribution behavior. It can also be seen from Figure 7-8 that the collapse of void results in a secondary cylindrical shock wave. This wave can interact with the voids downstream and can either enhance or diminish the intensity of the shock depending on the location of downstream void. This will be examined in the section below on the interaction of multiple voids.

7.6.3 Comparison

The results for the collapse of single void were also compared with experiments. In a recently published paper in the Journal of Fluid Mechanics Swantek et al.[89] have performed experimental studies for the void collapse phenomenon in a mixture of agarose and glycerol gradient buffer. These studies were done for the void sizes of 3mm. The voids were modeled as a cylindrical tube which is the key modeling assumption in the present 2D study was well and therefore the basis for comparison with experiments is substantial. The key observations made in experiments for a collapse of single void are compared to computational results and can be summarized as follows:

- During the early stage of collapse the region upstream of the void has a velocity significantly greater than the free stream velocity. This observation can be corroborated by stage 2 shown in Figure 7-8, where the velocity is ~1250m/s, more than twice the value of free stream velocity. The magnitude of the vertical component of the velocity approaches more than three times the magnitude of free stream velocity (500 m/s) before the collapse of the void as observed in experiments. This can be seen in stage 3 of Figure 7-8.
- A shielding region of zero velocity downstream the void is shown in (stage 1-stage 3) Figure 7-8 and is in agreement with experiment. This happens due to the diffraction of the shock wave around the void leaving the immediate downstream

region with zero velocity. The results for normalized void diameter with normalized collapse time were also compared and are shown in Figure 7-10. The initial period of acceleration corresponding to normalized time of 0.25 as observed in Figure 7-10 was in good agreement with the results of Swantek et al.

- In the present work, the impact speeds are high enough so that the void collapse phenomenon is totally hydrodynamic. Therefore the void collapse times should be comparable to Rayleigh collapse times[90] for a bubble. Rayleigh defined the time of collapse for a spherical bubble, t_c in terms of its radius R, the pressure at infinity P_∞ and the internal pressure P_v as

$$t_c = 0.915\left(\frac{\rho}{P_\infty - P_v}\right)^{0.5} R \tag{7.3}$$

Johnsen et al.[91] have observed the time of collapse of a bubble for a pressure ratio of 714. It was observed that shock collapse times are one unit time greater than the Rayleigh collapse time[89, 91]. Rayleigh collapse times[90] for three different speeds (500m/s, 1000m/s and 1500 m/s) were compared with void collapse times from current simulations. Figure 7-11 shows that the void collapse times are one time unit higher than the Rayleigh collapse time which is in good agreement with [89] and [91]. This can be because of the plasticity effects and due to the inclusion of shock passage times in void collapse times. It is also shown in Figure 7-11 that void collapse time without shock inclusion time coincides with Rayleigh line.

7.7 Multiple voids

7.7.1 Inline Voids

The conventional notion of void-void interactions in a shocked heterogeneous material is that in a field of voids, the collapse of one void will led to strong pressure waves and temperature pulses which will lead to more intense collapse of the surrounding voids. Thus, voids are pictured to obtain a better understanding of what happens when shocks interact with multiple voids, first the behavior of two inline tandem voids in a two-dimensional setting is examined. As it was shown in the above cases, a secondary shock wave emanates from the point of collapse and can affect the load imposed on the voids downstream. To study the effect of mutual separation and position of two voids in an otherwise homogeneous material, the gap (G) between voids was varied from0.5 D to 2D, where D is the diameter of a void.

For G= 0.5D, the first (i.e. upstream) void behaved in a similar manner as a single void, but the results for the second void were counterintuitive as there was no further increase in maximum temperature following its collapse(Figure 7-12 and Figure 7-14). Moreover, the downstream void collapsed with much lower temperature compared to upstream void as shown in Figure 7-14. This can be due to shielding of the downstream void. As seen from Figure 7-13, the velocity immediately above the upstream void is close to zero even at the later stages of its collapse. This results in complete shielding of downstream void from incoming shock wave. The downstream void is not exposed to any flow until the upstream void has collapsed. A reduced interaction of downstream void with the incident shock wave results in a much lower collapse temperature. This is the ―shielding” effect that is also observed in the experiments of Swantek et al.

The other interesting result from the computations is the difference in the interface evolution for tandem voids. The interface evolution of the upstream void is similar to the case shown in section 7.6.2 for a single void, with the void being compressed uniformly under the influence of shock loading. On the other hand, the second void collapses in a pinching fashion as shown in Figure 7-16. The velocity field in Figure 7-17 clearly shows that the upstream void is under a uniform shock compression compared to the downstream void, which momentarily interacts with a high speed jet formed during the collapse of upstream void. The complex velocity field generated due to collapse of the upstream void interacts in an entirely different manner as it has a high speed jet impinging onto the downstream void.

The rise in temperature due to hydrodynamic impact of the second void was lower than that of the first void for small gaps between the voids, but reached the same value as for a single void as the inter-void gap was increased as shown in Figure 7-14. The variation of energy distribution for inline voids is shown in Figure 7-15. It can be seen that the void arrangement with G=0.5D did not have sharp rise in total internal energy during the collapse of downstream void. This is due to the lower value of temperature during the collapse of downstream void. Swantek et al.[89] also studied inline tandem voids with G=D. The key experimental observation in their case was also related to shielding of the downstream void due to the presence of the upstream one. From the present computations, it is observed that the velocity value is higher in the inter-void region (Figure 7-17) compared to free stream velocity. A comparison of velocity contours at selected cross-sections: one diameter above the centerline, at the centerline and one diameter below the centerline are shown in Figure 7-18. It can be seen in Figure 7-18 that the velocity field at the center line is a maximum in the inter-void region which is in good agreement with experiment[89].

7.7.2 Offset Voids

As discussed above the main goal of this study is to understand the behavior of shock loading of a HMX material with randomly placed many voids. While the above section dealt with inline voids, the offset setting can be one of the arrangements among any two voids in a random arrangement. The inline voids separated with G=0.5D discussed above were offset with a distance (G_o) varying from D to 2.5D. Here G_o is the horizontal (offset) distance between the centers of two voids. When the voids are in an offset condition as opposed to inline, since the downstream void is not in the direct path of the hydrodynamic jet emanating from the first void, the temperature rise due to collapse of second void is higher than any of the inline cases shown above. The setup and profile of maximum temperature for these cases is shown in Figure 7-19. The variation of energy distribution in domain with time is shown in Figure 7-22.

It is observed that initially, as G_o is increased the downstream void collapsed with a higher temperature. But for G_o>1.375D the value of maximum temperature started to fall as shown in Figure 7-20 and Figure 7-21. As the gap is increased further, the downstream void has no influence of upstream void and behaves as a single void. This happens for G_o=2.5D. The enormous rise in temperature of downstream void in the case of 2D>G_o>1.125D is due to both uniform compression and due to the effect of a secondary shock wave initiated due to the collapse of the upstream void. In the offset setting, the downstream void is not shielded by the upstream void and is compressed uniformly by the planar shock wave from one side, as shown in Figure 7-23. While that process is going on, the high speed secondary shock wave due to collapse of the upstream void compresses the downstream void in the direction of the offset as shown by velocity vector field in Figure 7-24. This can also be seen from the evolution of the void interfaces (Figure 7-25).The two processes are the key reason for the enormous rise in temperature for the offset arrangement.

7.7.3 Voids at 10% Volume Fraction of HMX

As was shown in the previous cases, the interaction between two voids in an otherwise homogeneous matrix can lead to a range of responses of a given void depending on its position relative to other voids. Inline voids can lead to shielding effects while offset voids can lead to enhancement of the collapse phenomenon due to the combination of the incident shock and shocks reflected from other voids. In this section, we examine the effect of collections of voids accounting for a range of void volume fraction (10%-25%) distributed randomly in a homogeneous HMX material. The initial loading velocity of 500 m/s is used for all the cases. The first simulation is done to incorporate voids randomly at 10% void volume fraction. The domain size is 100 μm X 100 μm with a uniform grid size of 0.1 μm. This level of resolution corresponds to approximately 100 mesh points along the void diameter. The parallel version of code was used to reduce the computational time, details of which are given in CHAPTER 4. A total of 24 processors were used to decompose the computational domain. The initial domain decomposition with embedded voids represented as levelsets is shown in Figure 7-26. Figure 7-27 shows the initial configuration of voids with the voids being numbered from 1-10, in order to track the temperature of each void individually during collapse The maximum temperature peaks corresponding to numbered voids and variation of energy distribution are shown in Figure 7-27and Figure 7-28 respectively.

The results shown in the above sections for inline and offset arrangements of two voids are useful in understanding the behavior of the voids in the random arrangement by observing the relative position of voids and the corresponding peaks in maximum temperature during their collapse, as shown in Figure 7-27. The void 1 and void 2 collapse just as in a single void case; void 3 collapses with a temperature slightly lower than single void case. The offset effect observed in the previous section can be seen in the collapse of void 4 and void 5, which collapse with a significantly higher temperature. The void 6 which is shielded by void 4 collapses with a lower temperature demonstrating the shielding effect. The offset effect can be seen again in the collapse of void 7 and void 10. The void 8 which has G~2D from void 5 collapses with the same temperature as void 5. The same scenario is observed for void 9 which has G~2D from void 7.

For the above case, from Figure 7-28, the ratio of the internal energy to the kinetic energy can be seen to decrease before the collapse of void 1 and void 2 due to increase in velocity of material at the lower surface of voids. But the internal energy increases after the collapse of void 1 and void 2 due to hydrodynamic impact which raises the temperature and pressure. As the void collapse is a local phenomenon, the global energy distribution does not give a clear picture of the response of the material with increase in number of voids. As observed for all the voids, the slope of the curve decreases with increase in the kinetic energy before the collapse of void but again switches sign due to the combined effect of plastic work and hydrodynamic impact; however these changes are attenuated after the collapse of the first few voids due to the complex interaction of shock fronts and the energy being released by the various voids nearly simultaneously. It can also be seen that the after the collapse of last void (void 10), the ratio of the internal energy to kinetic energy is close to 1. This indicates that the material is behaving as a nearly homogeneous (but porous) material. This nearly homogeneous behavior however masks the highly localized excursions of the temperature in the material, specifically at the void collapse sites. In terms of the run-up to detonation therefore the homogenized thermal energy picture does not capture the local hot spot formation; these hot spots can initiate chemical reactions locally and the accumulated effects of these reaction fronts can lead to the formation of a detonation front leading to initiation.

The temperature field corresponding to two different times (18 ns and 32 ns) is shown in Figure 7-29. The temperature field clearly shows the local hot spots where the temperature is much higher compared to bulk temperature of the material.

7.7.4 Voids at 15%-25% Volume Fraction of HMX

For higher volume fraction, the observable maximum temperature is observed to be highly dependent on the relative position of two voids in the matrix and not on the overall volume fraction; all the cases had at least one void which collapsed within the range of 1600 to 1800 K (Figure 7-31, Figure 7-33 and Figure 7-35). The comparison of maximum temperature achieved in given sample of HMX with variation of void volume fraction is also shown in Figure 7-36 . This clearly depicts that the maximum temperature achieved in a given HMX sample is independent of void volume fraction and is more dependent on different inline and offset configurations of voids locally.

However, the cases with higher volume fraction had many voids collapsing with temperatures less than 1000 K. This is due to increased shielding effect with increase in void volume fraction. The energy distribution as measured by the ratio of total internal energy to total kinetic energy gets close to one with increase in number of voids as shown in Figure 7-31, Figure 7-33 and Figure 7-35 .A comparison of energy distribution for different volume fractions is also shown in Figure 7-37(a) indicating the material behavior as homogeneous till the collapse of last void. As can be seen in Figure 7-30, Figure 7-32 and Figure 7-34 void collapse is a local phenomenon with higher temperatures being observed only in the vicinity of voids. The temperature rise in the region away from voids is similar to the temperature rise from shock heating of a homogeneous material.

To explain the overall study, two plots showing the variation of total internal energy and total kinetic energy with void fraction are shown in Figure 7-38 and Figure 7-39 respectively. It can be seen from Figure 7-38(a) that increase in porosity results in weakening in strength of shock as the shock wave passage times for a given sample increases. Figure 7-38(b) shows that for a given shock strength, the increase in porosity is making material more energetic with increase in thermal energy. The distribution of kinetic energy is shown in Figure 7-39(a) and Figure 7-39(b). The increase in total kinetic energy is also similar to increase in total internal energy till the collapse of last void. However the kinetic energy decreases sharply after the collapse of last void.

Conclusions and Future Work.

This chapter applied the techniques developed in the thesis to a challenging problem in multimaterial dynamics, viz. the response of a porous material to shock insult. For the first time the dynamics of the void collapse process in the presence of a collection of void is studied computationally, carrying the computations beyond the collapse stage. Several important physical insights were obtained from this study, consistent with recently published experimental observations of the response of 2-dimensional void arrays in a model material.

To gain an understanding of void interactions, two interacting voids were simulated, with the voids placed at various distances apart in an inline and offset fashion. It was found that the secondary shock wave generated from the collapse of an upstream void will not always have important consequence on voids downstream. A counter-intuitive result found in this study is that if the downstream voids are less than a diameter apart and are in line with the upstream void, the hot spot formed when the downstream void collapses will be weaker than that formed upon the collapse of the upstream void. This is due to the shielding effect of the upstream void on the downstream void, i.e. the incident shock wave tends to diffract around the upstream void and therefore the downstream void does not feel the full impact of the incident shock. The effect of lateral offset (with respect to the orientation of the incident shock) in void position is interesting as well. The offset void setting showed that the secondary shock wave can have an intensifying effect leading to an increase in temperature (over that of an isolated void) upon collapse of the void downstream; this is because the downstream void is compressed by the incident shock as it is not shielded by the upstream void and it is also further compressed by the secondary shock wave generated due to collapse of the upstream void. This dual mode compression results in a significant rise of temperature in the case of offset voids compared to the inline tandem voids.

The understanding gained from the simulations of two interacting voids was useful in analyzing a system with many voids. The void behavior in the case of 10%-25% void volume fraction correlated very well with the behavior of the inline tandem voids and offset voids. It was observed that the increase in the void volume fraction had no influence on maximum temperature achieved in the HMX sample. However the increased shielding effect was observed with the increase in void volume fraction. The energy distribution represented by the ratio of total internal energy to total kinetic energy depicted the material to be nearly homogeneous till the collapse of last void. This was due to the localized nature of void collapse phenomenon which was masked in global picture of energy distribution. Overall the findings of this study clearly showed that the void collapse is a local phenomenon and the traditional models based on continuum theories where the microstructural heterogeneities of the material is ignored or homogenized will not give the correct picture. The void-void interactions studied here clearly showed that these local events can have enormous influence on material behavior at macro level. The insights obtained from the present work are significant and novel and advance the understanding of the mechanics of void collapse when there are multiple voids interacting with shock loadings.

Table 7-1. Comparison with experimental and computational results for the final jet velocity and the final jet diameter.

	Jet velocity (m/s)	Jet diameter(cm)
Current Results(Computation)	2600	0.58
Cooper et.al.(Computation)	2640	0.48
Mali et.al.(Experimental)	2700	0.6

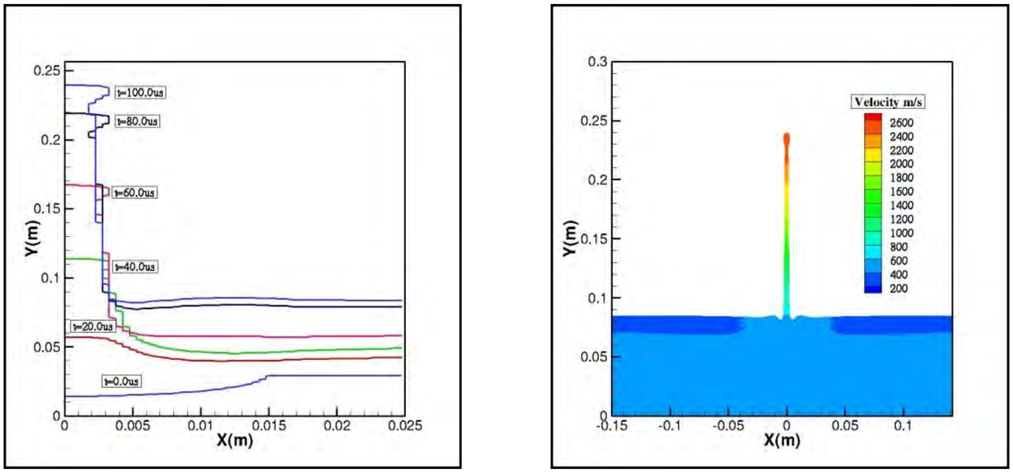

Figure 7-1. Computational results of Mali et al. Experiment a) Time history of jet profile b) Velocity contours of jet.

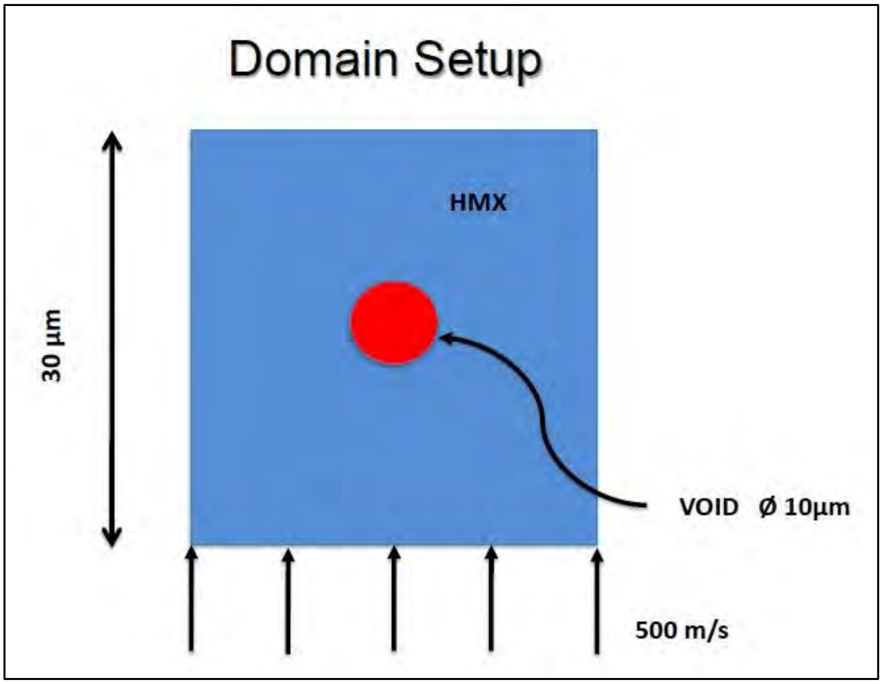

Figure 7-2. Initial Domain setup showing cylindrical void in HMX matrix.

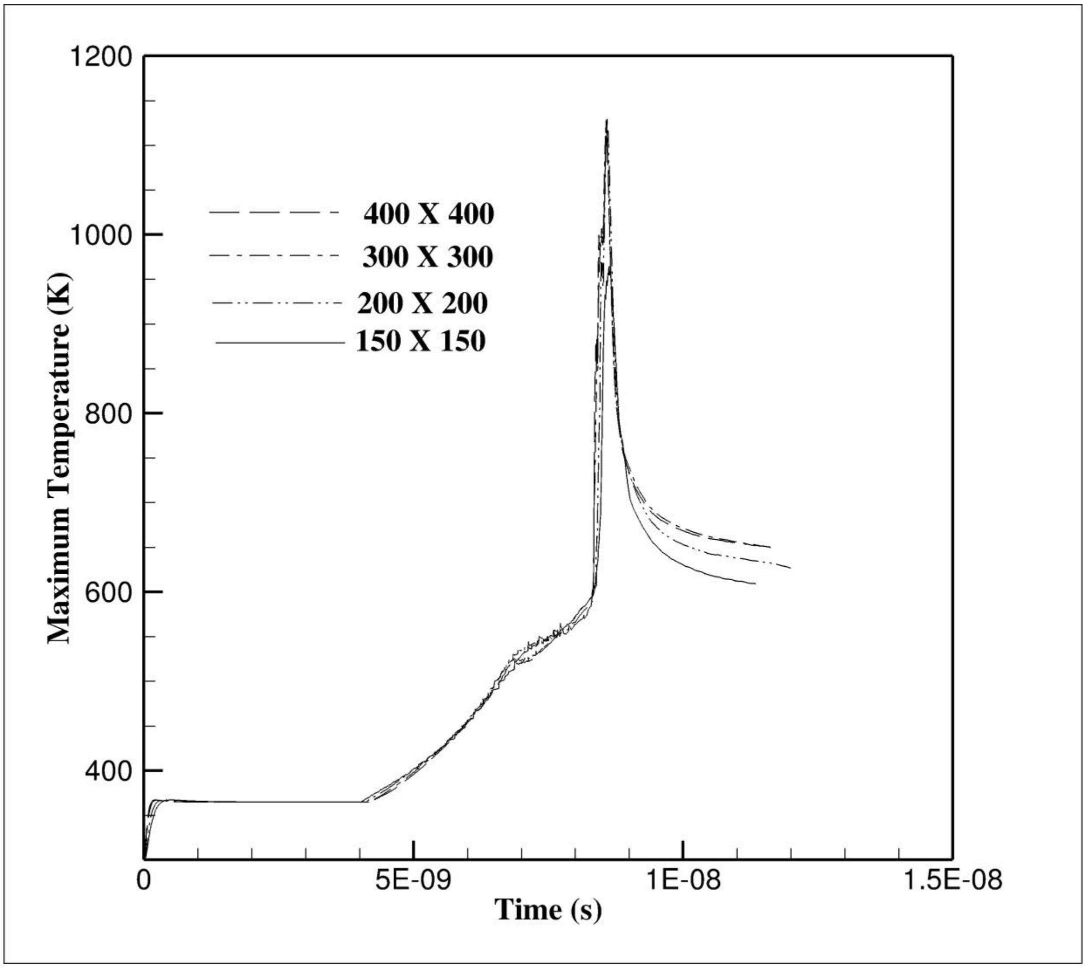

Figure 7-3. Grid-refinement study showing maximum temperature in the domain for collapse of single void with initial loading velocity of 500 m/s.

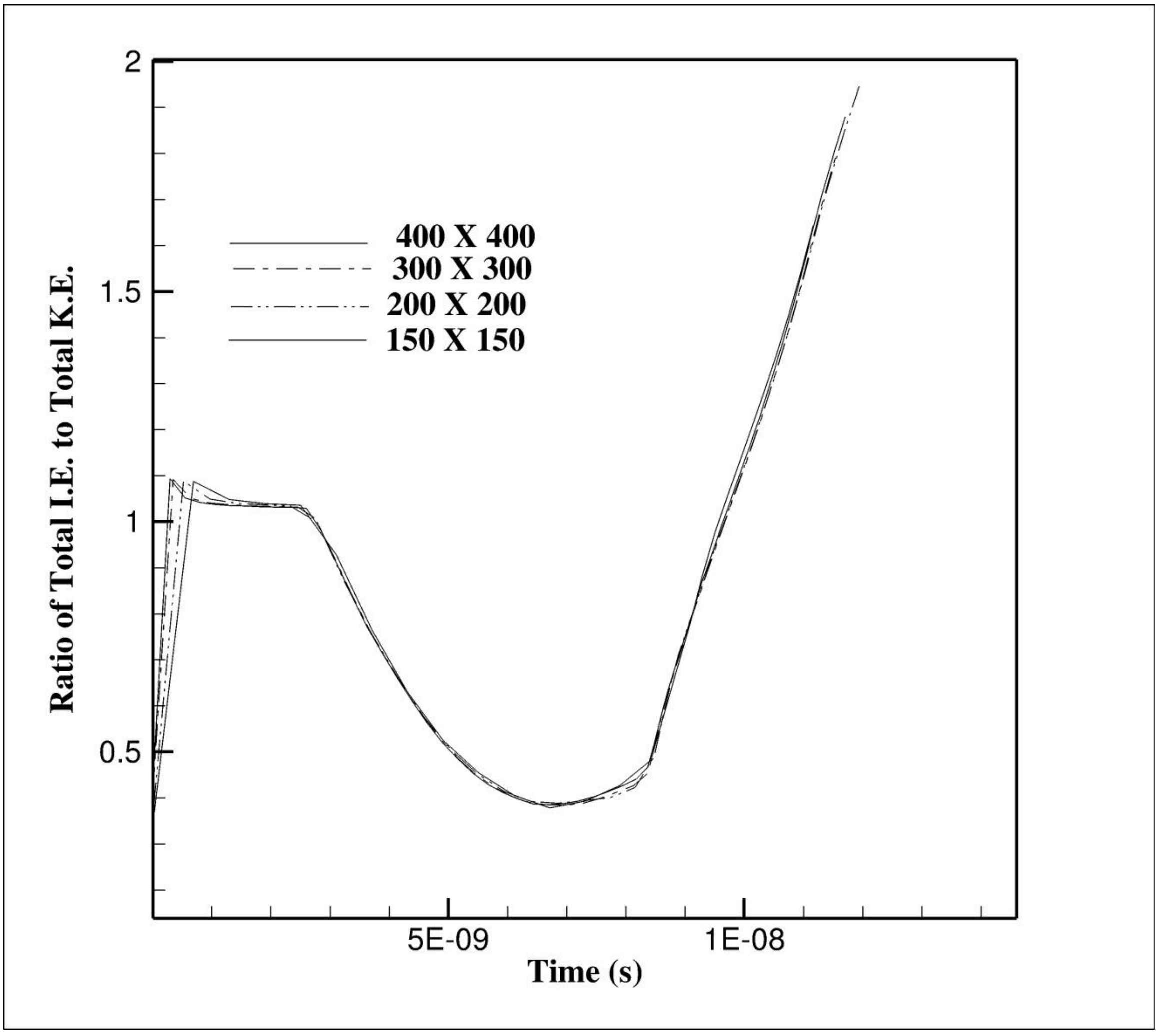

Figure 7-4. Grid-refinement study showing energy distribution in the domain for collapse of single void with initial loading velocity of 500m/s.

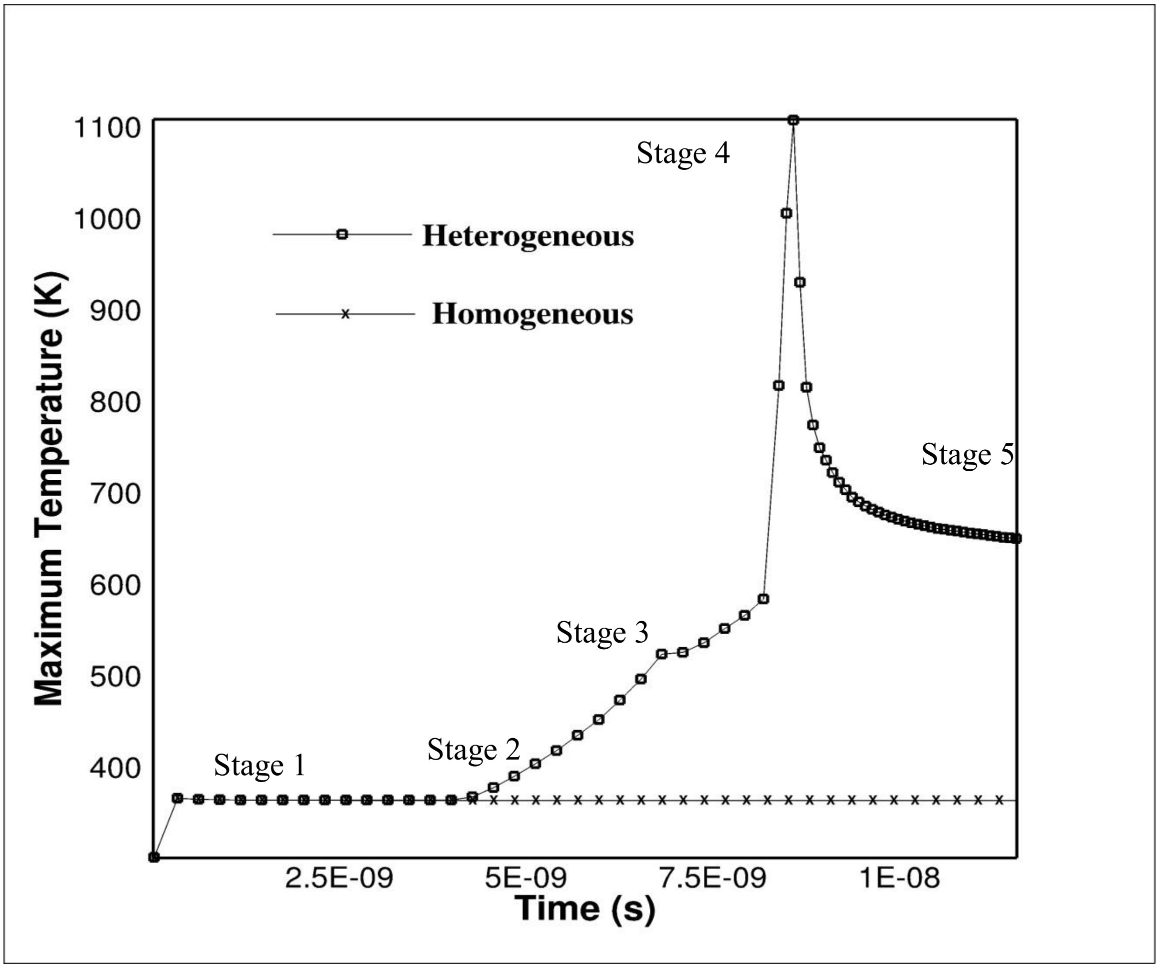

Figure 7-5. Variation of maximum temperature with time for homogeneous and heterogeneous HMX material with initial loading velocity of 500 m/s.

Stage 1 Stage 2

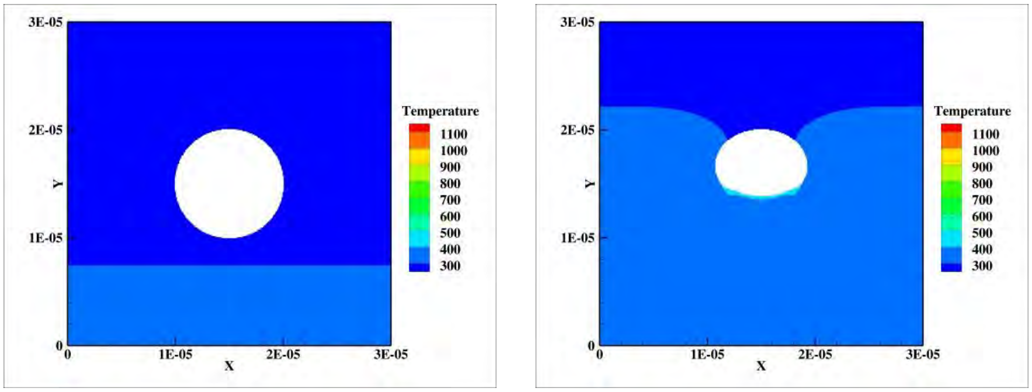

Stage 3 Stage 4

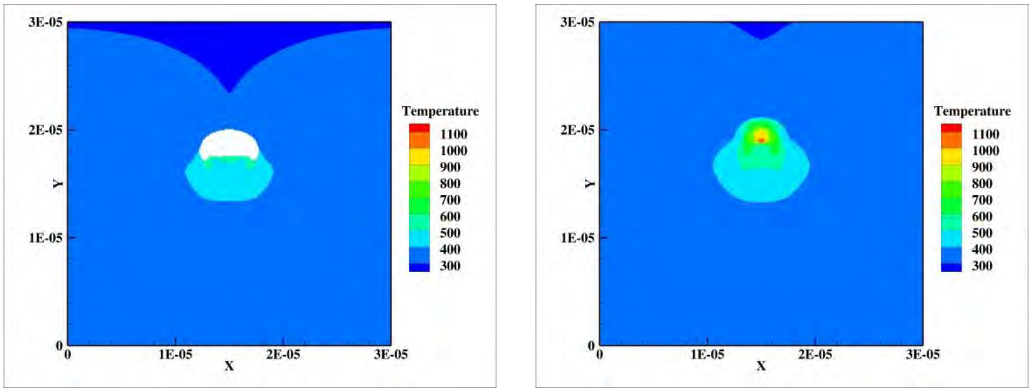

Stage 5

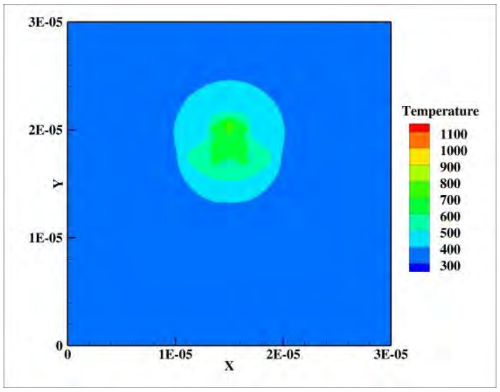

Figure 7-6. Different stages showing the variation of temperature in a heterogeneous HMX material.

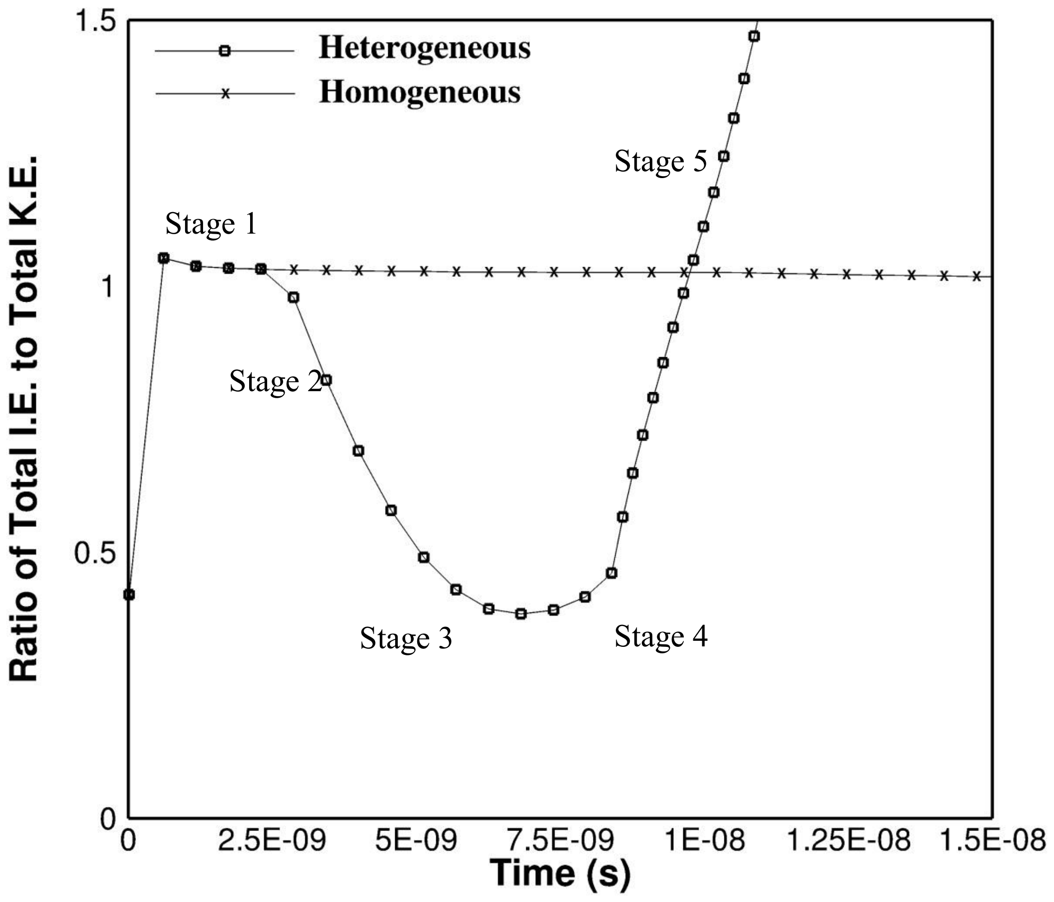

Figure 7-7. Variation in energy distribution with time in homogeneous and heterogeneous HMX material with initial loading velocity of 500 m/s.

Stage 1

Stage 2

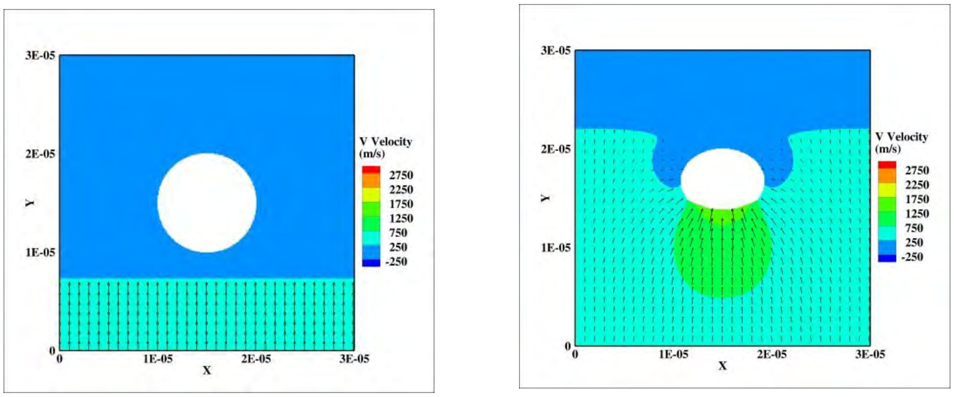

Stage 3

Stage 4

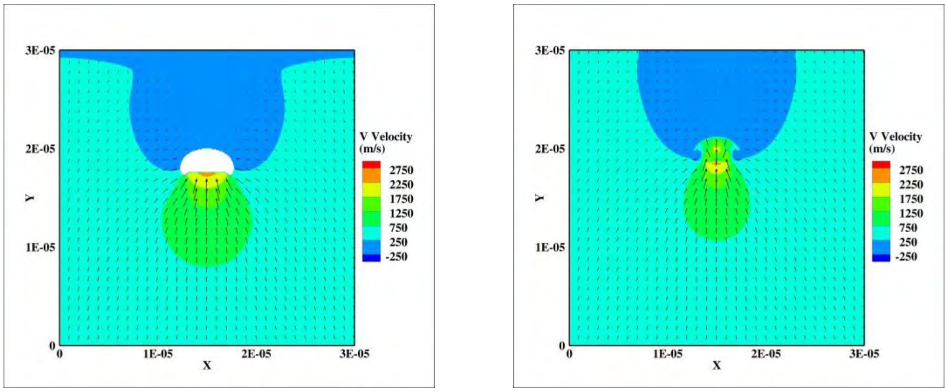

Stage 5

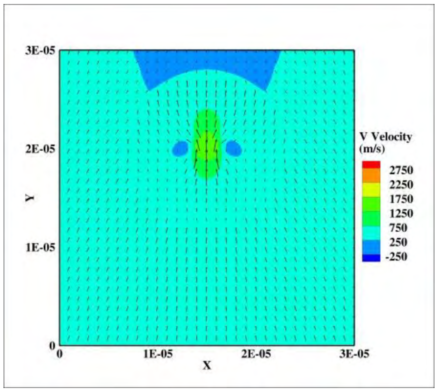

Figure 7-8. Different stages showing variation in velocity for heterogeneous HMX material.

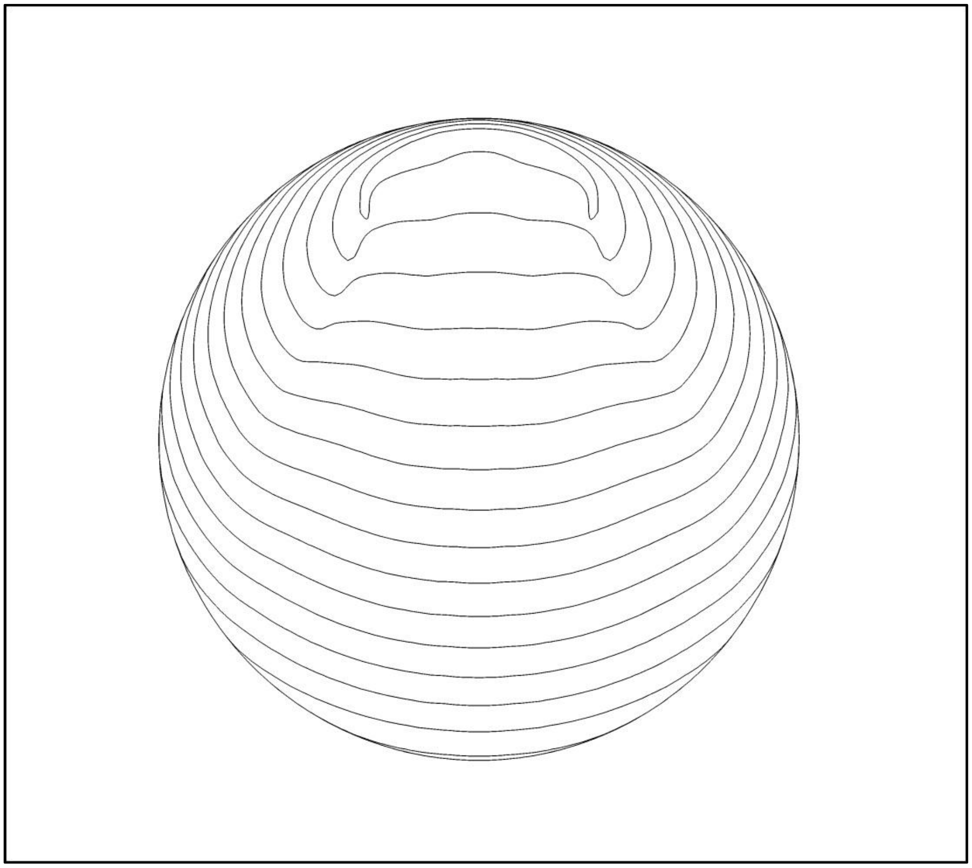

Figure 7-9. Evolution of the interface representing a single void in the HMX material. The shock loading velocity is 500m/s.

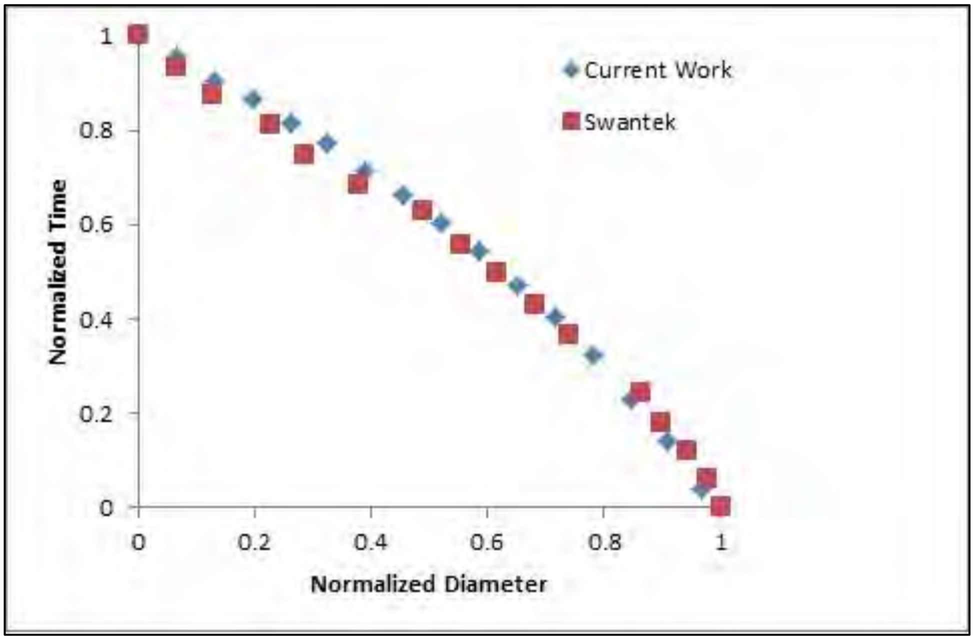

Figure 7-10. Normalized time vs. Normalized diameter for single cylindrical void. The results from current computation are compared with Swantek et al.[89]

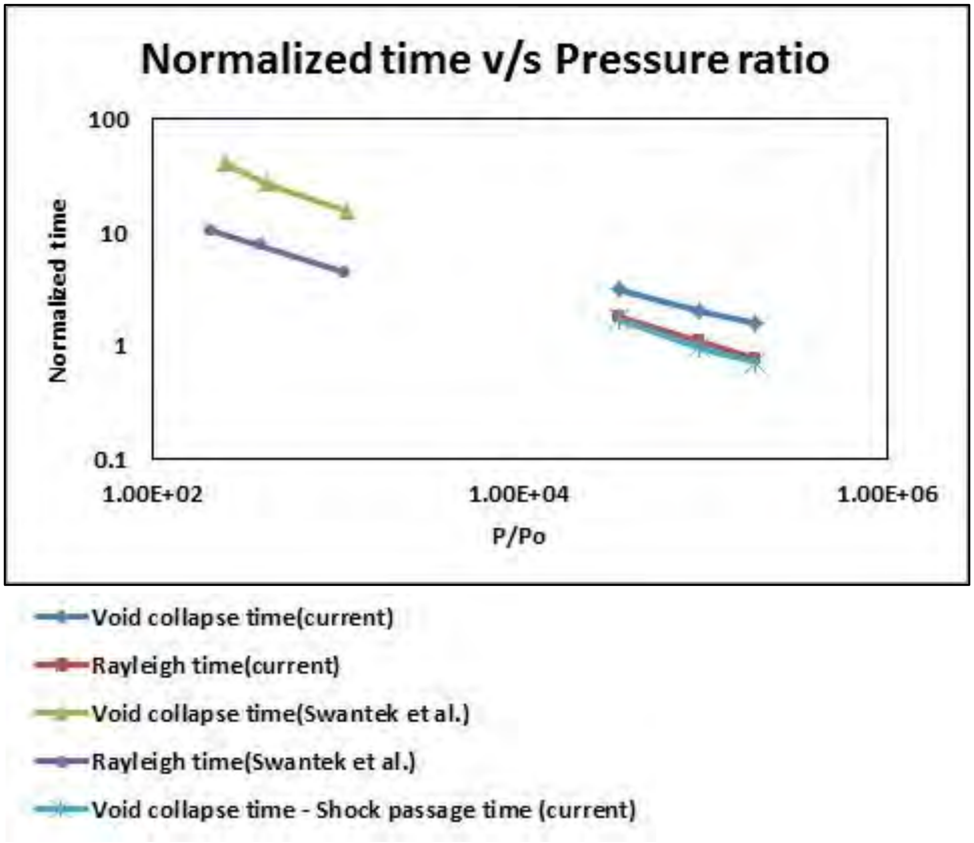

Figure 7-11. Normalized collapse time $\left(\frac{tc_0}{R}\right)$ vs. pressure ratio for cylindrical voids is shown. A comparison with Rayleigh collapse time $\left(t_c = 0.915\left(\frac{\rho}{P_\infty - P_v}\right)^{0.5} R\right)$ is also shown.

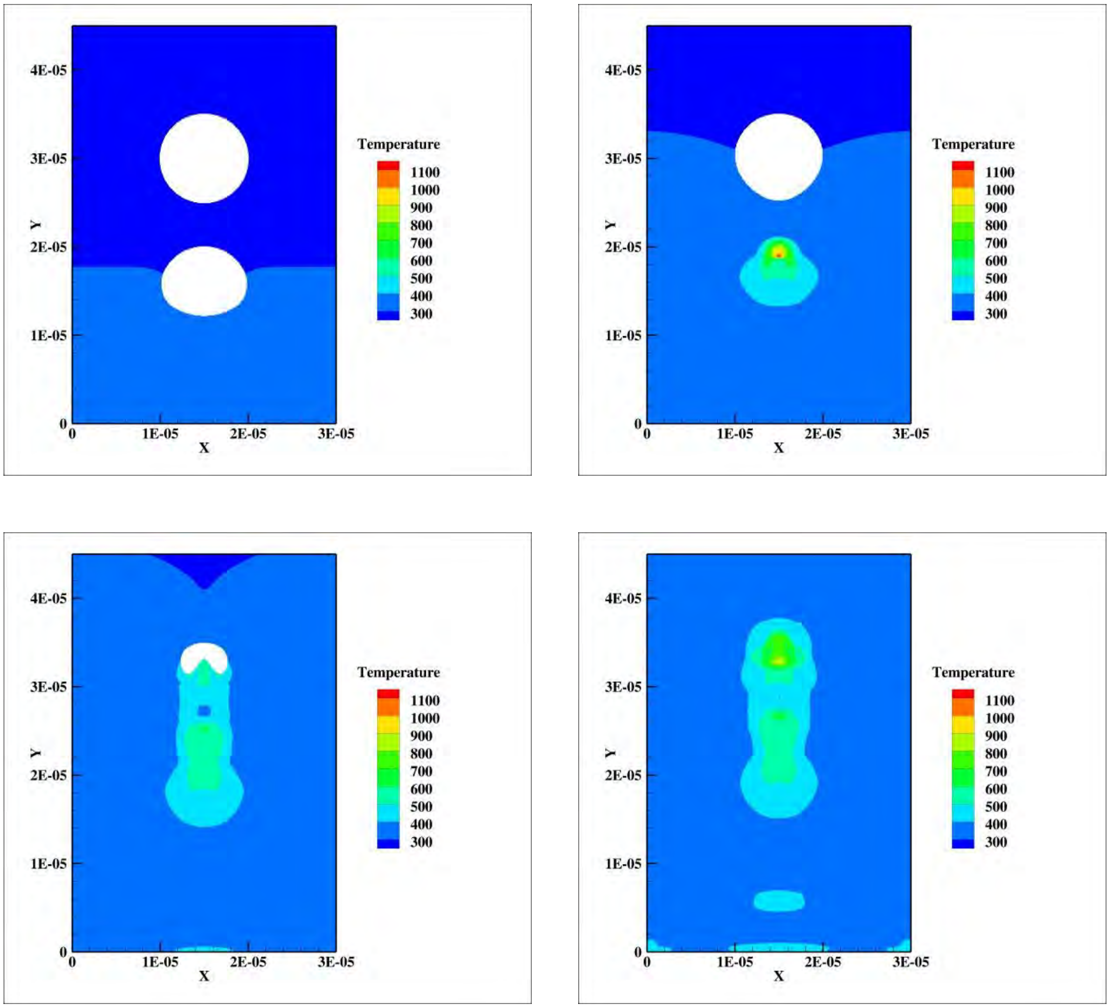

Figure 7-12. Snapshots of temperature field for inline tandem voids with G=0.5D for initial loading velocity of 500 m/s.

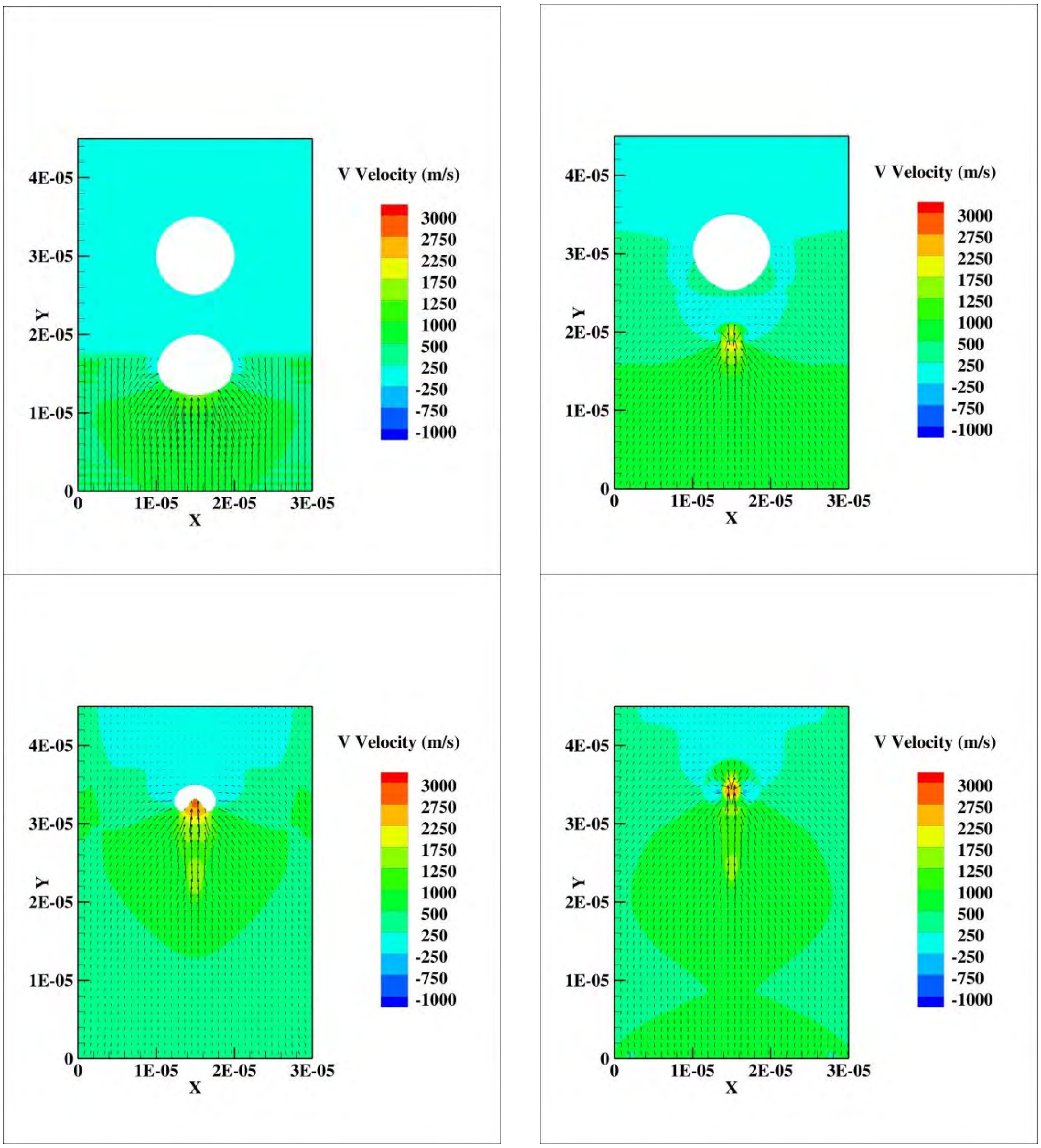

Figure 7-13.Snapshots of velocity vectors for inline tandem voids with G=0.5D for initial loading velocity of 500 m/s.

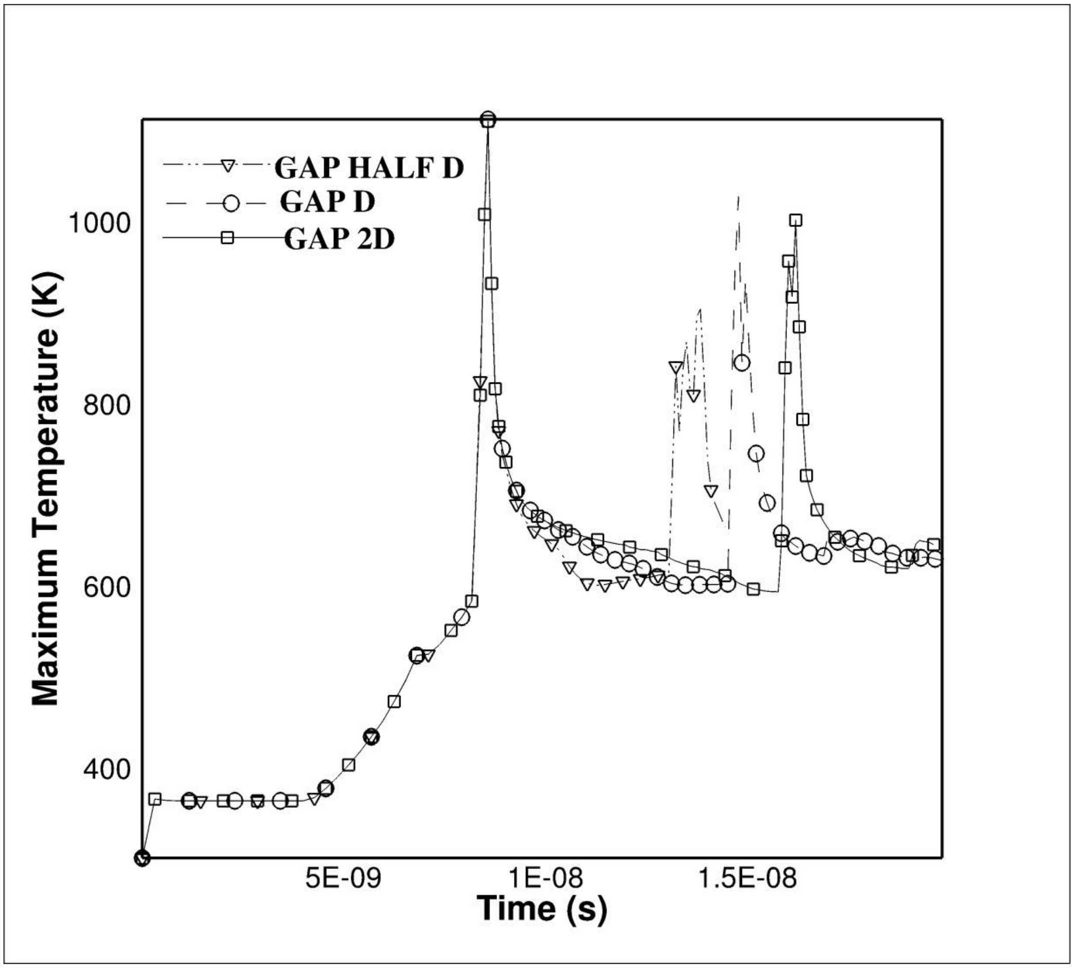

Figure 7-14. Variation in maximum temperature of domain with time for tandem inline voids in cylindrical setting with initial loading velocity of 500 m/s.

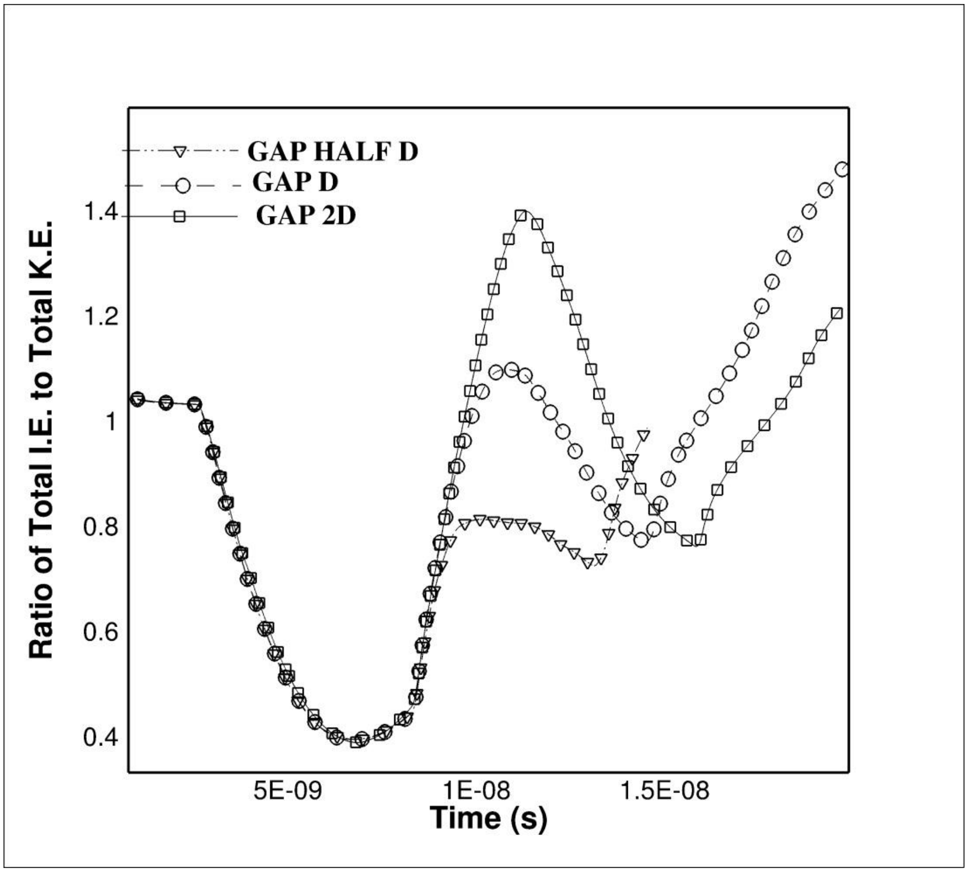

Figure 7-15. Variation in energy distribution of domain with time for tandem inline voids in cylindrical setting with initial loading velocity of 500 m/s.

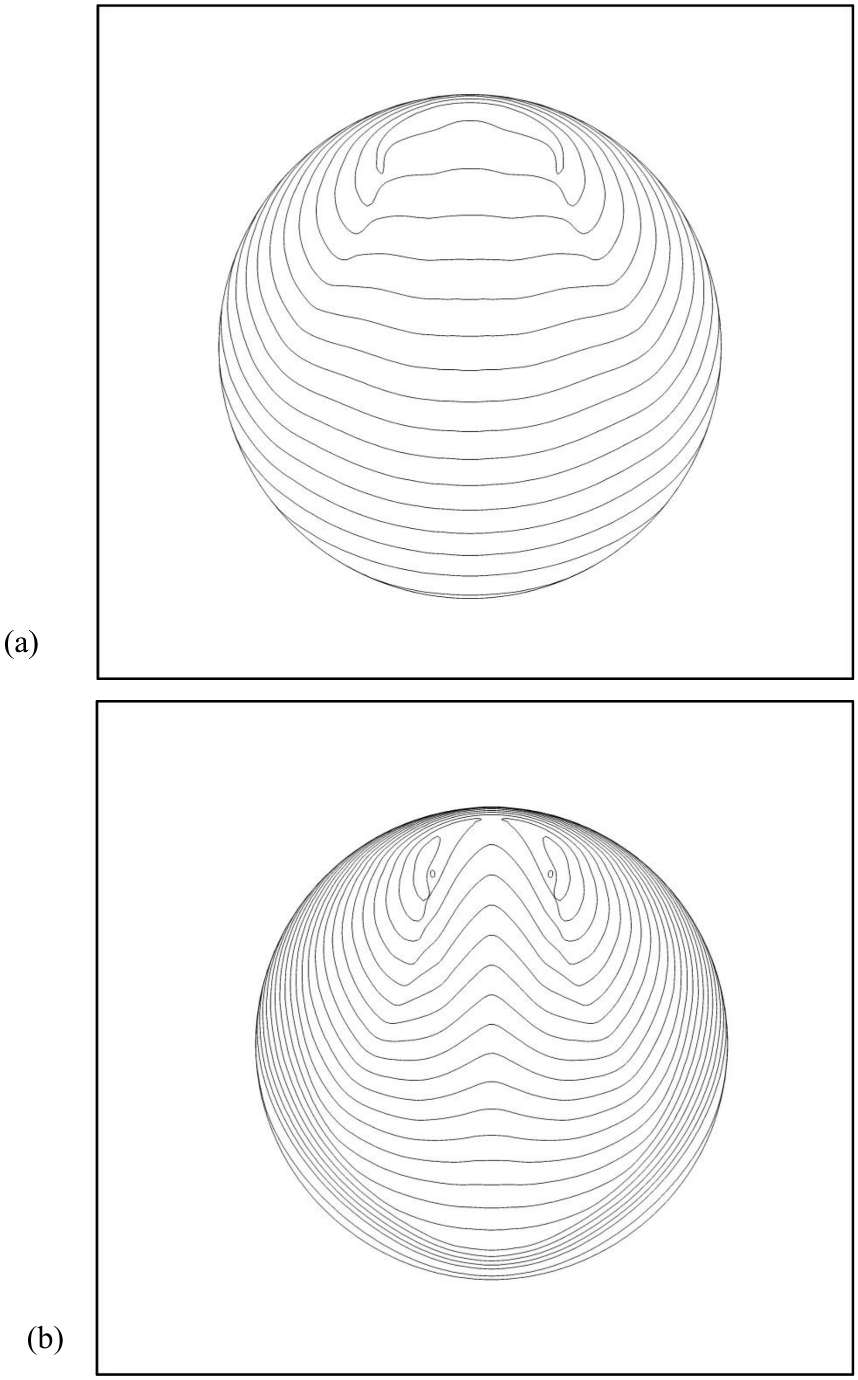

Figure 7-16. Evolution of void collapse in case of inline tandem voids with G=0.5D with initial loading velocity of 500 m/s: a) upstream void b) downstream void

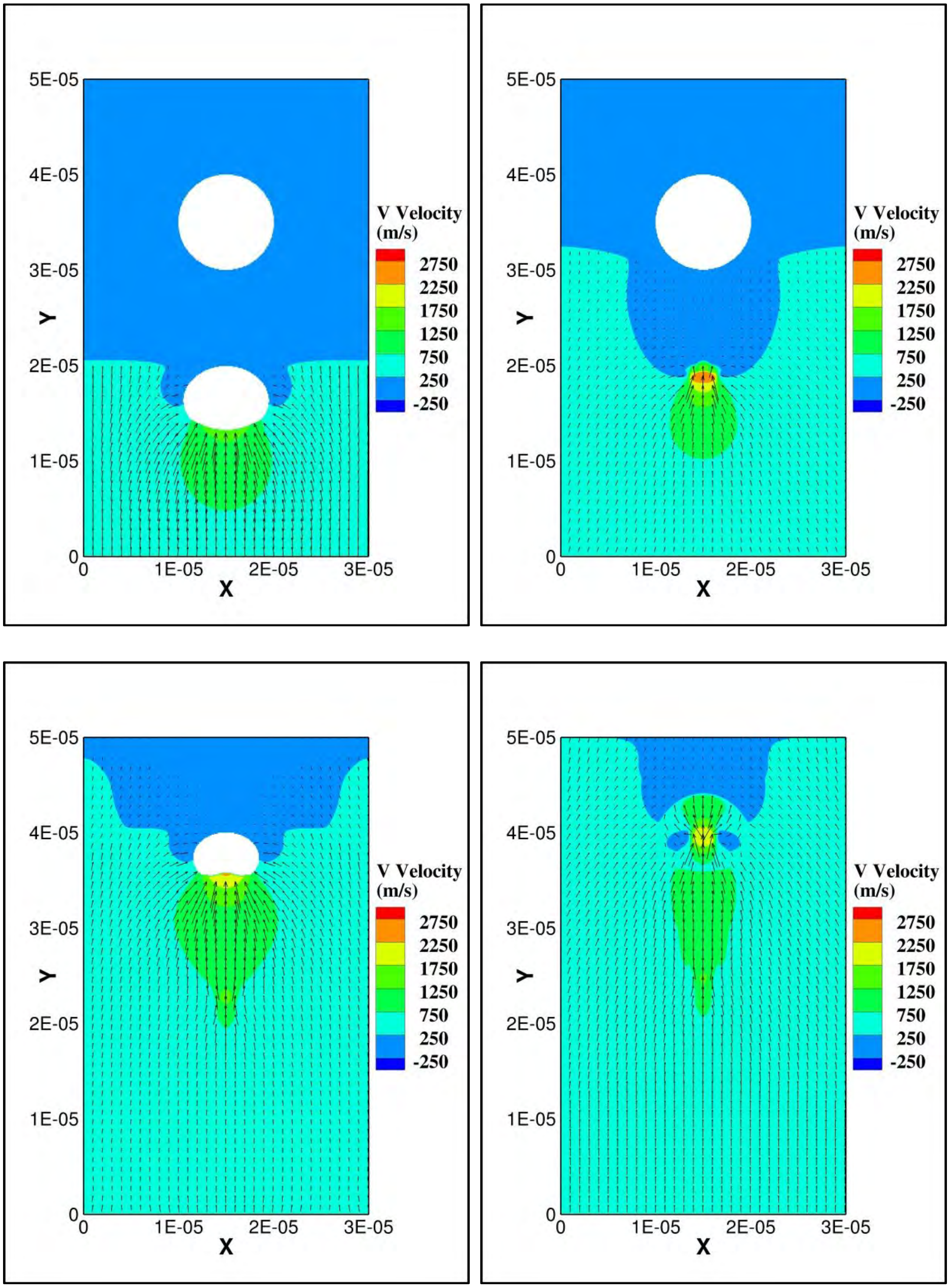

Figure 7-17. Snapshots of velocity vectors for inline tandem voids with G=D for initial loading velocity of 500 m/s.

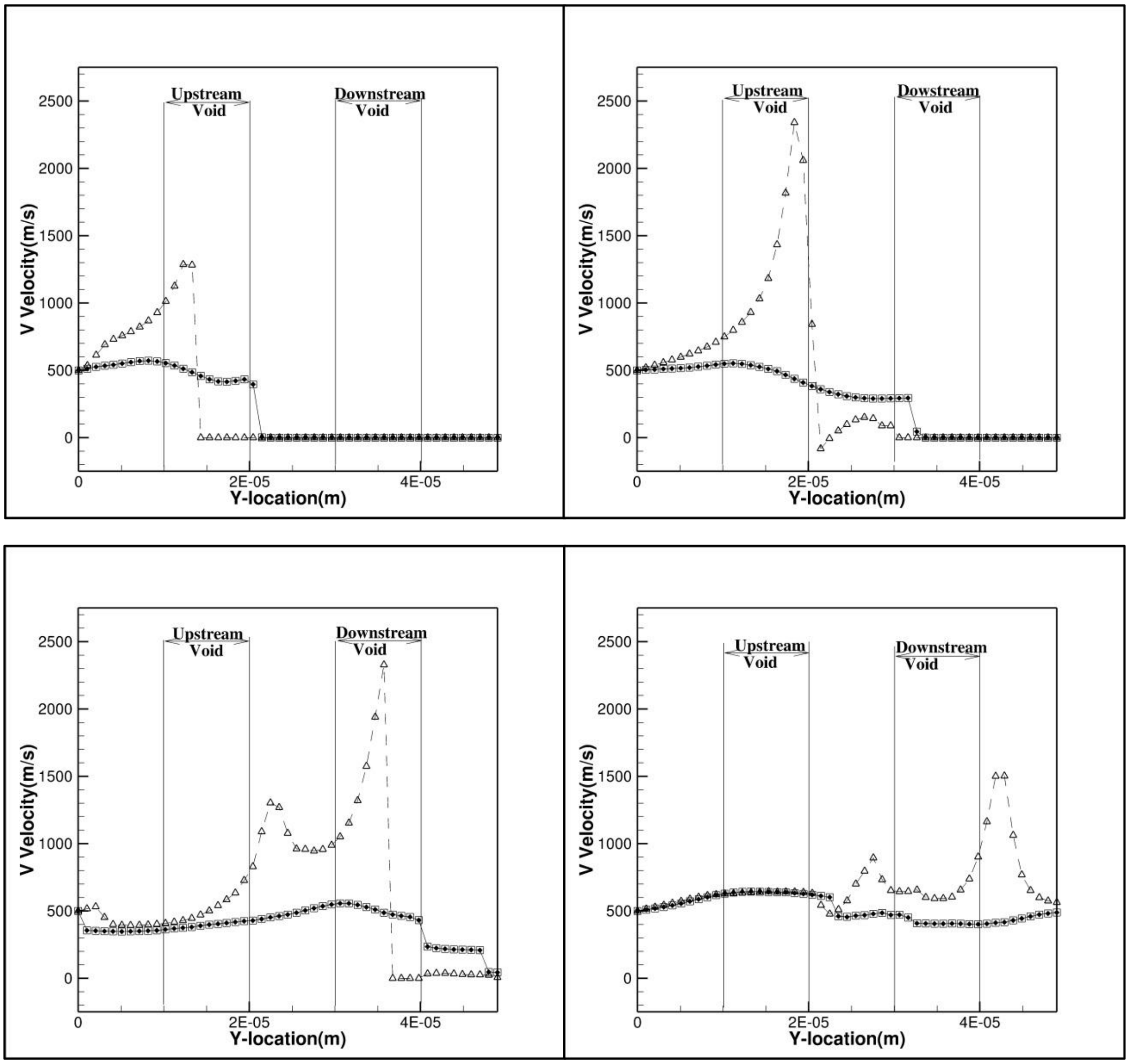

Figure 7-18. Velocity profile for inline tandem voids with G=D. The profiles are obtained at three cross-sections: above the centerline (•), centerline (Δ) and below the centerline (□).

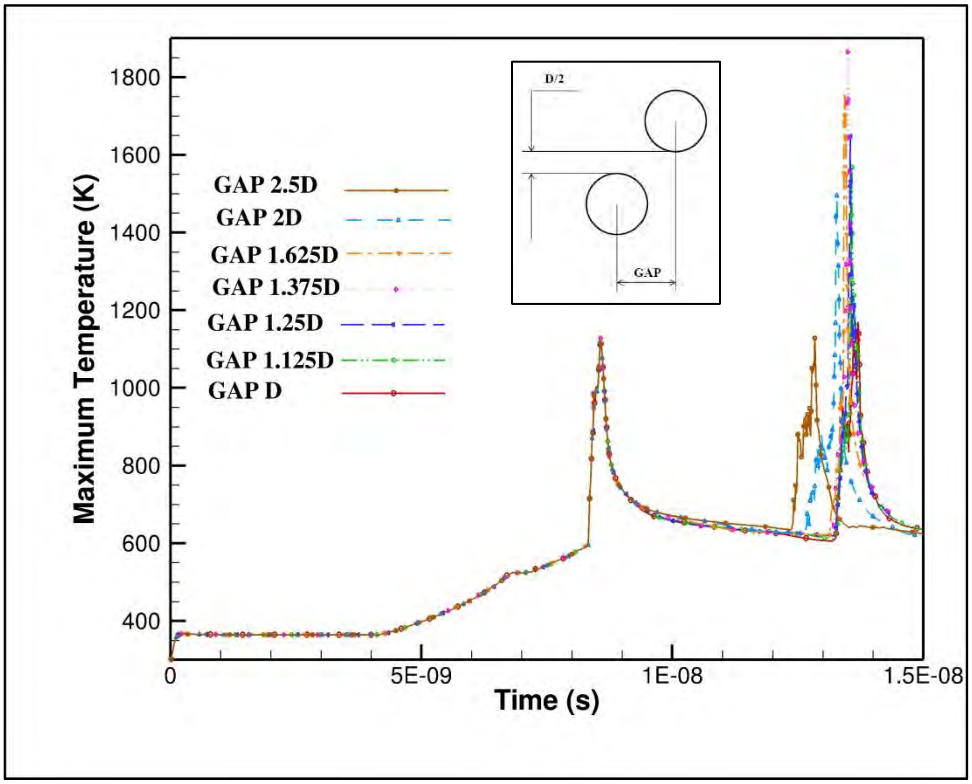

Figure 7-19. Variation in maximum temperature of domain with time for offset arrangement with initial loading velocity of 500 m/s.

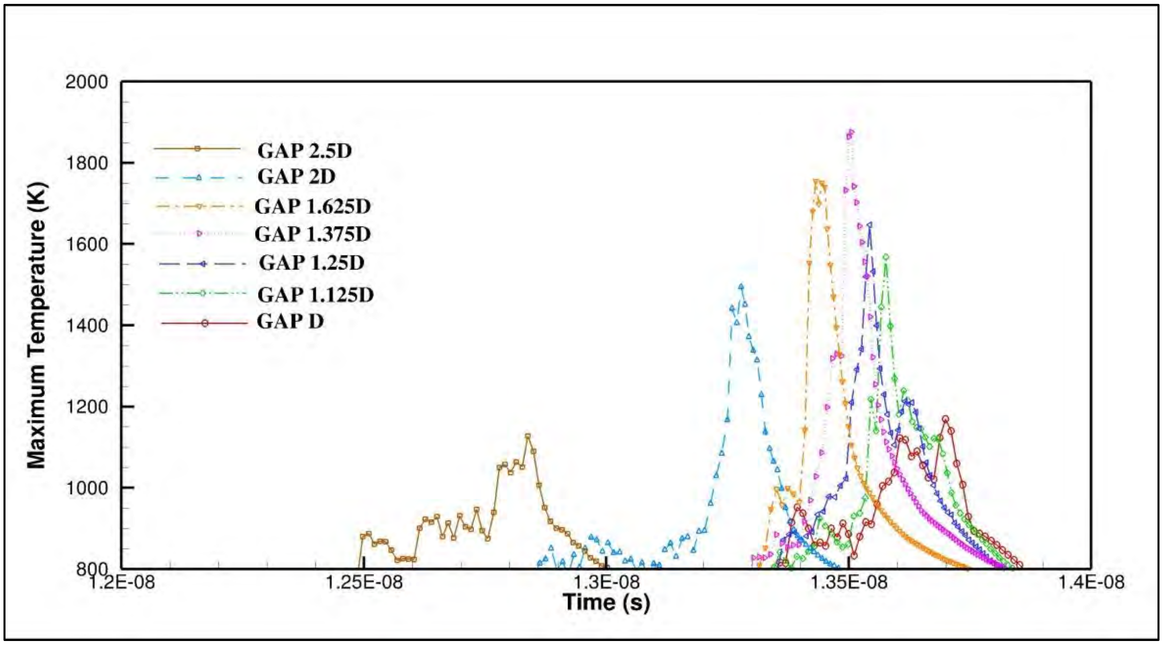

Figure 7-20. Variation in maximum temperature of domain with time for offset arrangement with initial loading velocity of 500 m/s. Plot shows the time during the collapse of downstream void.

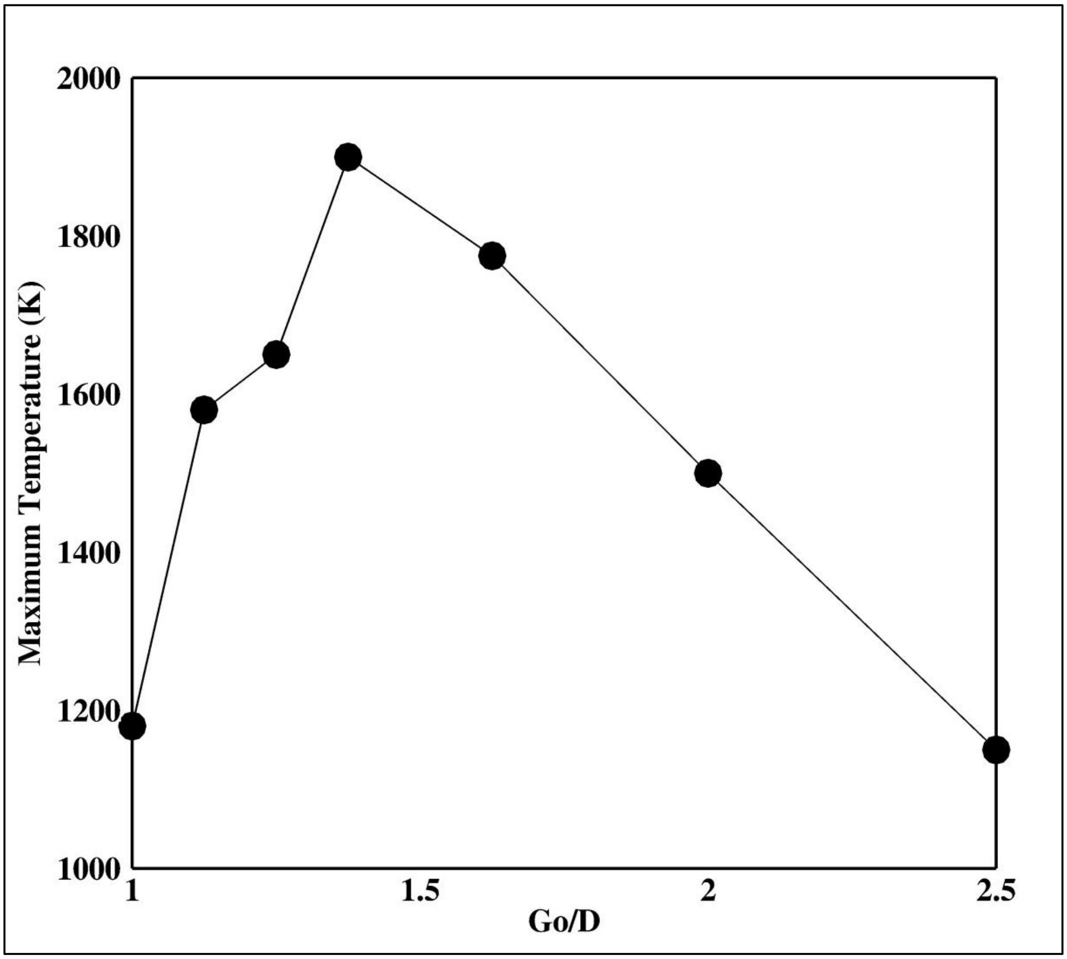

Figure 7-21. Variation in maximum temperature of domain with time for offset setting. Here G_o is the horizontal gap between the centers of the voids. The plot shows the variation of maximum temperature with G_o varying from D to 2.5D.

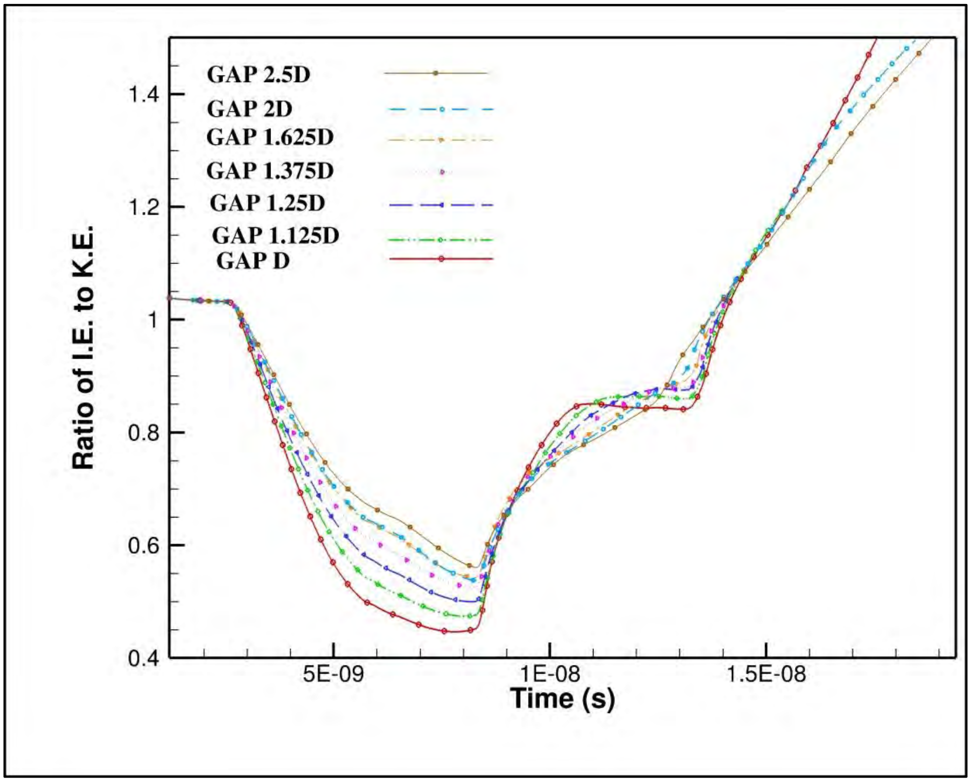

Figure 7-22. Variation in distribution of energy in domain with time for offset arrangement with initial loading velocity of 500 m/s.

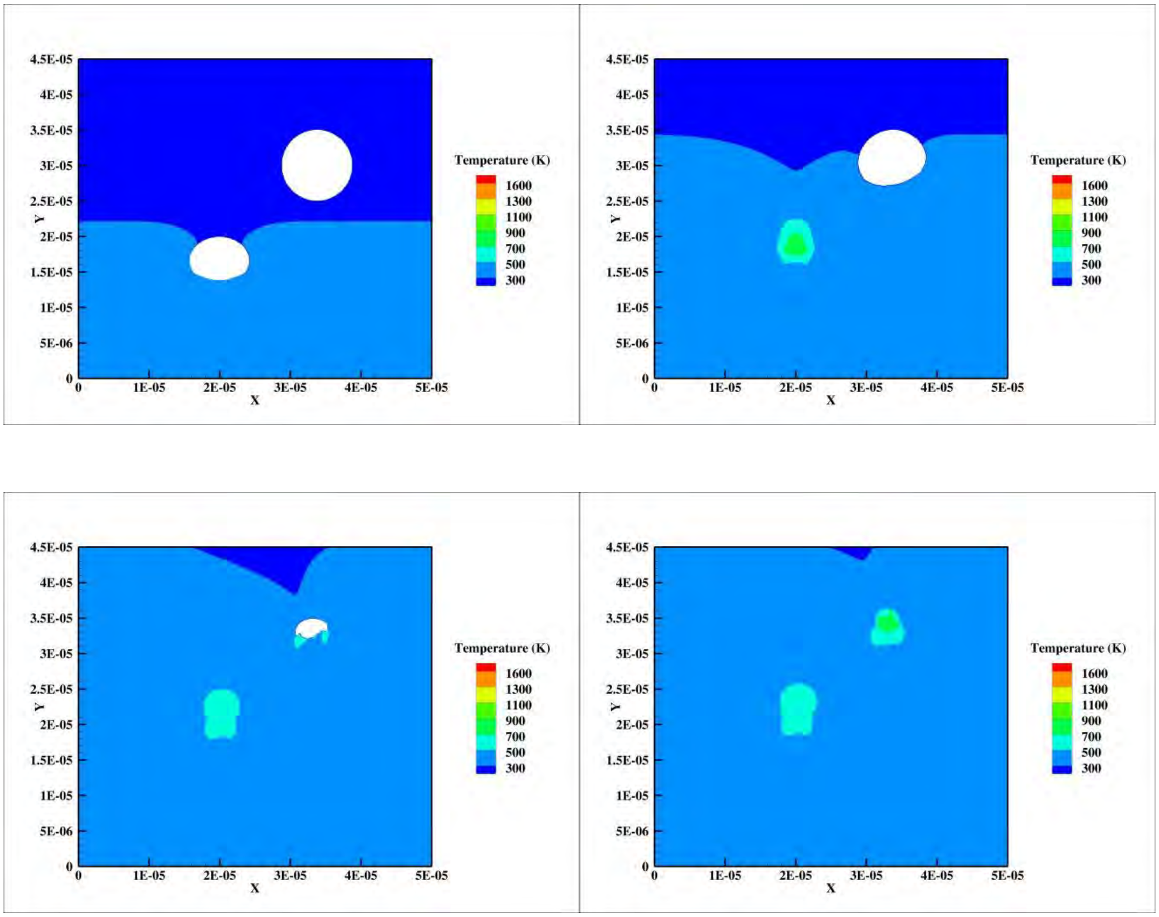

Figure 7-23. Snapshots of temperature field for offset arrangement with G_o=1.375D for initial loading velocity of 500 m/s.

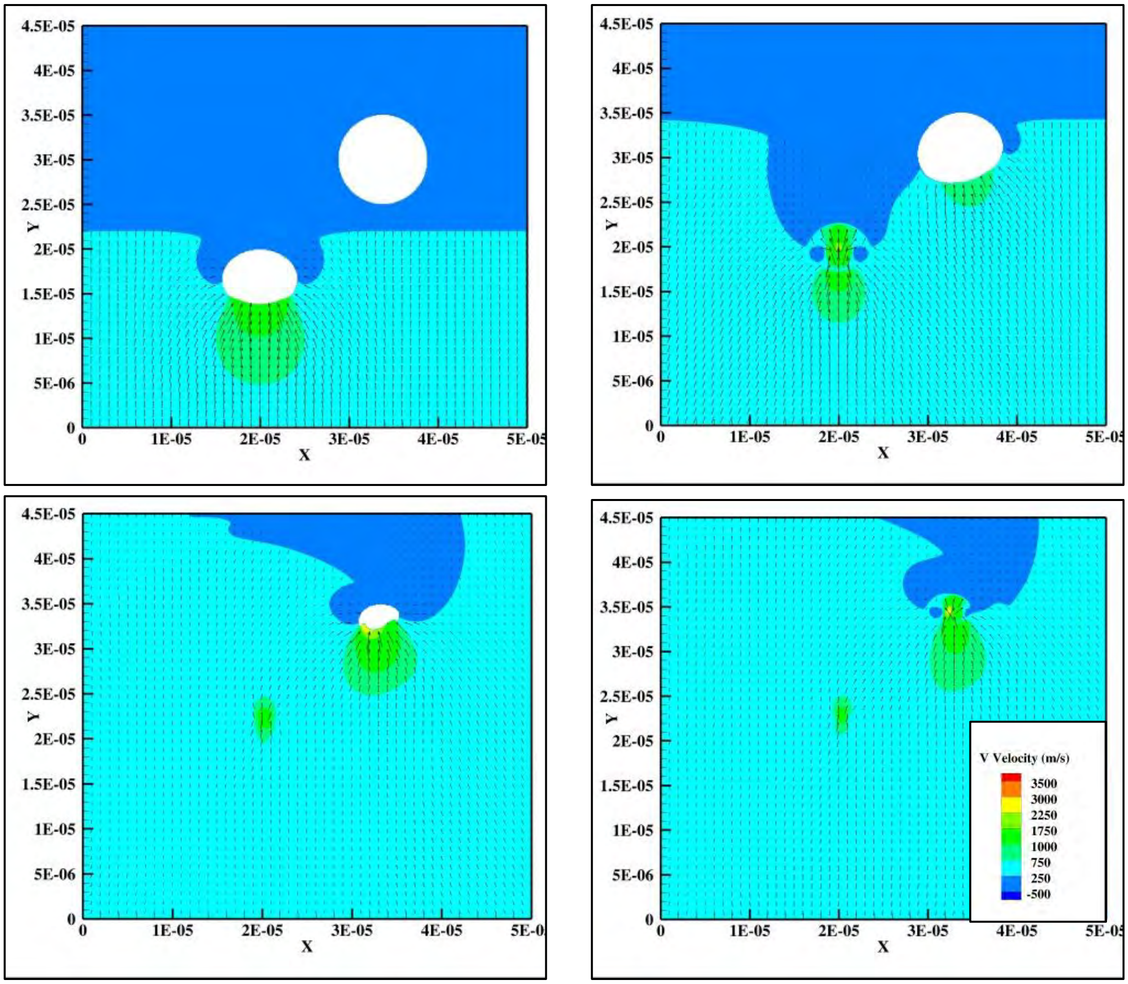

Figure 7-24. Snapshots of velocity vectors for offset arrangement with G_o=1.375D for initial loading velocity of 500 m/s.

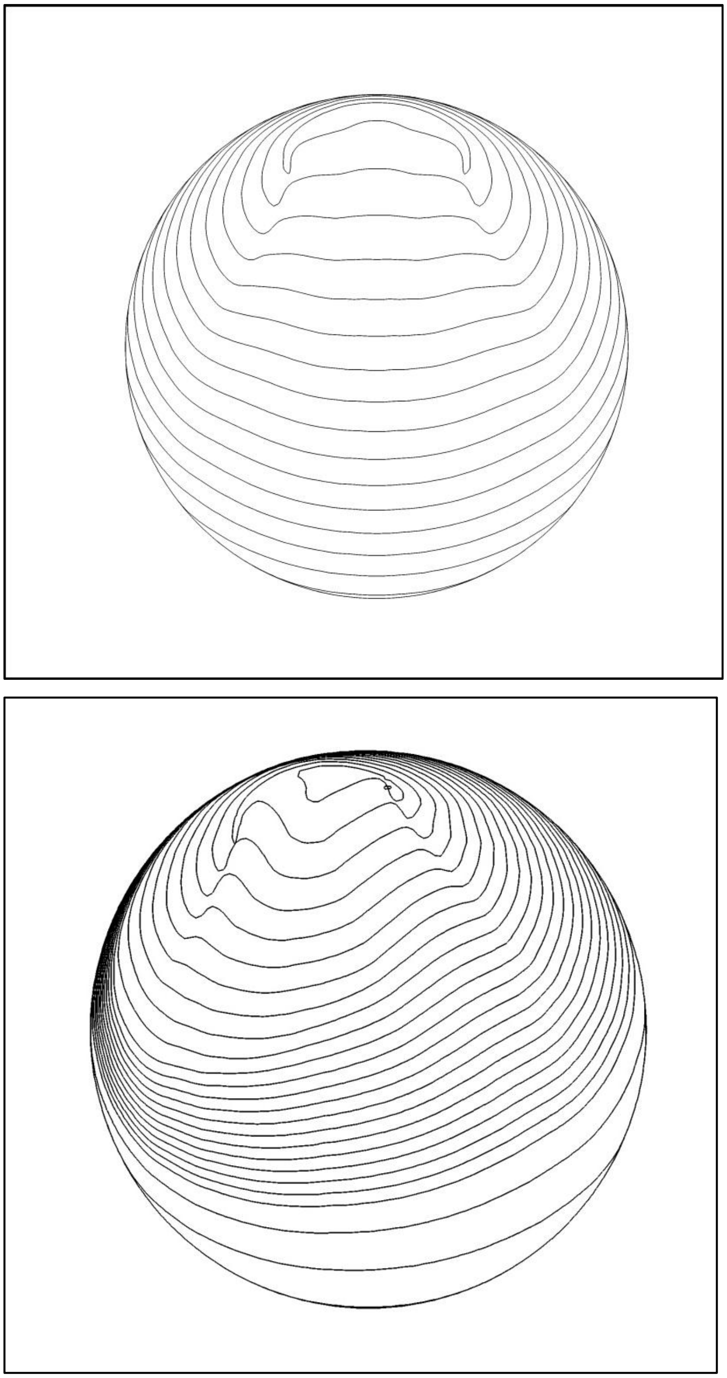

Figure 7-25. Evolution of void collapse in case for offset arrangement with G_o=1.375D for initial loading of 500 m/s: a) upstream void b) downstream void.

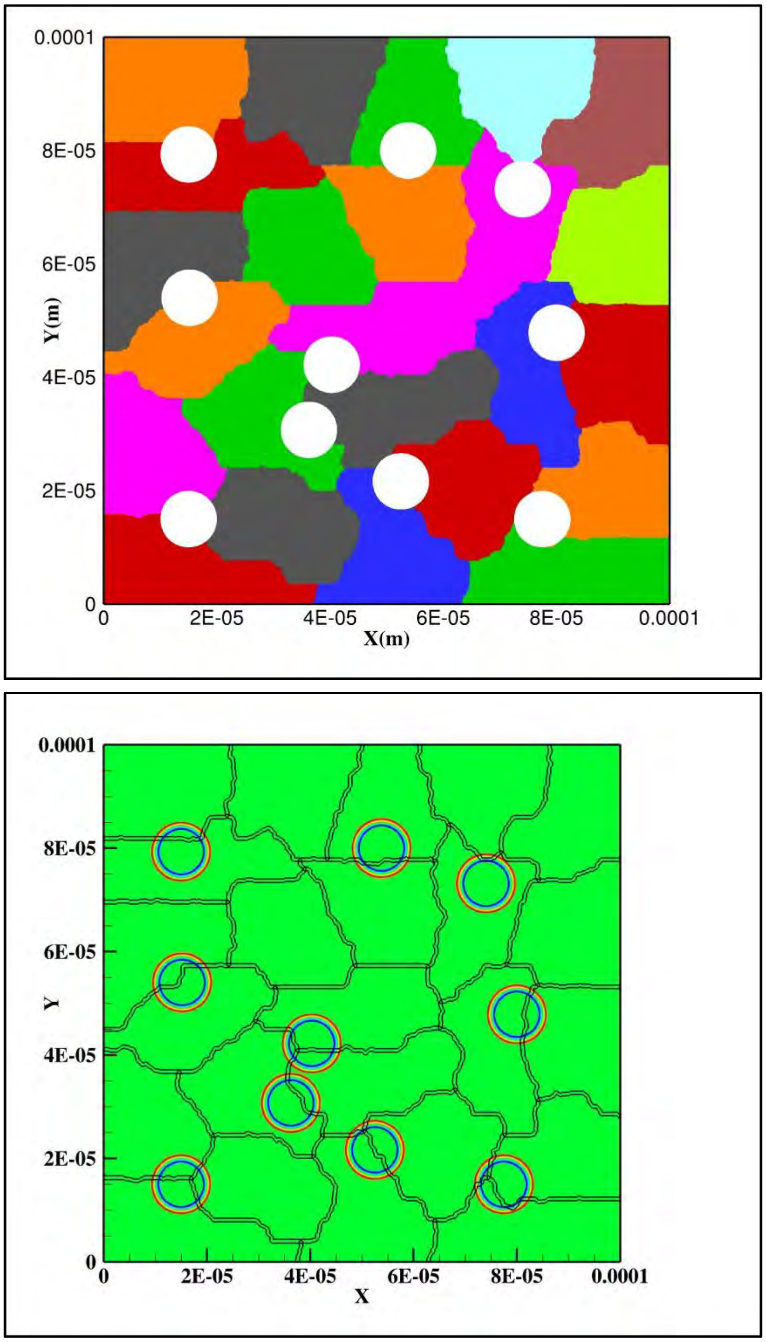

Figure 7-26. Load balanced domain decomposition created using METIS for 10 % volume fraction a) Initial domain consisting of 24 processors with embedded voids b) Voids embedded using level set function in the initial domain

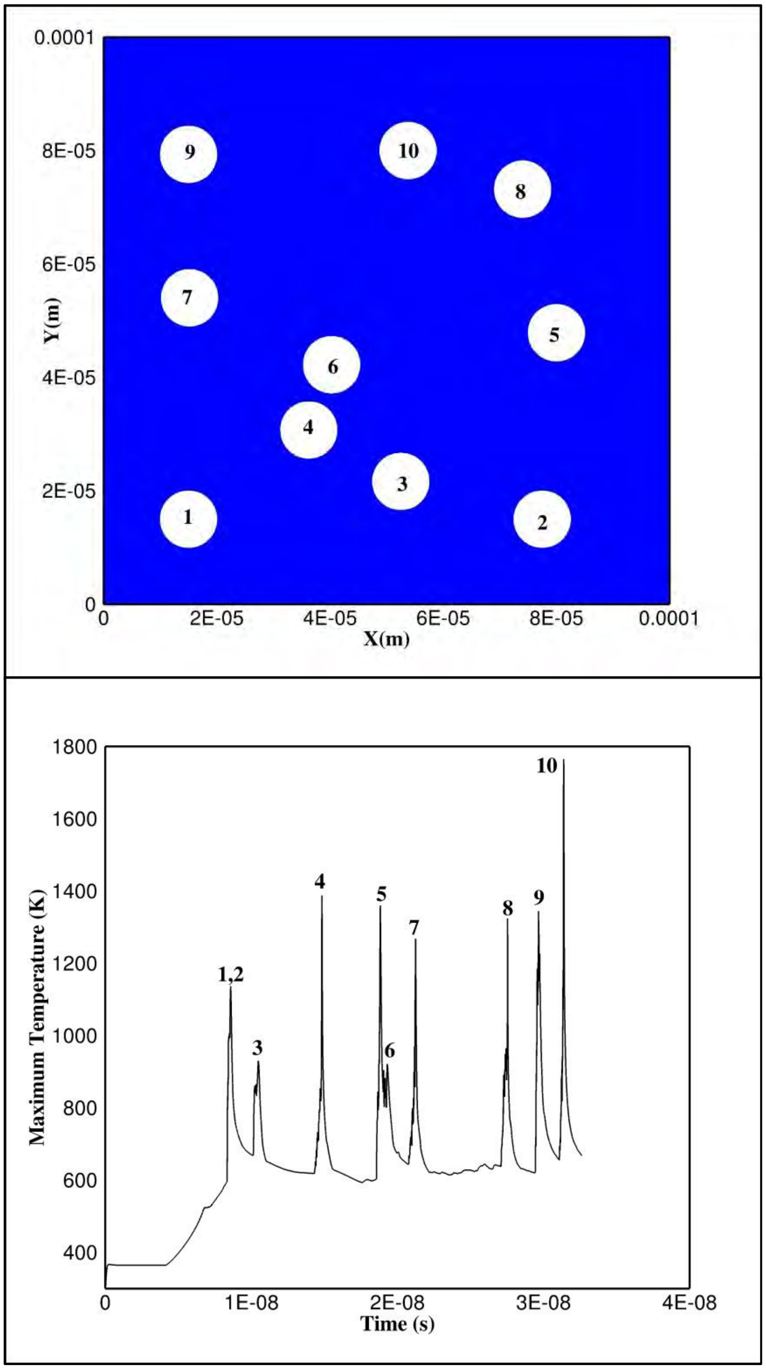

Figure 7-27.Voids as 10% volume fraction in HMX material a) Initial configuration b) Variation of maximum temperature in domain with time. Numbers (1-10) on peaks correspond to collapse of numbered voids in Initial configuration.

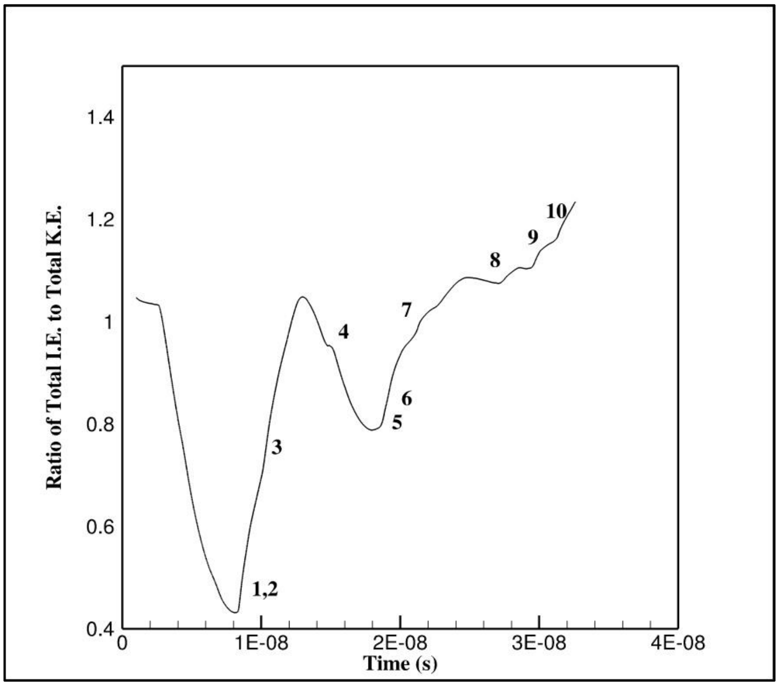

Figure 7-28. Variation of energy distribution with time for domain having voids as 10% volume fraction. Numbers (1-10) correspond to collapse of numbered voids in Initial configuration

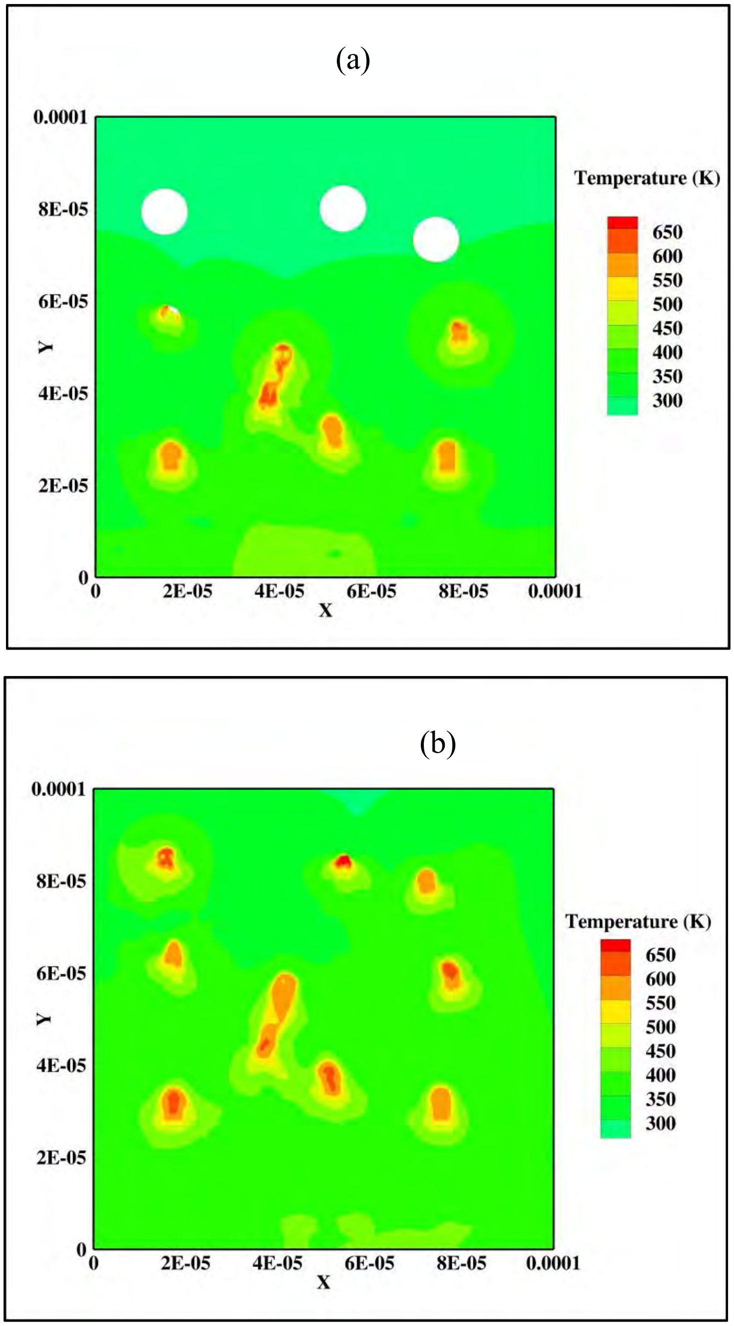

Figure 7-29. Snapshots of temperature field for voids as 10% volume fraction in HMX material at two instants. (a) 18μs (b) 22μs.

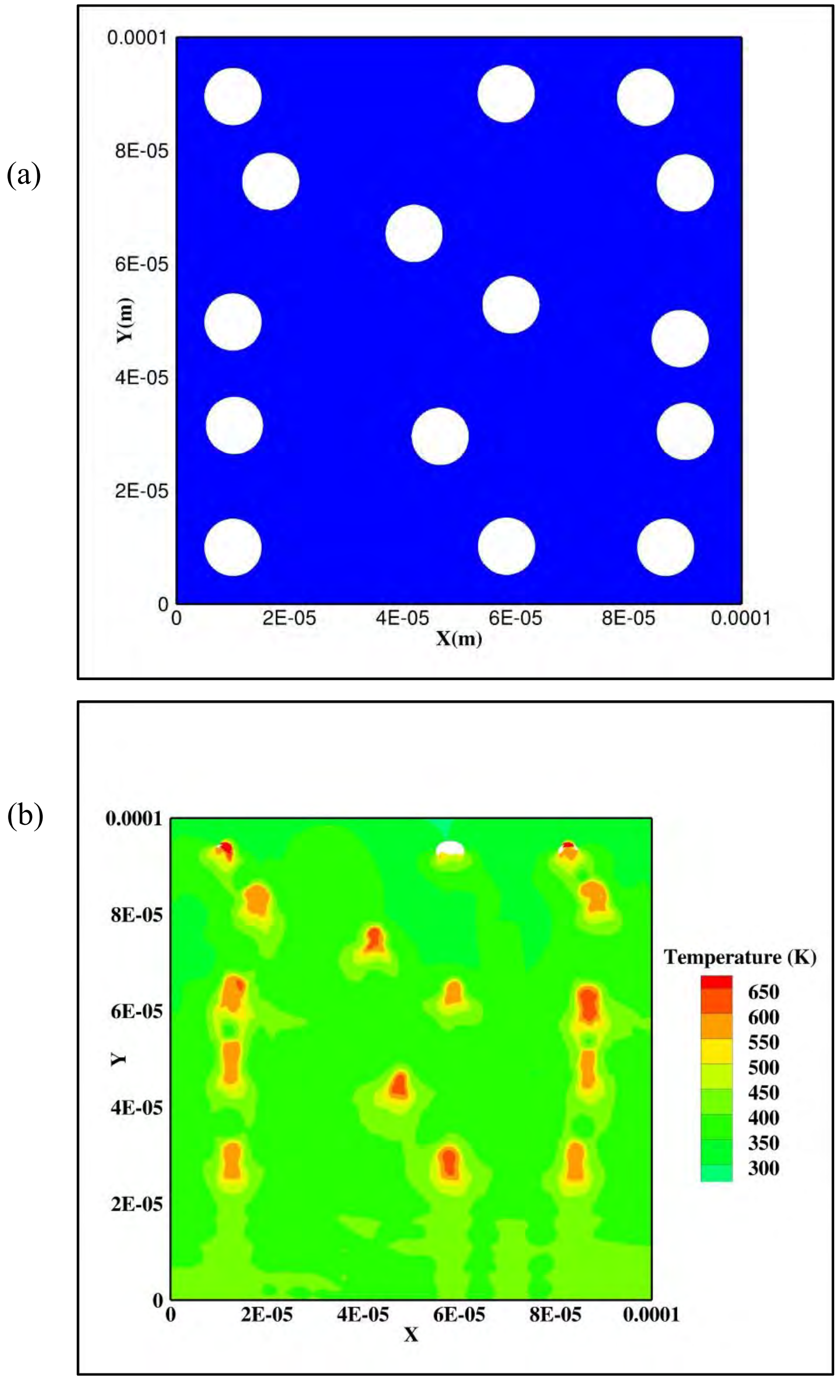

Figure 7-30. Voids as 15% volume fraction in HMX material a) Initial configuration b) Snapshots of temperature field at 32ns.

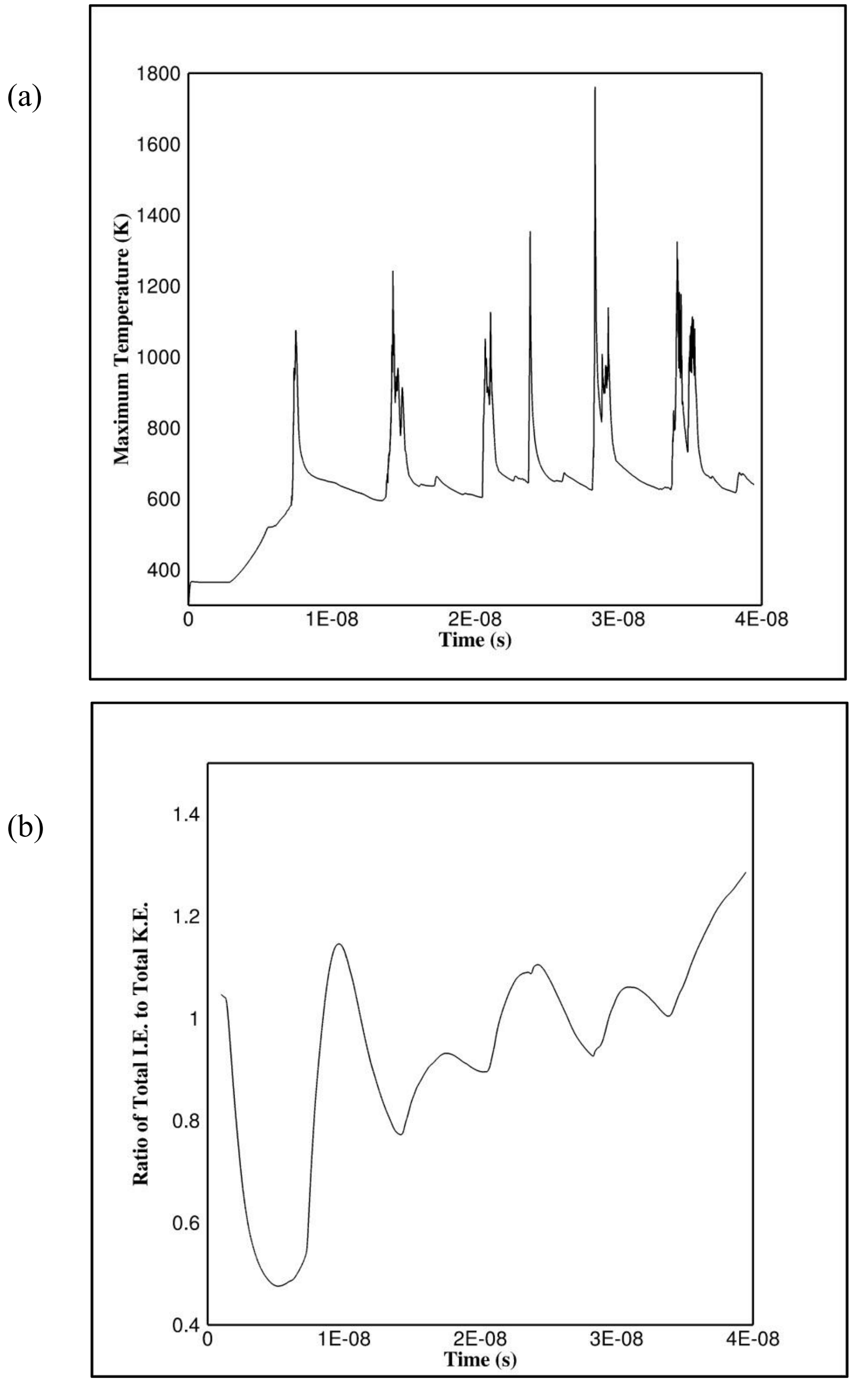

Figure 7-31. Voids as 15% volume fraction in HMX material a) Variation in maximum temperature with time b) Variation in energy distribution with time.

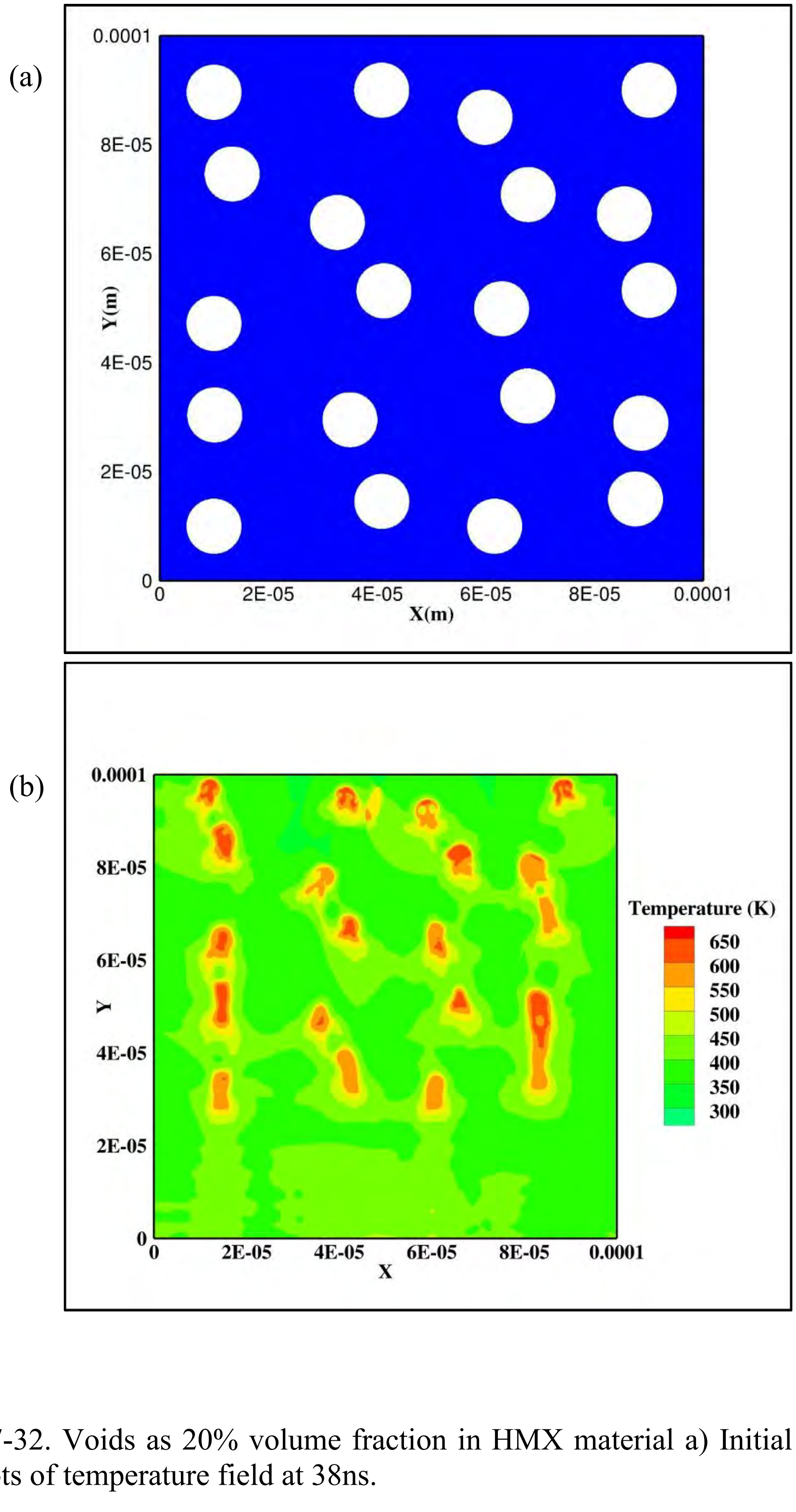

Figure 7-32. Voids as 20% volume fraction in HMX material a) Initial configuration b) Snapshots of temperature field at 38ns.

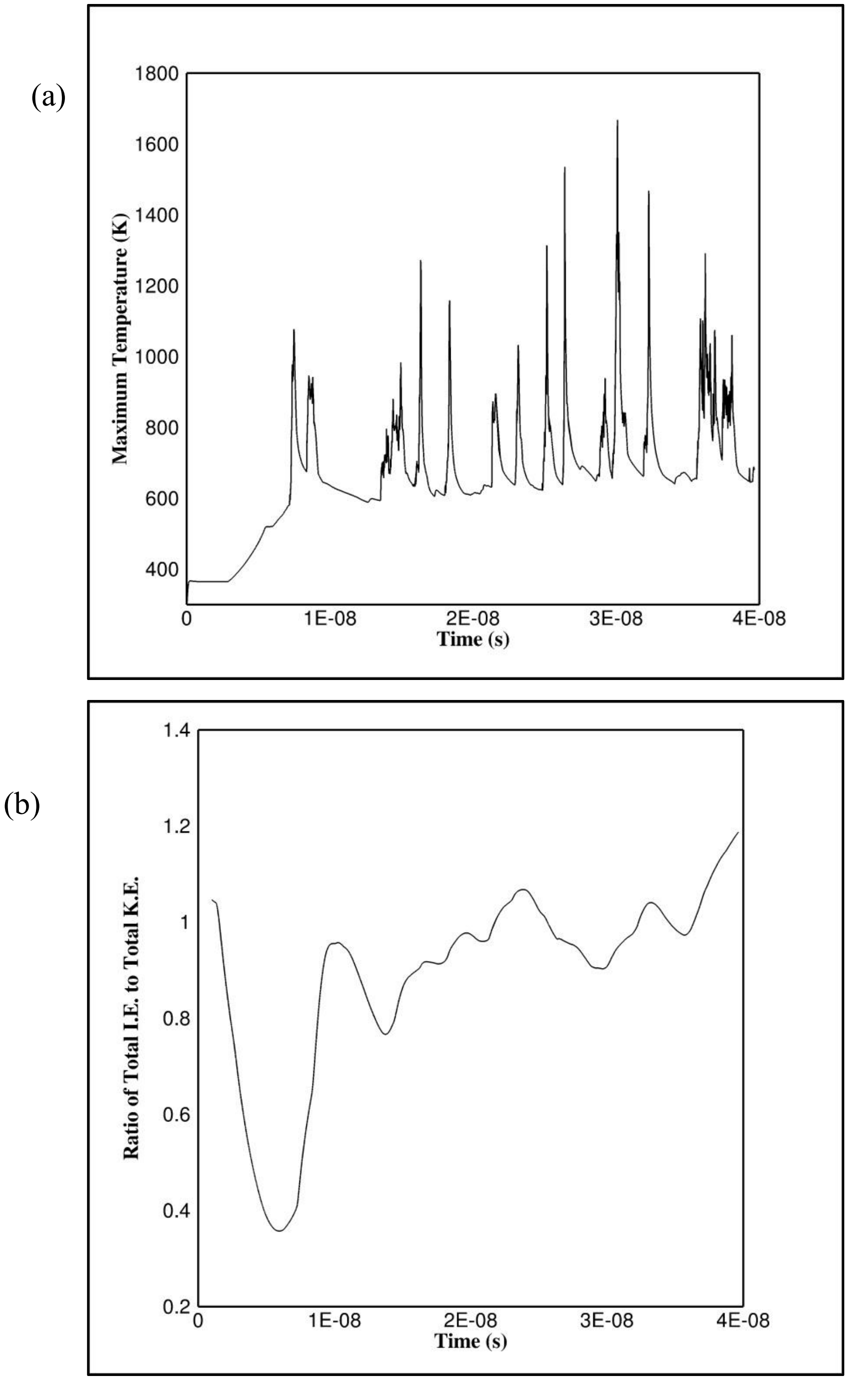

Figure 7-33. Voids as 20% volume fraction in HMX material a) Variation in maximum temperature with time b) Variation in energy distribution with time.

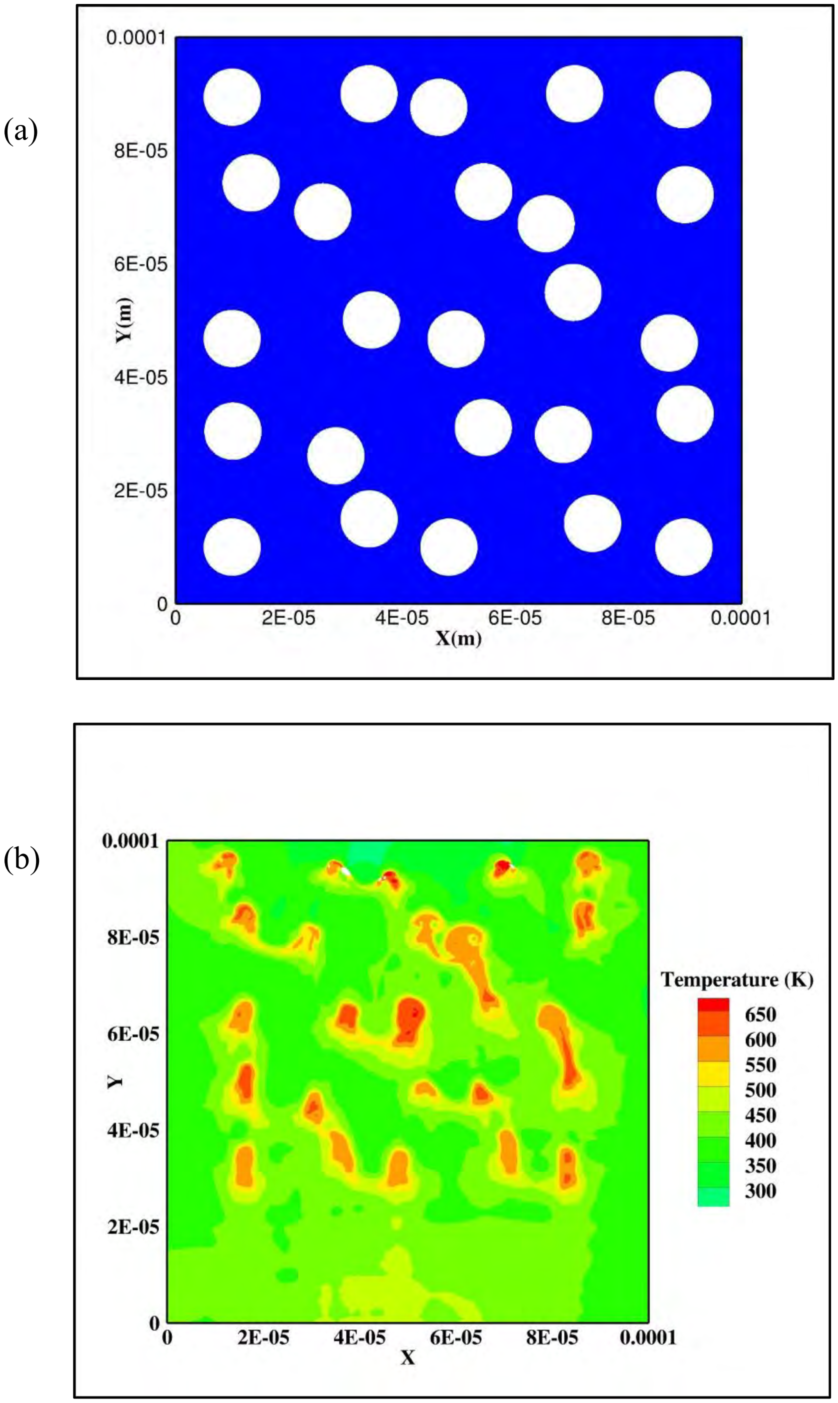

Figure 7-34. Voids as 25% volume fraction in HMX material a) Initial configuration b) Snapshots of temperature field at 40 ns.

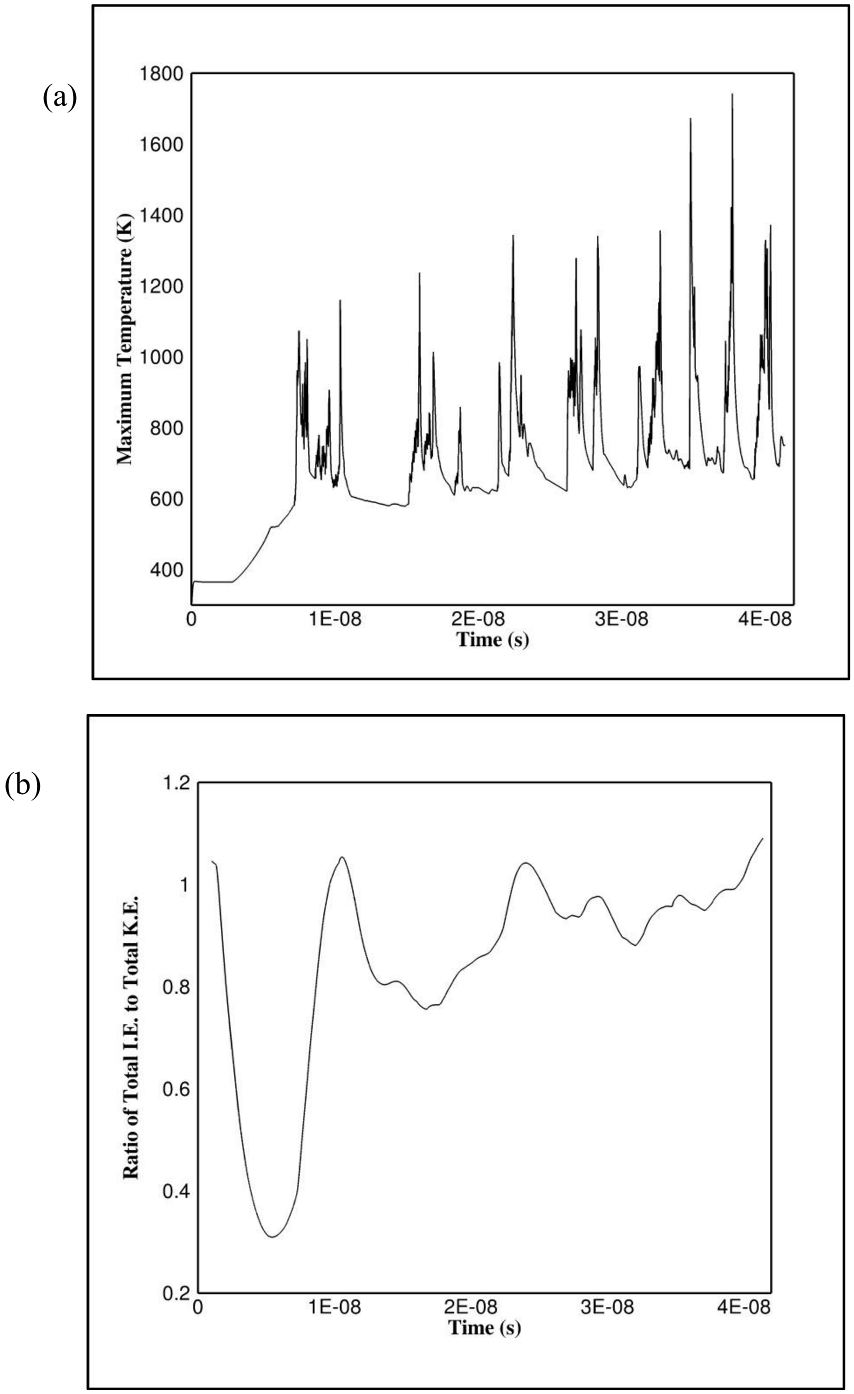

Figure 7-35. Voids as 25% volume fraction in HMX material a) Variation in maximum temperature with time b) Variation in energy distribution with time.

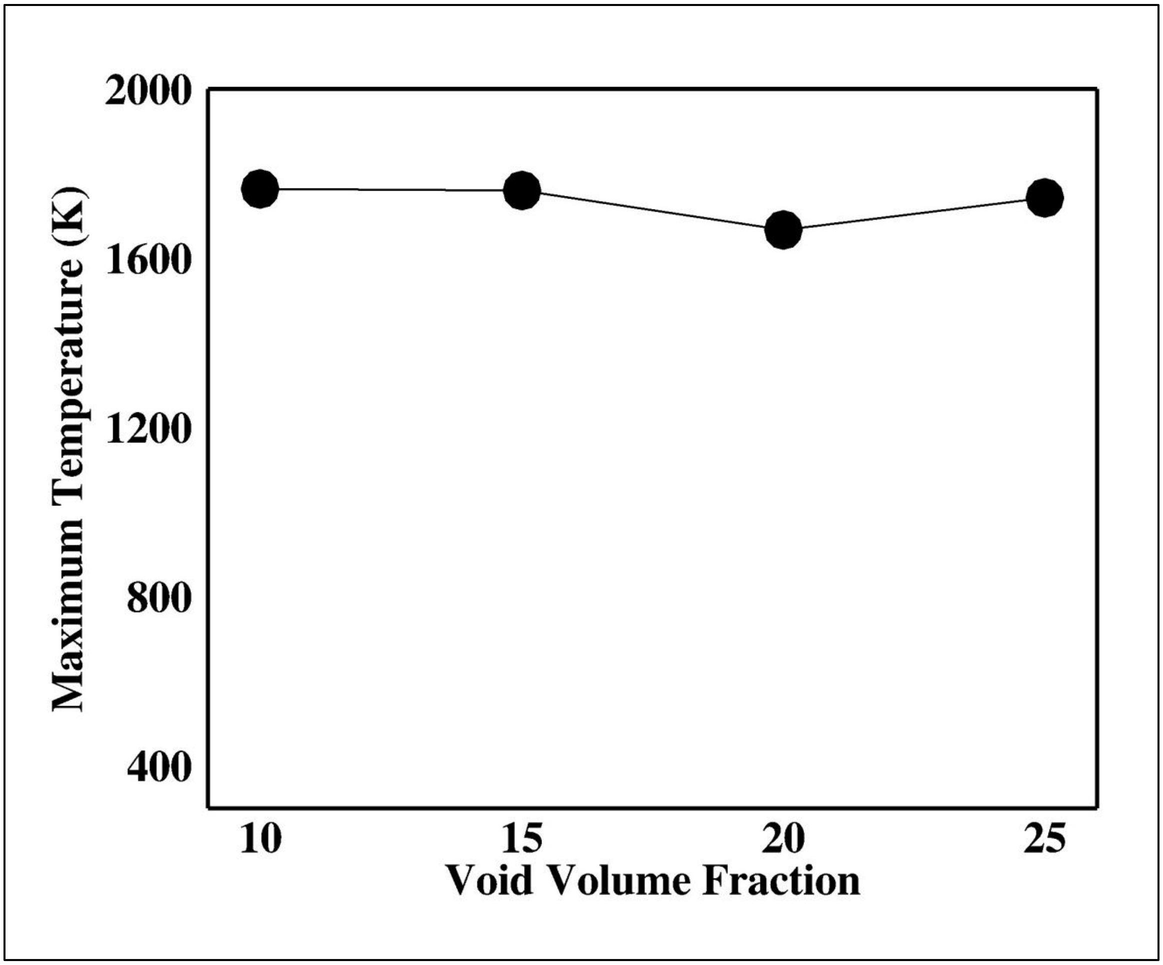

Figure 7-36. Variation of maximum temperature in a given HMX sample as a function of void volume fraction. The shock loading velocity is 500 m/s in all the cases.

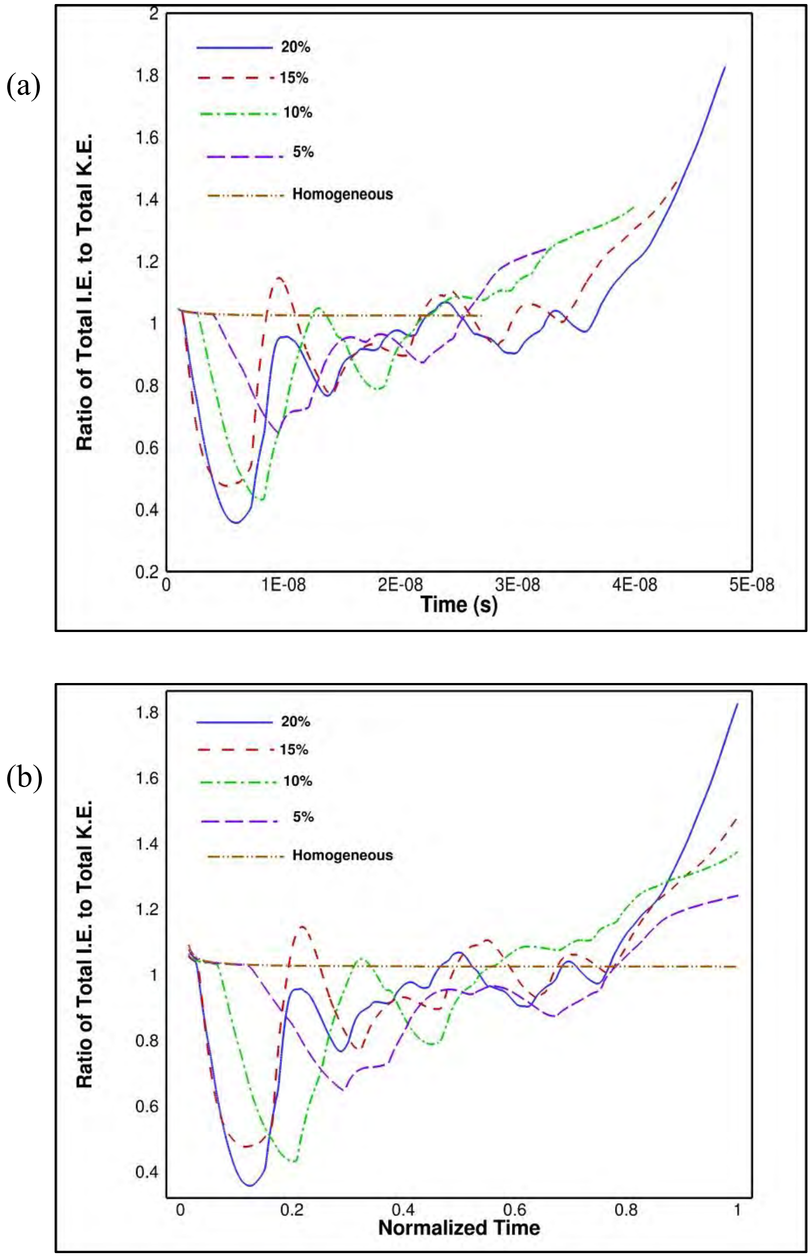

Figure 7-37. Variation of energy distribution for different HMX samples with void volume fraction ranging from 0% (Homogeneous) to 20%. The shock loading velocity is 500 m/s in all the cases. a) Variation with total time b) Variation with normalized time.

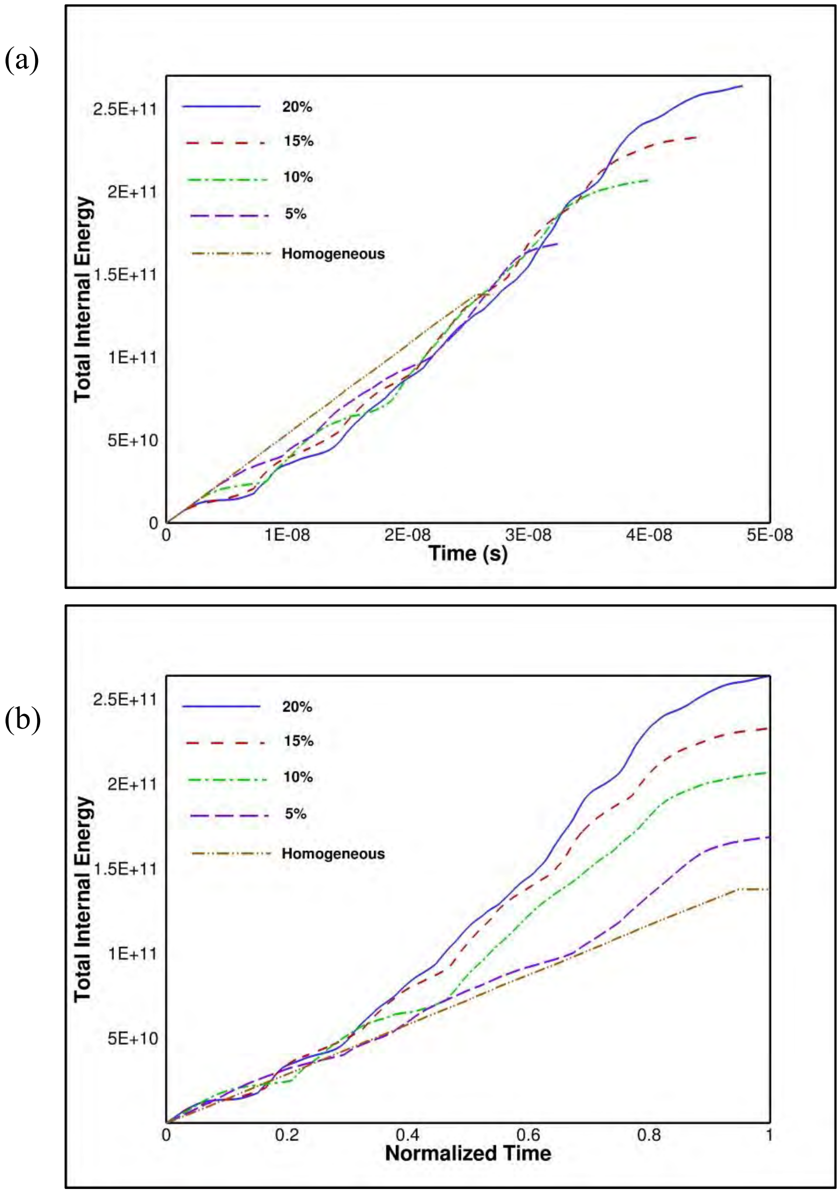

Figure 7-38. Variation of total internal energy for different HMX samples with void volume fraction ranging from 0% (Homogeneous) to 20%. The shock loading velocity is 500 m/s in all the cases. a) Variation with total time b) Variation with normalized time

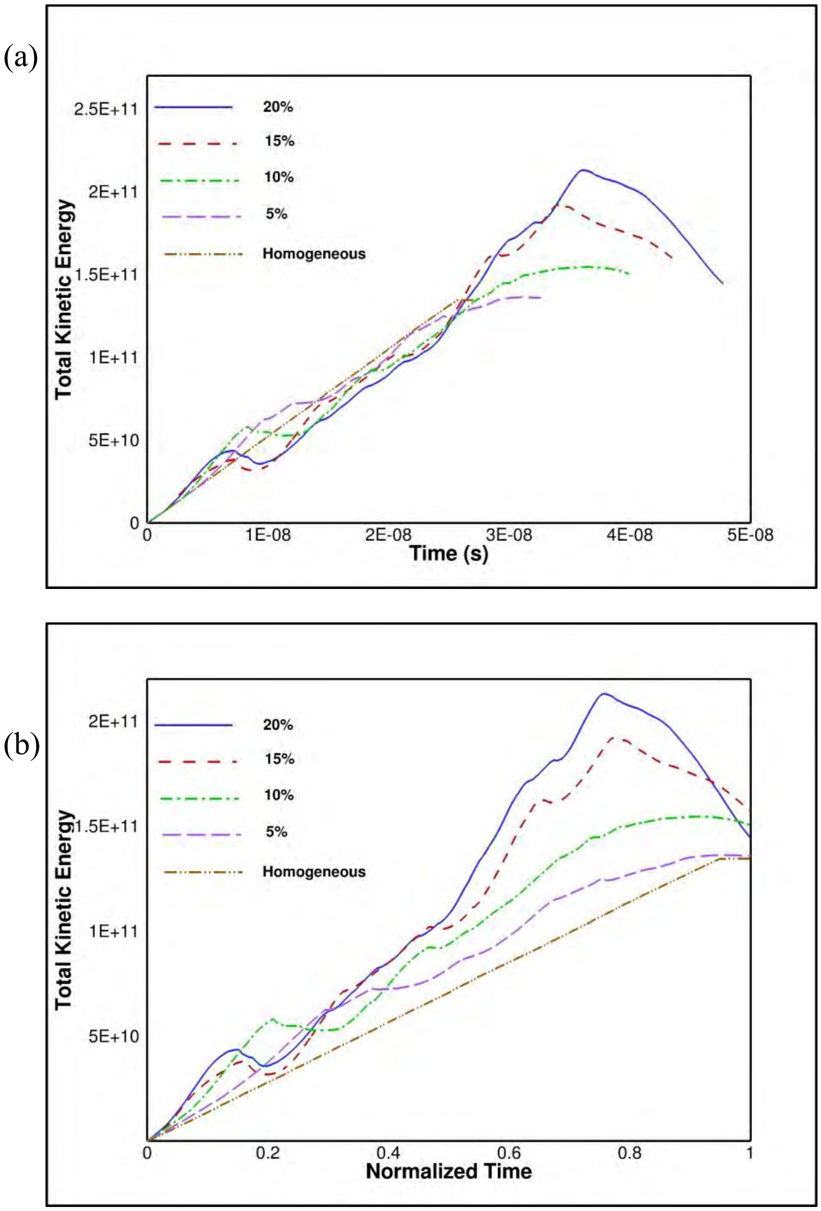

Figure 7-39. Variation of total kinetic energy for different HMX samples with void volume fraction ranging from 0% (Homogeneous) to 20%. The shock loading velocity is 500 m/s in all the cases. a) Variation with total time b) Variation with normalized time.

CHAPTER 8

CONCLUSIONS AND FUTURE WORK

8.1 The Contributions of This Thesis

A Cartesian grid-based three dimensional solver for solving impact, penetration and fragmentation type problems is developed. This work has addressed challenging tasks, specifically

1. The formulation and implementation of Ghost Fluid method in three dimensions was one of the most challenging tasks of this work. The boundary conditions were devised using a physical constraint on the deviatoric stress. The method developed was demonstrated with numerous examples of impact, penetration and fragmentation problems.
2. The efficient handling of level-sets in a parallel processing framework was one of the key contributions of this work. The narrowband method[51] used in this work led to a peculiar situation of corruption of level set field at the processor boundaries. This happened during the passage of an embedded object from one processor to another. An efficient algorithm to handle the level set entry was formulated and implemented. Various numerical examples in the multiprocessor environment for both two and three dimensions were shown to corroborate the successful implementation.
3. The parallelization of flow solver was done using localization of data. The current implementation strictly avoided any array sizes corresponding to global size of the problem. The higher order numerical schemes used in this work required multiple layers of ghost cells. An intelligent stencil mapping algorithm was used to construct the ghost layer. This algorithm avoided the traditional way of constructing ghost layer using recursion resulting in saving of computational time.

4. The developed code was also used to understand the mechanism of void collapse in heterogeneous media. This problem is important both from a performance and hazard standpoint in designing energetic materials for munitions-type application. For the first time the dynamics of the void collapse process in the presence of a collection of void is studied computationally, carrying the computations beyond the collapse stage. Several important physical insights were obtained from this study which included the local void-void interactions to give the overall picture of the material behavior at macro level.

The proposed method shows good agreement with other numerical techniques and experimental results for a wide range of high speed multimaterial interaction problems covering the range of impact, penetration, ejection, collapse, extrusion and fragmentation type problems. In each case careful benchmarking with other numerical results and where available with experimental data has been performed, demonstrating that the technique produces excellent agreement with the available data. In addition, the three-dimensional results shown in this work are first of a kind in an Eulerian framework. This places the current facility at the leading edge of techniques to solve the class of high-speed multimaterial interaction problems of the type targeted by the computer code. The capabilities of the present code are rivaled to some extent only by large scale computer codes developed over many decades at national laboratories such as Los Alamos and Sandia Labs. In fact, a survey of the open literature on advance hydrocodes indicates that the current capabilities may even outperform rival codes in accuracy, versatility and scope.

8.2 Future Work and Extensions

The framework developed in this work can be used to explore many directions. The work here can be extended in following ways:

1. The major emphasis of this work was to solve large scale three dimensional multimaterial problems. Due to the complexity of these problems, the scaling of the computational code was not performed. However the computational code was used to run on hundreds of processor with acceptable computational timings. The foremost task should be to perform a rigorous scaling analysis on 512 cores as a first step towards terra scale and eventually peta scale computing.
2. The local mesh refinement which is the part of serial version of computational code has to be incorporated for parallel computations. This is a challenging task and efforts in directions are currently underway.
3. The addition of reactive mechanics to existing framework can help in better understanding of energetic materials. The incorporation of chemical reactions should be easy to accommodate in this framework as it will just lead to addition of species equations and source terms [92].
4. The results for fragmentation reported in this thesis were without a damage model. The task of replacing numerical damage with a physical damage model is going on. This will help in doing simulations involving highly fragmented geometries and cases with fragmentation events leading to formation of debris.
5. It is shown in this work that individual components of the heterogeneous medium can be resolved in computations. The techniques for representing the energetic material microstructure have evolved [93], so that it is now possible to visualize (through x-ray and gamma-ray CT (computed tomography for example) the detailed microstructure of the material. This work is well established and was demonstrated in Ph.D. thesis of Seth Dillard[94]. The three dimensional solver established in this work can read in details of those meso-structures (in terms of

level set functions) to study the performance as well as hazardous effects of a given energetic material. This exercise of understanding a realistic energetic material can be another task for future.

6. The data intensive study of void collapse phenomena can be used to train an artificial neural network (ANN). This research on the same line was accomplished in the thesis work of Chris Lu[95] where data on the forces experienced by particles in a cloud are collected from DNS using a compressible Eulerian solver and provided to an artificial neural network (ANN). The simulations were performed for a range of control parameters, such as Mach number, particle radii, particle-fluid density ratio, position, and volume fraction. The same idea can be extended to study the voids for a range of void sizes, loading velocities, void volume fraction, and void locations. The trained ANN can be used for computing the macro-scale flow behavior in a sample of energetic material. This work is currently under development.

REFERENCES

1. J.Baker and A.Williams, *Hypervelocity penetration of plate targets by rod and rod-like projectiles.* International Journal of Imapact Engineering., 1987. **5**(1-4): p. 101-110.

2. Ahrens, T.J. and J. D.O'keefe, *Impact on the earth, ocean and atmosphere.* International Journal of Imapact Engineering., 1987. **5**(1-4): p. 13-32.

3. Benson, D. and W. Nellis, *Dynamic compaction of copper powder: Computation and experiment.* Applied Physics Letters, 2009. **65**(4): p. 418-420.

4. Smartt, S., et al., *The death of massive stars–I. Observational constraints on the progenitors of Type II P supernovae.* Monthly Notices of the Royal Astronomical Society, 2009. **395**(3): p. 1409-1437.

5. Liu, W., et al., *Metallic glass coating on metals plate by adjusted explosive welding technique.* Applied Surface Science, 2009. **255**(23): p. 9343-9347.

6. Walters, W.P. and J.A. Zukas., *Fundamentals of Shaped Charges.* 1989: Wiley-Interscience.

7. Udaykumar, H.S., et al., *An Eulerian method for computation of multi-material impact with ENO shock-capturing and sharp interfaces.* Journal of Computational Physics., 2003. **186**(1).

8. J.Benson, D., *Computational methods in lagrangian and eulerian hydrocodes.* Comput. Methods Appl. Mech. Eng., 1995. **99**(2-3): p. 235-394.

9. Anderson, C.E., *An overview of the theory of hydrocodes.* International Journal of Imapact Engineering., 1987. **5**(1-4): p. 33-59.

10. Sambasivan, S.K. and H. UdayKumar, *Sharp interface simulations with Local Mesh Refinement for multi-material dynamics in strongly shocked flows.* Computers & Fluids, 2010. **39**(9): p. 1456-1479.

11. Camacho.G.T. and M.Ortiz., *Adaptive lagrangian modelling of ballistic penetration of metallic targets.* Comput. Methods Appl. Mech. Eng., 1997. **142**(3-4): p. 269-301.

12. Cooper, S., D. Benson, and V. Nesterenko, *A numerical exploration of the role of void geometry on void collapse and hot spot formation in ductile materials.* International Journal of Plasticity, 2000. **16**(5): p. 525-540.

13. Yoo, Y.H. and M. Lee, *A three-dimensional FE analysis of large deformations for impact loadings using tetrahedral elements.* Computational mechanics, 2003. **30**(2): p. 96-105.

14. Paik, S., et al., *Parallel performance of large scale impact simulations on Linux cluster super computer.* Computers & Structures, 2006. **84**(10-11): p. 732-741.

15. Hu, W., L. Guang Yao, and Z. Zhi Hua, *Parallel point interpolation method for three-dimensional metal forming simulations.* Engineering analysis with boundary elements, 2007. **31**(4): p. 326-342.

16. Zhou, C., G. Liu, and K. Lou, *Three-dimensional penetration simulation using smoothed particle hydrodynamics.* International Journal of Computational Methods, 2007. **4**(4): p. 671-692.

17. Belytschko, T., P. Krysl, and Y. Krongauz, *A three dimensional explicit element free galerkin method.* International Journal for Numerical Methods in Fluids, 1997. **24**(12): p. 1253-1270.

18. Kothe, D., et al., *PAGOSA: A massively-parallel, multi-material hydro-dynamics model for three-dimensional high-speed flow and high-rate deformation*. 1992, technical report la-ur-92-4306, Los Alamos National Laboratory.

19. Bordas, S., T. Rabczuk, and G. Zi, *Three-dimensional crack initiation, propagation, branching and junction in non-linear materials by an extended meshfree method without asymptotic enrichment.* Engineering Fracture Mechanics, 2008. **75**(5): p. 943-960.

20. Souli, M., A. Ouahsine, and L. Lewin, *ALE formulation for fluid-structure interaction problems.* Computer methods in applied mechanics and engineering, 2000. **190**(5-7): p. 659-675.

21. Finnegan, S., et al. *A study of obliquity effects on perforation and ricochet processes in thin plates impacted by compact fragments*. in *Proc. 14th Int. Symp. Ballistics*. 1993.

22. Ma, S. and X. Zhang, *Material Point Method for Impact and Explosion Problems.* Computational Mechanics, 2009: p. 156-166.

23. Ma, S., X. Zhang, and X. Qiu, *Comparison study of MPM and SPH in modeling hypervelocity impact problems.* International Journal of Impact Engineering, 2009. **36**(2): p. 272-282.

24. Naghdi, P., *A critical review of the state of finite plasticity.* Zeitschrift für Angewandte Mathematik und Physik (ZAMP), 1990. **41**(3): p. 315-394.

25. Xiao, H., O. Bruhns, and A. Meyers, *Elastoplasticity beyond small deformations.* Acta Mechanica, 2006. **182**(1): p. 31-111.

26. Tran, L.B. and H.S. UdayKumar., *A particle levelset based sharp interface cartesian grid method for impact, penetration, and void collapse.* Journal of Computational Physics., 2004. **193**(2): p. 469-510.

27. Wu., H.-C., *Continuum Mechanics and Plasticity.* 2004: Chapman & Hall/CRC Press.

28. Khan, A. and S. Huang, *Continuum theory of plasticity*. 1995: Wiley New York.

29. Truesdell, C., *A first course in rational continuum mechanics*. Vol. 1. 1977: Academic Press.

30. Van der Pijl, S., et al., *A mass conserving Level Set method for modelling of multi phase flows.* International Journal for Numerical Methods in Fluids, 2005. **47**(4): p. 339-361.

31. Nourgaliev, R., et al., *On improving mass conservation of level set by reducing spatial discretization errors.* Int. J. Multiphase Flow, 2005. **31**(12): p. 1329–1336.

32. Sethian, J.A., *Level set methods and fast marching methods.* Journal of Computing and Information Technology, 2003. **11**(1): p. 1-2.

33. Adalsteinsson, D. and J.A. Sethian, *The Fast Construction of Extension Velocities in Level Set Methods* 1.* Journal of Computational Physics, 1999. **148**(1): p. 2-22.

34. Paik, S.H., et al., *Parallel performance of large scale impact simulations on Linux cluster super computer.* Computers & structures, 2006. **84**(10-11): p. 732-741.

35. Baer, M. and J. Nunziato, *A two-phase mixture theory for the deflagration-to-detonation transition (DDT) in reactive granular materials.* International journal of multiphase flow, 1986. **12**(6): p. 861-889.

36. Udaykumar, H., et al., *An Eulerian method for computation of multimaterial impact with ENO shock-capturing and sharp interfaces.* Journal of Computational Physics, 2003. **186**(1): p. 136-177.

37. R.P.Fedkiw, et al., *A non oscillatory Eulerian approach to interfaces in multi-material flows (the Ghost Fluid Method).* Journal of Computational Physics., 1999. **152**(2): p. 457-492.

38. Kapahi, A., S.Sambasivan, J.Mousel and H.S.Udaykumar, *3-dimensional Sharp-Interface Eulerian computations of high speed impact, penetration and fragmentation.* submitted to Journal of Computational Physics., 2011.

39. Kapahi, A., J.Mousel, S.Sambasivan and H.S.Udaykumar, *Three Dimensional Compressible Multi-material Flow Computations Using a Parallelized Levelset-based Solver.*, in *Plasticity of Crystalline Materials: From Dislocations to Continuum*. 2011, John Wiley & Sons.

40. Sambasivan, S., A.Kapahi and H.S.Udaykumar, *Simulation of high speed impact, penetration and fragmentation problems on locally refined Cartesian grids.* submitted to Journal of Computational Physics., 2011.

41. Liu, X. and S. Osher, *Convex ENO high order multi-dimensional schemes without field by field decomposition or staggered grids.* Journal of Computational Physics, 1998. **142**(2): p. 304-330.

42. Simo, J. and T. Hughes, *General return mapping algorithms for rate-independent plasticity*. 1987: Elsevier: Tucson, Arizona.

43. Johnson, G.R. and W.H. Cook, *Fracture characteristics of three metals subjected to various strains, strain rates, temperatures and pressures.* Engineering Fracture Mechanics, 1985. **21**(1): p. 31-48.

44. Ponthot., J.-P., *Unified stress update algorithms for numerical simulation of large deformation elasto-plastic and elasto-viscoplastic process.* International Journal of Plasticity., 2002. **18**(1): p. 91-126.

45. Zel'Dovich, Y.B. and Y.P. Raizer, *Physics of shock waves and high-temperature hydrodynamic phenomena*. 2002: Dover Pubns.

46. Ponthot, J.P., *An extension of the radial return algorithm to account for rate-dependent effects in frictional contact and visco-plasticity.* Journal of Materials Processing Technology, 1998. **80**: p. 628-634.

47. J.C.Simo and T.J.R. Hughes., *Computational Inelasticity.* 2000: Springer.

48. Glimm, J., D. Marchesin, and O. McBryan, *A numerical method for two phase flow with an unstable interface.* Journal of Computational Physics, 1981. **39**(1): p. 179-200.

49. C.W.Shu and S.Osher., *Efficient implementation of Essentially Non-Oscillatory shock capturing schemes II.* Journal of Computational Physics., 1989. **83**(1): p. 32-78.

50. Sethian., J.A., *Levelset Methods and Fast Marching Methods: Evolving Interfaces in computaional geometry, Fluid Mechanics, Computer Vision, and Material Science.* 1999: Cambridge University Press.

51. J.A.Sethian., *Evolution, implementation, application of levelsets and fast marching methods for advancing fronts.* Journal of Computational Physics., 2001. **169**(2): p. 503-555.

52. Dalrymple, R.A., *Particle Methods and Waves, with Emphasis on SPH.* 2007.

53. Kang, M., R. Fedkiw, and X. Liu, *A boundary condition capturing method for multiphase incompressible flow.* Journal of Scientific Computing, 2000. **15**(3): p. 323-360.

54. Gropp, W., E. Lusk, and A. Skjellum, *Using mpi*. 1999: MIT press.

55. Karypis, G., K. Schloegel, and V. Kumar, *Parmetis---parallel graph partitioning and sparse matrix ordering library, version 2.0.* Univ. of Minnesota, Minneapolis, MN, 1998.

56. Peigin, S., et al., *Parallel large scale high accuracy Navier-Stokes computations on distributed memory clusters.* The Journal of Supercomputing, 2004. **27**(1): p. 49-68.

57. Cormen, T., *Introduction to algorithms*. 2001: The MIT press.

58. Carter, J. and M. Wegman, *Universal classes of hash functions.* Journal of computer and system sciences, 1979. **18**(2): p. 143-154.

59. Udaykumar, H., S. Krishnan, and S. Marella, *Adaptively refined, parallelised sharp interface Cartesian grid method for three-dimensional moving boundary problems.* International Journal of Computational Fluid Dynamics, 2009. **23**(1): p. 1-24.

60. Sambasivan, S. and H.S. Udaykumar., *Ghost fluid method for Strong Shock Interactions. Part2: Immersed Solid Boundaries.* AIAA., 2009. **47**(10): p. 2923-2937.

61. Emery, A., *An evaluation of several differencing methods for inviscid fluid flow problems.* Journal of Computational Physics, 1968. **2**(3): p. 306-331.

62. Woodward, P. and P. Colella, *The numerical simulation of two-dimensional fluid flow with strong shocks.* Journal of Computational Physics, 1984. **54**(1): p. 115-173.

63. Nourgaliev, R., T. Dinh, and T. Theofanous, *The Characteristics-Based matching (CBM) method for compressible flow with moving boundaries and interfaces.* TRANSACTIONS-AMERICAN SOCIETY OF MECHANICAL ENGINEERS JOURNAL OF FLUIDS ENGINEERING, 2004. **126**: p. 586-604.

64. Taylor., G.I., *The use of flat ended projectiles for determining dynamic yield stress. i. theoretical considerations.* Proceedings of the Royal Society of London. Series A. Mathematical and Physical Sciences., 1948. **194**: p. 289-299.

65. Fedorov, A., Y. Kharlamova, and T. Khmel', *Reflection of a shock wave in a dusty cloud.* Combustion, Explosion, and Shock Waves, 2007. **43**(1): p. 104-113.

66. Meyers, M., *Dynamic behavior of materials*. 1994: Wiley-Interscience.

67. Zhu, Y. and S. Cescotto, *Unified and mixed formulation of the 4 node quadrilateral elements by assumed strain method: Application to thermomechanical problems.* International journal for numerical methods in engineering, 1995. **38**(4): p. 685-716.

68. Gray III, G., et al. *Influence of Shock Prestraining and Grain Size on the Dynamic Tensile Extrusion Response of Copper: Experiments and Simulation*. in *AIP Conference Proceedings*. 2006.

69. Lee, E. and C. Tarver, *Phenomenological model of shock initiation in heterogeneous explosives.* Physics of Fluids, 1980. **23**: p. 2362.

70. Menikoff, R. and T. Sewell, *Constituent properties of HMX needed for mesoscale simulations.* Combustion Theory and Modelling, 2002. **6**(1): p. 103-125.

71. Bowden, F., A. Yoffe, and P. Levy, *Fast reactions in solids.* Physics Today, 1959. **12**: p. 58.

72. Chaudhri, M. and J. Field, *The role of rapidly compressed gas pockets in the initiation of condensed explosives.* Proceedings of the Royal Society of London. Series A, Mathematical and Physical Sciences, 1974. **340**(1620): p. 113-128.

73. Mader, C., *Numerical modeling of explosives and propellants*. 1998: CRC Pr I Llc.

74. Khasainov, B., et al. *Two-phase visco-plastic model of shock initiation of detonation in high density pressed explosives*. in *7th Symposium (International) on Detonation, Annapolis, MD*. 1981.

75. Field, J., *Hot spot ignition mechanisms for explosives.* Accounts of Chemical Research, 1992. **25**(11): p. 489-496.

76. Baer, M., *Modeling heterogeneous energetic materials at the mesoscale.* Thermochimica Acta, 2002. **384**(1-2): p. 351-367.

77. Menikoff, R. and E. Kober. *Compaction waves in granular HMX*. in *AIP Conference Proceedings*. 2000: IOP INSTITUTE OF PHYSICS PUBLISHING LTD.

78. Baer, M., *Mesoscale modeling of shocks in heterogeneous reactive materials.* ShockWave Science and Technology Reference Library, 2007: p. 321-356.

79. Tran, L. and H. Udaykumar, *Simulation of void collapse in an energetic material, Part 1: Inert case.* Journal of propulsion and power, 2006. **22**(5): p. 947.

80. Wackerle, J., et al., *Symposium (International) on High Dynamic Pressures*. 1978, Commissariat a l'Energie Atomique, Paris.

81. Tarver, C.M. *What is a Shock Wave to an Explosive Molecule?* in *AIP Conference Proceedings*. 2002.

82. Anslyn, E.V. and D.A. Dougherty, *Modern physical organic chemistry*. 2006: University Science Books.

83. Zhang, F., P.A. Thibault, and R. Link, *Shock interaction with solid particles in condensed matter and related momentum transfer.* Proceedings of the Royal Society of London. Series A: Mathematical, Physical and Engineering Sciences, 2003. **459**(2031): p. 705.

84. Tran, L. and H. Udaykumar, *Simulation of void collapse in an energetic material, Part 2: Reactive case.* Journal of propulsion and power, 2006. **22**(5): p. 959-974.

85. Frost, D., T. Aslam, and L. Hill. *Application of detonation shock dynamics to the propagation of a detonation in nitromethane in a packed inert particle bed*. in *AIP Conference Proceedings*. 2000.

86. Reaugh, J., *Grain-scale dynamics in explosives*. 2002, Lawrence Livermore National Lab., CA (US).

87. Benson, D., *Computational methods in Lagrangian and Eulerian hydrocodes.* Computer methods in Applied mechanics and Engineering, 1992. **99**(2-3): p. 235-394.

88. MALI, V., V. PAI, and A. SKOVPIN, *Study of the disintegration of plane jets(on grooved metal surfaces).* Fizika Goreniia i Vzryva, 1974. **10**: p. 755-761.

89. Swantek, A. and J. Austin, *Collapse of void arrays under stress wave loading.* Journal of Fluid Mechanics, 2010. **649**(1): p. 399-427.

90. Brujan, E., *Cavitation in Non-Newtonian Fluids: With Biomedical and Bioengineering Applications*. 2010: Springer Verlag.

91. Johnsen, E. and T. Colonius, *Numerical simulations of non-spherical bubble collapse.* J. Fluid Mech, 2009. **629**: p. 231â€“262.

92. Fedkiw, R.P., B. Merriman, and S. Osher, *High accuracy numerical methods for thermally perfect gas flows with chemistry.* Journal of computational physics, 1997. **132**(2): p. 175-190.

93. Wellington, S. and H. Vinegar, *X-ray computed tomography.* J. Pet. Technol, 1987. **39**: p. 885-898.

94. Dillard, S.I., *Image based modeling of complex boundaries*. 2012, THE UNIVERSITY OF IOWA.

95. Lu, C., *Artificial neural network for behavior learning from meso-scale simulations, application to multi-scale multimaterial flows.* 2010.